ABSTRACT

Title of dissertation: SEMI-ACTIVE SIX DEGREE OF FREEDOM VIBRATION CONTROL

Nicholas Louis Wilson
Doctor of Philosophy, 2012

Dissertation directed by: Professor Norman M. Wereley
Department of Aerospace Engineering

This body of work develops a modular, semi-active isolation suspension for 6-DOF vibration control of ground support equipment near a rocket launch. The objective is to provide vibration and shock attenuation for a broad disturbance spectrum with semi-actively controlled magnetorheological (MR) dampers. MR dampers have adaptable rheological properties that can be quickly altered by the application of an external magnetic field, allowing the device to be tailored to the source disturbance. These changes are large, reversible, and rapid (10^{-3} s), which make MR fluid an excellent medium for mechanical vibration damping.

This work addresses several practical issues the MR suspension may face, including perturbations in operating temperature, payload mass, and center of gravity. A model of a single, linear-stroke MR damper is developed to capture the force behavior for practical operating temperatures between 0^0C and 100^0C. The impact of temperature and payload mass on the attenuation performance is evaluated through a simplified 1-DOF system. The analysis is extended to a multi-damper suspension for 6-DOF vibration control and a mathematical model is derived to describe the system dynamics. Several control laws are formulated in the 6-DOF framework, considering both centralized and decentralized algorithms. The mathematical model is validated experimentally with a full-scale, deliverable system tested at George Washington University's Earthquake Engineering Laboratory shake table in response to simulated disturbances from NASA's Space Shuttle Mobile Launch Platform during the STS-31 launch. The model is used to analyze the attenuation ability of the suspension considering MR damper orientation, control strategy, and perturbations in payload mass, center of gravity location, and operating temperature.

The semi-active suspension is shown to be a robust, adaptable solution with low power consumption requirements compared to the state of the art.

SEMI-ACTIVE SIX DEGREE OF FREEDOM VIBRATION CONTROL

by

Nicholas Louis Wilson

Dissertation submitted to the Faculty of the Graduate School of the
University of Maryland, College Park in partial fulfillment
of the requirements for the degree of
Doctor of Philosophy
2012

Advisory Committee:
Professor Norman M. Wereley, Chair/Advisor
Professor Inderjit Chopra
Professor Sung Lee
Professor Allison Flatau
Professor Amr Baz

Dedication

This work is dedicated to my mother, Colleen, my north star in the night sky, and to my late grandfather, Louis Lieb (Poppy), who saw and nurtured in me infinite potential.

Acknowledgments

> “Attitudes are contagious, so make sure yours is worth catching.”

These are the individuals that infected me with inspiration and encouragement.

First and foremost, my graduate advisor, Prof. Norman Wereley, deserves much credit. He gave me the opportunity to do exciting research and obtain my graduate degrees at the University of Maryland. Ever since he shook my hand and said “Welcome to the team”, he has created a great environment to conduct research. His guidance, patience, expertise, and financial and moral support have been invaluable.

Thank you to professors Amr Baz, Inderjit Chopra, Allison Flatau, and Sung Lee for serving on my Ph.D. defense committee and providing insightful comments on this dissertation.

Thank you to Stanley Starr and Curtis Ihlefeld at NASA for supporting my research through the DoD STTR program and for hosting me at Kennedy Space Center through the GSRP fellowship program during the summer of 2009.

Thank you to Greg Hiemenz at Techno-Sciences, Inc. for giving me the opportunity to work on challenging and exciting research projects. When it came to the business side of engineering, you taught me how to be a salesman in the sense of clearly identifying the problem and clearly presenting the solution. Thank you also to Pete Chen for the opportunity to work with Techno-Sciences, Inc. during my graduate career.

Thank you to Mike Perna and Howie Grossenbacher for all of your machining and welding services that supported all my experimental work.

Young-Tai Choi (Dr. Choi), thank you for all that you have taught me. While your jocular personality precedes your intellect, the latter must not be overlooked. Your wealth of knowledge amazed me daily.

Wei (Peter) Hu, thank you for teaching me all I know about MR damper construction. Peter's work ethic and mastery of mechanical design has left me to believe him to be the epitome of what an engineer ought to be.

Thank you to Ben Woods for your friendship and your witty, playful humor. Your presence is always uplifting. There has never been a day in which I've seen you with a bad attitude. Our many long nights camped out in the Manufacturing Building, fooling around instead of completing our homework assignments that were due the next day, will not be forgotten. You are a brilliant individual and I thank you for all the things you have taught me. Your passion for discovering how things work and innovating original solutions to engineering problems is inspiring.

Thank you to all my grad school friends and partners in crime who kept me sane and provided appropriate distractions during my graduate school years. If not for you, one of two things would have happened - I would never have finished my doctoral degree or I would have completed it much sooner. For all the happy hours, soccer games, musical jam sessions, road trips, and practice zombie-apocalypse shooting conventions, I thank you Robbie, Ben, Becnel, Greg, Conroy, Aaron, Hyslop, Hari, Jürgen, Grum, Ted, Ami, Brandon, and the rest of my fellow grad students.

Thank you to Prof. William Fourney for inspiring me at the beginning of my undergraduate studies to study aerospace engineering. Thank you to Nick Rosenfeld, who gave me my first exposure to graduate research. I was comforted through your explanation that with research it is sometimes okay to completely not know what you are doing. Thank you also to my close friends Dan Volk and Ed Nowottnick, as well as the retired airline pilot I met in Dublin, Ireland, who all unknowingly gave me the final push to pursue a doctoral degree.

Last, but certainly not least, I owe much gratitude to my family. “Go placidly, amid the noise and haste...” is the beginning to an old poem my grandfather had me memorize one summer, which now, many years later, I know summarizes the virtue of focus necessary to accomplish your goals. Although he passed before I began graduate school, he was always by my side through its entirety as I kept my favorite photo of the two of us on my desk at school, which captured a typical summer day on the family boat with me at the helm at age 4.

Thank you to my brother, Sam. You are a proper friend and my thrill-seeking companion. You are always a great source of laughter. Thank you to my sister, Emily, for your love and support. Thank you to my dogs, Guinness and Wahoo, for your endless enthusiasm for chasing squirrels and tennis balls.

Finally, I would not be where I am today without my parents, Paul and Colleen. Thank you for the immeasurable number of things you have given me, among them the moral support to complete graduate school.

Table of Contents

List of Tables

List of Figures

Nomenclature

ΔP_p	Pressure change across piston, N/m^2
P_0	Static pressure, N/m^2
P_i	Pressure of chamber #i, N/m^2
ΔP_i	Pressure change in chamber #i, N/m^2
R_f	Zero-field flow resistance, N s/m^5
A_f	Cross-sectional area of active gap, m^2
x_f	Fluid displacement in annulus, m
x	Piston displacement, m
I_f	Fluid inertance, kg/m^4
ΔP_{MR}	Pressure change due to MR yield stress, N/m^2
ρ	Density, kg/m^3
l	Active gap length, m
μ	viscosity, Pa s
d	Active gap seperation, m
D_h	Hydraulic diameter, m
b	Circumference of active gap, m
τ_y	Yield shear stress, N/m^2
H	Magnetic field intensity, T
C_i	Compliance for chamber #i, m^5/N
A_p	Piston head area, m^2
A_r	Cross-sectional area of piston rod, m^2
y	Displacement of accumulator, m
f	Damper force, N
f_0	Force offset, N
k_d	Damper stiffness, N/m
c_{po}	Post-yield damping, N s/m
m_f	Fluid inertia, kg
f_y	Yield force, N
λ_1	Shaping parameter, s$^-$1
λ_2	Shaping parameter, s/m
γ	Dynamic stiffness, N/m
J	Cost function
t	Time, s
N	Number of time indices
N	Number of MR Dampers
E	Dissipated energy, Joules
ω	Frequency, rad/s
$b(t)$	Boundary function
Re	Reynolds number
j	$\sqrt{-1}$
T_r	Transmissibility
ω	Frequency, rad/s
ω_n	Natural frequency, rad/s

x	Absolute displacement of payload
w	Absolute displacement of base
k_a	Axial stiffness of coil spring
k_l	Lateral stiffness of coil spring
f_d	Damper force
q	Damper stroke displacement
g	Gravity
C_{sky}	Skyhook gain
ζ	Damping ratio
ζ_{eq}	Equivalent damping ratio
C_{eq}	Equivalent viscous damping
φ	Electrical current, A
E	Dissipated energy
$\overline{\boldsymbol{x}}$	Generalized displacement of body frame
$\overline{\boldsymbol{w}}$	Generalized displacement of base
$\boldsymbol{p}_{nB}$	Position vector to point n from point B
$\boldsymbol{P}_{nB}$	Skew-symmetric matrix of $\boldsymbol{p}_{nB}$
$\overline{\boldsymbol{M}}$	Generalized mass matrix
$\overline{\boldsymbol{K}}$	Generalized stiffness matrix
τ	Time constant
$A(t, \boldsymbol{x})$	State matrix
B	Input matrix
$E(t, \boldsymbol{x})$	Disturbance matrix
$C(t, \boldsymbol{x})$	Output matrix
D	Feedthrough matrix
$F(t, \boldsymbol{x})$	Output disturbance matrix
$\boldsymbol{u}$	System input
m_i	i^{th} performance metric
$\boldsymbol{V}$	Eigenvector matrix
Q_c	Controllability matrix
ϵ_j	Effectiveness factor for j^{th} mode

Subscripts and Superscripts

k	Time index
O	Global frame
B	Body frame
K_i	i^{th} spring frame
D_i	i^{th} damper frame

Acronyms

CCF	Complex Correlation Coefficient
CG	Center of Gravity
DAQ	Data Acquisition
DOF	Degree of Freedom
EFV	Expeditionary Fighting Vehicle
ER	Electrorheological
FRF	Frequency Response Function
GSE	Ground Support Equipment
IC	Integrated Circuit
LVDT	Linear Variable Differential Transformer
MIMO	Multiple-Input/Multiple-Output
MLP	Mobile Launch Platform
MR	Magnetorheological
NASA	National Aeronautics and Space Administration
PSD	Power Spectral Density
RMS	Root Mean Square
SMC	Sliding Mode Control

Chapter 1

Introduction to Vibration Isolation

1.1 Motivation

Vibration is a phenomenon defined as oscillations about an equilibrium point. Vibration can be transmitted through any medium such as the atomosphere (ie. sound, or pressure waves), or through solid materials (ie. mechanical vibration). There are many sources of vibration, such as earthquakes, interal combustion engines, rocket blasts, a mass imbalance in a rotary environment, or contact disturbances to a road vehicle.

Occasionally vibration is desirable. This is the case with musical instruments, jackhammers, or agitation machines used to vigorously shake cans of paint. However, often vibration is undesired, as it can cause discomfort (ie. audible noise), or damage sensitive equipment. Therefore, it is often necessary to isolate the source of vibration. This is typically done in one of two ways: (1) through impedance mis-matching, which is accomplished by augmenting the mass or stiffness properties of the system (ie. tuned mass damper), or (2) through absorbing or dissipating energy transmitted from the vibration source. The former is a technique that shifts the natural frequencies of the system away from a particular disturbance frequency. This can be achieved in several ways, from as simple as judiciously adding mass to the system, or with slightly more sophistication, through the use of adjustable stiffness elements, allowing the suspension to be adaptable. The latter does not alter the undamped dynamics of the system, but rather introduces a dissipative element into the system to attenuate resonant behavior. This too can be achieved in several ways and is the subject of the next section.

1.2 Methods of Damping

Damping devices can be classified into three general categories: passive, active, and semi-active. Passive damping devices are characterized by having a fixed force/velocity relationship as seen in figure 1.1, and by their inability to introduce net energy into the system in which they belong, assuring stability. Examples of passive damping include viscous fluid shearing, frictional surface-to-surface contact, or plastic deformation of a solid material. While these devices are inherently stable, require no control logic, and are relatively low maintenance, the performance is limited due to the inability to adapt to perturbations in system parameters and disturbances.

Fully active devices (ie. force generators) include hydraulic and pneumatic actuators, piezo-electric elements, and electric motors. Control algorithms dictate the operation of an active device through processing information obtained with sensors. Active devices have the ability to exert a force independent of the relative motion of the device. This ability is shown in figure 1.1, as the active device is capable of exerting force in all four quadrants of the force vs. velocity plane, regardless of the relative velocity of the device. This ability allows active devices to both inject energy into, and dissipate energy from, a dynamic system. This provides superior performance compared to passive systems and offers the ability to adapt to perturbations of system parameters and disturbances. However, there are drawbacks. The ability to inject energy into the system may cause unstable behavior, requiring robust control logic to ensure stability. Furthermore, active devices often require bulky or heavy support hardware, and also consume large amounts of power for operation.

Semi-active devices attempt to capture the adaptive nature of a fully active device while also benefitting from the low power consumption and stable operation of a passive device. Examples of a semi-active device include dampers with mechanically adjustable bypass orficies, and magnetorheological (MR) and electrorheological (ER) dampers. Semi-active devices have adaptable damping properties, providing a variable force/velocity relationship that may occupy the upper right-most and lower left-most dissipative quadrants, as seen in figure 1.1. Since the semi-active device can only dissipate energy from the system, the power consumption is low, requiring only enough power to alter the damping properties, and the device is inherently stable.

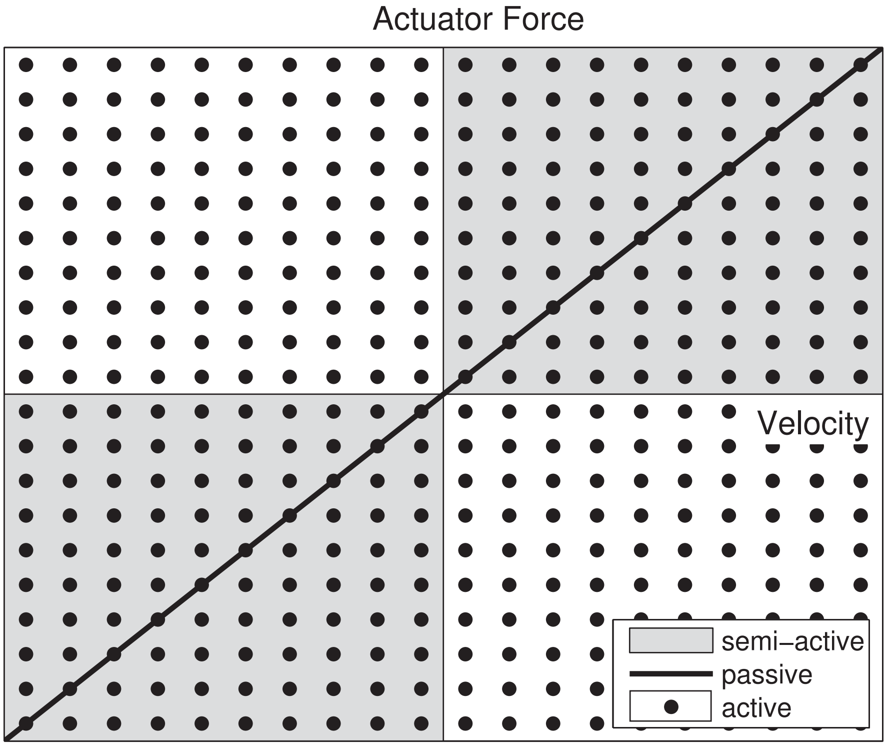

Figure 1.1: Comparison of force exertion capability for passive, semi-active, and active devices.

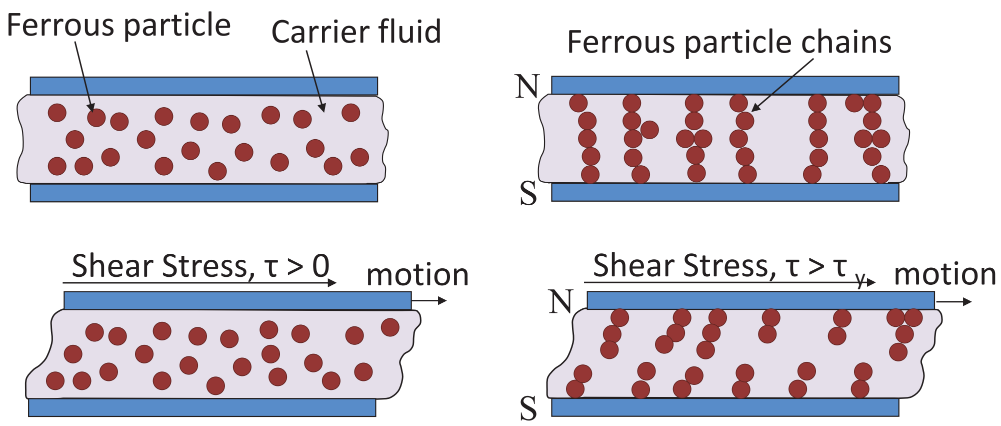

(a) No magnetic field. (b) Field applied.

Figure 1.2: In the absence of magnetic field the MR fluid behaves as a Newtonian fluid, however with the application of magnetic field the ferrous particles form chains creating a yield stress τ_y that must be overcome before motion may occur.

1.3 MR Technology

MR fluid is a biphasic suspension with magnetically dependent, anisotropic properties. The suspension is composed of a carrier fluid (typically either mineral oil, synthetic oil, water, or glycol) and micron-sized (typically 0.1 - 10 μm) iron (Fe) particles. The typical particle to fluid volume fraction is between 20 - 40 percent by volume.

Figure 1.2 depicts the formation of the partical chains with the application of magnetic field and the need to overcome the yield shear stress before motion can occur. The formation of the particle chains between the two parallel surfaces is rapid and occurs on the order of milliseconds ($<$ 15 ms). The magnetized gap thickness is typically between 0.5 - 2 mm.

There are three primary ways the fluid may flow through the magnetized gap. Figure 1.3 illustates the flow, shear, and squeeze modes of operation.

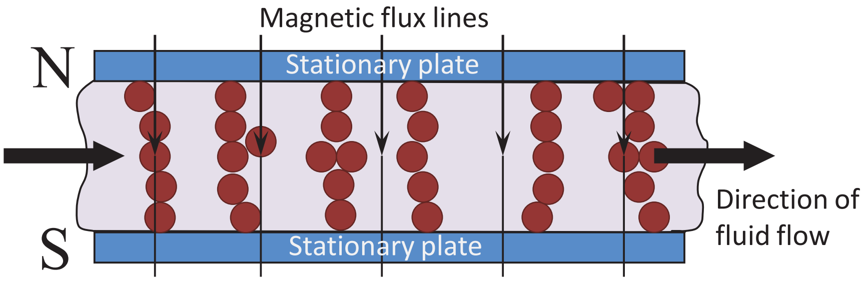

(a) Flow mode.

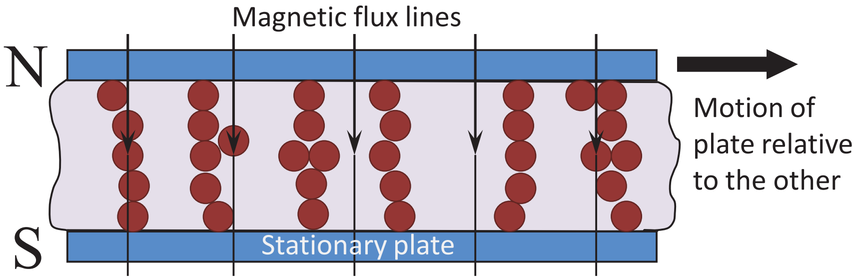

(b) Shear mode.

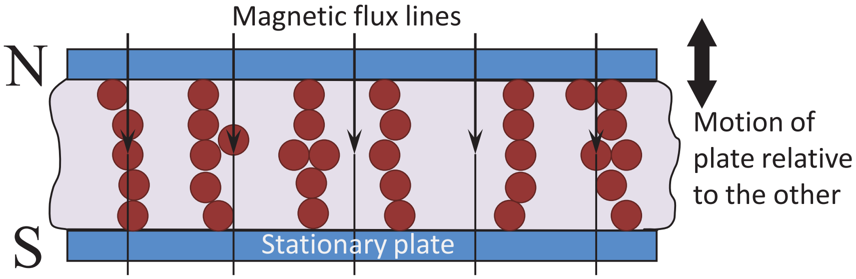

(c) Squeeze mode.

Figure 1.3: Modes of operation for MR fluid dampers.

1.3.1 Flow Mode

The flow mode of operation forces the MR fluid to flow between two stationary, parallel plates in figure 1.3(a) which create a magnetized gap with the magnetic flux lines perpendicular to the plates. A pressure differential forces the fluid to flow through the gap and severe the particle chains. Flow mode operation allows for hydraulic amplification which is useful for high force applications such as shock absorption. Examples of flow mode devices include crashworthy occupant seating [20, 38, 76], landing gear for aircraft [8, 19], primary suspensions for automobiles, seismic damping elements for civil structures, and lag dampers for helicopter main rotors [41].

1.3.2 Shear Mode

The shear mode operation translates one side of the gap in-plane relative to the other as in figure 1.3(b). Shear mode operation allows for high dynamic range due to low field-off stresses. Examples of shear mode devices include rotary dampers for occupant crash protection in helicopters [37], rotary clutches and brakes [27], and rheometer testing machines.

1.3.3 Squeeze Mode

The squeeze mode operation translates one side of the gap parallel to the magnetic flux lines as in figure 1.3(c). Due to the small required gap thickness, the squeeze mode is limited to low stroke applications. Squeeze mode operation is

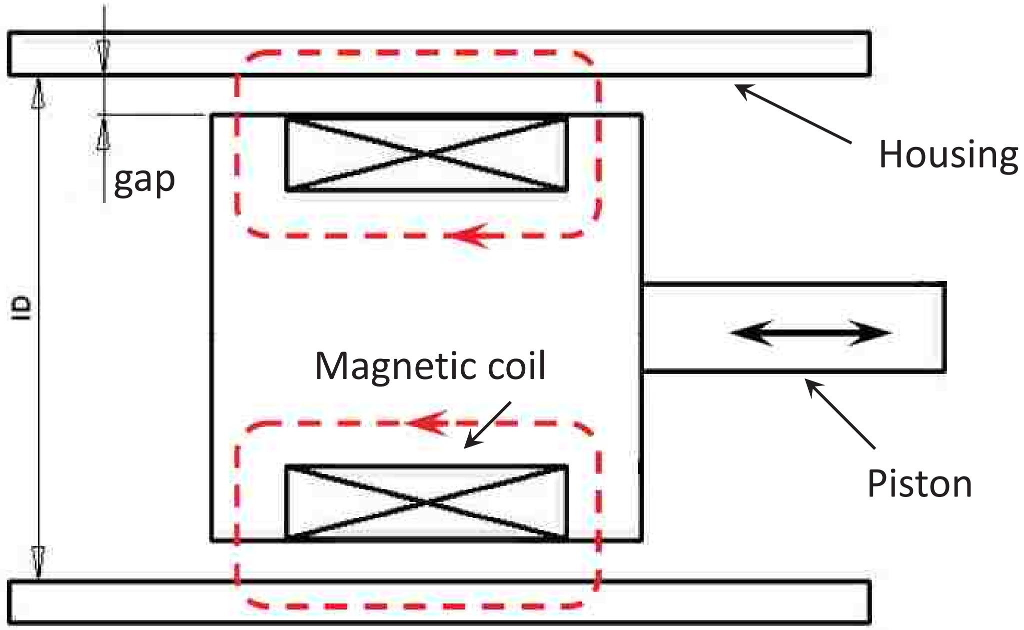

Figure 1.4: Schematic of a mixed mode damper combining flow and shear modes.

applicable to variable stiffness devices, engine mounts [82], and rotating shafts [75].

1.3.4 Mixed Mode

MR dampers can also be designed to use a combination of the three primary operation modes. A floating piston design shown in figure 1.4 combines both flow and shear modes, and Brigley et al. [9] designed a mixed mode damper that employs all three primary modes.

1.4 6-DOF Isolation

Often many systems experience multi-axis vibration and require damping along each DOF. Figure 1.5 gives examples, including occupant seating systems for marine-based vehicles, primary suspensions for land-based vehicles, helicopter main

(a) Occupant seating systems for marine-based vehicles. (b) Primary suspensions for land-based vehicles. (c) Helicopter main rotors.

(d) High-precision pointing devices. (e) Ground support equipment and electronics for rocket launches. (f) Seismic structural protection of buildings.

Figure 1.5: Multi-axis vibration applications.

rotors, high-precision optical instruments and precision pointing devices, ground support equipment and electronics for rocket launches, and seismic structural protection of buildings. These real systems in three-dimensional space can often be viewed as rigid bodies that have six DOF, comprising of 3 translational DOF along orthogonal axes and 3 rotational DOF about those same axes.

1.4.1 Passive

Passive techniques have been used to address 6-DOF isolation. Modern automobiles and high-performance off-road vehicles have suspensions that isolate passengers in the cabin from disturbances originating from the interaction between the

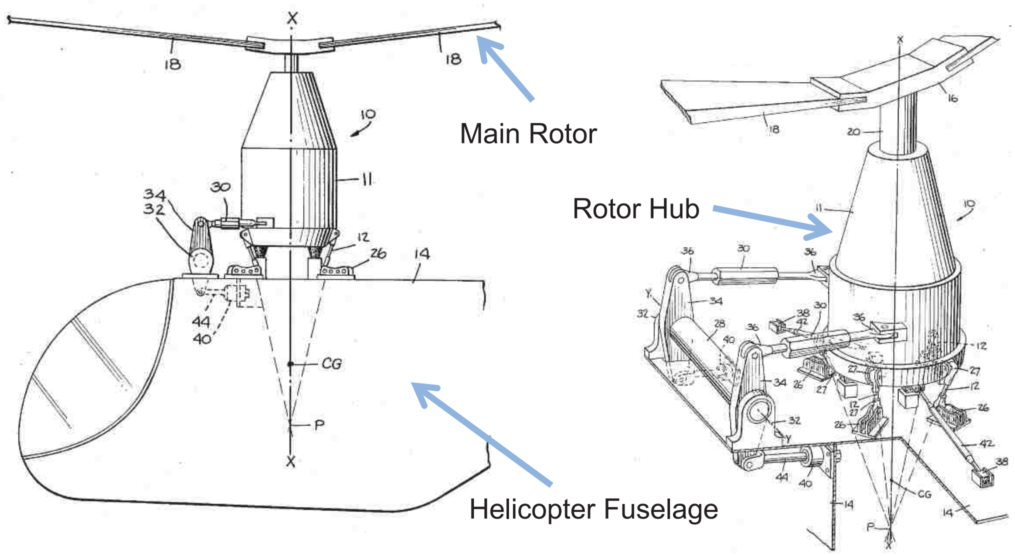

Figure 1.6: Passive isolation of helicopter main rotor vibrations [6].

road surface and automobile wheels. Balke et al. [6] suggests the use of linkages and elastomeric elements to isolate a rotorcraft fuselage from the vibration of a helicopter main rotor in figure 1.6. Platus [62] describes an apparatus of bi-stable stiffness elements in figure 1.7 which strive to preserve an acceptable static deflection while shifting the natural frequency of the system much lower than is possible with linear springs, however this technology is limited to only small deflections. The Shockwave Seat company [3] manufactures 6-DOF isolation systems for high-performance, marine-based occupant seating systems for rough ocean conditions, using passive peumatic shock absorbers in figure 1.8. Klembczyk and Mosher [47] designed a passive suspension using several coil springs and viscous dampers to provide isolation from rocket-blast induced vibration for all 6-DOF of a large piece of equipment onboard NASA's Mobile Launch Platform (MLP) in figure 1.9.

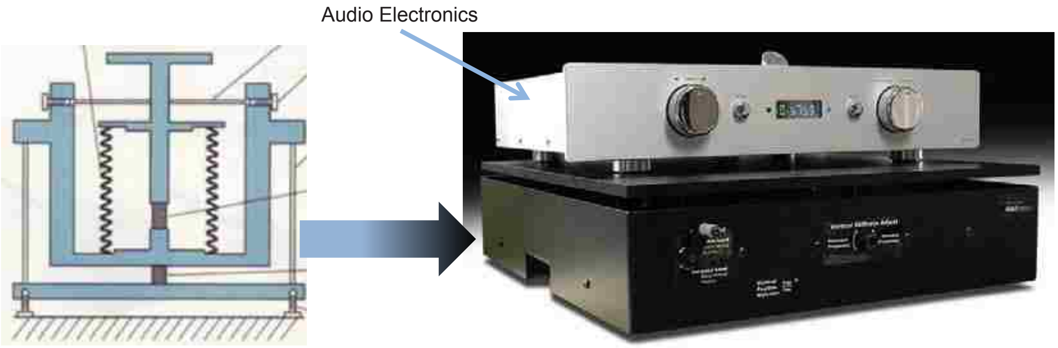

Figure 1.7: Bi-stable stiffness device offering passive 6-DOF isolation [62].

Figure 1.8: Shockwave Seat company 6-DOF isolation, marine-based occupant seating systems for rough ocean conditions.

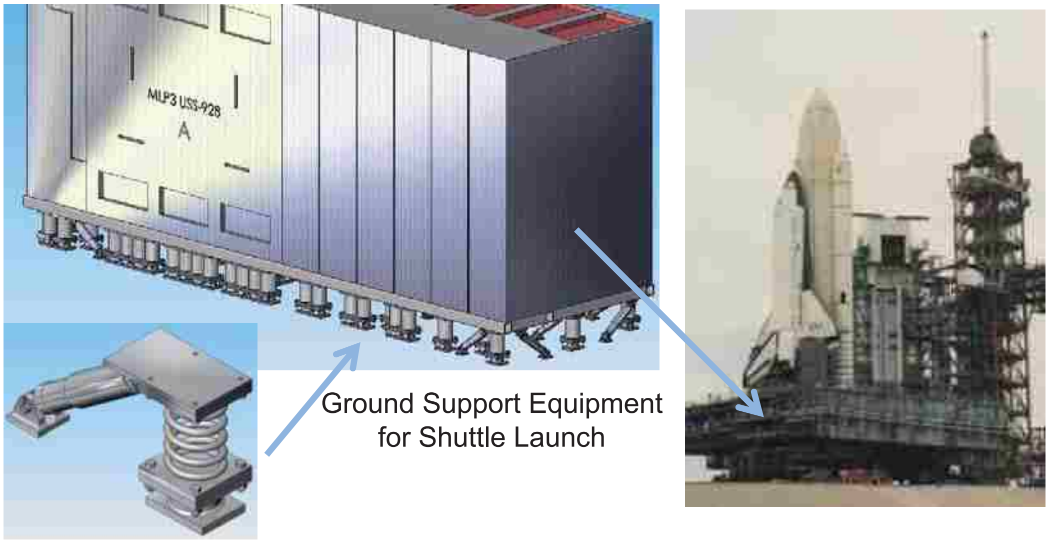

Figure 1.9: Passive 6-DOF isolation from rocket-blast induced shock and vibration on NASA's Mobile Launch Platform (MLP) [47].

1.4.2 Active

Active suspensions have been used to provide 6-DOF isolation. The origins of these devices date back to Stewart [70] who publicized a parallel manipulator in figure 1.10 invented by Eric Gough in the 1950s as a platform to mechanically test automotive tires under combined loads [32]. This parallel manipulator is commonly refered to as either a "hexapod", "Gough/Stewart", or simply "Stewart", platform which uses six prismatic actuators to synergistically position a platform relative to the base with six degrees of freedom (ie. 3 translational, 3 rotational). In addition to mechanical testing of automotive tires, these devices have been used for aviation flight simulation in figure 1.11, and robotic orthopedic surgery in figure 1.12 [50].

Hexapod manipulators have also been used as isolation suspensions. Thayer et al. [71] and Hanieh [36] apply active control strategies to cubic hexapod manipulators designed with voice coil and piezoelectric actuators, shown respectively in figures 1.13 and 1.15, to provide isolation to sensitive spacecraft payloads.

1.4.3 Semi-Active

Semi-active devices provide an adaptable, low-cost, low-maintanance solution to isolating shock and vibration. Several rigid body suspensions have been modeled as simplified single-DOF systems. Ahmadian and Vahdati [4] simplified a ground vehicle suspension as only a quarter-car model. Others have considered simplified suspension models for ground vehicles, capturing roll, pitch, and/or heave DOFs ($<$ six-DOF) as in figure 1.15 [10, 16, 67, 83]. The primary suspensions of many popular consumer automobiles are now equiped with MR dampers. This trend began in 2002 with the introduction of the MagneRide suspension in the Cadillac Seville STS from the automobile manufacturer General Motors [1].

Several researchers have investigated multi-axis vibration suspensions with fixed bases. Brigley et al. [9] investigated a multi-directional, mixed mode MR isolator with limited stroke capability in figure 1.16. The Shockwave Seat company [3] is begining to offer its multi-axis occupant seating suspensions for high performance, marine-based applications in figure 1.8 with MR technology. Unsal [72] models a cubic hexapod mechanism in figure 1.17 that employs both actuators and semi-active MR dampers arranged in-series to provide precision positioning as well as vibration control for space applications. Jean et al. [43] constructed a hexapod suspension using only MR dampers in figure 1.18 and showed good vibration attenuation with the Frobineus norm of transmissibility. A similar hexapod MR damper design in figure 1.19 was used on the 2005 DARPA Grand Challenge autonomous

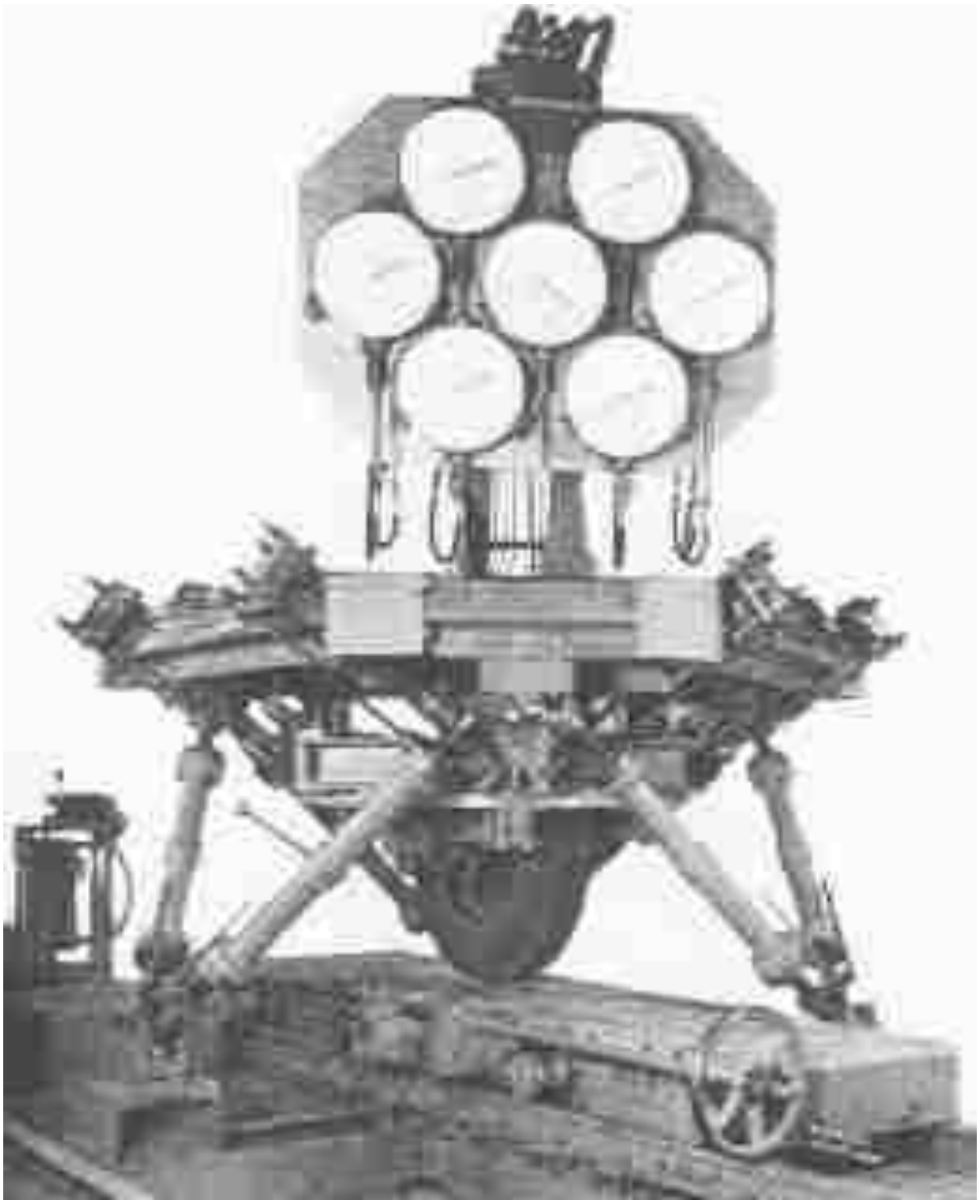

Figure 1.10: Universal Tyre-Testing Machine developed by Gough [32].

Figure 1.11: Flight simulator motion achieved with a hexapod manipulator.

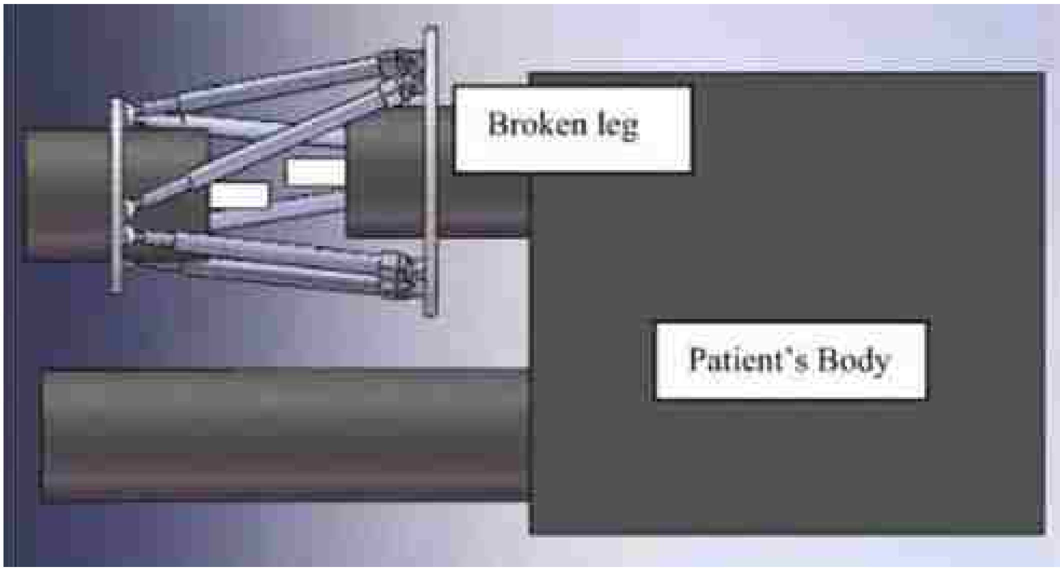

Figure 1.12: Robotic 6-DOF Stewart platform to assist in orthopedic surgery [50].

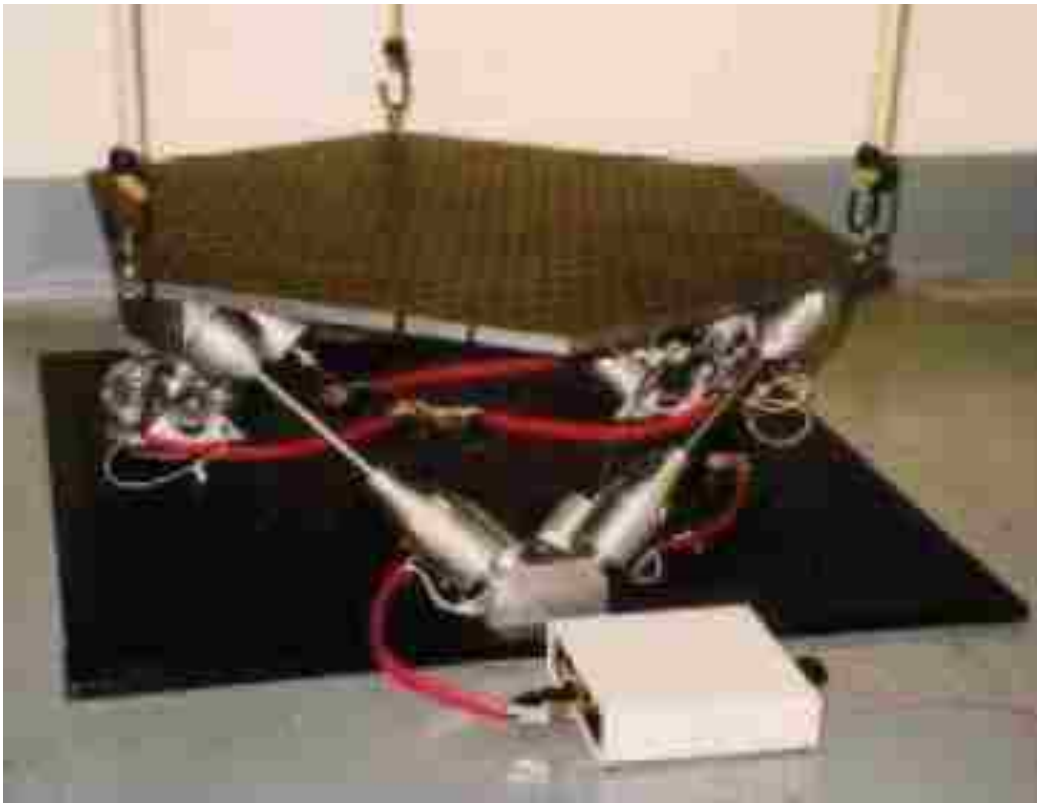

Figure 1.13: Cubic hexapod manipulator with voice coil actuators [71].

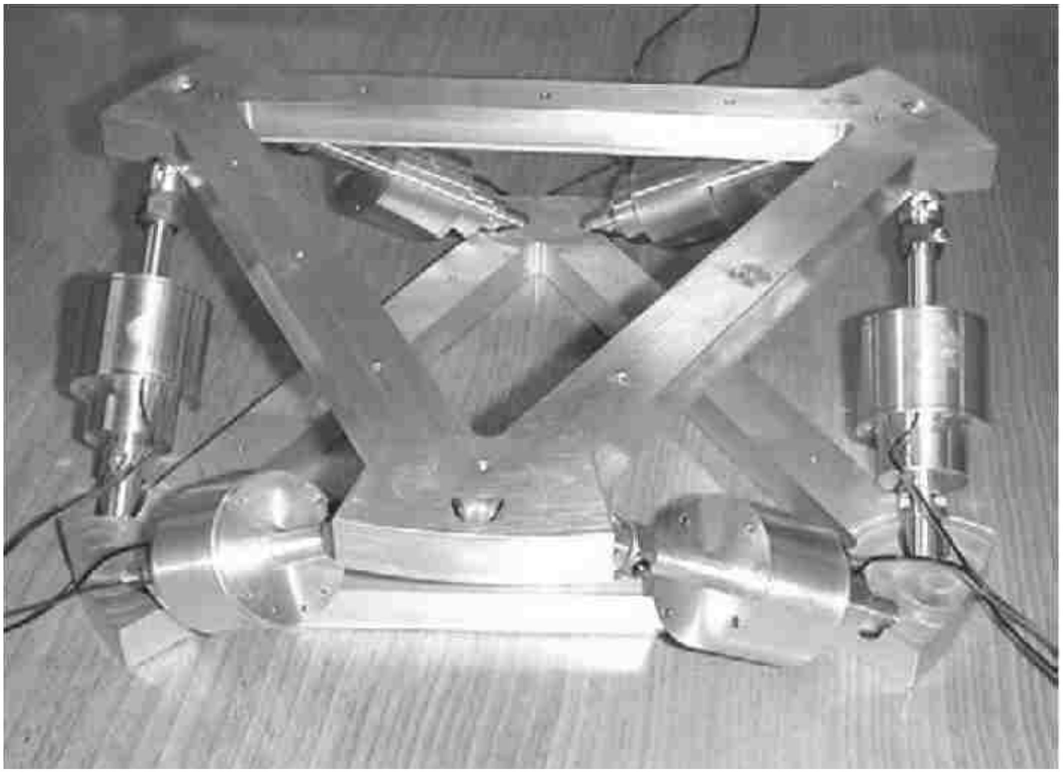

Figure 1.14: Cubic hexapod manipulator with piezoelectric actuators [36].

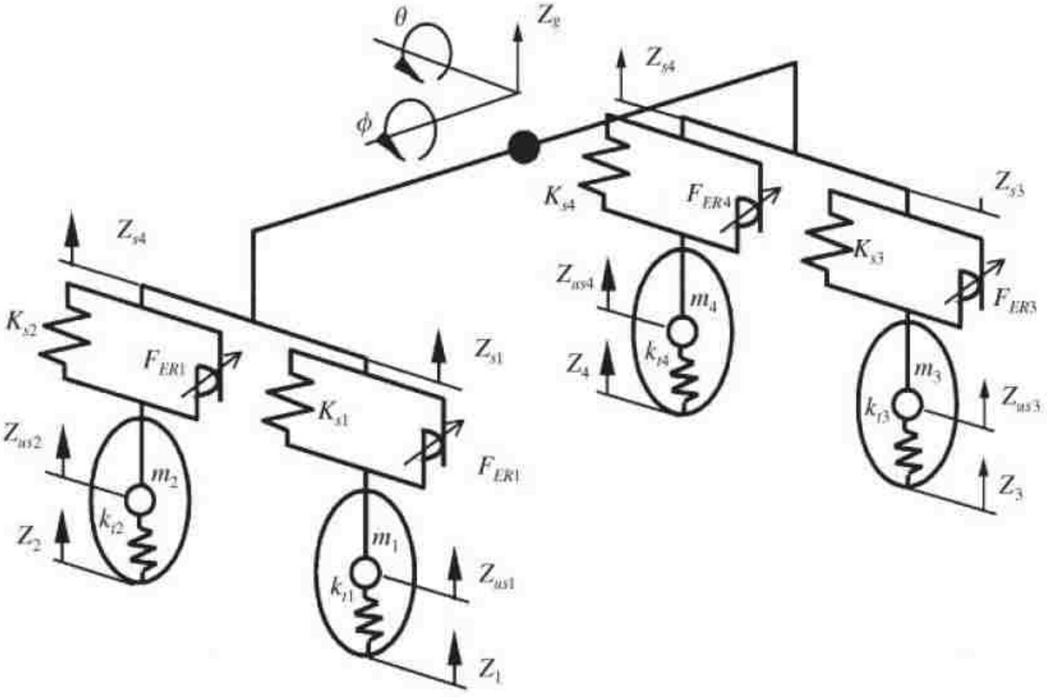

Figure 1.15: Simplified full car model capturing the roll, pitch, and heave DOFs [16].

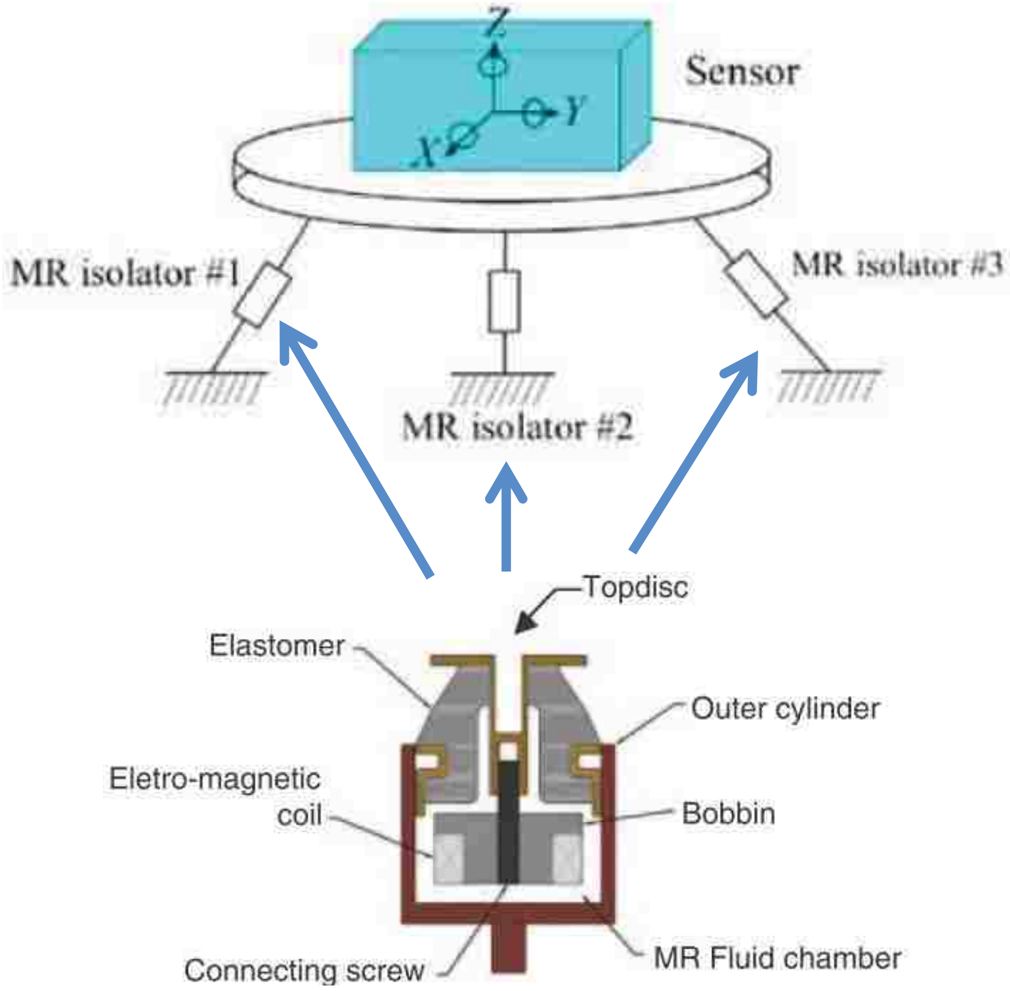

Figure 1.16: Multi-directional, mixed mode MR isolator [9].

ground vehicle entry from Carnegie Mellon University to isolate electronics onboard the vehicle [2].

1.5 Dissertation Outline

The motivation of this present body of work is to develop a semi-active suspension to provide 6-DOF isolation for ground support equipment near a rocket launch. Semi-active, MR fluid technology is selected due to its adaptive capabilities, low

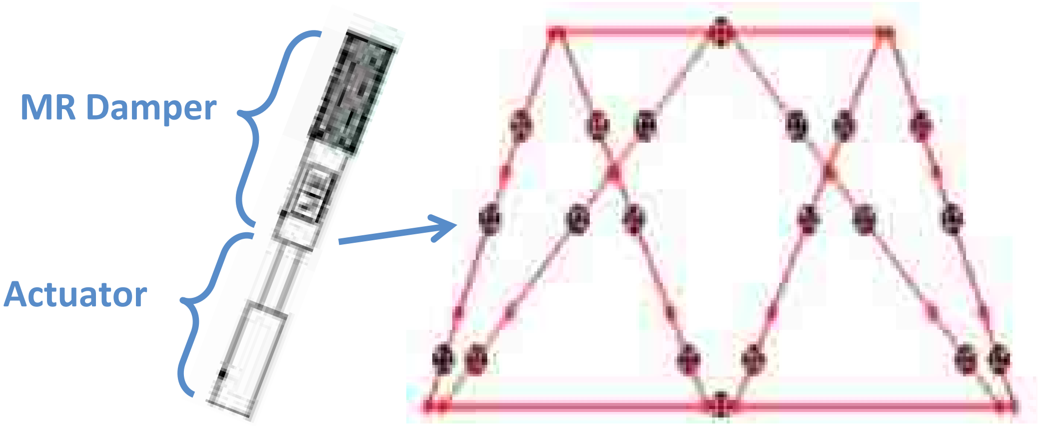

Figure 1.17: Model of a cubic hexapod mechanism that utilizes both actuators and semi-active MR dampers, arranged in-series, to provide precision positioning as well as vibration control [72].

power consumption, and stable, fail-safe operation.

In this discussion, practical design considerations are taken into account. The implications of perturbations in the system properties are studied and the isolation performance is evaluated. A large stroke capability for the suspension is pursued so that the suspension may possess low stiffness and yield good high frequency isolation. There are limitations to the cubic hexapod design, which has been previously studied [2, 43, 72]. It is not modular in the sense that it requires exactly six linkages. Adding or subtracting linkages would disrupt the orthogonality of the cubic configuration. The ability to add or subtract individual leg subsystems from the suspension accommodates payloads of varying size and mass without the need to redesign a fixed number of MR dampers or springs. It is desired to have a modular suspension design that could scale with payload mass and geometric size.

Chapter 1 begins by identifying sources of vibration and several examples where it is desired to eliminate vibration from the system. Semi-active damping

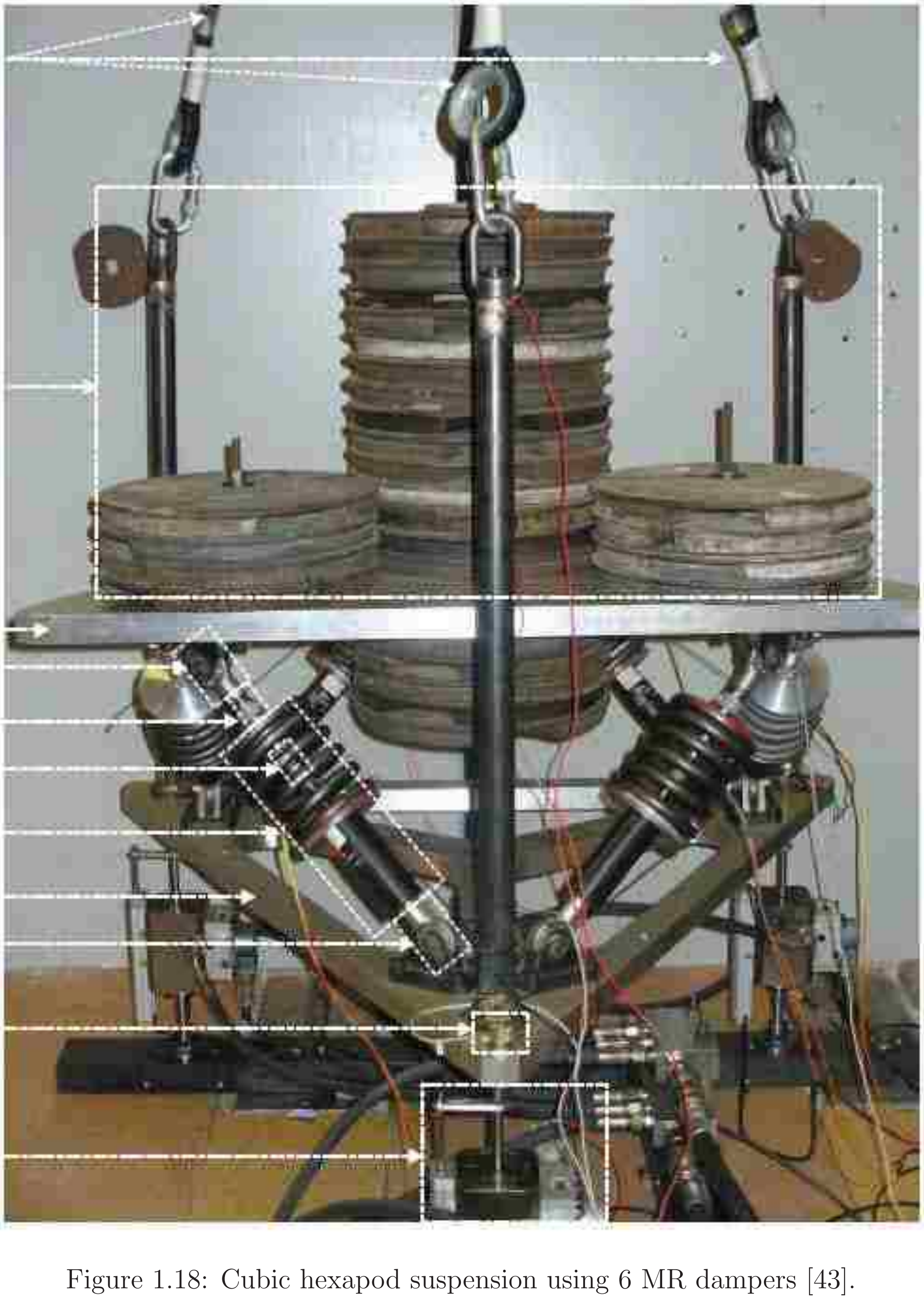

Figure 1.18: Cubic hexapod suspension using 6 MR dampers [43].

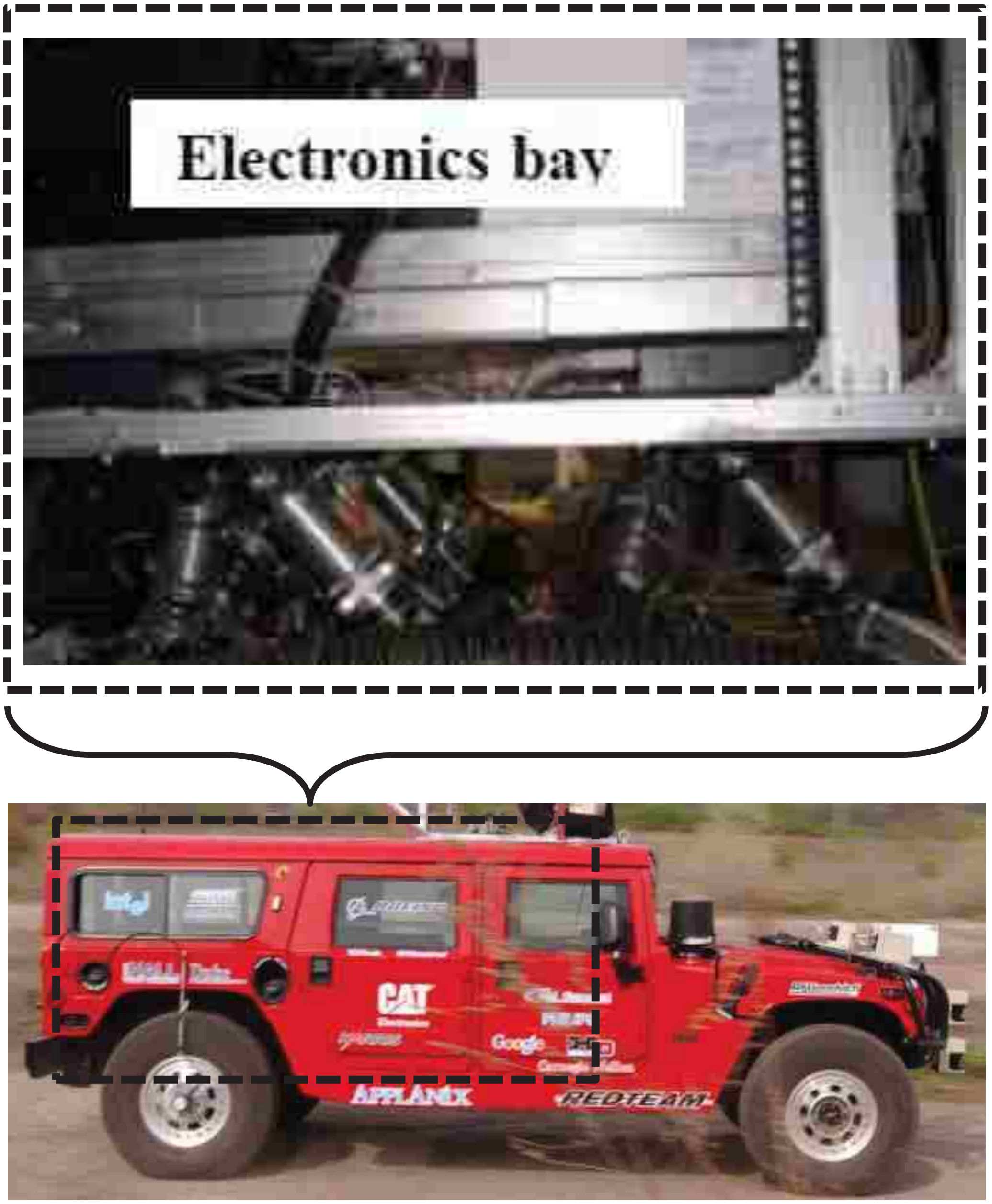

Figure 1.19: Hexapod MR damper suspension used on the 2005 DARPA Grand Challenge autonomous ground vehicle entry from Carnegie Mellon University to isolate electronics onboard the vehicle [2].

and MR fluids are introduced and the state of the art for multi-directional vibration supression is discussed.

Chapter 2 develops a hydro-mechanical analysis to model the MR damper behavior considering perturbations in operating temperature.

Chapter 3 uses the damper model to examine a base-disturbed, single-DOF system and investigates the robust isolation performance of the MR suspension when subjected to perturbations in operating temperature and payload mass.

Chapter 4 derives a mathematical model of the full 6-DOF dynamics of the semi-active suspension system as well as control laws to govern the behavior of the MR dampers.

Chapter 5 discusses the design and characterization of the MR damper and coil spring suspension. A single suspension leg is used to evaluate control law performance and calibrate the control gains. The full 6-DOF experimental testing is discussed and the results are presented. The mathematical model is validated using the measured data.

Chapter 6 develops an analysis of the MR damper orientations within the suspension and it is shown that the dampers can be oriented to attenuate all six resonant modes of the rigid body system and provide high frequency isolation of system disturbances. Also, the isolation performance of the suspension is evaluated using centralized and decentralized control laws, as well as considering perturbations in payload mass, center of gravity, and operating temperature.

Chapter 7 summarizes the original contributions of this dissertation and identifies future work in this research area.

Chapter 2

Analysis of a Magnetorheological Damper Incorporating Temperature Dependence

2.1 Introduction

Aside from external environmental heating, a magnetorheological (MR) damper may internally self-heat due to both resistive heating by the electromagnetic coil and, to a greater extent, by dissipating mechanical energy into thermal energy. Temperature can significantly alter damper behavior as the fluid viscosity and accumulator gas pressure are highly dependent on temperature. Therefore, to improve the understanding of the behavior of a linear stroke MR damper designed for a ground vehicle seat suspension, its performance is characterized over temperatures ranging from 0^0C to 100^0C. A hydro-mechanical analysis is used to represent MR damper behavior when it is subjected to large temperature perturbations, and captures contributions from fluid viscosity, fluid inertia, and pneumatic compressibility. The effect of damper self-heating on the identified model parameters is presented, and the connection of these parameters to physical properties is also discussed.

2.2 Background

Magnetorheological (MR) fluids have rheological properties that can be quickly altered by the application of an external magnetic field. The changes are manifested by large changes in yield stress (nominally, $0 - 60$ kPa), reversible, and rapid (on the order of milliseconds) [13], which make MR fluid an excellent working fluid for mechanical vibration damping and shock isolation devices. Linear stroke MR dampers or MR energy absorbers can be used for such applications as protective occupant seating [20, 38, 76] and aircraft landing gear suspensions [8, 19].

MR fluids consist of micron-sized ferrous particles suspended in a carrier fluid such as oil, water, or glycol [13]. The MR fluid inside a damper can experience large variations in temperature due to resistive heating of the electromagnetic coil and, to a greater extent, fluid agitation as the damper strokes in response to mechanical excitation. Energy is dissipated by transforming mechanical energy into thermal energy by shearing the fluid as it flows through an orifice in the piston traveling through the hydraulic cylinder. Temperature can significantly affect the rheological properties of the MR fluid [54]. The viscosity of the carrier fluid is strongly linked to temperature, as with any simple liquid, due to the molecular kinetic energy of the material [15]. Also, the pressure of a damper's pneumatic accumulator is directly proportional to the temperature of the gas inside the accumulator [15].

Consequently, research has been conducted to study how to compensate for these temperature effects. Gordaninejad and Breese [31] developed an energy balance framework to predict the heat generation of MR fluid dampers as a function of energy entering a defined control volume through mechanical and electrical work, or leaving via thermal conduction. Dogruoz et al. [26] experimentally enhanced heat dissipation out of an MR damper using thermally conductive heat-sink fins to minimize the loss in passive damping for fail-safe damper applications. Batterbee and Sims [7] showed that feedback controllers for MR shock absorption applications can exhibit reduced force-tracking performance as temperature increases due to a reduction in viscous damping and yield force. Liu et al. [49] investigated a control strategy for vibration reduction with an MR damper and demonstrated improved isolation performance using temperature compensation over uncompensated control. A key concern in each of these studies was how to model changes in damper behavior as a result of thermal perturbations.

Although several models have been proposed to capture the force behavior of MR fluid dampers [74], few models have addressed the effect of temperature. Sahin et al. [64] measured the rheological properties of an MR grease with a shear mode rheometer, and proposed a temperature dependent Herschel-Bulkley model to represent these behaviors, showing temperature has an appreciable effect on the field-induced dynamic yield stress. Temperature can significantly alter the damper force. Not only can temperature changes alter the maximum achievable force, but also change the hysteresis and phase relationship of the damper force relative to the piston motion. These changes can be pronounced in both pre-yield and post-yield damper behavior.

Modeling pre-yield force hysteresis is well documented [22, 29, 68, 78]. Post-yield force behavior has also been studied. Kamath and Wereley [44] developed a model that uses a nonlinear combination of linear mechanisms that can capture an extensive spectrum of damper behavior in both the pre-yield and post-yield domains. Yang et al. [81] extended the versatile Bouc-Wen model to include an inertia term capable of capturing the MR fluid stiction phenomenon as well as fluid inertial and shear thinning effects. However, this extended Bouc-Wen model requires a large number of parameters. Peel et al. [61] proposed a dynamic model capable of capturing post-yield stiffness and inertial behavior. Çeşmeci and Engin [14] noted the influence of inertia on the force hysteresis near maximum piston velocity. Powell [63] proposed a model with physical mechanical elements that is capable of capturing the post-yield inertia effects observed in experimental rheometer data and attributes this to a nonlinear softening of the post-yield fluid elasticity. However, none of these models have considered the post-yield behavior in the context of temperature perturbations.

This study uses hydro-mechanical analysis to develop a physically motivated model that captures the force behavior of a linear stroke MR damper over temperatures ranging from 0^0C to 100^0C. The parameters of the model are well motivated by the physical properties of the damper and MR fluid, and the measured trends of the parameters are presented as a function of operating temperature and applied magnetic field.

Figure 2.1: Magnetorheological (MR) seat damper.

2.3 Damper Characterization

The experimental testing is carried out using an MR damper (figure 3.4) designed for occupant seat isolation onboard the US Marine Corps's amphibious Expeditionary Fighting Vehicle (EFV) [42]. The EFV vehicle is subjected to a broad spectrum of vibrations and shocks in both land and sea mode operations, thus requiring low transmissibility over a large frequency range. The MR seat isolator was designed and fabricated at the University of Maryland and uses a commercially available fluid (Lord MRF-132DG) to achieve the desired maximum yield force (4.3 kN) and target field-off viscous damping (1.0 kNs/m) for the EFV seat application at an operating temperature of 50^0C. The MR valve operates as a purely flow mode device [77] and the pneumatic accumulator is filled with nitrogen gas, pressurized to 2.41 MPa (350 psi).

Damper characterization was performed on an MTS 810 material testing system inside of a temperature-controlled environmental chamber, as seen in figure 2.3. The MR damper was characterized at temperatures ranging from 0^0C to 100^0C. A thermocouple was installed inside the damper to directly measure the operating

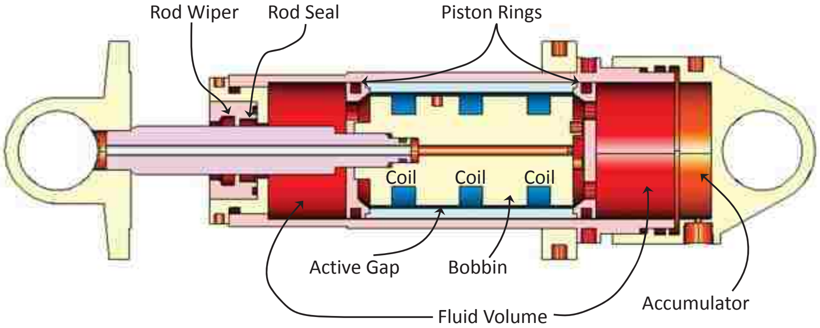

Figure 2.2: Internal construction of MR damper.

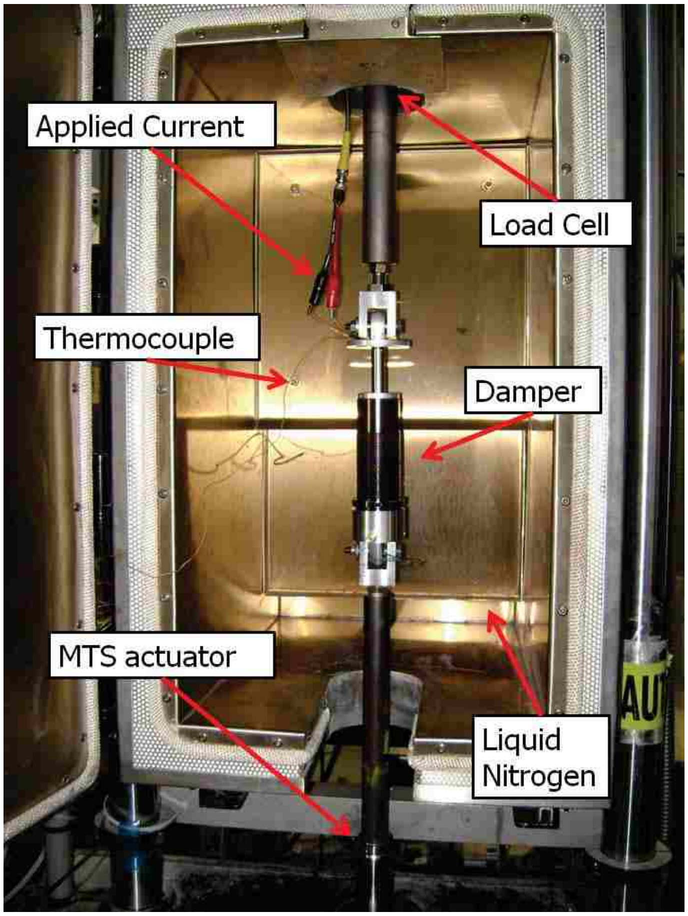

Figure 2.3: Temperature-controlled environmental chamber.

temperature of the MR fluid. The thermocouple was fixed to the surface of the steel bobbin and the lead wires were guided up through the hollow piston rod together with the lead wires of the MR coil. The maximum temperature was 100^0C because that is the rated temperature for safe operation of the damper's polyurethane rod seals. To achieve higher relevant temperatures, seals with a higher operating temperature can be utilized. Liquid nitrogen was fed into the environmental chamber to achieve temperatures below 0^0C. For each test, the damper was first cooled below 0^0C, as indicated by the thermocouple, then the chamber door was opened to ambient room temperature and excitation began. As a result of the mechanical excitation and the resistive heating from the electromagnetic coil, the damper would self-heat and the thermocouple reading would increase to 100^0C, which concluded the test. An excitation of 4 Hz and 7.62 mm (0.3 in) displacement amplitude was chosen as representative of the resonant condition of the EFV seat suspension system. This procedure was repeated for applied current levels of 0, 0.25, 0.5, 1.0, 1.5, 2.0, and 2.5 A to evaluate temperature effects over the full range of control. A linear variable differential transformer (LVDT) sensor was used to measure piston displacement and a load cell was used to measure transmitted force.

The measured displacement signal was filtered, using a Fourier series expansion, by selecting only the primary excitation frequency component (4 Hz), while the measured nonlinear damper force was left unfiltered. However, the bias force was removed from the measured data. Figure 2.4 depicts the operating temperature of the MR fluid as a function of time during the characterization of the damper at each applied field. The shortest test occured for the largest applied field (2.5 A), lasting

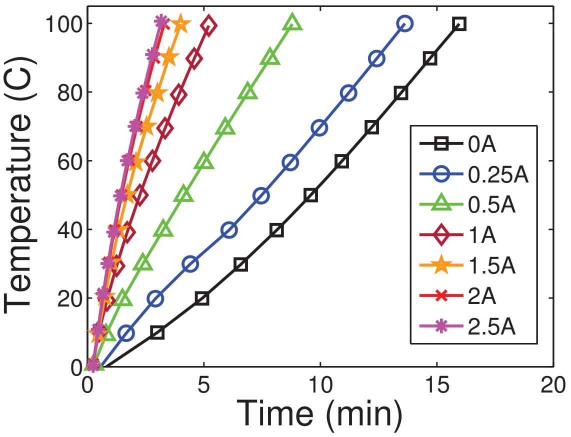

Figure 2.4: Operating temperature of MR fluid vs. time for several applied fields. Temperature reading was taken from a thermocouple affixed to bobbin in piston, and is representative of the MR fluid temperature.

around 3 minutes, indicating the operating temperature increased by approximately 0.1^0C per stroke cycle of the damper, providing accuracy of $\pm 0.05^0$C for each complete stroke cycle. Figure 2.5 shows the operating temperature and the envelope function using the Hilbert Transform [65] of the total damper force as a function of time during the damper characterization at 2.5 A, illustrating the gradual change in damper behavior as temperature increased over the duration of the test. From 0^0C to 100^0C, the measured peak damper force dropped 37% for an applied current of 2.5 A. The force and displacement signals were segmented into one cycle intervals and used for further modeling and analysis.

Representative force vs. piston displacement and velocity data are shown in figure 2.7, providing the qualitative trends of the damper force behavior as a function of operating temperature. Comparing figures 2.7(a) and 2.7(b), it can be seen that the area inside each force/displacement curve decreases as temperature rises, indicating a decrease in the dissipated energy per cycle. Figure 2.9 graphically defines

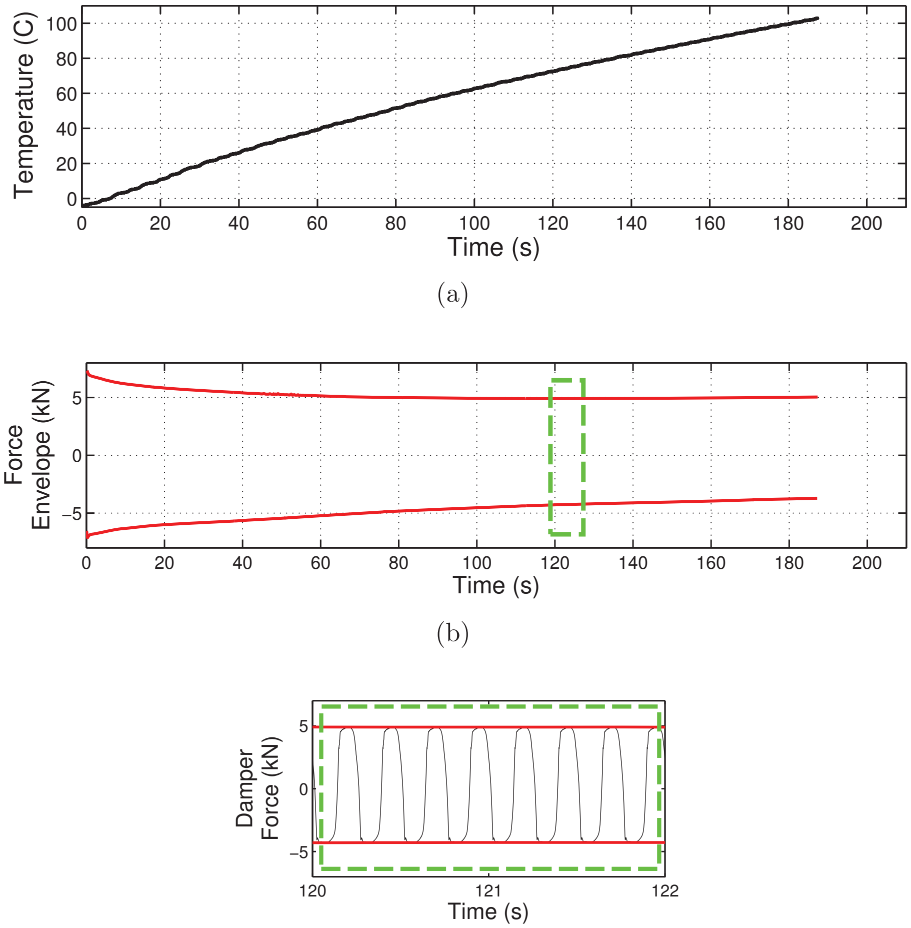

(a)

(b)

(c)

Figure 2.5: (a) Operating temperature of MR fluid during characterization as a function of time at 2.5 A constant field, (b) envelope of total damper force vs. time, and (c) total damper force and envelope over a portion of the characterization test in (b).

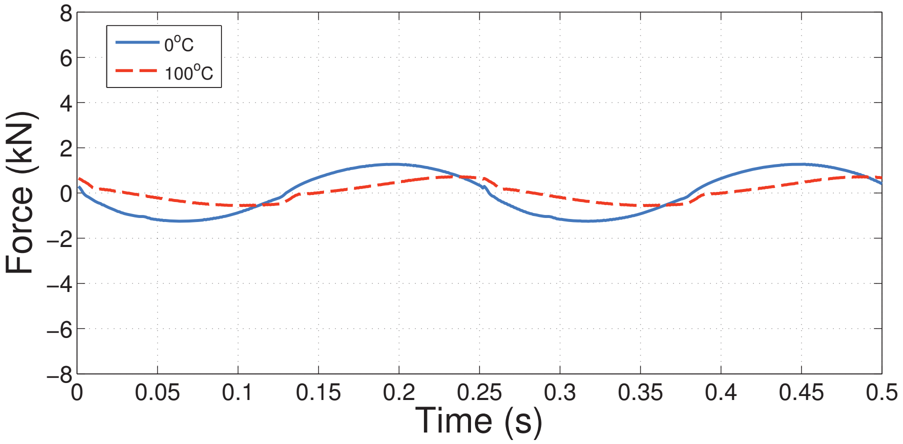

(a) 0 A of constant field.

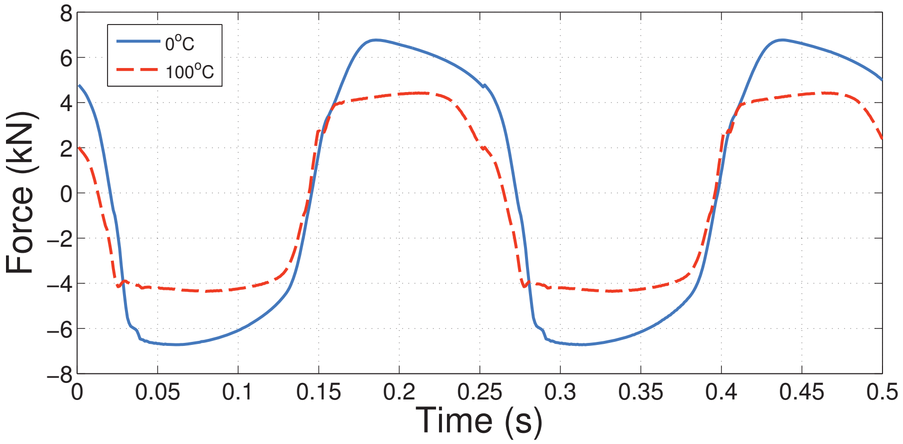

(b) 2.5 A of constant field.

Figure 2.6: Measured MR damper force vs. time.

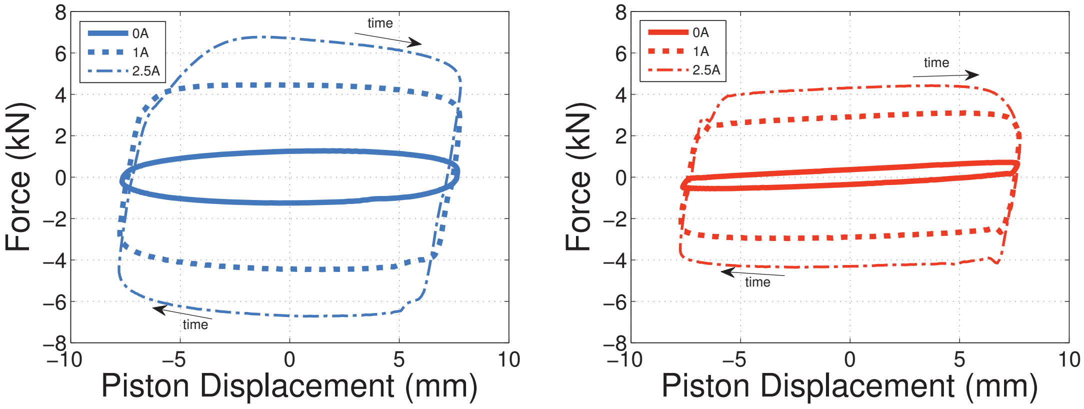

(a) Force vs. piston displacement data at 0^0C. (b) Force vs. piston displacement data at 100^0C.

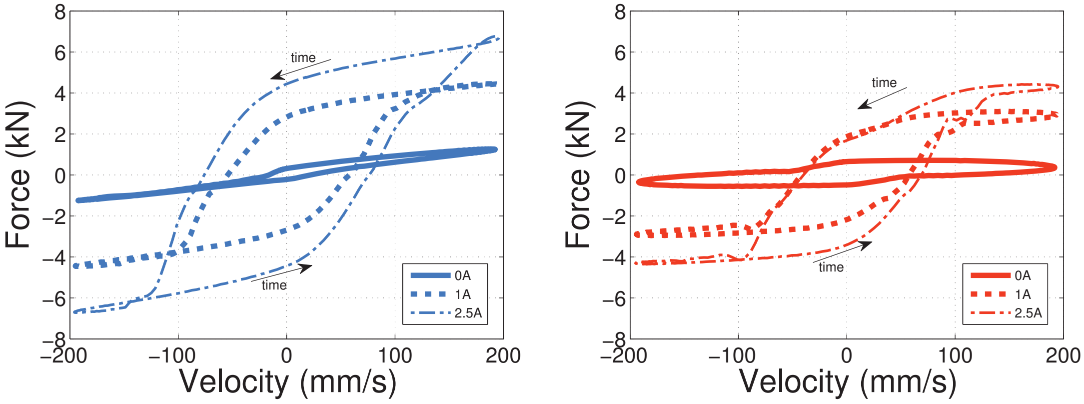

(c) Force vs. piston velocity data at 0^0C. (d) Force vs. piston velocity data at 100^0C.

Figure 2.7: Measured force signals of the MR damper.

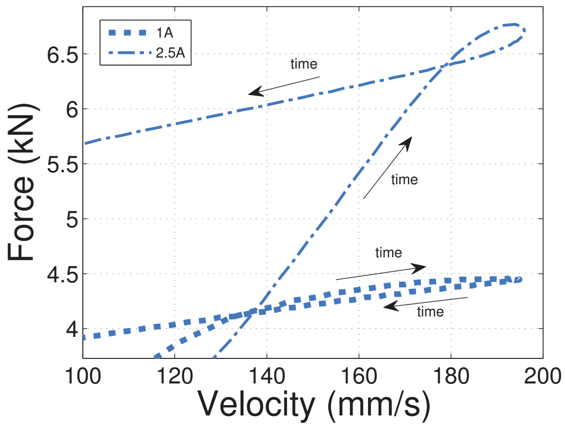

Figure 2.8: Zoomed view of figure 2.7(c) showing the force overshoot phenomenon in the force vs. piston velocity data at 0^0C.

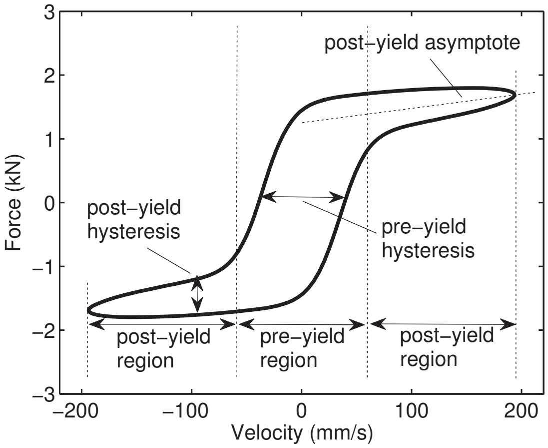

Figure 2.9: Representative force vs. piston velocity curve highlighting key features.

the post-yield force asymptote, which approximately intercepts the zero-velocity axis at the yield force and has a slope equal to the post-yield damping. Examining the force vs. velocity curves in figures 2.7(c) and 2.7(d), as temperature rises, the post-yield asymptotes rotate clockwise and translate toward a lower force level, illustrating the decrease in both the post-yield damping and yield force, respectively. Also seen in figures 2.7(c) and 2.7(d), the separation (or thickness) between the accelerating and decelerating portions of the curve along the post-yield asymptotes increases with with rising temperature, signifying an increase in damper stiffness. This is also indicated in figure 2.7(b) by the counter-clockwise rotation of the force vs. displacement curves. Another interesting phenomenon is the force overshoot, shown in figures 2.7(c) and 2.8 at 1.0 and 2.5 A, where the maximum force occurs before the maximum piston velocity is reached. This behavior is the result of coupling between the fluid inertia and the fluid pressure. The force overshoot is strongly dependent upon the damper stiffness (pressure), noting that at high temperature,

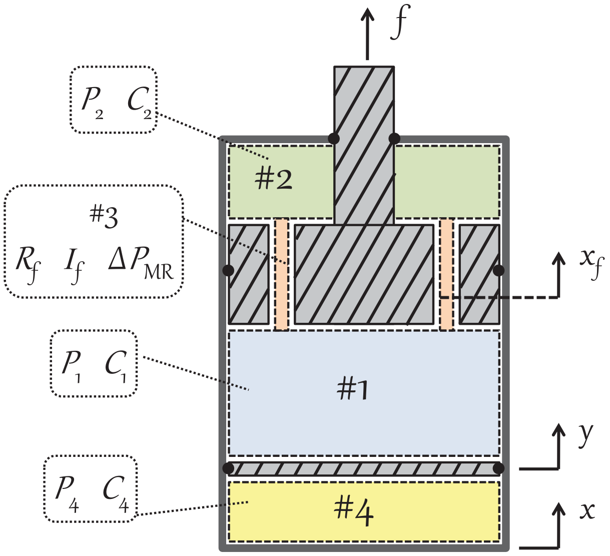

Figure 2.10: Hydromechanical representation of the MR damper.

as in figure 2.7(d), this behavior is not present.

2.4 Damper Analysis

A physically motivated analysis is derived from damper geometry and material properties. The final form of the model is expressed using temperature-dependent, lumped parameters that describe the damper force in response to a given excitation.

2.4.1 Derivation

A hydro-mechanical analysis, first established by Singh et al. [69] for passive dampers, and adapted by Hong et al. [40] for ER/MR dampers, is used to capture the behaviour of the MR damper. Figure 2.10 shows the physical representation of the model. The pressure drop across the piston head ΔP_p due to the fluid passing through the active gap can be written as

$$\Delta P_p = P_1 - P_2 = R_f A_f \dot{x}_f + I_f A_f \ddot{x}_f + \Delta P_{MR} \tanh\left((\dot{x} + \lambda_1 x)\lambda_2\right) \tag{2.1}$$

where

$$I_f = \frac{\rho l}{A_f} \tag{2.2}$$

$$R_f = \frac{12\mu l}{A_f d^2} \tag{2.3}$$

$$\Delta P_{MR} = \frac{2l}{d}\tau_y(H) \tag{2.4}$$

Here, I_f is the fluid inertance, R_f is the zero-field flow resistance, and ΔP_{MR} is the magnitude of the pressure drop due to the yield stress of the MR fluid. The hyperbolic tangent function $\tanh(\cdot)$, with rate parameters λ_1 and λ_2, was developed by Choi et al. [22], and adopted by others [35, 48]. It effectively captures the pre-yield hysteretic damper behavior and describes the on-set of the yield stress. The yield shear stress τ_y is a function of the magnetic field intensity H, ρ is the fluid density, μ is the zero-field fluid viscosity, A_f is the cross-sectional area of the active gap, l is the total active gap length in the direction of flow, d is the separation between the active gap walls, x is the piston displacement, and x_f is the displacement of the fluid inside the active gap.

The pressure of chambers #1 and #2 can be expressed, respectively, as

$$P_1 = P_0 + \Delta P_1 \tag{2.5}$$

$$P_2 = P_0 + \Delta P_2 \tag{2.6}$$

where P_0 is the constant static pressure, ΔP_1 is the pressure change of chamber #1 from static, and ΔP_2 is the pressure change of chamber #2 from static.

The rate of change of pressure equated to volume flow rate of each chamber can be expressed as follows

$$C_1 \dot{P}_1 = A_p \dot{y} - A_f \dot{x}_f \tag{2.7}$$

$$C_2 \dot{P}_2 = A_f \dot{x}_f - (A_p - A_r)\dot{x} \tag{2.8}$$

$$C_4 \dot{P}_4 = A_p \dot{x} - A_p \dot{y} \tag{2.9}$$

where C_1, C_2, and C_4 are the fluid compliances for chambers #1, #2, and #4, respectively, A_p is the area of the piston head, A_r is the cross-sectional area of the piston rod, and y is the displacement of the pneumatic accumulator. Equations (2.1) and (2.7) - (2.9) are the governing equations of the fluid flow inside the damper. The damper force is given as

$$f = P_1 A_p - P_2 (A_p - A_r) \tag{2.10}$$

and by substituting for P_2 with equation (2.1) we have

$$f = P_1 A_r + \left(R_f A_f \dot{x}_f + I_f A_f \ddot{x}_f + \Delta P_{MR} \tanh\left((\dot{x} + \lambda_1 x)\lambda_2\right)\right)(A_p - A_r) \tag{2.11}$$

Substituting equation (2.9) into (2.7) and rearranging gives

$$C_1 \dot{P}_1 = A_p \dot{x} - C_4 \dot{P}_4 - A_f \dot{x}_f \tag{2.12}$$

By assuming that $\dot{P}_4 \approx \dot{P}_1$, we can rearrange and integrate equation (2.12) to find

$$\Delta P_1 = \frac{A_p}{C_1 + C_4} x - \frac{A_f}{C_1 + C_4} x_f \tag{2.13}$$

The compliance C_2 is relatively small because the compressibility of the MR fluid is low, so we assume $C_2 \dot{P}_2 \approx 0$ in equation (2.8), giving

$$\dot{x}_f = \frac{A_p - A_r}{A_f} \dot{x} \tag{2.14}$$

Equations (2.5), (2.13) and (2.14) are substituted into (2.11) to give the damper force

$$\begin{aligned} f &= P_0 A_r + \frac{A_r^2}{C_1 + C_4} x + R_f (A_p - A_r)^2 \dot{x} + I_f (A_p - A_r)^2 \ddot{x} \\ &\quad + \Delta P_{MR} (A_p - A_r) \tanh\left((\dot{x} + \lambda_1 x)\lambda_2\right) \end{aligned} \tag{2.15}$$

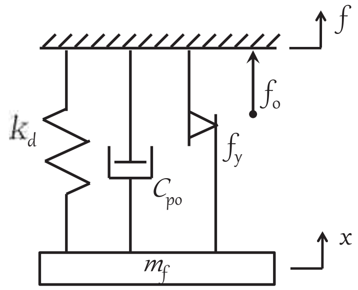

Figure 2.11: Nonlinear model of the MR damper.

The damper force can be expressed in a condensed lumped parameter form as

$$f = f_0 + k_d x + c_{po}\dot{x} + m_f\ddot{x} + f_y \tanh\left((\dot{x} + \lambda_1 x)\lambda_2\right) \tag{2.16}$$

where

$$f_0 = P_0 A_r \tag{2.17}$$

$$k_d = \frac{A_r^2}{C_1 + C_4} \tag{2.18}$$

$$c_{po} = R_f (A_p - A_r)^2 \tag{2.19}$$

$$m_f = I_f (A_p - A_r)^2 \tag{2.20}$$

$$f_y = \Delta P_{MR} (A_p - A_r) \tag{2.21}$$

Figure 3.5 shows the proposed lump parameter model with stiffness element k_d, post-yield damping c_{po}, yield force f_y, fluid inertial m_f, damper body displacement x, force off-set f_0, and damper force f.

Figure 2.12 shows how the model parameters contribute toward the force/velocity curve.

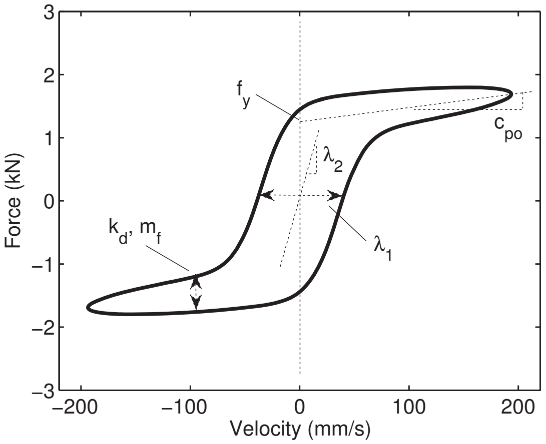

Figure 2.12: Representative force vs. piston velocity curve highlighting the contributions from the model parameters.

2.5 Modeling Results and Discussion

A constrained least-mean-squared error minimization was performed to identify the model parameters from the measure data using the following cost function:

$$J(f_0, k_d, c_{po}, m_f, f_y, \lambda_1, \lambda_2) = \sum_{k=1}^{N} [f(t_k) - \hat{f}(t_k)]^2 \tag{2.22}$$

Here, $f(t_k)$ is the measured force, $\hat{f}(t_k)$ is the modeled force calculated using equation (2.16), and t_k is the time at which the k^{th} sample was taken. The cost function, J, was minimized while constraining all seven parameters to be greater than zero. This minimization procedure was performed at temperature measurements from 0^0C to 100^0C, in increments of 1^0C.

Representative plots of the measured and modeled force-velocity curves for low and high temperature operation are seen in figure 2.13. There is good correlation

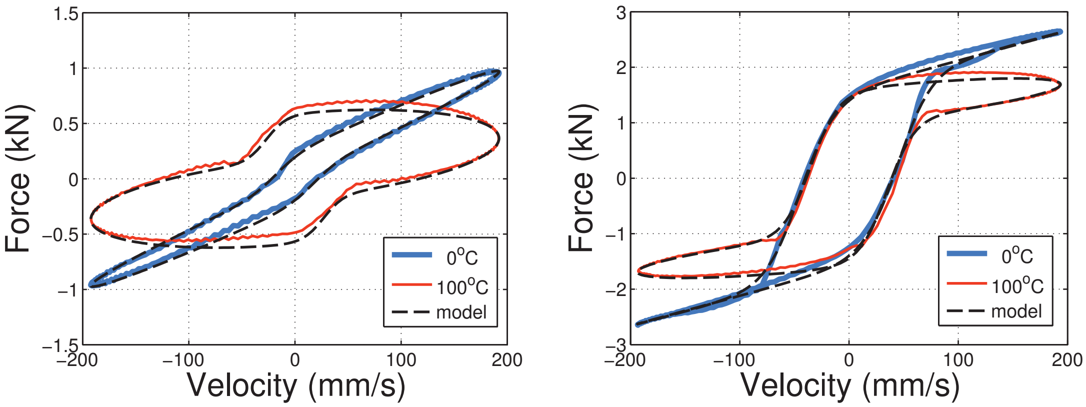

(a) Field off.

(b) 0.5 A.

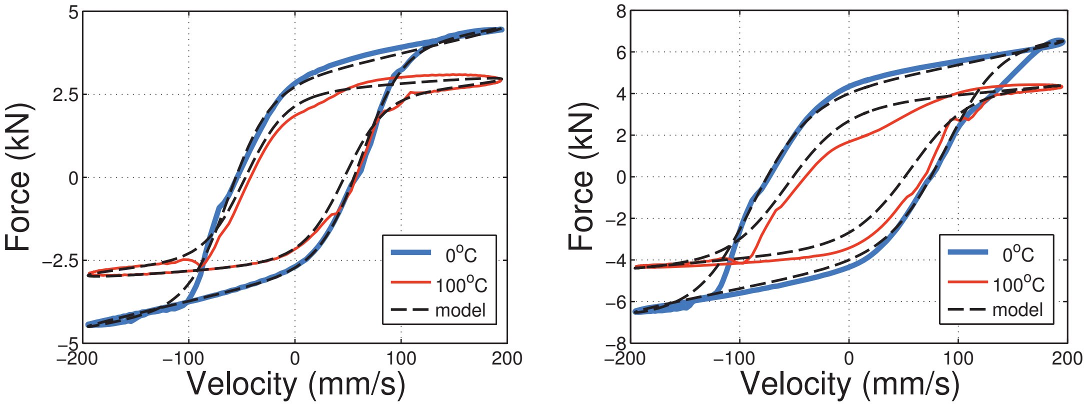

(c) 1 A.

(d) 2.5 A.

Figure 2.13: Force vs. velocity curves of the MR damper measured data and model. (Note that the bias force was removed from the data.)

between the model and the measured data across both the entire tested temperature range and applied fields. The hysteresis at high piston velocity, due to increased stiffness at high temperature, is captured with the model. At cold temperatures, the model captures the force overshoot phenomenon seen at applied fields of 1.0 and 2.5 A in figure 2.14.

2.5.1 Quantification of Modeling Error

To quantitatively evaluate the correlation between model and experiment, two error metrics are used. The first metric is the energy error and it quantifies the extent

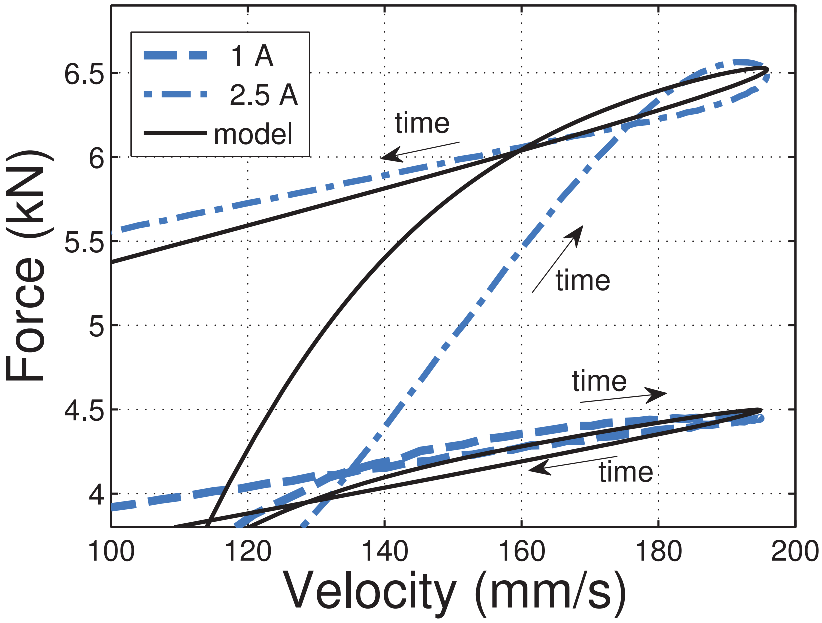

Figure 2.14: Zoomed view of figures 2.13(c) and 2.13(d) showing the model capturing the force overshoot phenomenon in the force vs. piston velocity data at 0^0C.

the model differs from the measured data in terms of the dissipated energy. This is determined by calculating the dissipated energy over one cycle using

$$E = \oint f(t)dx = \int_0^{2\pi/\omega} f(t)\dot{x}(t)dt \tag{2.23}$$

The energy error is then calculated using

$$\Delta E\% = 100 \left| \frac{E - \hat{E}}{E} \right| \tag{2.24}$$

where E is the energy calculated from the experimental data and $\hat{E}$ is the energy calculated from the model.

The second model performance metric is the complex correlation coefficient

(CCF) [23, 33]. This method compares the boundaries or perimeters of two 2D geometries to assess their similarity. The boundary functions are given by

$$\begin{aligned} b(t) &= x(t) + jf(t) \qquad (2.25) \\ \hat{b}(t) &= x(t) + j\hat{f}(t) \qquad (2.26) \end{aligned}$$

where b is the boundary function for the damper displacement and measured force, and $\hat{b}$ is the boundary function for the damper displacement and modeled force. The CCF is then given by

$$CCF = \frac{\int b(t)\hat{b}^*(t)dt}{[(\int b(t)b^*(t)dt)(\int \hat{b}(t)\hat{b}^*(t)dt)]^{1/2}} \qquad (2.27)$$

where $b^*(t)$ and $\hat{b}^*(t)$ are the complex conjugates of $b(t)$ and $\hat{b}(t)$, respectively. If the two geometries being compared are identical then the CCF will equal unity. This performance metric evaluates both the magnitude and phase of the model.

Figure 2.15 shows the level of correlation between model and data using both performance metrics. Note that for all cases, the energy error is $< 1\%$ and the complex correlation metric was $> 99\%$. Thus, the model very accurately represents the measured data.

2.5.2 Model Parameters

The behavior of the model parameters versus operating temperature is presented in figure 3.6.

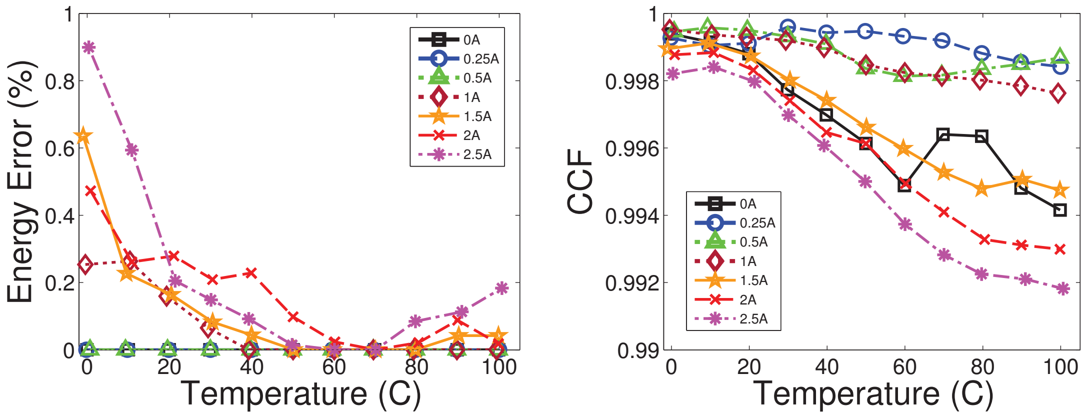

(a) Energy error vs. operating temperature.

(b) CCF vs. operating temperature.

Figure 2.15: Model correlation metrics.

2.5.2.1 Force Offset, f_0, and Stiffness, k_d

Figures 3.6(a) and 3.6(b) show the force offset f_0 and stiffness k_d terms increasing linearly with operating temperature. As the operating temperature increases from 0^0C to 100^0C, the mean value of the stiffness k_d, across all measured applied fields, increases over 300%. The compliance of the nitrogen-filled accumulator, chamber #4 (figure 2.10), is much greater than that of the hydrocarbon oil based MR fluid chamber #1 ($C_4 >> C_1$), so we may rewrite equation (2.18) as

$$k_d \approx \frac{A_r^2}{C_4} \tag{2.28}$$

and conclude that the stiffness k_d is primarily attributed to the compressibility of the nitrogen-filled pnuematic accumulator. Assuming nitrogen gas obeys the ideal gas law, the accumulator pressure is linearly proportional to temperature, explaining the trend we see in figure 3.6(b).

The force offset f_0 is also directly proportional to the static internal pressure

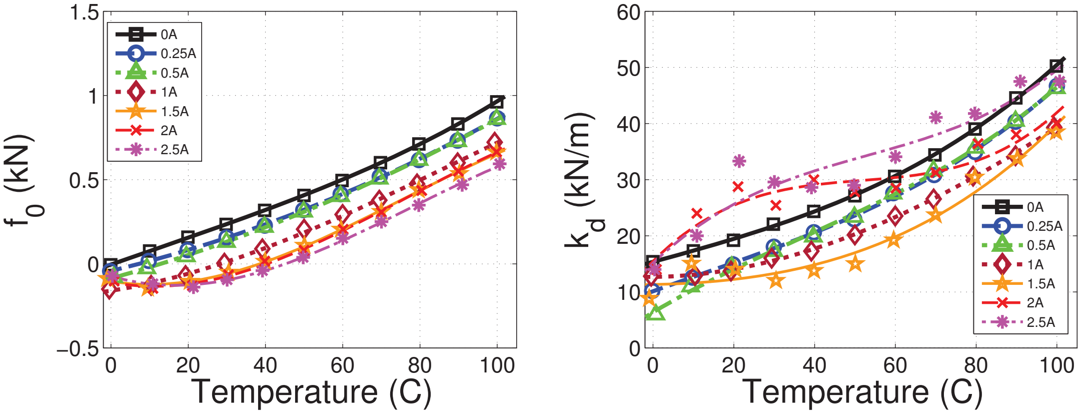

(a) Force offset f_0.

(b) Stiffness k_d.

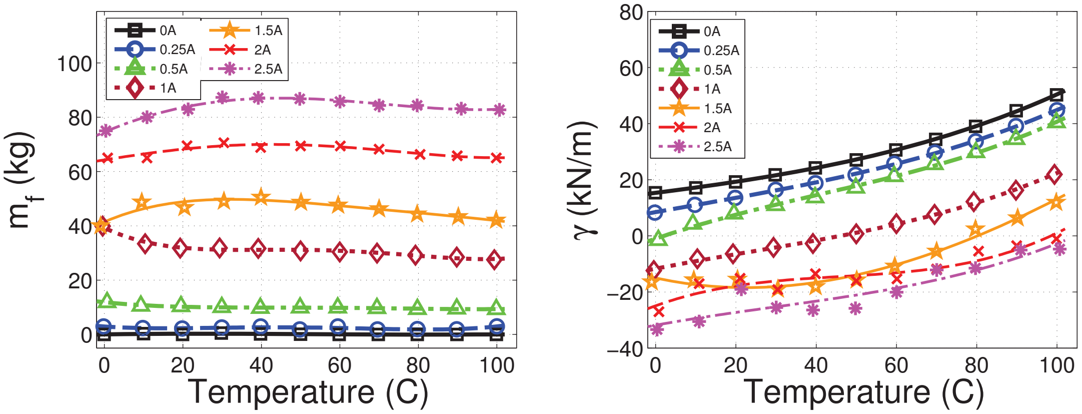

(c) Inertia m_f.

(d) γ.

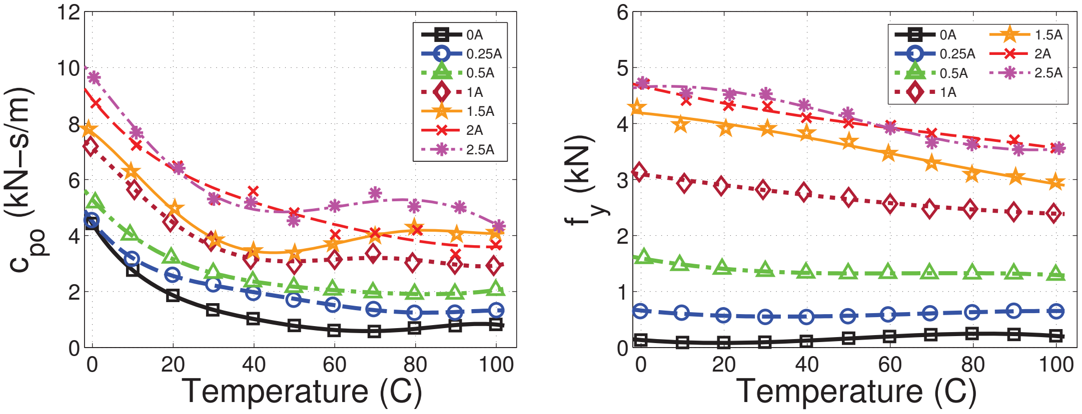

(e) Post-yield damping c_{po}.

(f) Yield force f_y.

Figure 2.16: Model parameters as a function of operating temperature.

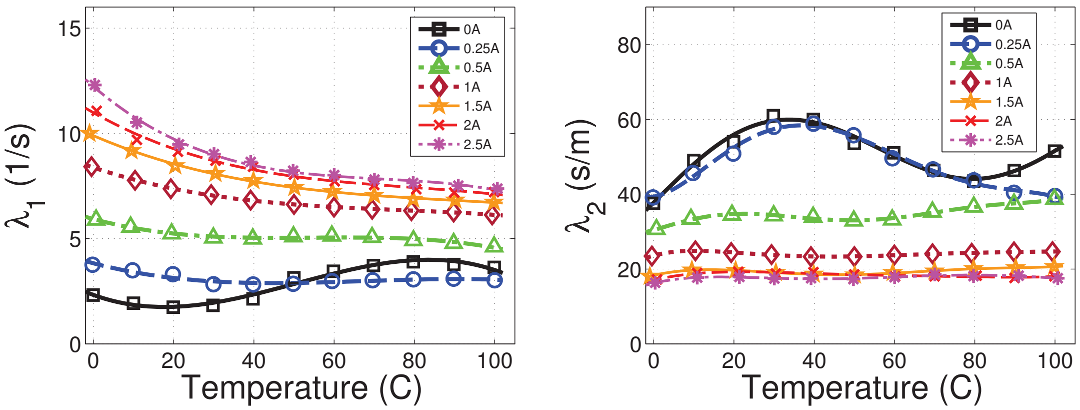

(a) λ_1.

(b) λ_2.

Figure 2.17: Model parameters as a function of operating temperature.

of the damper P_0 in equation (2.17), again explaining the linear relationship with temperature in 3.6(a) for all applied fields. As applied field increases, the trend lines for f_0 shift lower in value. This is attributed to any asymmetry in the damper force between the compression and extension portions of the stroke cycle which may become more prominent as the applied field increases.

2.5.2.2 Inertia, m_f

Considering equations (2.2) - (2.4) and (2.20), the inertia, m_f, is physically connected to the fluid density and damper geometry. The Lord MRF132-DG fluid used in this study is composed of a hydrocarbon-based carrier fluid, similar to the Shell Vitrea series oil. It has been shown [80] that the density of Shell Vitrea 460 decreases by $6-8\%$ as the temperature increases from 0^0C to 100^0C within the pressure range of 0.1 to 8 MPa. Figure 3.6(c) reveals the inertia m_f is relatively constant as a function of temperature, assuming a value of zero in the absence of applied field (0 A) and increases as a function of applied field. While the fluid density may change slightly with temperature, the temperature trends in figure 3.6(c) do not clearly reflect this perturbation.

It is interesting to consider the combined effect of m_f and k_d. By assuming a harmonic excitation of $x = \sin(\omega t)$ and ignoring the static offset force f_0, equation (2.16) becomes

$$f = \gamma x + c_{po}\dot{x} + f_y \tanh\left((\dot{x} + \lambda_1 x)\lambda_2\right) \tag{2.29}$$

where $\gamma = (k_d - \omega^2 m_f)$ and is dependent upon k_d, m_f, and the excitation frequency ω. Figure 3.6(d) presents γ as a function of temperature for several applied fields. Assuming m_f is relatively temperature independent, k_d accounts for the linear temperature dependence of γ and the role of m_f serves only to translate the trend lines vertically in figure 3.6(d).

Figure 2.18 shows the effect γ has on the damper force at high piston velocity. A value of $\gamma = 0$ indicates a net absence of both damper stiffness and inertia terms that contribute towards total damper force. While both may be physically present, they act in such a way that one cancels the effect of the other, so that only the MR yield-force f_y and post-yield damping c_{po} determine damper force. When $\gamma > 0$, the stiffness term k_d dominates the expression for γ, which can be visually seen in figure 2.18 as a thickening of the hysteresis along the high piston velocity asymptote. This occurs at low applied fields and high operating temperatures. When $\gamma < 0$, the inertial term m_f dominates the expression for γ, indicating that fluid inertia has the more significant contribution to damper force. This can visually be seen in

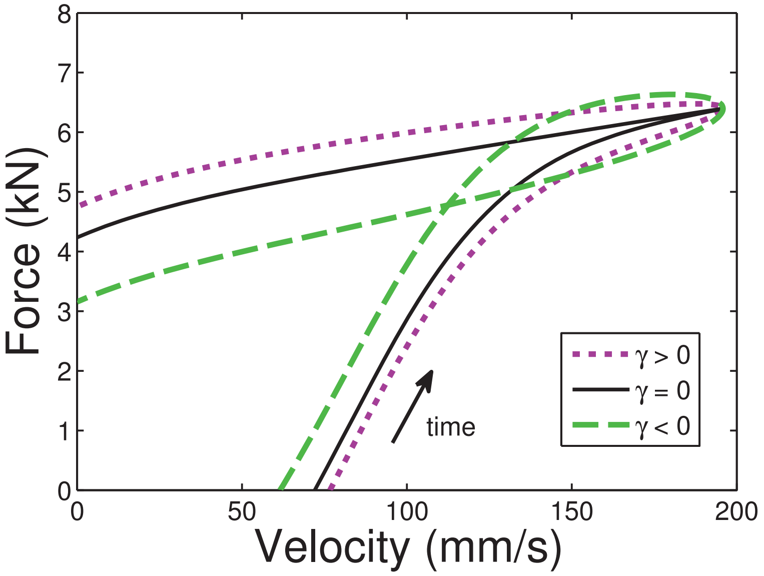

Figure 2.18: Sensitivity of the term γ.

figure 2.18 as an overshoot of the damper force as the piston positively accelerates just prior to achieving maximum piston velocity. This is found to occur at lower operating temperatures and higher applied fields.

2.5.2.3 Post-yield Damping, c_{po}

Figure 3.6(e) shows that the post-yield damping c_{po} decreases significantly as temperature rises for all applied fields. At the field-off condition, the post-yield damping decreases 80% at 100^0C when compared from 0^0C. This reduction in viscosity is a result of the increase in thermal energy of the fluid. The post-yield viscous damping c_{po} is physically connected to the fluid viscosity and internal geometry of the piston head such that

$$c_{po} = \frac{12\mu l}{bd^3}(A_p - A_r)^2 \tag{2.30}$$

where the circumference of the active gap $b = A_f/d$, and μ is the temperature-dependent fluid viscosity which obeys an Arrhenius or Williams-Landel-Ferry model [11], capturing the exponential decay seen in figure 3.6(e). The origin of the field-dependent nature of c_{po} is not clear, but it may be capturing the fluid's field-dependent transition from pre-yield to fully post-yield flow, or may be attributed to a reduction in the annular gap thickness d caused by truncated chains of iron particales magnetically attached to the valve walls.

2.5.2.4 Yield Force, f_y

Figure 3.6(f) shows the yield force f_y decreases as temperature rises for large applied fields but remains generally constant for fields corresponding to 0.25 and 0 A. The nonzero yield force for the field-off condition is due to passive friction that exists due to contact between the damper piston and seals. At large applied fields, the yield force can decrease by up to 30% over temperatures ranging from 0^0C to 100^0C.

Iron (Fe) is a ferromagnetic material possessing a Curie temperature of 770^0C. Far below this Curie temperature, Morrish [57] shows the spontaneous magnetization (that which exists in the absence of external magnetic field) of iron (Fe) decreases by only 2% from 0^0C to 100^0C, and alone can not explain the large 30% reduction in yield force in figure 3.6(f). Indeed, Sheng et al. [66] have conducted static shear mode testing of an MR fluid with a drag-cup type rheometer and stepper motor at operating temperatures from 20^0C to 140^0C and shown the change in yield stress of the MR fluid due to temperature effects to be negligible.

Kciuk and Turczyn [46] suggests yield stress decreases as a result of the fluid's reduced volume fraction due to increases in temperature. Based on an 8% decrease in fluid density from 0^0C to 100^0C [80], the volume fraction would decrease 7.5% from 0.32 to 0.296. Using an empirical model [12] relating yield stress to volume faction, this temperature increase corresponds to an 11% decrease in yield stress.

Mao et al. [52] study MR damper behavior at high piston velocities (5 m/s) and propose a Reynolds number dependent model that accurately captures the off-state damper force for piston velocities up to 5 m/s, which include turbulent, or transition, flows that develop for velocities > 2.5 m/s (or $Re > 2,000$). However, the model over-predicts the on-state damper force (viscous and MR yield force) at high piston velocities (> 2.5 m/s) which Mao et al. attributes to a loss in yield force due to the recirculation and turbulent nature of the flow. At a piston velocity of 5 m/s ($Re \approx 4,000$), Mao et al. shows the measured MR yield force is reduced by approximately 20% from the value predicted by the model.

Reynolds number is defined as

$$Re = \rho \dot{x}_f D_h / \mu \tag{2.31}$$

where $\dot{x}_f$ is the average fluid velocity through the MR valve and D_h is the hydraulic diameter, where $D_h = 2d$. The Reynolds number can increase due to both higher fluid velocities as well as decreases in fluid viscosity, the latter of which can be seen in figure 3.6(e) as a large 80% reduction in viscous damping. If we assume that this reduction in viscous damping is purely due to a change in fluid viscosity

μ and we hold ρ, $\dot{x}_f$, and D_h constant, then Reynolds number increases by 500% from $Re = 25$ at 0^0C to $Re = 125$ at 100^0C. Despite this large percentage increase, the fluid is operating within the laminar region throughout the entire temperature range, and may not explain the reduction in MR yield force seen in figure 3.6(f). Further testing is necessary to accurately identify the mechanism to which the yield force is most sensitive.

2.5.2.5 Shape parameters, λ_1 and λ_2

The hyperbolic tangent shape function in equation (2.16) is used to describe the onset of the yield force using the two parameters λ_1 and λ_2. The λ_1 term is coupled with the piston displacement which lags piston velocity by 90 degrees, thereby introducing the appropriate phase to the applied yield force. As the value of λ_1 increases the width of the low-velocity hysteresis loop increases due to the piston displacement influencing the behavior of the shaping function. The λ_2 term is coupled with the overall value of the quantity $(\dot{x} + \lambda_1 x)$, which thereby dictates the rate at which the fluid becomes fully yielded. As the value of λ_2 increases the slope of the hysteresis loop becomes more steep.

Figure 3.7(a) shows a decrease in λ_1 as temperature rises for all applied fields except for the field-off condition. Physically this indicates a phase lead shift in the on-set of the fluid yielding which can be attributed to the higher stiffness of the accumulator forcing the fluid to pass through the active annulus. Graphically this can be seen in the force/velocity plots (figure 2.13) as a reduction in the horizontal width of the low-velocity hysteresis. As the applied field is increased, the value of λ_1

increases, indicating a phase lag shift in the on-set of the fluid yielding. This delay can be physically attributed to a larger pressure required to build on the leading face of the piston head before fluid may flow through the annulus.

Figure 3.7(b) reveals λ_2 remains fairly constant as a function of temperature for each applied field except for the field-off and 0.25 A condition, which both show a large increase in value around the 10^0C to 60^0C range. However, this aberation only has a small effect on the model fit as the yield force is not well developed at these low applied fields. As the applied field is increased, the value of λ_2 decreases, which can be seen graphically in figure 2.13 as a clockwise rotation of the slope of the low-velocity hysteresis. Physically, this reduction in λ_2 indicates a longer period of time required to develop a fully yielded fluid flow, and is expected considering a larger pressure must develop before the yield stress of the fluid is overcome.

2.6 Conclusions

A linear stroke, MR fluid damper was built and characterized over temperatures ranging from 0^0C to 100^0C. The measured peak damper force, for a constant applied field of 2.5 A, was shown to decrease by 37% as temperature increased from 0^0C to 100^0C. Aside from external heating, an MR damper may internally self-heat due to both resistive heating by the electromagnetic coil and, to a greater extent, by dissipating mechanical energy into thermal energy. Temperature can significantly alter damper behavior as the fluid viscosity and accumulator gas pressure are highly dependent on temperature. Several existing damper models exhibit the ability to capture key features of the pre-yield and post-yield force behavior of an MR damper that can be observed across a large temperature range, however few models have addressed the implications of temperature. In order to accurately model the damper force over temperatures ranging from 0^0C to 100^0C and to gain insight into how temperature affects damper force behavior, a hydro-mechanical analysis of the MR damper was developed which provided a lump parameter model with a physical connection to damper geometry and MR fluid properties.

It was shown that the proposed model captured the pre-yield hysteresis with the hyperbolic tangent function prescribing the onset of the yield force with the shaping parameters λ_1 and λ_2. λ_1 is dependent on temperature and is correlated with the accumulator pressure, while λ_2 is relatively insensitive to temperature but correlated with the applied field. The yield force f_y is shown to be dependent on temperature and decreases by up to 30% as temperature increased from 0^0C to 100^0C. Further investigation is required to better identify the mechanism causing this temperature-related decrease in yield force.

The model also captured the post-yield force behavior which can dramatically change over temperatures ranging from 0^0C to 100^0C. The post-yield damping c_{po} was shown to be directly proportional to fluid viscosity, which is highly temperature dependent, and decreased up to 85%. The stiffness k_d was shown to be linearly porportional to temperature over the temperature range of 0^0C to 100^0C and increases significantly by several hundred percent. The fluid interia m_f was found to be fairly insensitive to temperature, but dependent on applied field. As temperature increased, the time at which the peak force occured during the stroke cycle could shift. This was most evident at large applied fields (ie. 2.5 A) as the peak force shifted from occuring before the maximum piston velocity was reached at mid-stroke to ocurring after. This is due to stiffness and inertial effects. The parameter k_d provides the mechanism to capture the damper stiffness from the pnuematic accumulator and the parameter m_f provides the mechanism to capture the effects of fluid inertia. As k_d increases, the peak force shifts toward occuring after the maximum piston velocity, and as m_f increases relative to k_d the peak force shifts toward occuring before the maximum piston velocity, causing the force overshoot phenomenon at large applied fields.

Chapter 3

Impact of Temperature on Magnetorheological Damper Vibration Control

3.1 Introduction

The isolation performance of a single degree-of-freedom magnetorheological (MR) suspension, exposed to a broad frequency spectrum disturbance as temperature and payload mass vary, is analyzed. Aside from external environmental heating, an MR damper may internally self-heat due to both resistive heating by the electromagnetic coil and, to a greater extent, by dissipating mechanical energy into thermal energy. Temperature can significantly change damper behavior as the fluid viscosity and accumulator gas pressure are highly dependent on temperature. The analysis shows an MR suspension with an appropriately chosen control strategy, subject to practical temperature and payload mass perturbations ranging from 0^0C to 100^0C and 46.5 kg to 96 kg, respectively, can provide robust, broadband vibration attenuation.

3.2 Background

Magnetorheological (MR) fluids are a type of material with rheological properties that can be quickly altered by the application of an external magnetic field, offering adaptable damping characteristics. MR fluids consist of micron-sized ferrous particles suspended in a carrier fluid such as oil, water, or glycol [13]. The MR fluid inside a damper can experience large variations in temperature due to resistive heating of the electromagnetic coil and, to a greater extent, fluid agitation as the damper dissipates mechanical energy into thermal energy by shearing the fluid as it flows through an orifice in the piston traveling through the hydraulic cylinder.

Temperature can significantly affect the rheological properties of the MR fluid [54]. Sahin et al. [64] measured the rheological properties of an MR grease with a shear mode rheometer and proposed a temperature dependent Herschel-Bulkley model, showing temperature has an appreciable effect on the field-induced dynamic yield stress. Wilson et al. [79] developed an analysis that captures the temperature dependent force behavior of an MR damper, and highlights significant losses in yield force and viscous damping, and a significant increase in the pneumatic accumulator pressure. Batterbee and Sims [7] showed feedback controllers for MR shock absorption applications can exhibit reduced force-tracking performance as temperature increases due to a reduction in viscous damping and yield force.

Consequently, research has been conducted to study how to compensate for these temperature effects. Gordaninejad and Breese [31] developed an energy balance framework to predict the heat generation of MR fluid dampers as a function of energy entering a defined control volume through mechanical and electrical work, or leaving through termal conduction. Dogruoz et al. [26] attempted to enhance heat transfer from an MR damper through the use of thermally conductive heat-sink fins to minimize the loss of zero-field, viscous damping for fail-safe damper applications. Liu et al. [49] investigated a control strategy for vibration reduction with an MR damper and demonstrated improved isolation performance using temperature compensation over uncompensated control. However, in a practical sense, additional sensors and hardware for temperature measurement are undesirable because of the added cost and maintenance requirements.

Temperature can indeed impact the isolation performance of an MR suspension. At elevated temperatures, a decrease in fluid viscosity may enhance isolation for high frequency disturbances due to a larger dynamic force range between the on and off state [51]. A loss in the MR yield stress reduces the maximum achievable total damping force, equating to a loss in control authority at resonance. An increase in damper stiffness may shift the natural frequency of the system higher and degrade isolation.

This paper investigates the robust nature of a semi-active control law, without temperature or payload mass compensation, applied to a single degree-of-freedom system when the MR damper experiences perturbations in operating temperature ranging from 0^0C to 100^0C, and the suspension experiences perturbations in payload mass ranging from 46.5 kg to 96 kg. The purpose of this study is to show that an appropriately chosen controller provides performance robustness to practical temperature and payload mass perturbations that are encountered in magnetorheological isolation systems.

3.3 A Review of Isolation

An isolation suspension is designed to attenuate vibration transmitted to a payload from an external disturbance. There are several features a suspension must possess to successfully meet this objective. These features impact the frequency response of the system which is a ratio of the transmitted acceleration to the payload from the base mount as a function of disturbance frequency. A representative frequency response function (FRF) for a single-DOF, second order linear system is shown in Fig. 3.1(a). Meirovitch [55] gives an excellent analysis on the subject. Below the nondimensional crossover frequency, $\omega/\omega_n = \sqrt{2}$, where ω is the disturbance frequency and ω_n is the natural frequency, the transmissibility is greater than or equal to unity (ie. $Tr \geq 1$) and defined as amplification, and above the crossover frequency, $Tr \leq 1$ and defined as isolation. The largest amplification in the FRF is defined as resonance and occurs at or below $\omega/\omega_n = 1$, depending on the amount of damping in the system.

Ideally, it is desired to have isolation ($Tr \leq 1$) for all disturbance frequencies. For a passive system, Fig. 3.1(a) shows that isolation is achieved only for frequencies $\omega > \sqrt{2}\omega_n$. Thus, in order to attain isolation for all disturbance frequencies, ω_n must hypothetically equal zero, causing the FRF in Fig. 3.2 to compress toward the left.

The natural frequency ω_n is purely a function of payload mass and suspension stiffness. Assuming that for any application the payload mass is fixed, the suspension stiffness is the only adjustable parameter in the design, and reducing the stiffness toward zero would provide full spectrum isolation. However, a lower limit constraint is placed on the suspension stiffness in order to satisfy a maximum allowable static deflection. This deflection criteria is gravity dependent and often established to ensure sufficient rattle space and avoid impingement with the surounding environment. Therefore, it is common practice to lower the suspension stiffness until the maximum allowable static deflection is reached, shifting ω_n as low as possible.

Second, it is desired to minimize the amplification at resonance. This is accomplished by adding damping to the system. As the damping ratio ζ increases, where ζ is the non-dimensional ratio between the actual system damping and critical damping, the resonant transmissibility decreases, however, simultaneously the transmissibility above $\sqrt{2}\omega_n$ increases. As ζ approaches infinity the transmissibility for all disturbance frequencies approaches unity. This is the trade-off when designing an passive isolation suspension.

A suspension with adaptable damping can overcome the trade-off between high or low damping faced by a passive system. Ideally, that suspension would exhibit high damping at disturbance frequencies below $\sqrt{2}\omega_n$ while exhibiting low damping above $\sqrt{2}\omega_n$, thereby tracing the lower "semi-acitve" curve in Figure 3.1(a). MR dampers can provide this adaptability. In the absence of magnetic field, only passive viscous damping presists, establishing a lower damping limit. With the application of field, the ferrous particles form chains due to magnetic attraction

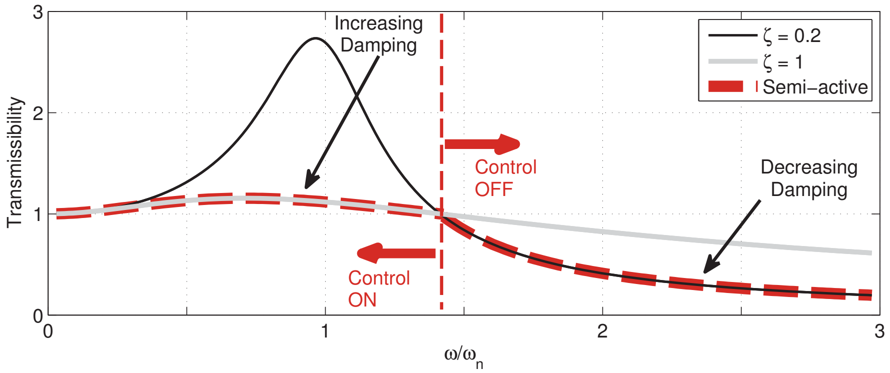

(a) Frequency response.

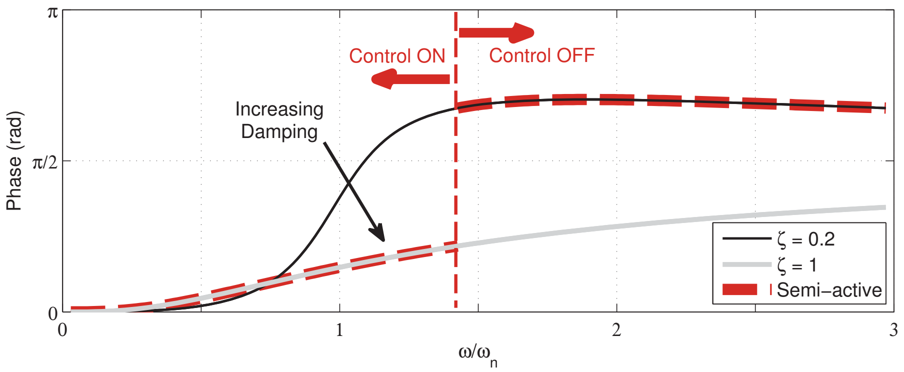

(b) Response phase angle.

Figure 3.1: Frequency response function.

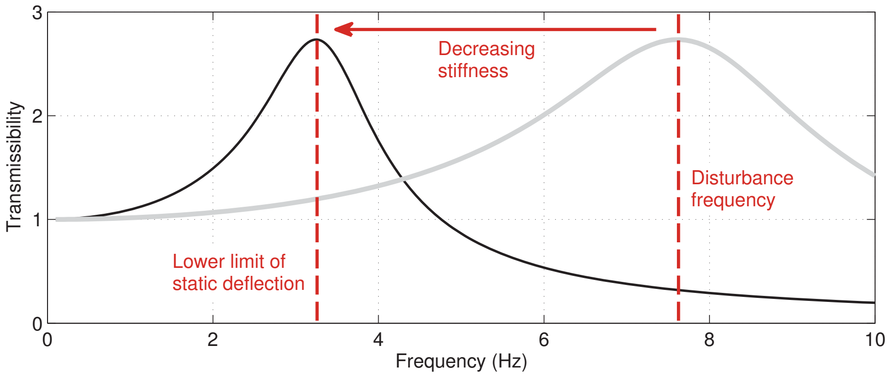

Figure 3.2: Effect of stiffness on frequency response.

which must be severed before fluid may flow. This creates a yield stress, in addition to the viscous stress, causing increased damping. In practice, high damping is commanded when the direction of the payload's absolute velocity is the same as the relative velocity between payload and base, while low damping is commanded when the two velocities are of opposite direction. This strategy stems from the phase lag between the payload relative to the base, seen in Figure 3.1(b). Phase lag is proportional to the duration of time it is desired to have high or low damping in the suspension. A phase lag of zero indicates the two velocities share the same direction 100% of the vibratory cycle, causing high damping to be desired 100% of the cycle. Conversely, a phase lag of π indicates the two velocities share the same direction 0% of the vibratory cycle, causing low damping to be desired 100% of the cycle. An appropriately chosen control strategy can exploit the implications of phase lag and achieve these desireable damping properties.

3.4 System Description

The robust nature of an MR damper's ability to provide vibration attenuation while experiencing large perturbations in operating temperature and payload mass is investigated through analyzing the frequency response of a base excited system in figure 3.3. This system is a model of an occupant seat suspension designed for the US Marine Corps's amphibious Expeditionary Fighting Vehicle (EFV) [42]. Figure 3.4 shows the MR damper designed for the EFV occupant seat suspension, which was built at the University of Maryland. The EFV vehicle can encounter broad

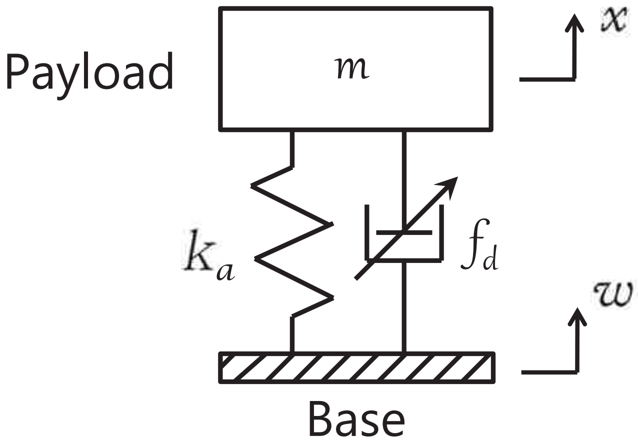

Figure 3.3: Single degree-of-freedom MR seat suspension system.

spectrum vibration and shock, in both land and sea mode operation, requiring low transmissibility over a large frequency range. The highly nonlinear system prohibits an analytical solution of the frequency response, thus a computational study is conducted using a steady-state harmonic base excitation.

The EFV vehicle may be operated by seated occupants of varying mass, therefore three occupant weight-classes are considered which bound the study - a 95^{th} and 50^{th} percentile male and a 5^{th} percentile female, taken to weigh 96.0, 77.5, and 46.5 kg, respectively. It is assumed that 29% of the occupant's weight (ie. the legs) is being supported by the floor [34]. In addition to these masses, 11.4 kg of body worn equipment is added to the upper torso, and 2.3 kg is added to the head to account for a protective helmet.

Figure 3.4: Magnetorheological (MR) seat damper.

3.4.1 Equation of Motion

The governing equation of the system dynamics is given as

$$m\ddot{x} = f_k + f_d + f_g \tag{3.1}$$

where m is the mass of the occupant and seat, and x is the absolute displacement of the sprung mass. The force of the suspension's coil spring is given as

$$f_k = -k_a q, \tag{3.2}$$

where the axial stiffness $k_a = 55$ kN/m, the compressive stroke displacement of the piston $q = (x - w) \leq 0$, and w is the base displacement. The gravitational force

$$f_g = -mg, \tag{3.3}$$

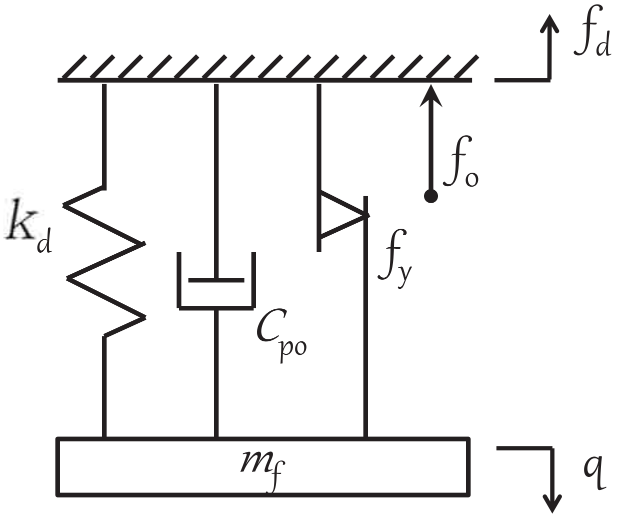

Figure 3.5: Nonlinear model of the MR damper.

where g is the acceleration of gravity. The MR damper force on the sprung mass, f_d, is modeled as [79]

$$f_d = f_o - k_d q - c_{po}\dot{q} - m_f\ddot{q} - f_y \tanh\left((\dot{q} + \lambda_1(q - q^*))\lambda_2\right). \tag{3.4}$$

and illustrated in figure 3.5, where k_d is the damper stiffness, c_{po} is the post-yield damping, f_y is the yield force, m_f is the fluid inertia, f_o is the force off-set, and q^* is the static equilibrium value of the compressed piston displacement. The temperature dependence of the model parameters from chapter 2 is presented in figure 3.6 and will be assumed for the analysis.

3.4.2 Control Law

Several semi-active control strategies have been used to govern an MR damper for vibration and shock isolation [5, 17, 21, 28, 45, 60]. The Skyhook algorithm was

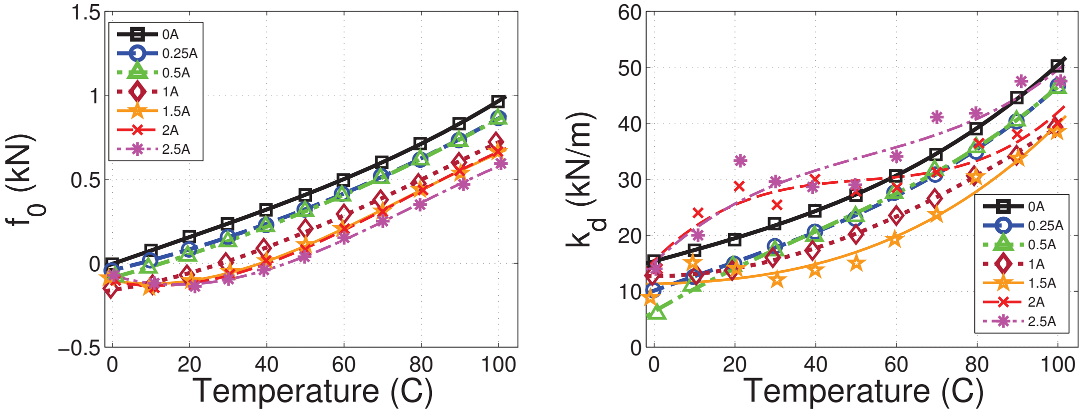

(a) Force offset f_0.

(b) Stiffness k_d.

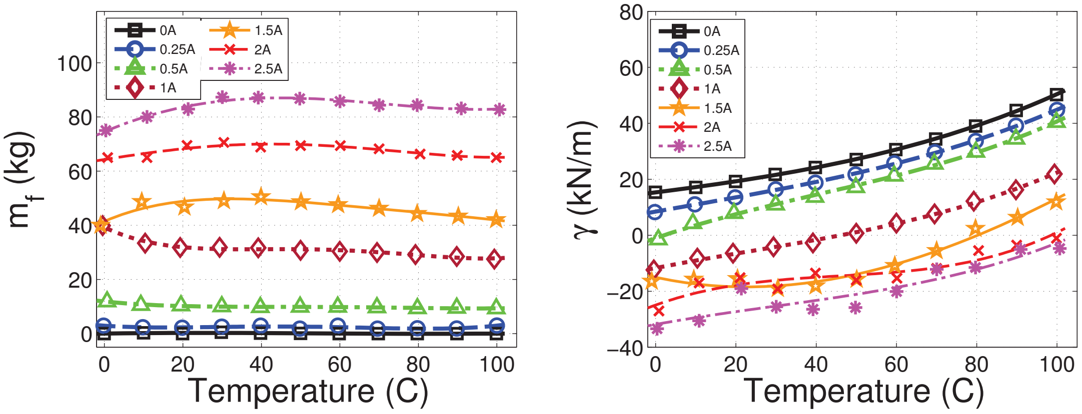

(c) Inertia m_f.

(d) γ.

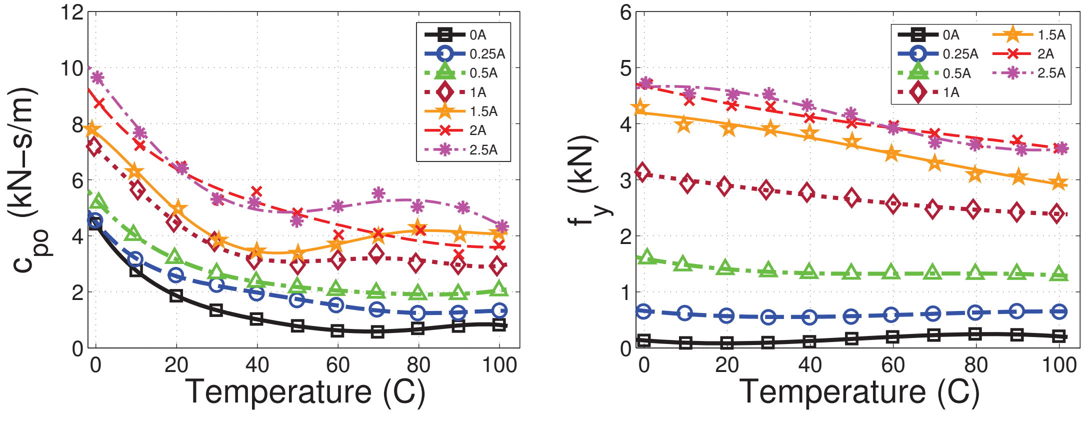

(e) Post-yield damping c_{po}.

(f) Yield force f_y.

Figure 3.6: Model parameters as a function of operating temperature.

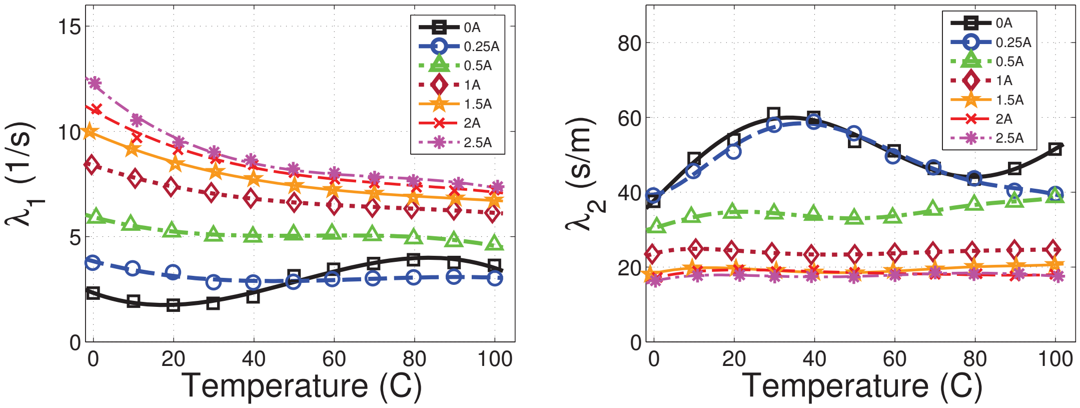

(a) λ_1.

(b) λ_2.

Figure 3.7: Model parameters as a function of operating temperature.

first proposed by Karnopp et al. [45] and aims to damp the absolute velocity of the payload by establishing an ficticious connection with an inertial reference, such as the sky, as seen in figure 4.5. Skyhook control is examined here due to its simple implementation and effective disturbance supression ability. The Skyhook control law uses velocity feedback to determine the desired damper force to apply on the suspended payload, and is given as

$$\hat{f}_d = \begin{cases} -C_{sky}\dot{x} & \dot{x}\dot{q} \geq 0 \\ 0 & \dot{x}\dot{q} < 0 \end{cases} \tag{3.5}$$

where C_{sky} is the velocity feedback gain. This strategy commands a force from the damper proportional to $\dot{x}$ when the absolute and relative velocities of the payload share the same sign, but switches to command zero force when the velocities have opposite signs because the MR damper is only a passive device and cannot inject energy into the system. Thus the magnitude of the commanded damper force $\hat{f}_d$

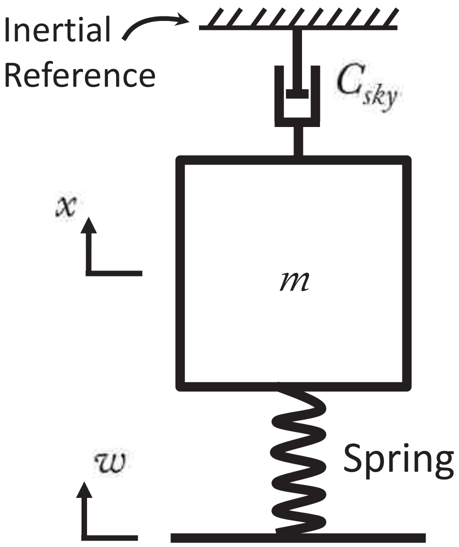

Figure 3.8: Ideal Skyhook configuration.

is dependent upon both the absolute payload velocity $\dot{x}$ and the relative velocity between the payload and base, $\dot{q}$.

This study considers a steady-state harmonic base excitation, maintaining a constant velocity amplitude $|\dot{w}|$ of 0.5 m/s across the frequency spectrum. Independent of frequency, the payload velocity $\dot{x}$ is directly proportionally to the base velocity $\dot{w}$. Thus if the harmonic amplitude of the base velocity $|\dot{w}|$ was to change as a function of excitation frequency, then the magnitude of the absolute payload velocity would change as well, independent of any system dynamics, thereby affecting the magnitude of the commanded damper force $\hat{f}_d$. Additionally, the commanded damper force is affected by system dynamics captured by $\dot{q}$. The relative phase shift between the payload and base velocities is a function of excitation frequency and affects the sign of the relative velocity $\dot{q}$, which thereby dictates the Skyhook switching in equation (3.5).

This study is interested in evaluating the robust ability of semi-active Skyhook control to attenuate vibration while the MR damper suspension is subject to temperature and payload mass perturbations. To focus the study solely on damper performance, and because the Skyhook control is a velocity feedback algorithm, the harmonic amplitude of the base velocity $|\dot{w}|$ is held constant. Changes in $|\dot{w}|$ affect the commanded damper force $\hat{f}_d$, thus this effect is decoupled from the analysis.

The Skyhook control gain, C_{sky}, was set to emulate a skyhook damper with a damping ratio $\zeta = 1$, which corresponds to values of 4.7, 5.2, and 5.5 kN s/m for a 5^{th} percentile female, 50^{th} percentile male, and 95^{th} percentile male, respectively. This was found to be appropriate from previous work [39, 45]. A value of unity for ζ corresponds to a critically damped system, where $C_{sky} = 2\zeta\sqrt{k_a m}$.

The model of the MR damper force on the body frame in equation (3.4) is used to determine the command current, $\hat{\varphi}$. The commanded force $\hat{f}_d$ is equated to the model force, and given here as

$$\hat{f}_d = f_o - k_d q - c_{po}\dot{q} - m_f\ddot{q} - f_y \tanh\left(\left(\dot{q} + \lambda_1(q - q^*)\right)\lambda_2\right) \tag{3.6}$$

where a quadratic relation between the model parameters and the command current

$\hat{\varphi}$ can be formed, with

$$\begin{aligned} f_o &= f_{o,2}\hat{\varphi}^2 + f_{o,1}\hat{\varphi} + f_{o,0} \\ k_d &= k_{d,2}\hat{\varphi}^2 + k_{d,1}\hat{\varphi} + k_{d,0} \\ c_{po} &= c_{po,2}\hat{\varphi}^2 + c_{po,1}\hat{\varphi} + c_{po,0} \\ m_f &= m_{f,2}\hat{\varphi}^2 + m_{f,1}\hat{\varphi} + m_{f,0} \\ f_y &= f_{y,2}\hat{\varphi}^2 + f_{y,1}\hat{\varphi} + f_{y,0} \\ \lambda_1 &= \lambda_{1,2}\hat{\varphi}^2 + \lambda_{1,1}\hat{\varphi} + \lambda_{1,0} \\ \lambda_2 &= \lambda_{2,2}\hat{\varphi}^2 + \lambda_{2,1}\hat{\varphi} + \lambda_{2,0} \end{aligned} \tag{3.7}$$

The coefficients of the quadratic relationships in equation (4.52) are determined from the characterization in figure 3.6. These coefficients are temperature dependent, and this analysis assumes the values in the control law are set *a priori* with the damper characterized at 50^0C, unless otherwise noted. Substituting equation (4.52) into equation (3.6), and rearranging, results in

$$0 = a\hat{\varphi}^2 + b\hat{\varphi} + c \tag{3.8}$$

where,

$$\begin{aligned} a = &\quad f_{o,2} - k_{d,2}q - c_{po,2}\dot{q} - m_{f,2}\ddot{q} - f_{y,2}\tanh\left((\dot{q} + \lambda_1^-(q - q^*))\lambda_2^-\right) \\ b = &\quad f_{o,1} - k_{d,1}q - c_{po,1}\dot{q} - m_{f,1}\ddot{q} - f_{y,1}\tanh\left((\dot{q} + \lambda_1^-(q - q^*))\lambda_2^-\right) \\ c = &\quad f_{o,0} - k_{d,0}q - c_{po,0}\dot{q} - m_{f,0}\ddot{q} - f_{y,0}\tanh\left((\dot{q} + \lambda_1^-(q - q^*))\lambda_2^-\right) - \hat{f}_d, \end{aligned} \tag{3.9}$$

and λ_1^- and λ_2^- are values from the previous discrete time step. The command current is then found using the quadratic formula,

$$\hat{\varphi} = \frac{-b + \sqrt{b^2 - 4ac}}{2a}. \tag{3.10}$$

A saturation range of $0 \leq \hat{\varphi} \leq \varphi_{max}$ is established to restrict the command current, $\hat{\varphi}$, to realistic values, where φ_{max} is the maximum available current from an external power supply. The condition $\hat{\varphi} < 0$ usually occurs when the magnitude of the passive, field-off damper force is greater than the magnitude of the command force $\hat{f}_d$. The command current is given as

$$\hat{\varphi} = \left\{ \begin{array}{cc} \varphi_{max}, & if\ \hat{\varphi} > \varphi_{max} \\ 0, & if\ \hat{\varphi} < 0,\ or\ \hat{\varphi} \notin \mathbb{R} \\ \hat{\varphi} & else \end{array} \right\}, \tag{3.11}$$

and $\hat{\varphi}$ serves as the control input to the system. Equation (3.11) is inserted into equations (3.4) and (4.52), and the system dynamics in equation (4.8) are solved numerically with the stiff differential equation solver ODE15s in MATLAB® [53].

3.5 Results of Isolation Study

3.5.1 Passive vs. Semi-active

Figure 3.9 shows the frequency response for a 50^{th} percentile male seated in the MR seat suspension system for both passive field-off and semi-active Skyhook control. For the passive system, as temperature increases from 0^0C to 100^0C the peak resonant amplification and crossover transmissibility shift higher in frequency due to the increased damper stiffness, and the resonant peak assumes a larger value (225% increase) due to the decrease in viscous damping. The semi-active system exhibits similar passive phenomena, namely the crossover transmissibility shifts higher in frequency due to increased stiffness and the high frequency isolation closely replicates the passive system due to the decrease in viscous damping. However, the semi-active Skyhook control offers robust attenuation capability at resonance despite the large temperature perturbation, allowing only a 15% increase in peak transmissibility. By quantifying the amount of damping in the isolation system we can gain some insight into the mechanism behind the robustness of the semi-active skyhook control.

The transmissibility for a base-excited, second-order system with a linear spring and viscous damper is given as [55]

$$T_r = \frac{|\ddot{x}|}{|\ddot{w}|} = \frac{[1 + 4\zeta^2(\frac{\omega}{\omega_n})^2]^{\frac{1}{2}}}{[(1 - (\frac{\omega}{\omega_n})^2)^2 + 4\zeta^2(\frac{\omega}{\omega_n})^2]^{\frac{1}{2}}} \tag{3.12}$$

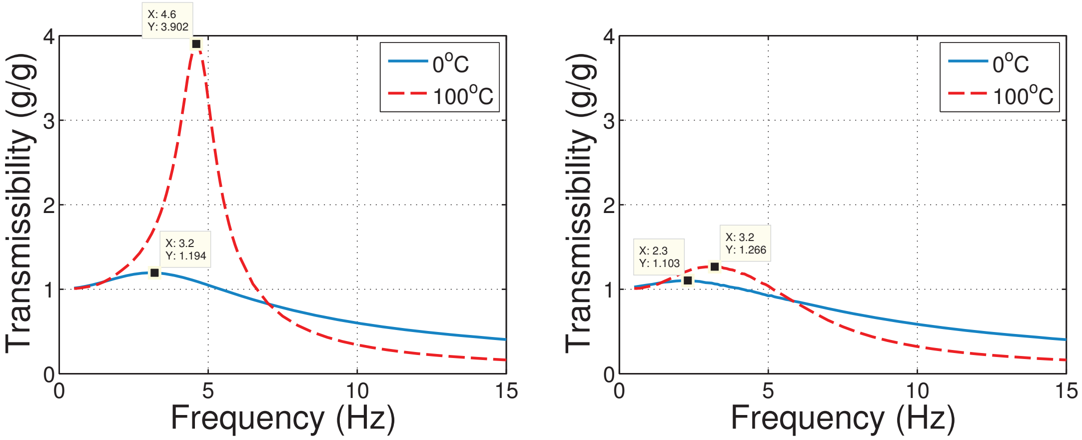

(a) Passive. (b) Semi-Active.

Figure 3.9: Frequency response for a 50^{th} percentile male seated in the MR seat suspension system subjected to passive field-off and semi-active Skyhook control.

where $|\ddot{x}|$ and $|\ddot{w}|$ are the acceleration amplitudes of the sprung mass and base, respectively, ζ is the damping ratio, ω is the excitation frequency of the base, and ω_n is the natural frequency of the system. By taking the partial derivative of equation (3.12) with respect to ζ we obtain

$$\frac{\partial T_r}{\partial \zeta} = \frac{4\zeta(\frac{\omega}{\omega_n})^2(T_r^{-1} - T_r)}{[1 - (\frac{\omega}{\omega_n})^2]^2 + 4\zeta^2(\frac{\omega}{\omega_n})^2} \tag{3.13}$$

Equations (3.12) and (3.13) are plotted versus damping ratio in figure 3.10 and show the influence damping ratio has on transmissibility, T_r, as well as the transmissibility gradient, $\partial T_r/\partial \zeta$, which is the sensitivity of transmissibility to a change in damping ratio. At system resonance ($\omega/\omega_n = 1$), a low damping ratio results in high transmissibility and great sensitivity to variations in damping ratio, which is the case for off-state, passive control. However, a large damping ratio allows the transmissibility to approach unity, where unity is the lower limit for

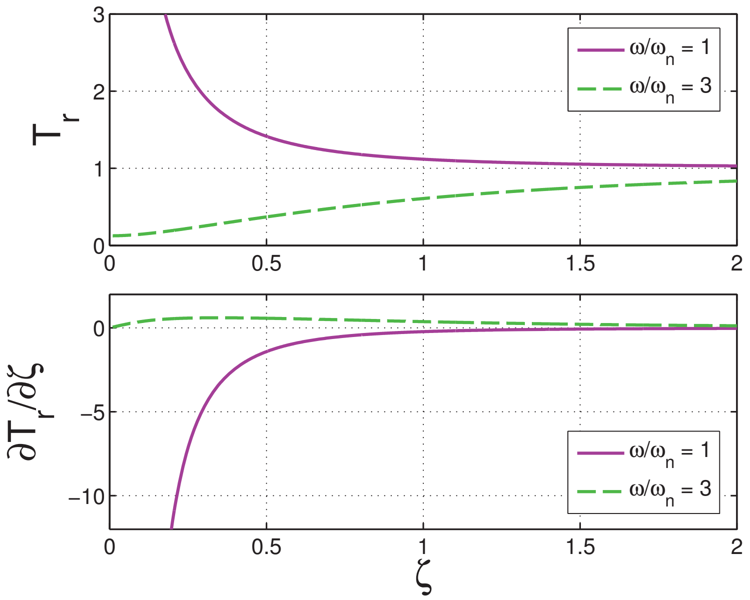

Figure 3.10: Transmissibility, T_r, and the transmissibility gradient, $\partial T_r/\partial\zeta$, vs. damping ratio.

attenuation at system resonance, and become nearly insensitive to variations in damping ratio. At excitation frequencies far above resonance, a low damping ratio results in excellent isolation, and some sensitivity to variations in ζ, however to a lesser extent than at resonance. As ζ increases for $\omega/\omega_n = 3$, the transmissibility worsens and approaches unity, while the sensitivity approaches zero.

By using a standard linearization technique we can analyze the nonlinear damping of the MR isolator as an equivalent viscous damping. Here, the damping force $f_d(t)$ is proportional to the relative piston velocity $[\dot{x}(t) - \dot{w}(t)]$ as

$$f_d(t) = C_{eq}[\dot{x}(t) - \dot{w}(t)] \tag{3.14}$$

The equivalent viscous damping, C_{eq}, is found by equating the energy dissipated by the damper over a cycle, E, to that of a viscous damper, giving

$$C_{eq}(\omega) = \frac{E}{\pi \omega Q^2} \tag{3.15}$$

where ω is the base excitation frequency, and Q is the steady-state amplitude of the relative piston displacement given as $Q = max[x(t) - w(t)]$. The energy dissipated over one cycle is given by

$$E = \oint f_d(t)dx = \int_0^{2\pi/\omega} f_d(t)[\dot{x}(t) - \dot{w}(t)]dt \tag{3.16}$$

and is computed numerically using an integration technique such as the trapezoidal rule. We nondimensionalize the equivalent viscous damping to obtain the frequency-dependent, equivalent damping ratio

$$\zeta_{eq}(\omega) = \frac{C_{eq}(\omega)}{2\sqrt{k_a m}}, \tag{3.17}$$

where k_a is the axial stiffness of the mechanical coil spring, and m is the sprung mass.

Figure 3.11 presents the equivalent damper ratio $\zeta_{eq}(\omega)$ as a function of excitation frequency for a 50^{th} percentile male occupant computed for both passive and semi-active Skyhook control operating at 0^0C and 100^0C. The damping ratio for a linear, second-order system is constant, however figure 3.11 shows the passive system having a large damping ratio at low frequencies then leveling off to a constant value at higher frequencies. This is due to the presence of passive friction in the system. At low frequencies below resonance the payload and base are essentially in phase and the passive friction causes the damper to lock up, restricting the damper to stroke. This reduction in relative motion between the payload and base causes the denominator of equation (3.15) to decrease, thereby increasing the damping ratio. By artificially removing the friction from the system the passive system exhibits only linear viscous damping, resulting in a constant value of damping ratio for all frequencies as expected in figure 3.12.

The semi-acitvely controlled system also exhibits high damping below resonance partly due to passive friction but also as a result of the additional dissipated energy attributed to the MR yield force as seen in figure 3.12, explaining the overall larger damping ratio values compared to the passive system. As excitation frequency increases above resonance the damping ratios for both passive and semi-active systems converge and level off to a constant value. At frequencies far above resonance the payload and base are completely out of phase, causing the semi-active controller to command nearly zero current, similar to the passive system, explaining the convergence of the damping ratio values.

When the system is subjected to passive field-off control in figure 3.9(a), resonance occurs at 3.2 Hz and 4.6 Hz for operation at 0^0C and 100^0C, respectively. At these resonant frequencies, a perturbation in temperature from 0^0C to 100^0C causes the damping ratio to drop 82% in value from 0.98 to 0.18 in figure 3.11, which corresponds to the highly sensitive region of $\partial T_r/\partial\zeta$ versus damping ratio for $\omega/\omega_n = 1$ in figure 3.10, and explains the large 225% increase in transmissibility at resonance from 1.2 to 3.9 for the field-off case in figure 3.9(a).

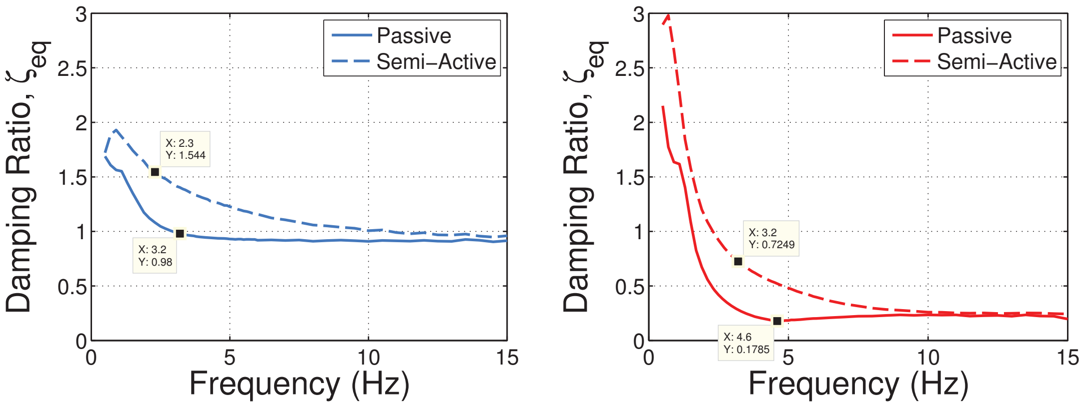

(a) Operating at 0^0C. (b) Operating at 100^0C.

Figure 3.11: Equivalent damping ratio, ζ_{eq}, as a function of excitation frequency with passive friction present in the system.

When the system is subjected to semi-active control in figure 3.9(b), the equivalent damping ratios in figure 3.11 at operating temperatures of 0^0C and 100^0C are relatively large at system resonance (2.3 Hz and 3.2 Hz, respectively) compared to the passive field-off system and drop off considerably as frequency increases, eventually converging with the values for the passive system. The semi-active system provides equivalent damping ratios of 1.54 and 0.72 at system resonance when operating at 0^0C and 100^0C, respectively. This 53% drop in equivalent damping ratio corresponds to an increase in transmissibility of only 15% from 1.1 to 1.27, as seen in figure 3.9(b), which is due to Skyhook control providing equivalent damping ratios in a relatively insensitive region of $\partial T_r/\partial\zeta$ versus damping ratio for $\omega/\omega_n = 1$ in figure 3.10. This explains why semi-active Skyhook control is robust to large temperature variations.

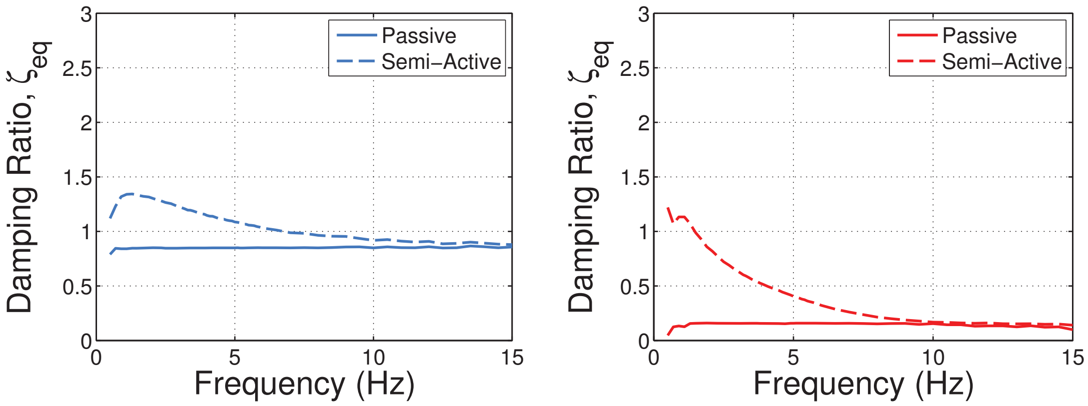

(a) Operating at 0^0C.

(b) Operating at 100^0C.

Figure 3.12: Equivalent damping ratio, ζ_{eq}, as a function of excitation frequency without passive friction present in the system.

3.5.2 Perturbation in occupant mass

Figure 3.13 presents the frequency response of the system governed by semi-active Skyhook control for both a 5^{th} percentile female and 95^{th} percentile male at operating temperatures of 0^0C and 100^0C. Comparing against the 5^{th} percentile female, the heavier 95^{th} percentile male occupant causes the resonance peak of the system to shift lower in frequency and assume a slightly larger peak value of transmissibility. The system with a 5^{th} female occupant possesses greater damping across the entire frequency spectrum compared to the system with a 95^{th} male occupant as seen in figure 3.14, explaining the better vibration attenuation at resonance. However, the damping ratios for both 5^{th} female and 95^{th} male are relatively large near resonance, yielding insensitivity of the transmissibility to changes in damping ratio and explaining only the minor degradation in vibration attenuation for the 95^{th} male occupant. At higher frequencies, the semi-active system approaches the behavior of a passive system, explaining the superior isolation for the heavier occupant. It

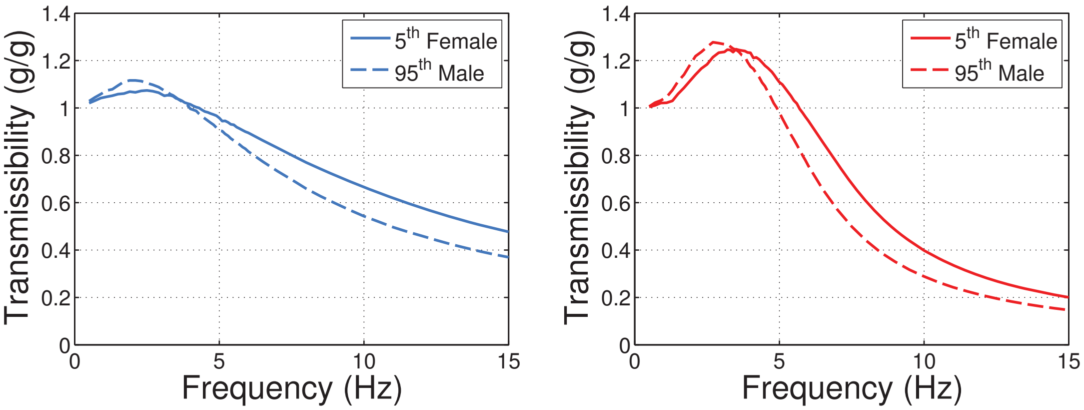

(a) Operating at 0^0C.

(b) Operating at 100^0C.

Figure 3.13: Frequency response for a 5^{th} percentile female and a 95^{th} percentile male occupant seated in the MR seat suspension system subjected to Skyhook control operating at two different temperatures.

is evident that changes in occupant weight (an over 100% increase), at both cold and hot operating temperatures, have a benign effect on the frequency response at resonance with Skyhook control, while also maintaining excellent high frequency isolation.

3.5.3 Effect of damper characterization temperature

Figure 3.15 presents the frequency response of the system for a 50^{th} percentile male subjected to semi-active Skyhook control with the damper characterized at two different temperatures: 0^0C and 50^0C. When the damper is characterized at low temperature (0^0C) but operated at high temperature (100^0C), relatively poor isolation performance is realized at system resonance compared to the damper characterized at high temperature as seen in figure 3.15(b). This is due to the controller assuming it is applying more control authority than it actually is applying due to a loss in yield force at higher temperatures. Figure 3.16(b) reiterates this fact

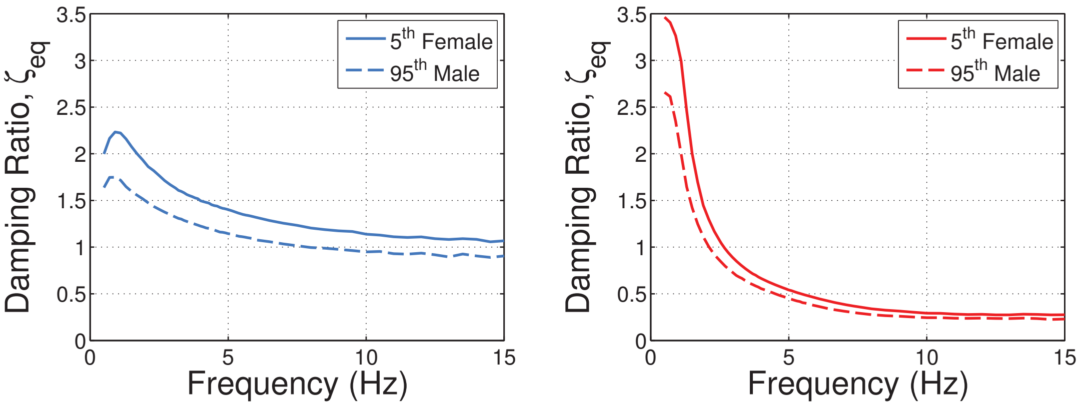

(a) Operating at 0^0C.   (b) Operating at 100^0C.

Figure 3.14: Equivalent damping ratio as a function of excitation frequency for a 5^{th} percentile female and a 95^{th} percentile male occupant subjected to Skyhook control operating at two different temperatures.

as the system characterized at 0^0C applies less current across the entire frequency spectrum compared to the system characterized at 50^0C. Futhermore, figure 3.17(b) shows that near resonance the system characterized at 0^0C provides less damping than the characterization at 50^0C and the low value of damping ratio causes high sensitivity to changes in damping ratio as shown in figure 3.10, explaining the large increase in transmissibility in figure 3.15(b). At high frequencies, both characterizations converge to the same transmissibility as a result of little influence from the semi-active control.

When the damper is characterized at high temperature (50^0C) but operated at low temperature (0^0C), the frequency response of the system exhibits similar behavior to when the damper is characterized at low temperature (0^0C), as seen in figure 3.15(a). The controller characterized at 50^0C applies more current across the entire frequency spectrum as shown in figure 3.16(a), however the damping ratios for both characterizations are large, as shown in figure 3.17(a), so the system is

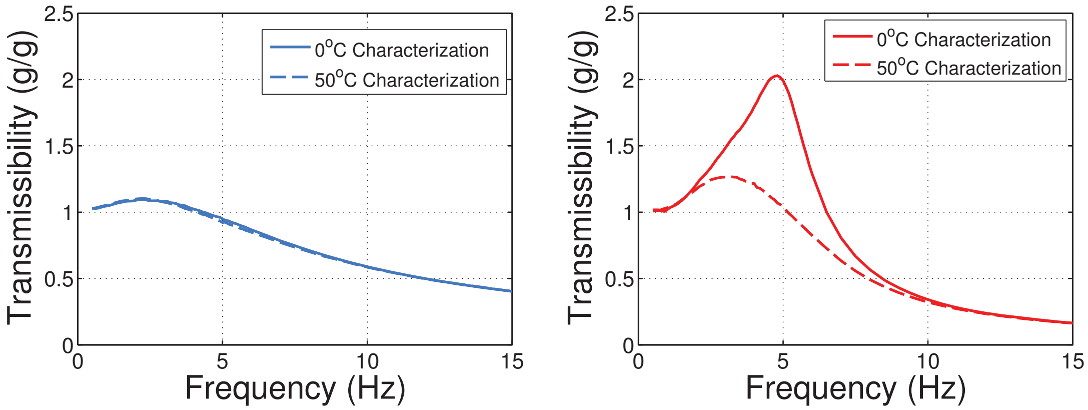

(a) Operating at 0^0C.

(b) Operating at 100^0C.

Figure 3.15: Frequency response for a 50^{th} percentile male when the MR damper is characterized at 0^0C and 50^0C, while the system is subjected to Skyhook control operating at two different temperatures.

relatively insensitive to a change in damping ratio, resulting in a negligible different in frequency response between the two characterization temperatures. Again at higher frequencies, both characterizations converge to the same transmissibility as expected. These results suggest it is better to characterize the damper at high temperature in order to obtain the best isolation performance.

3.6 Conclusions

The frequency response of an MR isolation suspension, subjected to perturbations in temperature and payload mass, was evaluated. It was shown that an appropriately chosen semi-active control law without temperature or payload mass compensation can offer robust performance while encountering practical operating temperatures ranging from 0^0C to 100^0C and payload masses ranging from 46.5 kg to 96 kg. Temperature compensation can enhance controller performance; however, it is not necessary to ensure sufficient vibration attenuation as temperature-induced

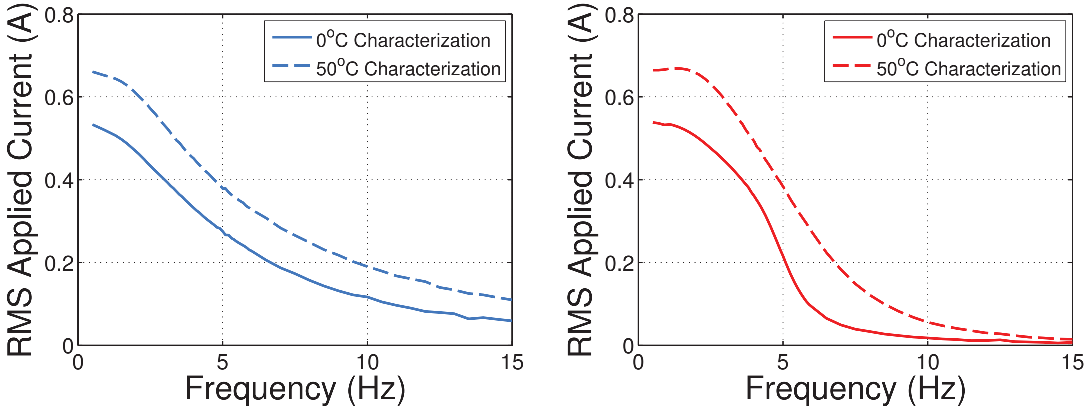

(a) Operating at 0^0C.

(b) Operating at 100^0C.

Figure 3.16: RMS applied current as a function of excitation frequency for a 50^{th} percentile male when the MR damper is characterized at 0^0C and 50^0C, while the system is subjected to Skyhook control operating at two different temperatures.

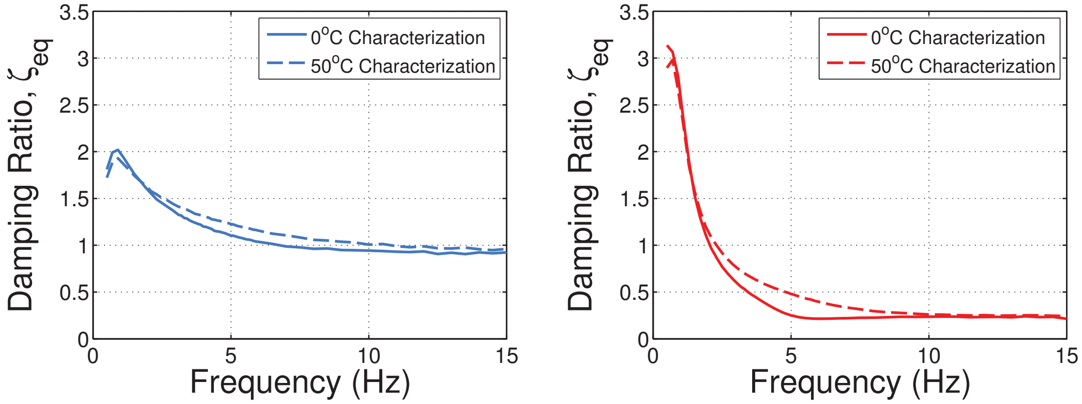

(a) Operating at 0^0C.

(b) Operating at 100^0C.

Figure 3.17: Equivalent damping ratio as a function of excitation frequency for a 50^{th} percentile male when the MR damper is characterized at 0^0C and 50^0C, while the system is subjected to Skyhook control operating at two different temperatures.

changes in the damping of the system have a fairly benign impact on the frequency response with an appropriately chosen control strategy. Indeed, in a practical sense, additional sensors and hardware are undesirable because of the added cost and maintenance requirements.

The parameters of the MR damper model were found to change significantly over the investigated temperature range. As operating temperature increased from 0^0C to 100^0C, the controllable yield force was found to decrease by up to 30% and the post-yield damping was found to decrease up to 85%, while the damper stiffness was found to increase significantly by several hundred percent. Despite these large changes in damper behavior, the semi-active Skyhook control offers robust vibration attenuation. For a 50^{th} percentile male occupant, the transmissibility increases by only 15% as temperature increases from 0^0C to 100^0C. For varying occupant mass, the worst degradation in resonant attenuation was less than 5% at 0^0C as payload mass increased from 46.5 kg to 96 kg.

An equivalent damping analysis was shown to explain the robust nature of the semi-active Skyhook control. The control law commands high damping at resonance, causing the transmissibility to be insensitive to changes in damping. Therefore, even though the damper behavior encounters rather large, temperature-induced changes, the effect on resonant amplification is benign. Also, an elevated operating temperature increases the damper stiffness, which increases the crossover frequency, degrading high frequency isolation. However, the control law significantly attenuates the resonant amplification, thereby decreasing the crossover frequency and reversing the effects of this phenomenon. Furthermore, a damper will always self-heat when excited, and an elevated temperature enhances high frequency isolation due to the reduction in passive viscous damping.

Chapter 4

6-DOF Modeling

4.1 Introduction

A mathematical model is developed to capture the mechanical dynamics of a semi-actively controlled, 6-DOF suspension system. The model is generalized for N suspension legs, and several control laws are presented to attenuate transmition of vibratory loads to the payload. The philosophy of these traditionally 1-DOF control laws is extended to a 6-DOF system, through both decentralized and centralized strategies.

4.2 Model

4.2.1 Coordinate Frames

Figure 4.1 shows a visual representation of the mathematical model of the system. The payload is assumed to be a rigid body supported from below by N suspension legs which connect between the ground floor and the bottom of the payload. A single suspension leg will be defined here as one coil spring and one MR damper, as seen in figure 4.2. The global coordinate frame $(O, \hat{\mathbf{e}}_1, \hat{\mathbf{e}}_2, \hat{\mathbf{e}}_3)$ is set with the orthonormal $\hat{\mathbf{e}}_1$ and $\hat{\mathbf{e}}_2$ axes parallel to the ground floor and the $\hat{\mathbf{e}}_3$ axis normal to the ground floor, where the unit vectors $\hat{\mathbf{e}}_1 = [1, 0, 0]^T$, $\hat{\mathbf{e}}_2 = [0, 1, 0]^T$, and $\hat{\mathbf{e}}_3 = [0, 0, 1]^T$.

The origin of the body coordinate frame $(B, \hat{\mathbf{b}}_1, \hat{\mathbf{b}}_2, \hat{\mathbf{b}}_3)$ is located at the center of gravity (CG) of the payload. The generalized displacement vector of the body frame w.r.t. the global frame O is defined as

$$ {}^{O}\overline{\boldsymbol{x}}(t) = \begin{bmatrix} {}^{O}\boldsymbol{x}_t(t) \\ {}^{O}\boldsymbol{x}_r(t) \end{bmatrix}, \tag{4.1} $$

where ${}^{O}\boldsymbol{x}_t(t) = [x_x(t), y_x(t), z_x(t)]^T$ is the translational displacement vector and ${}^{O}\boldsymbol{x}_r(t) = [\phi_x(t), \theta_x(t), \psi_x(t)]^T$ is the rotational displacement vector. The translational displacements $x_x(t)$, $y_x(t)$, and $z_x(t)$, and the angular displacements $\phi_x(t)$, $\theta_x(t)$, and $\psi_x(t)$, correspond to displacements and rotations about the $\hat{\mathbf{b}}_1$, $\hat{\mathbf{b}}_2$, and $\hat{\mathbf{b}}_3$ body axes, respectively. The superscript *bar* (ie. $\overline{\boldsymbol{x}}$) indicates the generalized form of the variable, as in the generalized displacement vector includes both translational and rotational displacement, and the generalized stiffness matrix includes both translational and rotational stiffness.

The generalized displacement vector of the base floor coordinate frame (A, $\hat{\mathbf{a}}_1$, $\hat{\mathbf{a}}_2$, $\hat{\mathbf{a}}_3$) w.r.t. the global frame O is defined as

$$ {}^{O}\overline{\boldsymbol{w}}(t) = \begin{bmatrix} {}^{O}\boldsymbol{w}_t(t) \\ {}^{O}\boldsymbol{w}_r(t) \end{bmatrix}, \tag{4.2} $$

where ${}^{O}\boldsymbol{w}_t(t) = [x_w(t), y_w(t), z_w(t)]^T$ is the translational displacement vector and ${}^{O}\boldsymbol{w}_r(t) = [\phi_w(t), \theta_w(t), \psi_w(t)]^T$ is the rotational displacement vector. The transla-

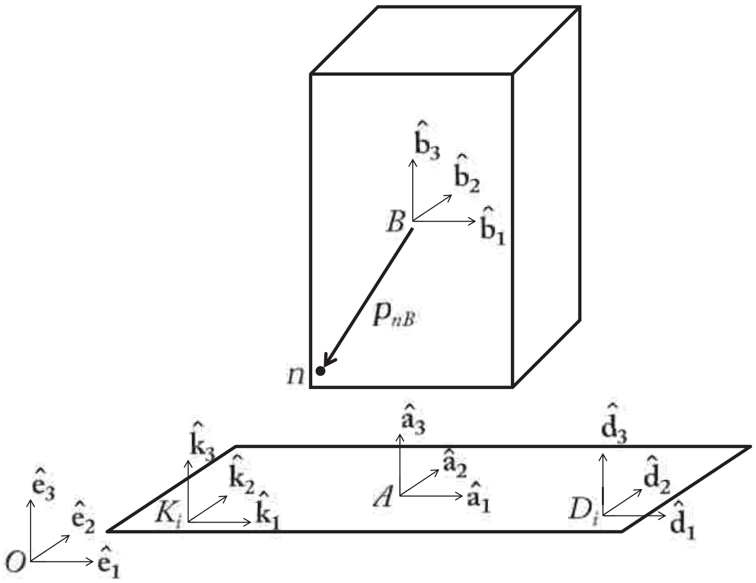

Figure 4.1: Coordinate frames of the 6-DOF system.

tional displacements $x_w(t)$, $y_w(t)$, and $z_w(t)$, and the angular displacements $\phi_w(t)$, $\theta_w(t)$, and $\psi_w(t)$, correspond to displacements and rotations about the $\hat{\mathbf{a}}_1$, $\hat{\mathbf{a}}_2$, and $\hat{\mathbf{a}}_3$ body axes, respectively. The rotational displacements of the base ${}^O\boldsymbol{w}_r(t) = [0,0,0]^T$ for this analysis.

If the rotational displacements of the body frame w.r.t. the global frame O are assumed small, and the body frame B and global frame O share the same initial orientation, then the position vector of any point n fixed in the body frame can be expressed w.r.t. the global frame as

$$\begin{aligned} {}^O\boldsymbol{p}_{nB}(t) &= {}^B\boldsymbol{p}_{nB} - {}^B\boldsymbol{p}_{nB} \times {}^O\boldsymbol{x}_r(t) \\ &= {}^B\boldsymbol{p}_{nB} + \begin{bmatrix} \mathbf{0}_{3\times3} & -{}^B\boldsymbol{P}_{nB} \end{bmatrix} {}^O\overline{\boldsymbol{x}}(t), \end{aligned} \tag{4.3}$$

where $\mathbf{0}_{3\times3}$ is a (3x3) matrix of zeros, ${}^B\boldsymbol{p}_{nB} = \begin{bmatrix} p_x & p_y & p_z \end{bmatrix}^T$ is the position vector

Figure 4.2: Single suspension leg.

to point n from B w.r.t. the body frame, and ${}^{B}\boldsymbol{P}_{nB}$ is the (3x3) skew-symmetric matrix defined for vector cross product operations given as

$$ {}^{B}\boldsymbol{P}_{nB} = \begin{bmatrix} 0 & -p_z & p_y \\ p_z & 0 & -p_x \\ -p_y & p_x & 0 \end{bmatrix}. \tag{4.4} $$

The translational displacement of any point n fixed in the body frame can be expressed w.r.t. the global frame as

$$ \begin{aligned} {}^{O}\boldsymbol{x}_n(t) &= {}^{O}\boldsymbol{x}_t(t) - {}^{O}\boldsymbol{p}_{nB}(t) \times {}^{O}\boldsymbol{x}_r(t) \\ &= \begin{bmatrix} \boldsymbol{I}_{3\times3} & -{}^{O}\boldsymbol{P}_{nB}(t) \end{bmatrix} {}^{O}\overline{\boldsymbol{x}}(t), \end{aligned} \tag{4.5} $$

where $\boldsymbol{I}_{3\times3}$ is the (3x3) identity matrix, ${}^{O}\boldsymbol{p}_{nB}(t)$ is the position vector of point n w.r.t. the global frame, and ${}^{O}\boldsymbol{P}_{nB}(t)$ is the (3x3) matrix defined similarly for vector cross product operations.

Matrices and vectors expressed in one reference frame can be transformed to another frame through a transformation matrix. The transformation matrix $\boldsymbol{T}_{K_iO}$ transforms a matrix or vector from the global frame O to the i^{th} coil spring frame K_i. The transformation for the i^{th} coil spring can be described using Euler angles ϕ_{K_i}, θ_{K_i}, and ψ_{K_i} corresponding to rotations about the $\hat{\mathbf{k}}_{1_i}$, $\hat{\mathbf{k}}_{2_i}$, and $\hat{\mathbf{k}}_{3_i}$ axes of the local stiffness matrix, respectively. For brevity, $\phi = \phi_{K_i}$, $\theta = \theta_{K_i}$, and $\psi = \psi_{K_i}$. The elementary rotation matrices are

$$\begin{aligned}
\mathbf{T}_1(\phi) &= \begin{bmatrix} 1 & 0 & 0 \\ 0 & c(\phi) & -s(\phi) \\ 0 & s(\phi) & c(\phi) \end{bmatrix}, \\
\mathbf{T}_2(\theta) &= \begin{bmatrix} c(\theta) & 0 & s(\theta) \\ 0 & 1 & 0 \\ -s(\theta) & 0 & c(\theta) \end{bmatrix}, \\
\mathbf{T}_3(\psi) &= \begin{bmatrix} c(\psi) & -s(\psi) & 0 \\ s(\psi) & c(\psi) & 0 \\ 0 & 0 & 1 \end{bmatrix}. \qquad (4.6)
\end{aligned}$$

Starting with the coordinate frames O and K_i aligned, sequentially rotate K_i by ψ, then rotate K_i by θ, then rotate K_i by ϕ. This gives the rotation matrix from frame K_i to frame O as $\boldsymbol{T}_{OK_i} = \boldsymbol{T}_3(\psi)\mathbf{T}_2(\theta)\mathbf{T}_1(\phi)$, or

$$\mathbf{T}_{OK_i} = \begin{bmatrix} c(\psi)c(\theta) & (c(\psi)s(\theta)s(\psi) - s(\psi)c(\psi)) & (c(\psi)s(\theta)c(\phi) + s(\psi)s(\phi) \\ s(\psi)c(\theta) & (s(\psi)s(\theta)s(\phi) + c(\psi)c(\phi)) & (s(\psi)s(\theta)c(\phi) - c(\psi)s(\phi)) \\ -s(\theta) & c(\theta)s(\phi) & c(\theta)c(\phi) \end{bmatrix}, \qquad (4.7)$$

where $c(\theta) = cos(\theta)$ and $s(\theta) = sin(\theta)$. $\mathbf{T}_{OK_i}$ is an orthogonal matrix, thus $\mathbf{T}_{K_iO} = \mathbf{T}_{OK_i}^T$, where $\mathbf{T}_{K_iO}$ is the transformation matrix from the global frame O to the local fixed frame K_i. The transformation matrices $\boldsymbol{T}_{BO}$ and $\boldsymbol{T}_{D_iO}$ are similarly defined.

4.2.2 Equation Of Motion

The equation of motion is given as

$$^{O}\overline{\boldsymbol{M}}\,^{O}\ddot{\bar{\boldsymbol{x}}} = {}^{O}\bar{\boldsymbol{f}}_K + {}^{O}\bar{\boldsymbol{f}}_D + {}^{O}\bar{\boldsymbol{f}}_g, \tag{4.8}$$

where $^{O}\overline{\boldsymbol{M}}$ is the generalized global mass matrix, and $^{O}\bar{\boldsymbol{f}}_K$, $^{O}\bar{\boldsymbol{f}}_D$, and $^{O}\bar{\boldsymbol{f}}_g$ are the generalized global forces on the body frame due to the coil springs, MR dampers, and gravity, respectively.

The generalized mass matrix is given in the local body frame B as

$$^{B}\overline{\boldsymbol{M}} = \begin{bmatrix} m & 0 & 0 & 0 & 0 & 0 \\ 0 & m & 0 & 0 & 0 & 0 \\ 0 & 0 & m & 0 & 0 & 0 \\ 0 & 0 & 0 & I_{xx} & -I_{xy} & -I_{zx} \\ 0 & 0 & 0 & -I_{xy} & I_{yy} & -I_{yz} \\ 0 & 0 & 0 & -I_{zx} & -I_{yz} & I_{zz} \end{bmatrix}, \tag{4.9}$$

where m is the mass of the payload and I_{ij} are the elements in the inertia tensor. The generalized mass matrix can be expressed in the global frame as

$$^{O}\overline{\boldsymbol{M}} = \boldsymbol{T}_{BO}^{T}\,{}^{B}\overline{\boldsymbol{M}}\boldsymbol{T}_{BO}. \tag{4.10}$$

The generalized force vector $^{O}\bar{\boldsymbol{f}}_g$ due to gravity applied to the body frame B is

$$^{O}\bar{\boldsymbol{f}}_g = \begin{bmatrix} 0 & 0 & -mg & 0 & 0 & 0 \end{bmatrix}^{T}, \tag{4.11}$$

where g is the gravitational acceleration.

The stiffness of the i^{th} coil spring is defined in its local coordinate frame $(K_i, \hat{\mathbf{k}}_1, \hat{\mathbf{k}}_2, \hat{\mathbf{k}}_3)$ in figure 4.3(a) and assumed to have constant orthogonal stiffness

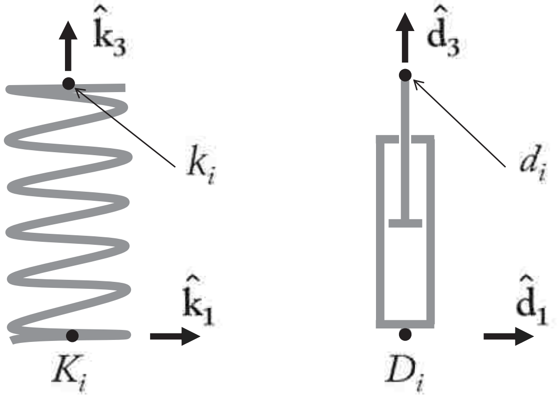

(a) K_i coordinate frame. (b) D_i coordinate frame.

Figure 4.3: Coordinates frames of the i^{th} coil spring and MR damper.

values defined as

$$^{K_i}\boldsymbol{K}_i = \begin{bmatrix} k_l & 0 & 0 \\ 0 & k_l & 0 \\ 0 & 0 & k_a \end{bmatrix}, \tag{4.12}$$

where k_l and k_a are the lateral and axial stiffnesses of the coil spring, respectively. The stiffness matrix can be expressed in the global frame as

$$^{O}\boldsymbol{K}_i = \boldsymbol{T}_{K_iO}^{T}\,{}^{K_i}\boldsymbol{K}_i\boldsymbol{T}_{K_iO}. \tag{4.13}$$

The generalized force vector due to all N coil springs applied to the body frame B can be expressed as

$$^{O}\bar{\boldsymbol{f}}_K = \sum_{i}^{N} {}^{O}\bar{\boldsymbol{f}}_{K_i}, \tag{4.14}$$

where,

$$^{O}\bar{\boldsymbol{f}}_{K_i} = \begin{bmatrix} ^{O}\boldsymbol{f}_{K_i} & ^{O}\boldsymbol{t}_{K_i} \end{bmatrix}^T, \tag{4.15}$$

and $^{O}\boldsymbol{f}_{K_i}$ and $^{O}\boldsymbol{t}_{K_i}$ are the force and torque vectors applied to the body frame B due to the i^{th} coil spring, respectively. The force vector is given as

$$\begin{aligned}
{}^{O}\boldsymbol{f}_{K_i} &= {}^{O}\boldsymbol{K}_i({}^{O}\boldsymbol{w}_{K_i} - {}^{O}\boldsymbol{x}_{k_i}) \\
&= {}^{O}\boldsymbol{K}_i({}^{O}\boldsymbol{w}_t - \begin{bmatrix}\boldsymbol{I}_{3x3} & -{}^{0}\boldsymbol{P}_{k_iB}\end{bmatrix} {}^{O}\overline{\boldsymbol{x}}) \\
&= {}^{O}\boldsymbol{K}_i \begin{bmatrix}\boldsymbol{I}_{3x3} & -{}^{0}\boldsymbol{P}_{k_iB}\end{bmatrix} ({}^{O}\overline{\boldsymbol{w}} - {}^{O}\overline{\boldsymbol{x}}) \\
&= \begin{bmatrix}{}^{O}\boldsymbol{K}_i & -{}^{O}\boldsymbol{K}_i{}^{0}\boldsymbol{P}_{k_iB}\end{bmatrix} ({}^{O}\overline{\boldsymbol{w}} - {}^{O}\overline{\boldsymbol{x}}),
\end{aligned} \tag{4.16}$$

assuming ${}^{O}\boldsymbol{w}_r = [0 \;\; 0 \;\; 0]^T$. The torque vector is given as

$$\begin{aligned}
{}^{O}\boldsymbol{t}_{K_i} &= {}^{O}\boldsymbol{p}_{k_iB} \times {}^{O}\boldsymbol{f}_{K_i} \\
&= \begin{bmatrix}-{}^{O}\boldsymbol{P}^{T}_{k_iB}{}^{O}\boldsymbol{K}_i & {}^{O}\boldsymbol{P}^{T}_{k_iB}{}^{O}\boldsymbol{K}_i{}^{O}\boldsymbol{P}_{k_iB}\end{bmatrix} ({}^{O}\overline{\boldsymbol{w}} - {}^{O}\overline{\boldsymbol{x}}).
\end{aligned} \tag{4.17}$$

Therefore, the generalized force vector ${}^{O}\bar{\boldsymbol{f}}_K$ can be expressed as

$${}^{O}\bar{\boldsymbol{f}}_K = {}^{O}\overline{\boldsymbol{K}} \left(\bar{\boldsymbol{w}} - \bar{\boldsymbol{x}}\right), \tag{4.18}$$

where the combined generalized global stiffness matrix for all N coil springs

$${}^{O}\overline{\boldsymbol{K}} = \sum_{i}^{N} {}^{O}\overline{\boldsymbol{K}}_i \tag{4.19}$$

and

$${}^{O}\overline{\boldsymbol{K}}_i = \begin{bmatrix} {}^{O}\boldsymbol{K}_i & -{}^{O}\boldsymbol{K}_i{}^{O}\boldsymbol{P}_{k_iB} \\ -{}^{O}\boldsymbol{P}^{T}_{k_iB}{}^{O}\boldsymbol{K}_i & {}^{O}\boldsymbol{P}^{T}_{k_iB}{}^{O}\boldsymbol{K}_i{}^{O}\boldsymbol{P}_{k_iB} \end{bmatrix}. \tag{4.20}$$

The MR dampers are connected to the payload and base frame by universal spherical joints which allows only axial forces to be transmitted through the dampers. Thus, the force of the i^{th} MR damper is defined in its local coordinate frame $(D_i, \hat{\mathbf{d}}_1, \hat{\mathbf{d}}_2, \hat{\mathbf{d}}_3)$ in figure 4.3(b) as

$$ {}^{D_i}\boldsymbol{f}_{D_i} = \begin{bmatrix} 0 & 0 & f_{d_i} \end{bmatrix}^T , \tag{4.21} $$

where, the damper force is modeled as

$$ f_{d_i} = f_{o_i} - k_{d_i} q_i - c_{po_i} \dot{q}_i - m_{f_i} \ddot{q}_i - f_{y_i} \tanh\left((\dot{q}_i + \lambda_{1_i}(q_i - q_i^*)) \lambda_{2_i} \right) , \tag{4.22} $$

and q_i is the relative displacement of damper stroke, and q_i^* is the static equilibrium value of the damper stroke. The damper stroke is given as

$$ \begin{aligned} q_i &= \begin{bmatrix} 0 & 0 & 1 \end{bmatrix} \boldsymbol{T}_{D_iO} \left({}^O\boldsymbol{x}_{d_i} - {}^O\boldsymbol{w}_{D_i} \right) \\ &= \begin{bmatrix} 0 & 0 & 1 \end{bmatrix} \boldsymbol{T}_{D_iO} \left(\begin{bmatrix} \boldsymbol{I}_{3\times3} & -{}^O\boldsymbol{P}_{d_iB}(t) \end{bmatrix} {}^O\overline{\boldsymbol{x}} - {}^O\boldsymbol{w}_t \right) \\ &= \begin{bmatrix} 0 & 0 & 1 \end{bmatrix} \boldsymbol{T}_{D_iO} \begin{bmatrix} \boldsymbol{I}_{3\times3} & -{}^O\boldsymbol{P}_{d_iB}(t) \end{bmatrix} ({}^O\overline{\boldsymbol{x}} - {}^O\overline{\boldsymbol{w}}) \\ &= \boldsymbol{\Lambda}_i ({}^O\overline{\boldsymbol{x}} - {}^O\overline{\boldsymbol{w}}), \end{aligned} \tag{4.23} $$

where

$$ \boldsymbol{\Lambda}_i = \begin{bmatrix} 0 & 0 & 1 \end{bmatrix} \boldsymbol{T}_{D_iO} \begin{bmatrix} \boldsymbol{I}_{3\times3} & -{}^O\boldsymbol{P}_{d_iB}(t) \end{bmatrix} . \tag{4.24} $$

The stroke velocity and acceleration can be approximated as follows

$$ \dot{q}_i = \boldsymbol{\Lambda}_i ({}^O\dot{\overline{\boldsymbol{x}}} - {}^O\dot{\overline{\boldsymbol{w}}}), \tag{4.25} $$

$$ \ddot{q}_i = \boldsymbol{\Lambda}_i ({}^O\ddot{\overline{\boldsymbol{x}}} - {}^O\ddot{\overline{\boldsymbol{w}}}). \tag{4.26} $$

These results assume ${}^O\boldsymbol{w}_r = [0 \;\; 0 \;\; 0]^T$, so the translation of point D_i equals that of the base. ${}^O\boldsymbol{x}_{d_i}$ is the displacement of point d_i fixed to the body frame, ${}^O\boldsymbol{w}_{D_i}$ is the displacement of point D_i fixed to the frame A, and f_{d_i} is the damper force on the body frame. The model parameters (f_o, k_d, c_{po}, m_f, f_y, λ_1, and λ_2) have been defined previously in chapter 2.

The generalized global force vector due to all N dampers applied to the body frame B can be expressed as

$$
{}^{O}\bar{\boldsymbol{f}}_{D} = \sum_{i}^{N} {}^{O}\bar{\boldsymbol{f}}_{D_i}, \tag{4.27}
$$

where the generalized force vector due to the i^{th} MR damper

$$
\begin{aligned}
{}^{O}\overline{\boldsymbol{f}}_{D_i} &= \begin{bmatrix} \boldsymbol{I}_{3\times 3} & -{}^{O}\mathbf{P}^{T}_{d_iB} \end{bmatrix}^{T} \boldsymbol{T}^{T}_{D_iO} \begin{bmatrix} 0 & 0 & 1 \end{bmatrix}^{T} f_{d_i} \\
&= \boldsymbol{\Lambda}_i^{T} f_{d_i}.
\end{aligned} \tag{4.28}
$$

By inserting equations 4.22 and 4.51 into equation 4.27,

$$
\begin{aligned}
{}^{O}\bar{\boldsymbol{f}}_{D} = \sum_{i}^{N} & \boldsymbol{\Lambda}_i^{T} f_{o_i} - \boldsymbol{\Lambda}_i^{T} k_{d_i} \boldsymbol{\Lambda}_i ({}^{O}\overline{\boldsymbol{x}} - {}^{O}\overline{\boldsymbol{w}}) - \boldsymbol{\Lambda}_i^{T} c_{po_i} \boldsymbol{\Lambda}_i ({}^{O}\dot{\overline{\boldsymbol{x}}} - {}^{O}\dot{\overline{\boldsymbol{w}}}) \\
& - \boldsymbol{\Lambda}_i^{T} m_{f_i} \boldsymbol{\Lambda}_i ({}^{O}\ddot{\overline{\boldsymbol{x}}} - {}^{O}\ddot{\overline{\boldsymbol{w}}}) \\
& - \boldsymbol{\Lambda}_i^{T} f_{y_i} \tanh\left((\boldsymbol{\Lambda}_i ({}^{O}\dot{\overline{\boldsymbol{x}}} - {}^{O}\dot{\overline{\boldsymbol{w}}}) + \lambda_{1_i} (\boldsymbol{\Lambda}_i ({}^{O}\overline{\boldsymbol{x}} - {}^{O}\overline{\boldsymbol{w}}) - q_i^{*})) \lambda_{2_i} \right),
\end{aligned} \tag{4.29}
$$

where a quadratic relation between the model parameters and the applied current

φ_i is given as

$$\begin{aligned}
f_{o_i} &= f_{o_i,2}\,\varphi_i^2 + f_{o_i,1}\,\varphi_i + f_{o_i,0} \\
k_{d_i} &= k_{d_i,2}\,\varphi_i^2 + k_{d_i,1}\,\varphi_i + k_{d_i,0} \\
c_{po_i} &= c_{po_i,2}\,\varphi_i^2 + c_{po_i,1}\,\varphi_i + c_{po_i,0} \\
m_{f_i} &= m_{f_i,2}\,\varphi_i^2 + m_{f_i,1}\,\varphi_i + m_{f_i,0} \\
f_{y_i} &= f_{y_i,2}\,\varphi_i^2 + f_{y_i,1}\,\varphi_i + f_{y_i,0} \\
\lambda_{1_i} &= \lambda_{1_i,2}\,\varphi_i^2 + \lambda_{1_i,1}\,\varphi_i + \lambda_{1_i,0} \\
\lambda_{2_i} &= \lambda_{2_i,2}\,\varphi_i^2 + \lambda_{2_i,1}\,\varphi_i + \lambda_{2_i,0}. \qquad (4.30)
\end{aligned}$$

The damper force vector can be separated into a passive component and an active component as

$$ {}^O\bar{\boldsymbol{f}}_D = {}^O\bar{\boldsymbol{f}}_{D,0} + {}^O\bar{\boldsymbol{f}}_{D,a}. \qquad (4.31)$$

The passive, zero-field component is given as

$$\begin{aligned}
{}^O\bar{\boldsymbol{f}}_{D,0} &= {}^O\bar{\boldsymbol{f}}_{o,0} - {}^O\bar{\boldsymbol{k}}_{d,0}({}^O\overline{\boldsymbol{x}} - {}^O\overline{\boldsymbol{w}}) - {}^O\bar{\boldsymbol{c}}_{po,0}({}^O\dot{\overline{\boldsymbol{x}}} - {}^O\dot{\overline{\boldsymbol{w}}}) \\
&\quad - {}^O\bar{\boldsymbol{m}}_{f,0}({}^O\ddot{\overline{\boldsymbol{x}}} - {}^O\ddot{\overline{\boldsymbol{w}}}) - {}^O\bar{\boldsymbol{f}}_{y,0} \qquad (4.32)
\end{aligned}$$

where

$$\begin{aligned}
{}^{O}\bar{\boldsymbol{f}}_{o,0} &= \sum_{i}^{N} \boldsymbol{\Lambda}_i^T f_{o_i,0} \\
{}^{O}\bar{\boldsymbol{k}}_{d,0} &= \sum_{i}^{N} \boldsymbol{\Lambda}_i^T k_{d_i,0} \boldsymbol{\Lambda}_i \\
{}^{O}\bar{\boldsymbol{c}}_{po,0} &= \sum_{i}^{N} \boldsymbol{\Lambda}_i^T c_{po_i,0} \boldsymbol{\Lambda}_i \\
{}^{O}\bar{\boldsymbol{m}}_{f,0} &= \sum_{i}^{N} \boldsymbol{\Lambda}_i^T m_{f_i,0} \boldsymbol{\Lambda}_i \\
{}^{O}\bar{\boldsymbol{f}}_{y,0} &= \sum_{i}^{N} \boldsymbol{\Lambda}_i^T f_{y_i,0} \tanh\left((\boldsymbol{\Lambda}_i({}^{O}\dot{\overline{\boldsymbol{x}}} - {}^{O}\dot{\overline{\boldsymbol{w}}}) + \lambda_{1_i}(\boldsymbol{\Lambda}_i({}^{O}\overline{\boldsymbol{x}} - {}^{O}\overline{\boldsymbol{w}}) - q_i^*))\lambda_{2_i} \right),
\end{aligned} \tag{4.33}$$

The active component is given as

$${}^{O}\bar{\boldsymbol{f}}_{D,a} = \sum_{i}^{N} \boldsymbol{\beta}_{i,1}\, \varphi_i + \sum_{i}^{N} \boldsymbol{\beta}_{i,2}\, \varphi_i^2, \tag{4.34}$$

where

$$\begin{aligned}
\boldsymbol{\beta}_{i,1} &= \boldsymbol{\Lambda}_i^T f_{o_i,1} - \boldsymbol{\Lambda}_i^T k_{d_i,1} \boldsymbol{\Lambda}_i({}^{O}\overline{\boldsymbol{x}} - {}^{O}\overline{\boldsymbol{w}}) - \boldsymbol{\Lambda}_i^T c_{po_i,1} \boldsymbol{\Lambda}_i({}^{O}\dot{\overline{\boldsymbol{x}}} - {}^{O}\dot{\overline{\boldsymbol{w}}}) \\
&\quad - \boldsymbol{\Lambda}_i^T m_{f_i,1} \boldsymbol{\Lambda}_i({}^{O}\ddot{\overline{\boldsymbol{x}}} - {}^{O}\ddot{\overline{\boldsymbol{w}}}) \\
&\quad - \boldsymbol{\Lambda}_i^T f_{y_i,1} \tanh\left((\boldsymbol{\Lambda}_i({}^{O}\dot{\overline{\boldsymbol{x}}} - {}^{O}\dot{\overline{\boldsymbol{w}}}) + \lambda_{1_i}(\boldsymbol{\Lambda}_i({}^{O}\overline{\boldsymbol{x}} - {}^{O}\overline{\boldsymbol{w}}) - q_i^*))\lambda_{2_i} \right),
\end{aligned} \tag{4.35}$$

and

$$\begin{aligned}\boldsymbol{\beta}_{i,2} \;&=\; \boldsymbol{\Lambda}_i^T f_{o_i,2} - \boldsymbol{\Lambda}_i^T k_{d_i,2} \boldsymbol{\Lambda}_i ({}^O\overline{\boldsymbol{x}} - {}^O\overline{\boldsymbol{w}}) - \boldsymbol{\Lambda}_i^T c_{po_i,2} \boldsymbol{\Lambda}_i ({}^O\dot{\overline{\boldsymbol{x}}} - {}^O\dot{\overline{\boldsymbol{w}}}) \\ &\quad - \boldsymbol{\Lambda}_i^T m_{f_i,2} \boldsymbol{\Lambda}_i ({}^O\ddot{\overline{\boldsymbol{x}}} - {}^O\ddot{\overline{\boldsymbol{w}}}) \\ &\quad - \boldsymbol{\Lambda}_i^T f_{y_i,2} \tanh\left((\boldsymbol{\Lambda}_i ({}^O\dot{\overline{\boldsymbol{x}}} - {}^O\dot{\overline{\boldsymbol{w}}}) + \lambda_{1_i} (\boldsymbol{\Lambda}_i ({}^O\overline{\boldsymbol{x}} - {}^O\overline{\boldsymbol{w}}) - q_i^*)) \lambda_{2_i} \right). \end{aligned} \tag{4.36}$$

The active component can then be expressed as

$${}^O\bar{\boldsymbol{f}}_{D,a} \;=\; \bar{\boldsymbol{\beta}}\,\boldsymbol{\varphi} \tag{4.37}$$

where

$$\bar{\boldsymbol{\beta}} \;=\; \begin{bmatrix} \boldsymbol{\beta}_1 & \dots & \boldsymbol{\beta}_N \end{bmatrix}, \tag{4.38}$$

$$\boldsymbol{\beta}_i \;=\; \boldsymbol{\beta}_{i,1} + \boldsymbol{\beta}_{i,2}\,\varphi_i, \tag{4.39}$$

and

$$\boldsymbol{\varphi} = \begin{bmatrix} \varphi_1 & \dots & \varphi_N \end{bmatrix}^T. \tag{4.40}$$

The equation of motion (equation 4.8) can now be written as

$$\begin{aligned} {}^O\overline{\boldsymbol{M}}\,{}^O\ddot{\overline{\boldsymbol{x}}} \;&=\; {}^O\overline{\boldsymbol{K}}\,(\overline{\boldsymbol{w}} - \overline{\boldsymbol{x}}) + {}^O\bar{\boldsymbol{f}}_{o,0} - {}^O\bar{\boldsymbol{k}}_{d,0}({}^O\overline{\boldsymbol{x}} - {}^O\overline{\boldsymbol{w}}) - {}^O\bar{\boldsymbol{c}}_{po,0}({}^O\dot{\overline{\boldsymbol{x}}} - {}^O\dot{\overline{\boldsymbol{w}}}) \\ &\quad - {}^O\bar{\boldsymbol{m}}_{f,0}({}^O\ddot{\overline{\boldsymbol{x}}} - {}^O\ddot{\overline{\boldsymbol{w}}}) - {}^O\bar{\boldsymbol{f}}_{y,0} + \bar{\boldsymbol{\beta}}\,\boldsymbol{\varphi} + {}^O\bar{\boldsymbol{f}}_g. \end{aligned} \tag{4.41}$$

A delay exists between commanding the control input $\hat{\varphi}_i$ and the application of the actual electrical current φ_i. The delay behaves as a first-order filter given as

$$\dot{\varphi}_i = \frac{\hat{\varphi}_i - \varphi_i}{\tau}, \tag{4.42}$$

where τ is the time constant of the response delay of the electro-magnetic coil and power supply.

4.2.3 State Space

The equation of motion can be expressed in state space form, where the time derivative of each state variable can be expressed in terms of the state variables as $\dot{\boldsymbol{x}} = f(t, \boldsymbol{x}, \boldsymbol{u})$, where $\boldsymbol{x}$ are the state variables and $\boldsymbol{u}$ are the system inputs. The state equation describes a nonlinear system, however it can be cast into the familiar linear form as

$$\dot{\boldsymbol{x}} = A(t, \boldsymbol{x})\boldsymbol{x} + B\boldsymbol{u} + E(t, \boldsymbol{x})\boldsymbol{w}(t), \tag{4.43}$$

where $A(t, \boldsymbol{x})$ is the $n \times n$ state matrix, and B is the $n \times r$ input matrix, $E(t, \boldsymbol{x})$ is the $n \times w$ disturbance matrix, and $\boldsymbol{w}(t)$ are the exogenous system disturbances. The state matrix is given as

$$A(t, \boldsymbol{x}) = \begin{bmatrix} \mathbf{0}_{6\times6} & \boldsymbol{I}_{6\times6} & \mathbf{0}_{6\times N} \\ -\bar{\mu}^{-1}({}^{O}\overline{\boldsymbol{K}} + {}^{O}\bar{\boldsymbol{k}}_{d,0}) & -\bar{\mu}^{-1}\ {}^{O}\bar{\boldsymbol{c}}_{po,0} & \bar{\mu}^{-1}\ {}^{O}\bar{\boldsymbol{\beta}} \\ \mathbf{0}_{N\times6} & \mathbf{0}_{N\times6} & -(1/\tau)\boldsymbol{I}_{N\times N} \end{bmatrix}, \tag{4.44}$$

the input matrix as

$$B = \begin{bmatrix} \mathbf{0}_{6\times N} \\ \mathbf{0}_{6\times N} \\ (1/\tau)\boldsymbol{I}_{N\times N} \end{bmatrix} \tag{4.45}$$

the disturbance matrix as

$$E(t,\boldsymbol{x}) \;=\; \bar{\mu}^{-1} \begin{bmatrix} \mathbf{0}_{6\times 6} & \mathbf{0}_{6\times 6} & \mathbf{0}_{6\times 6} & \mathbf{0}_{6\times 1} \\ ({}^{O}\overline{\boldsymbol{K}} + {}^{O}\bar{\boldsymbol{k}}_{d,0}) & {}^{O}\bar{\boldsymbol{c}}_{po,0} & {}^{O}\bar{\boldsymbol{m}}_{f,0} & ({}^{O}\bar{\boldsymbol{f}}_{o,0} - {}^{O}\bar{\boldsymbol{f}}_{y,0} + {}^{O}\bar{\boldsymbol{f}}_{g}) \\ \mathbf{0}_{N\times 6} & \mathbf{0}_{N\times 6} & \mathbf{0}_{N\times 6} & \mathbf{0}_{N\times 1} \end{bmatrix}, \tag{4.46}$$

the state vector as

$$\boldsymbol{x} = \begin{bmatrix} {}^{O}\overline{\boldsymbol{x}} \\ {}^{O}\dot{\overline{\boldsymbol{x}}} \\ \boldsymbol{\varphi} \end{bmatrix}, \tag{4.47}$$

the input vector as

$$\boldsymbol{u} = \hat{\boldsymbol{\varphi}}, \tag{4.48}$$

and the disturbance vector as

$$\boldsymbol{w} = \begin{bmatrix} {}^{O}\overline{\boldsymbol{w}} \\ {}^{O}\dot{\overline{\boldsymbol{w}}} \\ {}^{O}\ddot{\overline{\boldsymbol{w}}} \\ 1 \end{bmatrix}, \tag{4.49}$$

where $\bar{\mu} = ({}^{O}\overline{\boldsymbol{M}} + {}^{O}\bar{\boldsymbol{m}}_{f,0})$.

The system outputs, $\boldsymbol{y}$, are the measured quantities of the system. The linear output equation is written in the familiar form as

$$\boldsymbol{y} = C(t,\boldsymbol{x})\boldsymbol{x} + D\boldsymbol{u} + F(t,\boldsymbol{x})\boldsymbol{w}(t), \tag{4.50}$$

where $\boldsymbol{y}$ are the output variables, $C(t,\boldsymbol{x})$ is the output matrix, D is the feedthrough matrix, and $F(t, \boldsymbol{x})$ is the output disturbance matrix. The next section discusses the control laws and the measured outputs used for feedback control.

4.3 Control Laws

Each control law specifies a $(N \times 1)$ command force $\hat{\boldsymbol{f}}_d$, composed of the N axial damper forces $\hat{f}_{d_i}$, at discrete time steps. The model of the MR damper force on the body frame in equation 4.22 is used to determine the command current $\hat{\varphi}_i$ for the i^{th} damper. The commanded force $\hat{f}_{d_i}$ is equated to the model force, given here as

$$\hat{f}_{d_i} = f_{o_i} - k_{d_i} q_i - c_{po_i} \dot{q}_i - m_{f_i} \ddot{q}_i - f_{y_i} \tanh\left((\dot{q}_i + \lambda_{1_i}(q_i - q_i^*))\lambda_{2_i}\right) \qquad (4.51)$$

where a quadratic relation between the model parameters and the command current $\hat{\varphi}_i$ can be formed as

$$\begin{aligned}
f_{o_i} &= f_{o_i,2}\hat{\varphi}_i^2 + f_{o_i,1}\hat{\varphi}_i + f_{o_i,0} \\
k_{d_i} &= k_{d_i,2}\hat{\varphi}_i^2 + k_{d_i,1}\hat{\varphi}_i + k_{d_i,0} \\
c_{po_i} &= c_{po_i,2}\hat{\varphi}_i^2 + c_{po_i,1}\hat{\varphi}_i + c_{po_i,0} \\
m_{f_i} &= m_{f_i,2}\hat{\varphi}_i^2 + m_{f_i,1}\hat{\varphi}_i + m_{f_i,0} \\
f_{y_i} &= f_{y_i,2}\hat{\varphi}_i^2 + f_{y_i,1}\hat{\varphi}_i + f_{y_i,0} \\
\lambda_{1_i} &= \lambda_{1_i,2}\hat{\varphi}_i^2 + \lambda_{1_i,1}\hat{\varphi}_i + \lambda_{1_i,0} \\
\lambda_{2_i} &= \lambda_{2_i,2}\hat{\varphi}_i^2 + \lambda_{2_i,1}\hat{\varphi}_i + \lambda_{2_i,0} \qquad (4.52)
\end{aligned}$$

Substituting equation 4.30 into equation 4.51, and rearranging, results in

$$0 = a\hat{\varphi}_i^2 + b\hat{\varphi}_i + c \tag{4.53}$$

where,

$$\begin{aligned} a = &\quad f_{o_i,2} - k_{d_i,2}q_i - c_{po_i,2}\dot{q}_i - m_{f_i,2}\ddot{q}_i - f_{y_i,2}\tanh\left((\dot{q}_i + \lambda_1^-(q_i - q_i^*))\lambda_2^-\right) \\ b = &\quad f_{o_i,1} - k_{d_i,1}q_i - c_{po_i,1}\dot{q}_i - m_{f_i,1}\ddot{q}_i - f_{y_i,1}\tanh\left((\dot{q}_i + \lambda_1^-(q_i - q_i^*))\lambda_2^-\right) \\ c = &\quad f_{o_i,0} - k_{d_i,0}q_i - c_{po_i,0}\dot{q}_i - m_{f_i,0}\ddot{q}_i - f_{y_i,0}\tanh\left((\dot{q}_i + \lambda_1^-(q_i - q_i^*))\lambda_2^-\right) - \hat{f}_{d_i}, \end{aligned} \tag{4.54}$$

and λ_1^- and λ_2^- are values from the previous discrete time step.

The command current is then found using the quadratic formula,

$$\hat{\varphi}_i = \frac{-b + \sqrt{b^2 - 4ac}}{2a} \tag{4.55}$$

A saturation range is established to restrict the command current $\hat{\varphi}_i$ below a maximum level of φ_{max} available from an external power supply and above a realistic minimum level of zero. The condition $\hat{\varphi}_i < 0$ usually occurs when the magnitude of the passive, field-off damper force is greater than the magnitude of the command force $\hat{f}_{d_i}$. The command current for the i^{th} damper is given as

$$\hat{\varphi}_i = \left\{ \begin{array}{cc} \varphi_{max}, & if\ \hat{\varphi}_i > \varphi_{max} \\ 0, & if\ \hat{\varphi}_i < 0,\ or\ \hat{\varphi}_i \notin \mathbb{R} \\ \hat{\varphi}_i & else \end{array} \right\}, \tag{4.56}$$

and the vector

$$\hat{\boldsymbol{\varphi}} = \begin{bmatrix} \hat{\varphi}_1 & ... & \hat{\varphi}_N \end{bmatrix}^T \tag{4.57}$$

is the control input $\boldsymbol{u}$ to the system, with $\boldsymbol{u} = \hat{\boldsymbol{\varphi}}$.

4.3.1 Decentralized Control

A decentralized control law considers only the states of the local control device subsystem, and has no knowledge of the states of other subsystems or the system as a whole. Figure 4.4 shows a block diagram of the closed-loop system dynamics using decentralized control. For decentralized control, there is a single tri-axial accelerometer and a single magnetostrictive, linear-stroke displacement sensor dedicated to each MR damper. The tri-axial accelerometer is fixed in the body frame B at point d_i and provides measurements ${}^B\ddot{\boldsymbol{x}}_{d_i} = \begin{bmatrix} {}^B\ddot{x}_{d_i} & {}^B\ddot{y}_{d_i} & {}^B\ddot{z}_{d_i} \end{bmatrix}^T$. The displacement sensor is installed inside the piston of each MR damper and provides the measurement q_i. The decentralized sensor suite vector $\boldsymbol{\eta}_i$ is given as

$$\boldsymbol{\eta}_i = \begin{bmatrix} \underset{(1 \times 3)}{{}^B\ddot{\boldsymbol{x}}_{d_i}^T} & \underset{(1 \times 1)}{q_i} \end{bmatrix}^T \tag{4.58}$$

Through numerical integration, ${}^B\dot{\boldsymbol{x}}_{d_i}$ and ${}^B\boldsymbol{x}_{d_i}$ can be calculated from the acceleration data, and through differentiation $\dot{q}_i$ and $\ddot{q}_i$ can be determined from the displacement sensor.

For decentralized control, the measured output for the i^{th} damper is $\boldsymbol{y}_i = \boldsymbol{\eta}_i$,

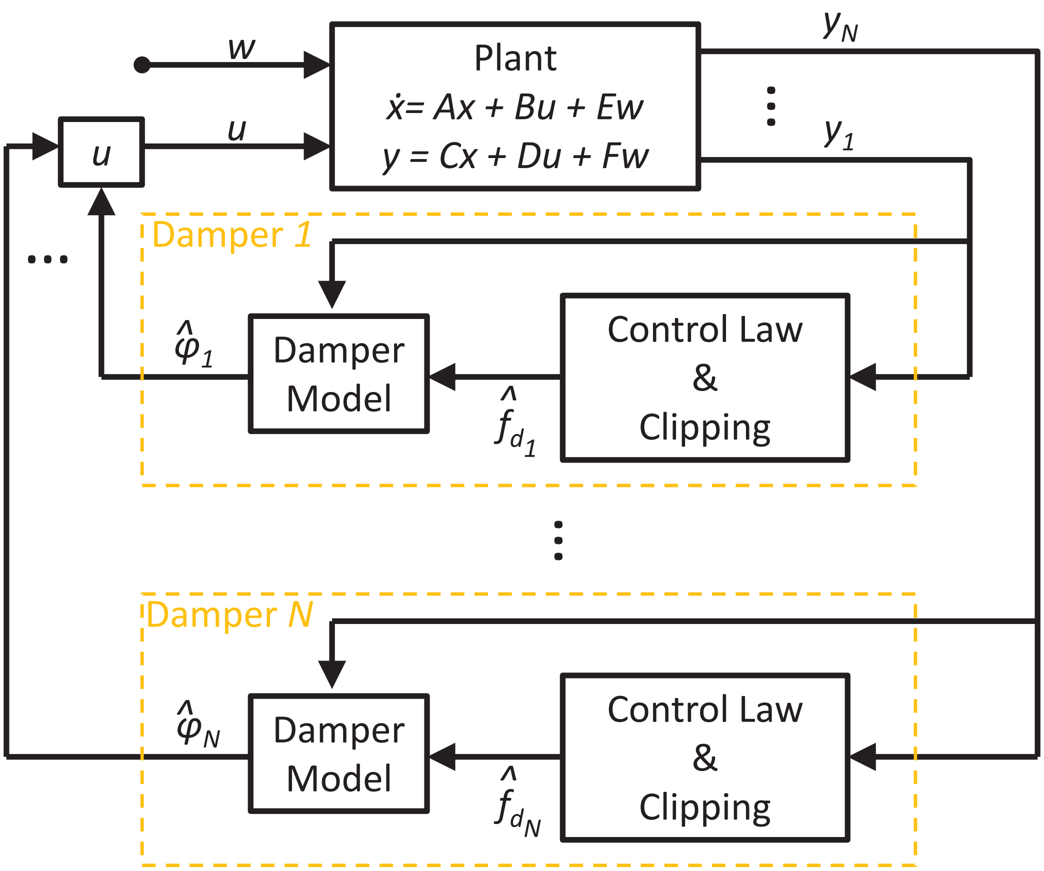

Figure 4.4: Block diagram of the closed-loop system dynamics using decentralized control.

and the output equation is given as

$$\boldsymbol{y}_i = C_i(t, \boldsymbol{x})\boldsymbol{x} + D_i\boldsymbol{u} + F_i(t, \boldsymbol{x})\boldsymbol{w}(t), \tag{4.59}$$

where

$$C_i(t, \boldsymbol{x}) = \begin{bmatrix} -\hbar_i({}^O\overline{\boldsymbol{K}} + {}^O\bar{\boldsymbol{k}}_{d,0}) & -\hbar_i \; {}^O\bar{\boldsymbol{c}}_{po,0} & \hbar_i \; {}^O\bar{\boldsymbol{\beta}} \\ \boldsymbol{\Lambda}_i & \boldsymbol{0}_{1\times 6} & \boldsymbol{0}_{1\times 6} \end{bmatrix} \tag{4.60}$$

$$D_i = \boldsymbol{0}_{4\times N} \tag{4.61}$$

$$F_i(t, \boldsymbol{x}) \;=\; \begin{bmatrix} \hbar_i({}^O\overline{\boldsymbol{K}} + {}^O\bar{\boldsymbol{k}}_{d,0}) & \hbar_i \; {}^O\bar{\boldsymbol{c}}_{po,0} & \hbar_i \; {}^O\bar{\boldsymbol{m}}_{f,0} & \hbar_i \; ({}^O\bar{\boldsymbol{f}}_{o,0} - {}^O\bar{\boldsymbol{f}}_{y,0} + {}^O\bar{\boldsymbol{f}}_g) \\ -\boldsymbol{\Lambda}_i & \boldsymbol{0}_{1\times 6} & \boldsymbol{0}_{1\times 6} & 0 \end{bmatrix} \tag{4.62}$$

and

$$\hbar_i = \boldsymbol{T}_{BO} \begin{bmatrix} \boldsymbol{I}_{3\times 3} & -{}^O\boldsymbol{P}_{d_i B}(t) \end{bmatrix} \bar{\mu}^{-1}. \tag{4.63}$$

4.3.1.1 Skyhook (decentralized)

The Skyhook algorithm aims to damp the absolute velocity of the payload by establishing an ficticious connection with an inertial reference, such as the sky, as seen in figure 4.5. This algorithm was first proposed by Karnopp et al. [45] for a single-DOF system, and is implemented previously for a semi-active suspension in Chapter 3.

Here, the Skyhook concept is extended to a 6-DOF system. For decentralized

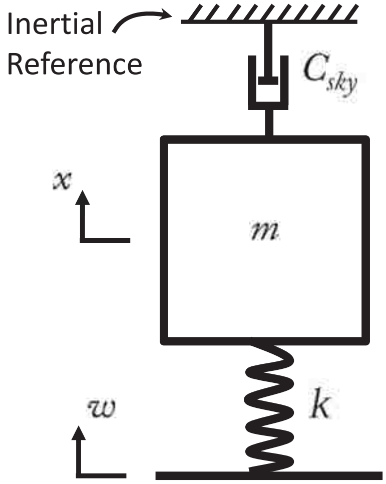

Figure 4.5: Ideal Skyhook configuration.

control, the Skyhook algorithm is applied locally where the control device connects with the payload. The payload is able to translate and rotate with 6 DOFs, thus it would be ideal to establish a Skyhook connection along each DOF. However, the MR dampers are linear stroking devices and are limited to applying force along only their axial direction. Therefore, the best option is to resolve the payload absolute velocity along the axial direction of the damper and apply the Skyhook algorithm. However, it is not possible to observe the orientation of each MR damper with the defined decentralized sensor suite vector $\boldsymbol{\eta}_i$. One solution is the orientation can be approximated as its static orientation, assuming that each damper frame rotates only by small angles. Alternatively, the local vertical velocity of the payload may be chosen as most critical and used in the Skyhook control law, which is done here.

The desired force input from the MR damper is given as

$$\nu_i = -G\ {}^{B}\dot{z}_{d_i}, \tag{4.64}$$

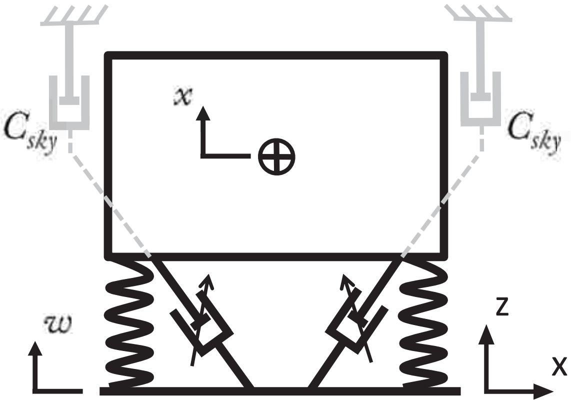

Figure 4.6: Concept of the decentralized Skyhook control.

where $G = C_{sky}$ is the control gain, and ${}^B\dot{z}_{d_i} = [0 \;\; 0 \;\; 1]\, {}^B\dot{\boldsymbol{x}}_{d_i}$ is the absolute velocity of point d_i along the body frame $\hat{\boldsymbol{b}}_3$ axis direction. By imposing the semi-active clipping criteria, we arrive at the command force

$$\hat{f}_{d_i} = \begin{Bmatrix} \nu_i, & \dot{q}_i \cdot {}^B\dot{z}_{d_i} \geq 0 \\ 0, & \dot{q}_i \cdot {}^B\dot{z}_{d_i} < 0 \end{Bmatrix} (i = 1, 2, ..., N). \tag{4.65}$$

4.3.1.2 Sliding Mode (decentralized)

Sliding mode control is a variable structure control law that assures robust performance in the presence of external disturbances and system uncertainties. For a practical suspension, perturbations in the damper stiffness, damper viscosity, payload mass, and orientation of the damper, are all possible. Therefore, the following parameter variations are considered in the control law design:

$$k_{a,min} \leq k_a \leq k_{a,max} \tag{4.66}$$

$$c_{min} \leq c \leq c_{max} \tag{4.67}$$

$$m_{N,min} \leq m_N \leq m_{N,max} \tag{4.68}$$

$$\theta_{d,min} \leq \theta_d \leq \theta_{d,max} \tag{4.69}$$

where k_a is the coil spring axial stiffness, c is the viscous damping of the MR damper, m_N is $1/N$ of the total payload mass (N is the number of dampers), and θ_d is the angle the damper makes with the horizon. Figure 4.7 shows these parameters in the model of a single leg of the suspension. The estimation errors of the parameter variations are bounded as follows

$$\bar{k}_a \geq \left|\hat{k}_a - k_a\right| \tag{4.70}$$

$$\bar{c} \geq |\hat{c} - c| \tag{4.71}$$

$$\mu \geq \frac{\hat{m}_N}{m_N} \tag{4.72}$$

where, $\hat{k}_a$, $\hat{c}$, and $\hat{m}_N$ are the estimates, and $\bar{k}_a$, $\bar{c}$, and μ are the bounds on the

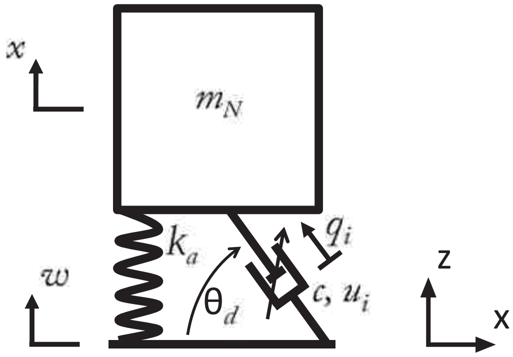

Figure 4.7: Concept of the decentralized Sliding Mode control (SMC).

estimation errors. The values are taken as

$$\begin{array}{llll}
k_{a,min} = 20\ kN/m, & c_{min} = 800\ Ns/m, & m_{N,min} = 150\ lb, & \theta_{d,min} = 45^o, \\
k_{a,max} = 30\ kN/m, & c_{max} = 2000\ Ns/m, & m_{N,max} = 300\ lb, & \theta_{d,max} = 90^o, \\
\hat{k}_a = 25\ kN/m, & \hat{c} = c_{max}, & \hat{m}_N = m_{N,max}, & \hat{\theta}_d = 45^o, \\
\bar{k}_a = 5\ kN/m, & \bar{c} = 1200\ Ns/m. & \mu = \frac{m_{N,max}}{m_{N,min}}, &
\end{array} \tag{4.73}$$

The control law is derived by considering only a single leg of the suspension, and the payload is assumed only to translate in the vertical direction. The single leg model is approximated as

$$m_N\ {}^O\ddot{z}_{d_i} = -k_a q_i \frac{1}{\sin(\theta_d)} - c\dot{q}_i \sin(\theta_d) + \nu_i \sin(\theta_d), \tag{4.74}$$

where ${}^O\ddot{z}_{d_i} = [0\ \ 0\ \ 1]\,{}^O\ddot{\boldsymbol{x}}_{d_i}$ is the vertical translational acceleration of point d_i along the $\hat{\boldsymbol{e}}_3$ axis w.r.t the global frame O, q_i is the damper stroke (where $q_i > 0$ for damper extension), and ν_i is the desired control force input. Assuming the rotational displacement of the body frame B rotates by only small angles, ${}^{O}\dot{\boldsymbol{x}}_{d_i} \approx {}^{B}\dot{\boldsymbol{x}}_{d_i}$. For brevity, $z = {}^{O}z_{d_i}$.

The objective of the sliding mode control is to bring the absolute motion of the payload to zero. To achieve this, a sliding surface function is defined as

$$\sigma = \dot{z} + Gz = 0, \tag{4.75}$$

where the slope of the sliding surface $G > 0$ to guarantee that variable $z(t)$ tends toward zero as t tends to infinity. The rate of convergence is determined by the value of G. The control law must drive the state of the system onto the sliding surface σ and keep it there. In order to prove the ability of the control law to achieve this task, a positive-definite, candidate Lyapunov function is chosen as

$$V = \frac{1}{2}\sigma^2, \tag{4.76}$$

with its time derivative as

$$\dot{V} = \sigma\dot{\sigma}. \tag{4.77}$$

To ensure stable robust control, the control input ν_i must satisfy the inequality

$\dot{V} < 0$. Therefore, we write

$$\begin{aligned} \sigma\dot{\sigma} &= \sigma\left[\ddot{z} + G\dot{z}\right] \\ &= \sigma\left[-\frac{k_a}{m_N} q_i \frac{1}{\sin(\theta_d)} - \frac{c}{m_N}\dot{q}_i \sin(\theta_d) + \frac{1}{m_N}\nu_i \sin(\theta_d) + G\dot{z}\right]. \end{aligned} \tag{4.78}$$

Similar to Choi and Wereley [18], by selecting the following control input

$$\begin{aligned} \nu_i &= \frac{\hat{k}_a q_i}{\sin^2(\hat{\theta}_d)} + \hat{c}\dot{q}_i + \hat{m}_N G\dot{z} \\ &\quad - \left[\frac{(\bar{k}_a + \hat{k}_a)\left|q_i\right|}{\sin^2(\theta_{d,min})} + \bar{c}\left|\dot{q}_i\right| + m_{N,max}(1+\mu)G\left|\dot{z}\right|\right]\mathrm{sgn}(\sigma), \end{aligned} \tag{4.79}$$

equation 4.78 becomes

$$\begin{aligned} \sigma\dot{\sigma} &= \sigma\Bigg[\frac{-k_a}{\sin(\theta_d)}\frac{q_i}{m_N} - \frac{c}{m_N}\dot{q}_i \sin(\theta_d) + G\dot{z} + \frac{\sin(\theta_d)}{m_N}\Bigg(\frac{\hat{k}_a q_i}{\sin^2(\hat{\theta}_d)} + \hat{c}\dot{q}_i \\ &\quad + \hat{m}_N G\dot{z} - \left[\frac{(\bar{k}_a + \hat{k}_a)|q_i|}{\sin^2(\theta_{d,min})} + \bar{c}|\dot{q}_i| + m_{N,max}(1+\mu)G|\dot{z}|\right]\mathrm{sgn}(\sigma)\Bigg)\Bigg] \\ &= \sigma\Bigg[\left(\hat{k}_a\frac{\sin(\theta_d)}{\sin^2(\hat{\theta}_d)} - k_a\frac{1}{\sin(\theta_d)}\right)\frac{q_i}{m_N} + \frac{\hat{c}-c}{m_N}\dot{q}_i\sin(\theta_d) \\ &\quad + \left(1 + \frac{\hat{m}_N}{m_N}\sin(\theta_d)\right)G\dot{z} \\ &\quad - \Bigg((\bar{k}_a + \hat{k}_a)\frac{\sin(\theta_d)}{\sin^2(\theta_{d,min})}\frac{|q_i|}{m_N} + \frac{\bar{c}}{m_N}\left|\dot{q}_i\right|\sin(\theta_d) \\ &\quad + \frac{m_{N,max}}{m_N}(1+\mu)\sin(\theta_d)G\left|\dot{z}\right|\Bigg)\mathrm{sgn}(\sigma)\Bigg] \\ &= \sigma\left[\alpha - \bar{\alpha}\mathrm{sgn}(\sigma)\right] \\ &= \sigma\alpha - \bar{\alpha}\left|\sigma\right|, \end{aligned} \tag{4.80}$$

where

$$\alpha = \left(\hat{k}_a \frac{\sin(\theta_d)}{\sin^2(\hat{\theta}_d)} - k_a \frac{1}{\sin(\theta_d)}\right) \frac{q_i}{m_N} + \frac{\hat{c} - c}{m_N} \dot{q}_i \sin(\theta_d) + \left(1 + \frac{\hat{m}_N}{m_N} \sin(\theta_d)\right) G\dot{z} \tag{4.81}$$

$$\bar{\alpha} = (\bar{k}_a + \hat{k}_a) \frac{\sin(\theta_d)}{\sin^2(\theta_{d,min})} \frac{|q_i|}{m_N} + \frac{\bar{c}}{m_N} |\dot{q}_i| \sin(\theta_d) + \frac{m_{N,max}}{m_N} (1 + \mu) \sin(\theta_d) G |\dot{z}| . \tag{4.82}$$

Now, it must be shown that $\bar{\alpha} \geq \alpha$. Considering the first terms of both equations 4.81 and 4.82,

$$\left(\hat{k}_a \frac{\sin(\theta_d)}{\sin^2(\hat{\theta}_d)} - k_a \frac{1}{\sin(\theta_d)}\right) \leq (\bar{k}_a + \hat{k}_a) \frac{\sin(\theta_d)}{\sin^2(\theta_{d,min})} \tag{4.83}$$

even with the most demanding case of $\theta_d = 90^o$ and $k_a = k_{a,min}$, resulting in

$$\begin{aligned} 2\hat{k}_a - k_{a,min} &\leq 2(\bar{k}_a + \hat{k}_a) \\ -k_{a,min} &\leq 2\hat{k}_a. \end{aligned} \tag{4.84}$$

Considering the second terms of both equations 4.81 and 4.82,

$$\hat{c} - c \leq \bar{c} \tag{4.85}$$

due to the parameter bounds in equation 4.71. Considering the third terms of both equations 4.81 and 4.82,

$$\left(1+\frac{\hat{m}_N}{m_N}\sin(\theta_d)\right) \leq \frac{m_{N,max}}{m_N}(1+\mu)\sin(\theta_d) \tag{4.86}$$

even with the most demanding case of $\theta_d = \theta_{d,min}$ and $m_N = m_{N,min}$, resulting in

$$\begin{aligned} \left(1+\frac{\hat{m}_N}{m_{N,min}}\sin(\theta_{d,min})\right) &\leq \frac{m_{N,max}}{m_{N,min}}(1+\mu)\sin(\theta_{d,min}) \\ 1+2(.707) &\leq 2(1+2)(.707) \\ 2.414 &\leq 4.242 \end{aligned} \tag{4.87}$$

Therefore, $\bar{\alpha} \geq \alpha$ in equation 4.80, and the control input ν_i in equation 4.79 satisfies the sliding mode condition $\sigma\dot{\sigma} < 0$. ■

By imposing the semi-active clipping criteria on equation 4.79, we arrive at the command force

$$\hat{f}_{d_i} = \begin{Bmatrix} \nu_i, & \dot{q}_i \cdot {}^{O}\dot{z}_{d_i} \geq 0 \\ 0, & \dot{q}_i \cdot {}^{O}\dot{z}_{d_i} < 0 \end{Bmatrix} (i = 1, 2, ..., N). \tag{4.88}$$

4.3.2 Centralized Control

A centralized control law is defined as a single decision-making algorithm that governs the behavior of the individual subsystems that compose the overall global system. Each control device is operated with the knowledge of the operation of every other control device. Figure 4.8 shows a block diagram of the closed-loop system dynamics using centralized control.

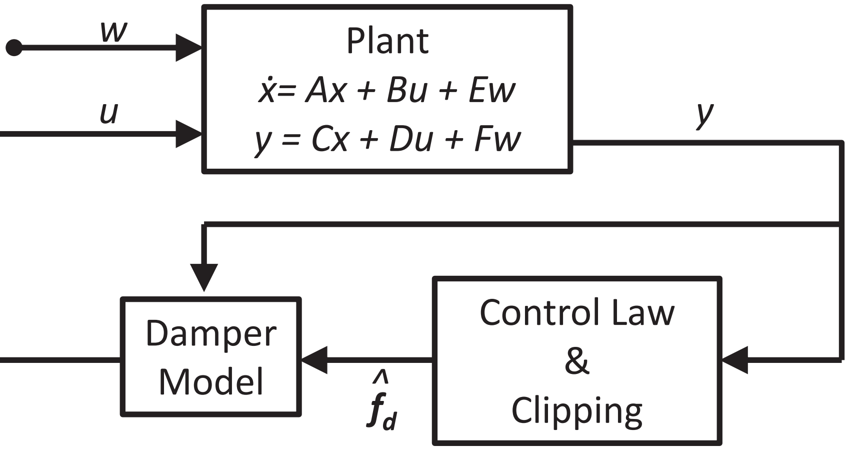

Figure 4.8: Block diagram of the closed-loop system dynamics using centralized control.

For centralized control, there are a total of $6+N$ sensors. There is a single tri-axial accelerometer and a single tri-axial gyroscope located at the payload CG, and a single magnetostrictive, linear-stroke displacement sensor installed inside the piston of all N MR dampers. The tri-axial accelerometer provides translational measurements ${}^{B}\ddot{\boldsymbol{x}}_t$ of the body frame B, the tri-axial gyroscope provides angular velocities ${}^{B}\dot{\boldsymbol{x}}_r$ of the body frame B, and each displacement sensor provides the stroke displacement q_i of the i^{th} MR damper. By assuming the rotational displacement of frame B to be small, the approximations ${}^{O}\ddot{\boldsymbol{x}}_t \approx {}^{B}\ddot{\boldsymbol{x}}_t$ and ${}^{O}\dot{\boldsymbol{x}}_r \approx {}^{B}\dot{\boldsymbol{x}}_r$ are valid. Therefore the centralized sensor suite $\boldsymbol{\eta}$ is given as

$$\boldsymbol{\eta} = \begin{bmatrix} {}^{O}\ddot{\boldsymbol{x}}_t^T & {}^{O}\dot{\boldsymbol{x}}_r^T & \boldsymbol{q}^T \\ (1\times 3) & (1\times 3) & (1\times N) \end{bmatrix}^T, \tag{4.89}$$

and through numerical integration and differentiation, ${}^{O}\dot{\boldsymbol{x}}_t$ can be determined from ${}^{O}\ddot{\boldsymbol{x}}_t$, and $\dot{\boldsymbol{q}}$ and $\ddot{\boldsymbol{q}}$ can be determined from $\boldsymbol{q}$. By taking the output $\boldsymbol{y}$ as

$$\boldsymbol{y} = \begin{bmatrix} {}^{O}\dot{\boldsymbol{x}} \\ \boldsymbol{q} \end{bmatrix}, \tag{4.90}$$

the output equation is given as

$$\boldsymbol{y} = C(t, \boldsymbol{x})\boldsymbol{x} + D\boldsymbol{u} + F(t, \boldsymbol{x})\boldsymbol{w}(t), \tag{4.91}$$

where

$$C(t, \boldsymbol{x}) = \begin{bmatrix} \mathbf{0}_{6\times 6} & \boldsymbol{I}_{6\times 6} & \mathbf{0}_{6\times N} \\ \boldsymbol{\Lambda} & \mathbf{0}_{4\times 6} & \mathbf{0}_{4\times N} \end{bmatrix}, \tag{4.92}$$

$$D = \mathbf{0}_{16\times N} \tag{4.93}$$

$$F(t, \boldsymbol{x}) \quad = \quad \begin{bmatrix} \mathbf{0}_{6\times 6} & \mathbf{0}_{6\times 6} & \mathbf{0}_{6\times 6} & 0 \\ -\boldsymbol{\Lambda} & \mathbf{0}_{4\times 6} & \mathbf{0}_{4\times 6} & 0 \end{bmatrix}, \tag{4.94}$$

and

$$\boldsymbol{\Lambda} = \begin{bmatrix} \boldsymbol{\Lambda}_1 \\ \boldsymbol{\Lambda}_2 \\ \vdots \\ \boldsymbol{\Lambda}_N \end{bmatrix}. \tag{4.95}$$

The centralized control law described here will identify a single control input, ${}^{O}\bar{\boldsymbol{\nu}}$, which is a generalized force vector desired to be exerted on the body frame to best attenuate base disturbances. For proper implementation, it is necessary to know the orientation of each damper. This knowledge allows the centralized control law to best delegate the desired forces $\hat{f}_{d_i}$ to each damper.

The generalized force vector exerted on the body frame due to all N dampers is given in equation 4.27 as

$$ {}^{O}\overline{\boldsymbol{f}}_{D} = \sum_{i=1}^{N} \left[\boldsymbol{I}_{3\times 3} \quad -{}^{O}\boldsymbol{P}_{d_iB}(t)\right]^{T} \boldsymbol{T}_{D_iO}^{T} \; {}^{D_i}\boldsymbol{f}_{D_i} \tag{4.96} $$

This expression can be written in a more compact form by defining the $(6\times N)$ Jacobian matrix $\boldsymbol{\Gamma}$, such that

$$ {}^{O}\overline{\boldsymbol{f}}_{D} = \boldsymbol{\Gamma}\boldsymbol{f}_{d}, \tag{4.97} $$

where $\boldsymbol{f}_d = [f_{d_1} \quad ... \quad f_{d_N}]^T$, and

$$ \boldsymbol{\Gamma} = \begin{bmatrix} \frac{1}{l_{D_1}} {}^{O}\boldsymbol{l}_{d_1D_1} & \cdots & \frac{1}{l_{D_N}} {}^{O}\boldsymbol{l}_{d_ND_N} \\ -\frac{1}{l_{D_1}} {}^{O}\boldsymbol{P}_{d_1B}^{T} \, {}^{O}\boldsymbol{l}_{d_1D_1} & \cdots & -\frac{1}{l_{D_N}} {}^{O}\boldsymbol{P}_{d_NB}^{T} \, {}^{O}\boldsymbol{l}_{d_ND_N} \end{bmatrix}. \tag{4.98} $$

The Jacobian matrix $\boldsymbol{\Gamma}$ contains all of the damper orientation information, which when pre-multiplied transforms the axial damper forces f_{d_i} into generalized force vectors in the global frame O. The orientation vector ${}^{O}\boldsymbol{l}_{d_iD_i}(t)$ of the i^{th} damper, from point D_i to point d_i, is given as

$$ {}^{O}\boldsymbol{l}_{d_iD_i}(t) = {}^{O}\boldsymbol{p}_{BA}(t) + {}^{O}\boldsymbol{p}_{d_iB}(t) - {}^{O}\boldsymbol{p}_{D_iA}. \tag{4.99} $$

The length of the i^{th} damper is given as $l_{D_i}(t) = \left\| {}^{O}\boldsymbol{l}_{d_iD_i}(t) \right\|$. The position vector ${}^{O}\boldsymbol{p}_{BA}(t)$ to frame B from frame A is given as

$$ {}^{O}\boldsymbol{p}_{BA}(t) = {}^{O}\boldsymbol{p}_{BA}(0) + \left[\boldsymbol{I}_{3\times 3} \quad \mathbf{0}_{3\times 3}\right] ({}^{O}\overline{\boldsymbol{x}}(t) - {}^{O}\overline{\boldsymbol{w}}(t)). \tag{4.100} $$

The position vector ${}^{O}\boldsymbol{p}_{d_iB}(t)$ to point d_i of the i^{th} damper from the body frame B is given as

$$ {}^{O}\boldsymbol{p}_{d_iB}(t) = {}^{B}\boldsymbol{p}_{d_iB} + \left[\mathbf{0}_{3\times 3} \quad -{}^{B}\boldsymbol{P}_{d_iB}\right] {}^{O}\overline{\boldsymbol{x}}(t). \tag{4.101} $$

The position vector ${}^{O}\boldsymbol{p}_{D_iA}(t)$ to frame D_i from frame A is given as

$$ {}^{O}\boldsymbol{p}_{D_iA}(t) = {}^{A}\boldsymbol{p}_{D_iA} + \begin{bmatrix} \mathbf{0}_{3\times 3} & -{}^{A}\boldsymbol{P}_{D_iA} \end{bmatrix} {}^{O}\overline{\boldsymbol{w}}(t), \tag{4.102} $$

however, it is assumed that ${}^{O}\boldsymbol{w}_r(t) = [0 \;\; 0 \;\; 0]^T$, so

$$ {}^{O}\boldsymbol{p}_{D_iA}(t) = {}^{A}\boldsymbol{p}_{D_iA}. \tag{4.103} $$

The position vectors ${}^{O}\boldsymbol{p}_{BA}(0)$, ${}^{B}\boldsymbol{p}_{d_iB}$, and ${}^{A}\boldsymbol{p}_{D_iA}$, and skew-symmetric matrix ${}^{B}\boldsymbol{P}_{d_iB}$, are all independent of time and known a priori. However, obtaining the time-dependent, absolute pose vectors ${}^{O}\overline{\boldsymbol{x}}(t)$ and ${}^{O}\overline{\boldsymbol{w}}(t)$ from sensor data proves difficult in practice. Integrating measured acceleration data twice to obtain position and orientation is prone to cumulative errors due to noise in the measured acceleration signals. Using a high-pass filter or Kalman filter may improve the accuracy by removing the 'drift' in the integrated signal. It may also be necessary to augment this approach with addition sensors such as vision-base pose estimation or range finding, sonar or laser sensors. The fildelity of these sensors must be robust in order to operate in the vibratory environment.

Another approach would be to utilize the relative displacement sensors in each MR damper. The dampers would have to be arranged so that the Jacobian matrix decribing the 6-DOF motion of the payload rigid body with the relative displacements of the damper is non-singular. The cubic Stewart platform is one such arrangement [36]. By assuming the displacements of the base floor are small, the generalized displacement of the payload could be indentified.

A different approach is taken in this study. By assuming the dampers rotate only by small angles, simplifications can be made which allow the orientation of the dampers for all time to be approximated as the orientation at static equilibrium. If at $t = 0$ the system is at the static equilibrium ${}^{O}\overline{\boldsymbol{x}}(0)$ and the base disturbance ${}^{O}\overline{\boldsymbol{w}}(0) = \mathbf{0}$, then $\boldsymbol{\Gamma} = \boldsymbol{\Gamma}(0)$ is a constant matrix and is known a priori. This reduces the number of sensors required to implement the control law as well as eliminate the need for estimated output states not directly measured, which are subject to uncertainty.

With the Jacobian matrix $\boldsymbol{\Gamma}$ known, it is then necessary for the centralized control law to delegate the desired forces $\hat{f}_{d_i}$ to each damper. MR dampers are semi-active devices that can only dissipate energy from the system, causing the desired control force to be 'clipped' when the desired force and relative stroke velocity have opposite signs. A further difficulty is the MR dampers are linear stroke devices with spherical end joints. Therefore, they can only apply a force along their axial direction, as the spherical end joints are incapable of transmitting torques. The centralized control input ${}^{O}\bar{\boldsymbol{\nu}}$ specifies 3 orthogonal forces and 3 orthogonal moments to be applied on the body frame. Ideally, the MR dampers would be able to exactly satisfy each of the desired forces and moments, requiring the dampers to be oriented so the system is fully controllable. One such configuration would orient the dampers to resemble a cubic Gough-Stewart platform [36], which is a parallel linkage mechanism with six supporting prismatic actuators connecting the base to the payload platform. The cubic configuration orients adjacent dampers orthogonal to one another, allowing the six dampers to apply decoupled forces and moments on the body frame. This feature would allow the dampers to exactly satisfy the desired forces and moments specified by the control law.

However, alternative configurations may not be capable of exactly matching the desired generalized force vector ${}^{O}\bar{\boldsymbol{\nu}}$ due to singularities existing when attempting to resolve the (6×1) generalized force vector into the N axial damper forces. The matrix $\mathbf{\Gamma}$ may be singular and not invertible if the number of dampers does not equal six ($N \neq 6$) or the columns of $\mathbf{\Gamma}$ are not all linearly independent. Therefore, we must determine the best possible control input, in a least-squares sense, using the Moore-Penrose psuedo-inverse, indicated by the superscript ${}^{+}$.

The best achieveble control input in the global O frame is then given as

$$\begin{aligned} {}^{O}\tilde{\bar{\boldsymbol{\nu}}} &= \mathbf{\Gamma}\mathbf{\Gamma}^{+}\ {}^{O}\bar{\boldsymbol{\nu}} \\ &= \mathbf{\Gamma}\tilde{\boldsymbol{f}}_d \end{aligned} \tag{4.104}$$

where,

$$\tilde{\boldsymbol{f}}_d = \mathbf{\Gamma}^{+}\ {}^{O}\bar{\boldsymbol{\nu}}, \tag{4.105}$$

is the $(N \times 1)$ vector composed of the best achieveble scalar damper forces for all N MR dampers.

Due to $\tilde{\boldsymbol{f}}_d$ being a fully active control command, it does not consider the necessary semi-active clipping. Clipping the force of one damper may impact the decision to clip the other dampers, thus to find the optimal semi-active control input, all possible clipping combinations are evaluated. This approach is similar to the centralized observer control proposed by Miller [56]. With four dampers, there are 16 combinations in total. The diagonal matrix $\boldsymbol{H}_j$ identifies each j^{th} combination, where a value of 1 turns the desired force on, and a value of 0 sets the damper force to zero. For example, $\boldsymbol{H}_j = diag(1,1,0,1)$ if dampers 1,2, and 4 were turned on, and damper 3 was turned off.

The desired control input for the j^{th} clipping combination now becomes

$$\begin{aligned} {}^O\tilde{\bar{\boldsymbol{\nu}}}_j &= \boldsymbol{\Gamma}(\boldsymbol{\Gamma}\boldsymbol{H}_j)^{+}\,{}^O\bar{\boldsymbol{\nu}} \\ &= \boldsymbol{\Gamma}\tilde{\boldsymbol{f}}_{d,j} \end{aligned} \tag{4.106}$$

where,

$$\tilde{\boldsymbol{f}}_{d,j} = (\boldsymbol{\Gamma}\boldsymbol{H}_j)^{+}\,{}^O\bar{\boldsymbol{\nu}}, \tag{4.107}$$

and

$$\tilde{\boldsymbol{f}}_{d,j} = \begin{bmatrix} \tilde{f}_{d_1,j} & \tilde{f}_{d_2,j} & \dots & \tilde{f}_{d_N,j} \end{bmatrix}^T. \tag{4.108}$$

An error metric is defined to select the clipping combination that provides the control input closest to the desired control ${}^O\bar{\boldsymbol{\nu}}$. This error metric is defined as

$$e_j = \left\| {}^O\bar{\boldsymbol{\nu}} - {}^O\tilde{\bar{\boldsymbol{\nu}}}_j \right\|. \tag{4.109}$$

Starting with the j^{th} combination that has the smallest error e_j, the optimal command force $\hat{\boldsymbol{f}}_d$ is selected as

$$\hat{\boldsymbol{f}}_d = \left\{ \tilde{\boldsymbol{f}}_{d,j}, \quad if\ \tilde{f}_{d_i,j}\dot{q}_i \leq 0 \ \ \forall\, i = 1,2,...,N \right\} \tag{4.110}$$

If the expression does not hold for all N dampers, then the clipping combination with the next larger error metric is evaluated until the expression is met.

4.3.2.1 Skyhook (centralized)

The Skyhook strategy is again extended to a 6-DOF system, but here it is applied in a centralized fashion. The rigid body payload is free to both translate and rotate about three orthogonal axes, allowing six independent motions to exist. The centralized Skyhook strategy attempts to damp these motions by attaching ficticious Skyhook dampers to the payload CG and aligning them with each of the six DOFs as seen in figure 4.9.

The desired control input ${}^{O}\bar{\boldsymbol{\nu}}$ is the (6×1) generalized force vector (forces and moments) we wish to apply to the body frame and is given as

$${}^{O}\bar{\boldsymbol{\nu}} = -\boldsymbol{G}\;{}^{O}\dot{\bar{\boldsymbol{x}}} \tag{4.111}$$

where $\boldsymbol{G} = diag(C_{sky,x}, C_{sky,y}, C_{sky,z}, C_{sky,\phi}, C_{sky,\theta}, C_{sky,\psi})$ is the gain matrix. Using the centralized delegation process described before, $\hat{\boldsymbol{f}}_d$ can be identified.

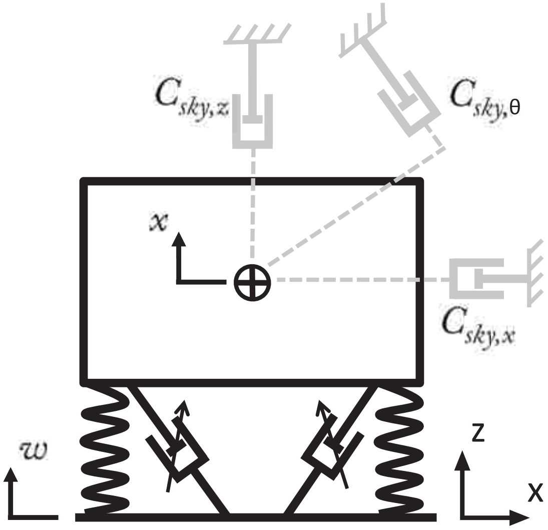

Figure 4.9: Concept of the centralized Skyhook control.

Chapter 5

Experiment Testing

5.1 Introduction

The experimental setup and testing of the 6-DOF system is presented in this chapter. The design of the suspension is discussed and the MR dampers and coil springs are experimentally characterized. Several performance metrics are established to select the control law gains and evaluate the ability of the system to attenuate base disturbances. The 6-DOF experimental setup is described and the test results are presented. The test results are used to validate the mathematical model of the suspension system.

5.2 Suspension Leg Design

5.2.1 MR Dampers

5.2.1.1 Damper Design

Several factors contribute to the design of the isolation suspension, such as: high frequency isolation, static deflection, maximum achievable field-dependent yield force, roll-over stability, and geometry constraints. Considering the trade-off between high frequency isolation and static deflection, the vertical translational resonance of the system was chosen to occur at $\omega_n = 2.2$ Hz. Considering the trade-off between obtaining a low zero-field damping ratio while maintaining an adequate maximum field-dependent yield force, the zero-field damping ratio ζ was chosen to be 0.16 and is expressed as

$$\zeta = \frac{C_m}{2\omega_n m_q}, \tag{5.1}$$

where $m_q = 136$ kg (300 lb) is one quarter of the full payload mass. This requires a zero-field damping of $C_m = 602$ N s/m.

The piston heads are equipped with a mixed mode type MR valve, which combines flow and shear modes of operation. A schematic of the MR valve is shown in figure 5.2. The zero-field damping, C_m, of a mixed mode valve is given as [77]

$$C_m = C_f \left(1 + \frac{A_d}{2A_p}\right), \tag{5.2}$$

where A_p is the piston area, and $A_d = bd$ is the annular gap area. The flow mode damping, C_f, is given as

$$C_f = \frac{12\mu_o l A_p^2}{bd^3}, \tag{5.3}$$

where μ_o is the zero-field viscosity of the MR fluid, l is the total active gap length in the direction of flow, b is the circumference of the piston head, and d is the separation distance between the active gap walls. The term D_p is the piston diameter, the circumference $b = \pi D_p$, and the piston area $A_p = \pi D_p^2/4$. A commercial bobbin supplied by Lord Corp. was used, thus the following values were fixed: $l = 30$ mm, $b = 154$ mm, and $A_p = 18.86$ cm^2. The dampers were filled with MRF-126 MR fluid supplied by Lord Corp., which has an experimentally measured zero-field viscosity of $\mu_o = 0.14$ Pa s for flow mode operation. Using these values, the gap thickness d can be found by rearranging equation 5.2 as

$$\frac{A_p C_m b}{6\mu_o l A_p^2} d^3 - bd - 2A_p = 0 \tag{5.4}$$

and solving the cubic equation, giving $d = 1.3$ mm, requiring the inner diameter of the damper cylinder to be 51.5 mm.

The MR dampers were designed to have a 6 in available stroke length and a pneumatic accumulator to accomodate the increase in rod volume during damper compression, shown in figure 5.1. The accumulator was filled with nitrogen gas and pressurized to 300 psi. The overall length of the damper $l_d = 23.5$ in, and the cylinder housing was made of 1020 low carbon steel.

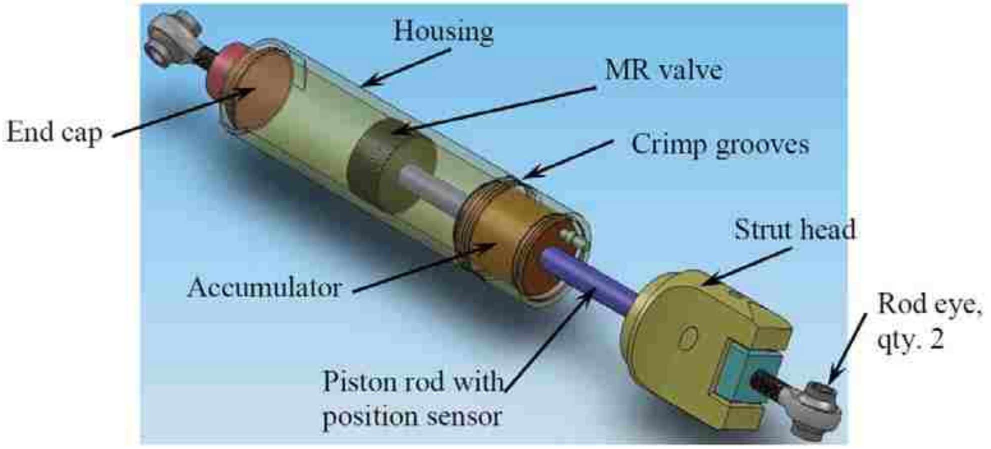

Figure 5.1: Schematic of the MR damper.

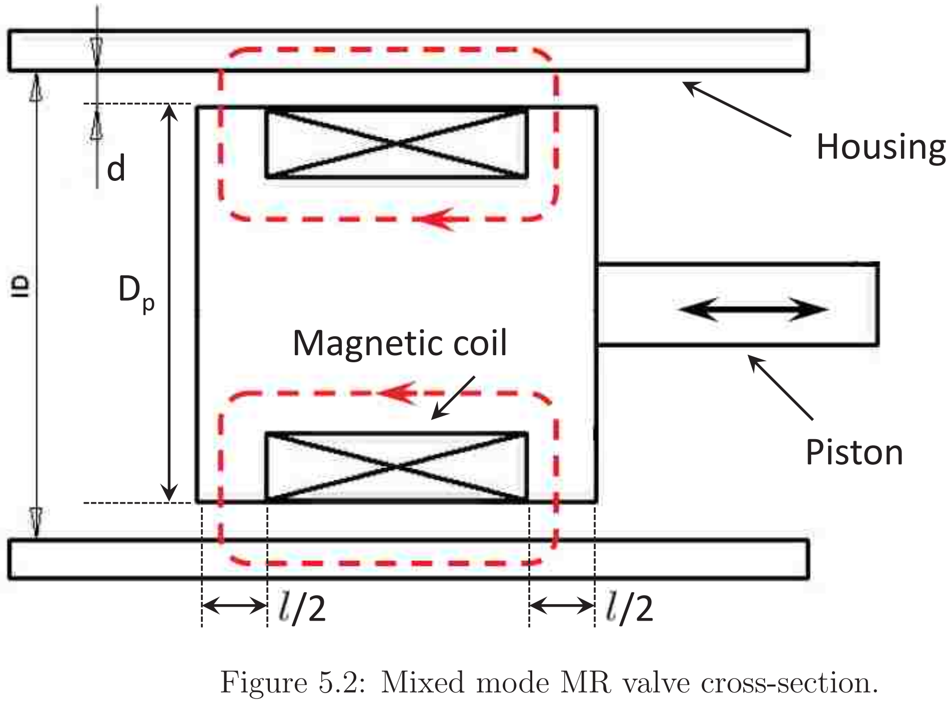

Figure 5.2: Mixed mode MR valve cross-section.

5.2.1.2 Characterization

All four MR dampers, seen in figure 5.3, were characterized on an MTS 810 material testing system. Based on the predicted stroking profile during a disturbance to the full-scale system, the dampers were characterized at the dominate operating level with a representative sinusoidal excitation of 0.25 in stroke amplitude at 2 Hz. The dampers were evaluated at applied currents of 0, 0.25, 1.0, and 2.5 A. The damper force f was modeled using

$$f = k_d x + c_{po}\dot{x} + m_f \ddot{x} + f_y \tanh\left(\left(\lambda_1 x + \dot{x}\right)\lambda_2\right), \tag{5.5}$$

where x is the piston displacement, k_d is the linear damper stiffness, c_{po} is the post-yield damping, m_f is the fluid inertia, f_y is the yield force, and λ_1 and λ_2 are shaping parameters used inside the hyperbolic tangent function. This model is fitted to the measured data for all four MR dampers.

Figures 5.4 and 5.5 show the measured force/velocity behavior of each damper together with the fitted damper model at applied currents of 0 and 2.5 A, respectively. The model matches the measured force data well for all dampers. The dissipated energy error metric in figure 5.6(a) shows the model fits the data with $< 0.35\%$ error, and the complex correlation coefficient (CCF) metric [23, 33] in figure 5.6(b) is > 0.98 for all dampers.

Figure 5.7 shows the optimized model parameter values for each damper. The damper stiffness k_d is relatively constant as a function of applied current at 10 kN/m and mostly dependent upon the accumulator pressure. The fluid inertia m_f generally

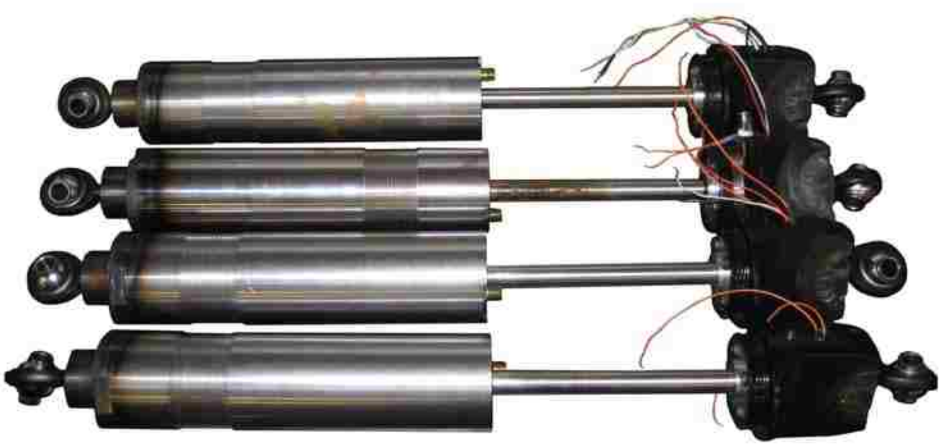

Figure 5.3: Characterized MR dampers.

increases as a function of applied current, suggesting dependence to the yield stress of the fluid. The post-yield damping c_{po} and yield force f_y of all the dampers show clear increasing trends with applied current, offering field-off (0 A) values near 500 N s/m and 150 N, respectively. The shaping parameters λ_1 and λ_2 show clear increasing and decreasing trends as a function of applied current, respectively, with λ_1 indicating the low-velocity hysteresis loop widens with increased applied current and λ_2 indicating the slope of the low-velocity hysteresis loop becomes less steep with increasing applied current.

5.2.2 Coil Spring

The coil spring is selected by first defining the desired mechanical properties of the spring, then choosing geometric properties which satisfy those mechanical properties. The best high frequency isolation is obtained when the natural frequencies of the system are lowered as much as possible. The lower limit for the vertical

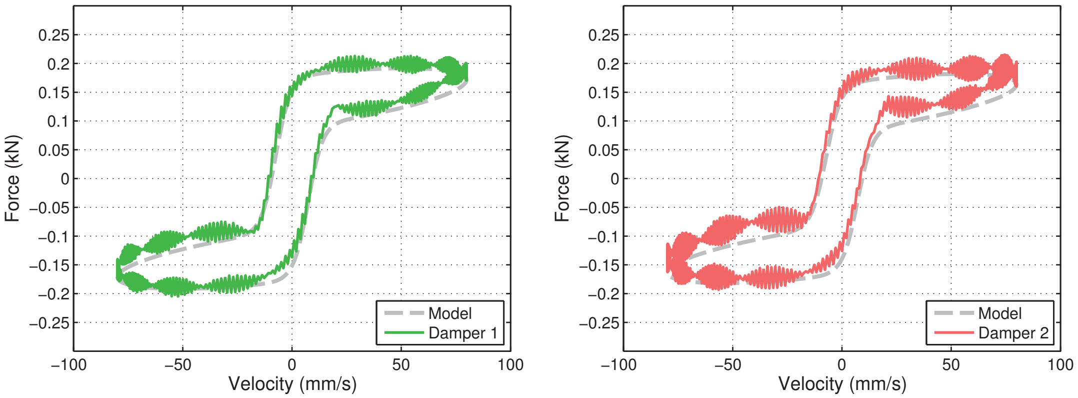

(a) Damper 1. (b) Damper 2.

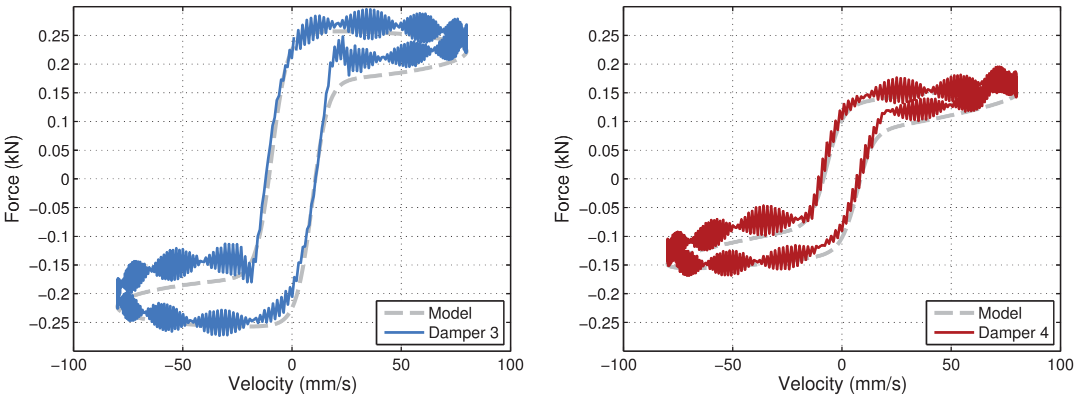

(c) Damper 3. (d) Damper 4.

Figure 5.4: Measured and modeled force vs. piston velocity curves of the MR dampers at 0 A of applied current.

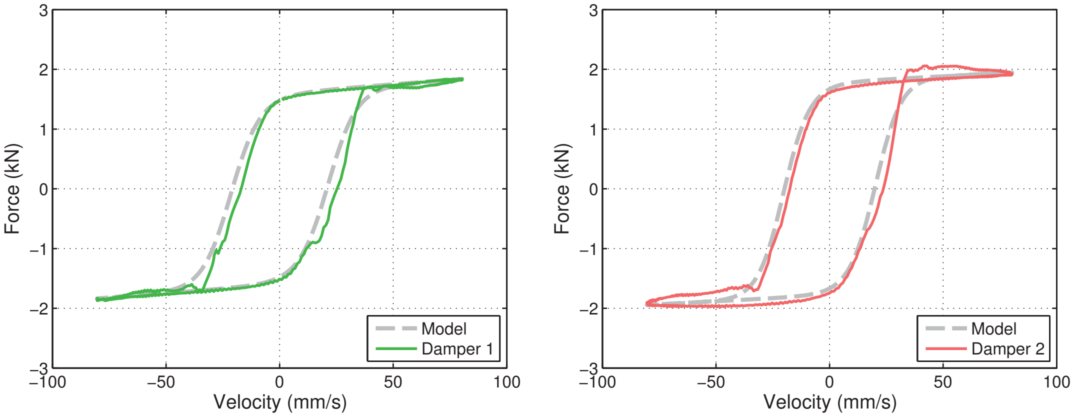

(a) Damper 1. (b) Damper 2.

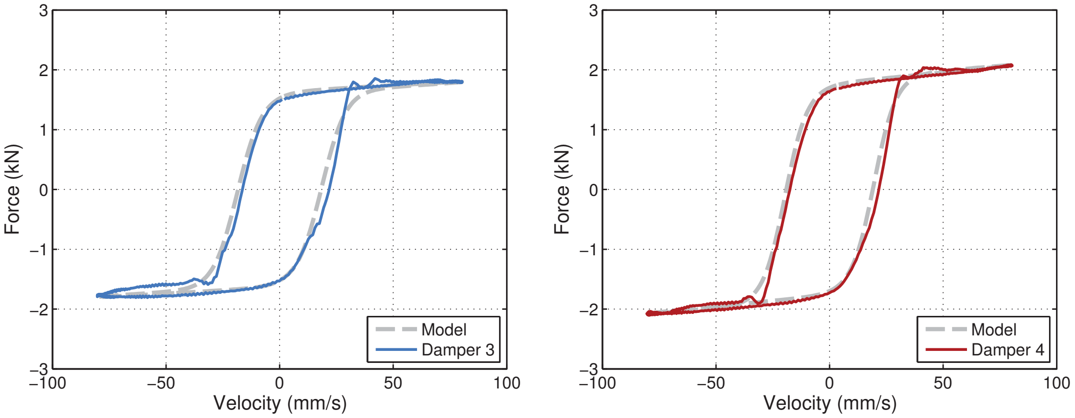

(c) Damper 3. (d) Damper 4.

Figure 5.5: Measured and modeled force vs. piston velocity curves of the MR dampers at 2.5 A of applied current.

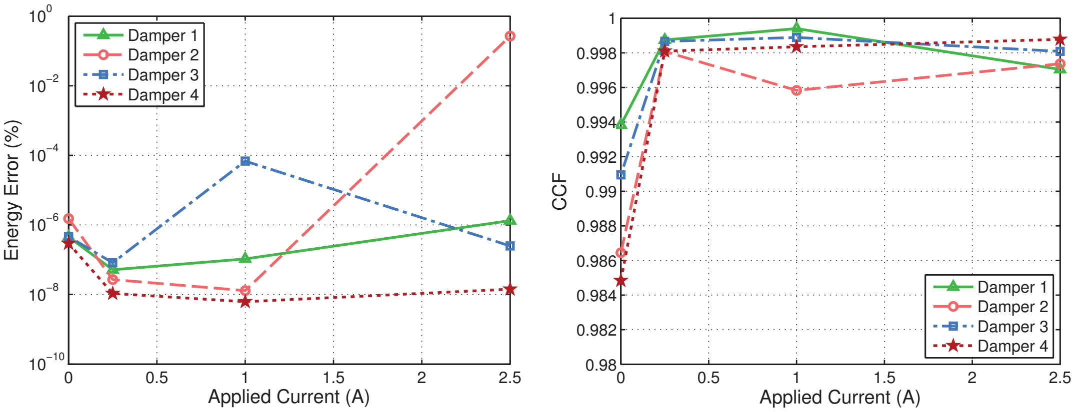

(a) Energy error. (b) Complex correlation coefficient.

Figure 5.6: MR damper model correlation metrics.

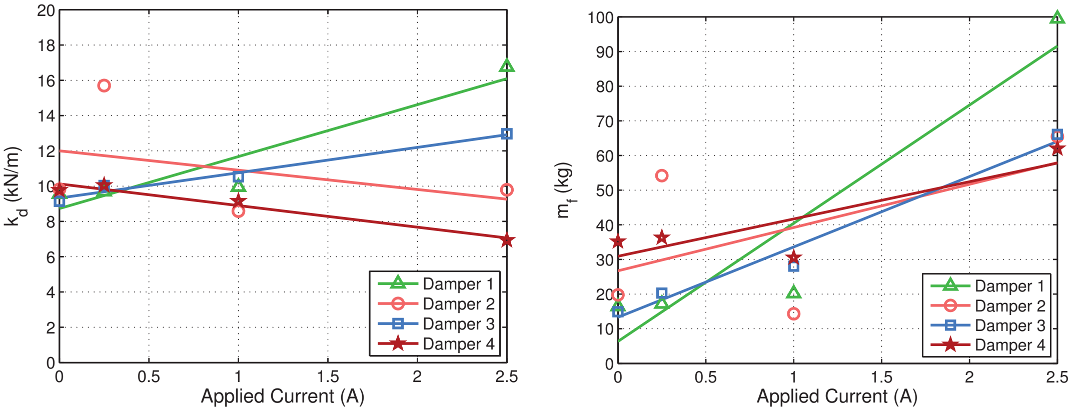

(a) Damper stiffness k_d.

(b) Fluid Inertia m_f.

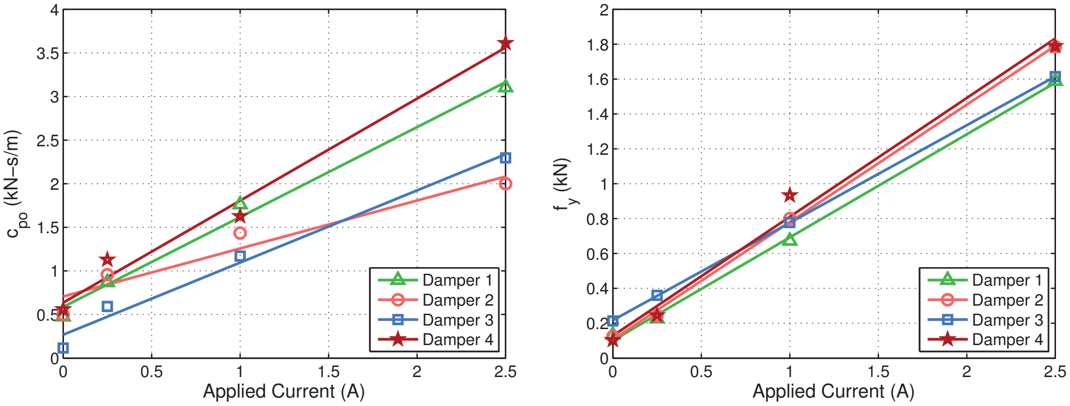

(c) Post-yield damping c_{po}.

(d) Yield force f_y.

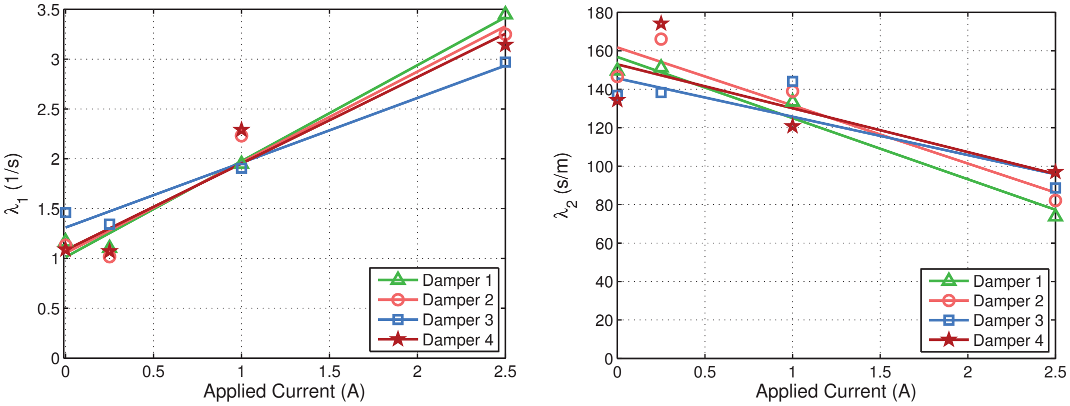

(e) Shaping parameter λ_1.

(f) Shaping parameter λ_2.

Figure 5.7: Damper model parameters evaluated at select applied currents and corresponding linear regression trends.

translational natural frequency (ie. stiffness) is set by the maximum allowable static deflection due to gravity, as the coil spring and MR damper must have adequate rattle space to move in without impinging on themselves or with the surrounding environment under normal operation. The natural frequency for a single DOF system is defined as

$$\omega_n = \sqrt{k_v/m_q}, \tag{5.6}$$

and with a mass $m_q = 136$ kg (300 lb) and a target natural frequency for translation in the vertical direction of $\omega_n = 2.2$ Hz, the required vertical stiffness $k_v = 26$ kN/m. The MR damper has an average stiffness $k_d = 10$ kN/m in figure 5.7(a), which when the damper is oriented at $\theta_d = 45^o$ to the horizontal, contributes 7.1 kN/m to the vertical direction. By taking the difference, the axial stiffness of the coil spring $k_a = 18.9$ kN/m (108 lb/in).

Knowing both the desired axial stiffness of the coil spring k_a, and the static stroke of the damper to be half of the total available stroke, a third consideration is roll-over stability. Crede [25] provides the following stability criteria for a spring-supported-mass system in order to prevent the mass from collapsing to the side:

$$\frac{k_l}{k_a} \geq \frac{1.2}{(l_o/\delta_s) - 1}, \tag{5.7}$$

where k_l is the lateral coil spring stiffness, l_o is the free (unloaded) length of the spring, and δ_s is the axial static deflection of the spring. Considering these three design criteria, the geometry of the coil spring is determined.

Figure 5.8 illustrates the configuration of the suspension leg. Static equilibrium

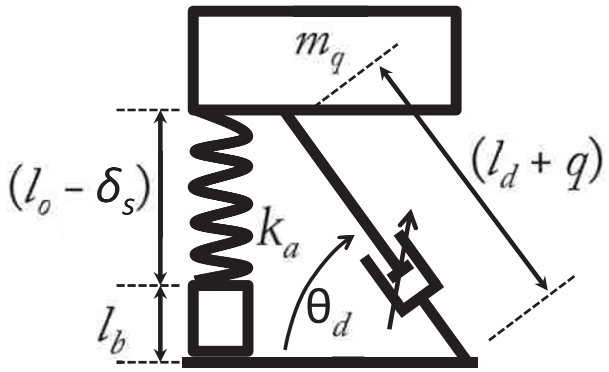

Figure 5.8: Suspension leg at static equilibrium.

of the payload occurs when the sum of the forces equals zero, so in the vertical direction

$$\begin{aligned} \sum F = 0 &= -m_q g + F_{spring} + F_{damper} \\ 0 &= -m_q g + k_a \delta_s - k_d q \sin(45^o) \end{aligned} \tag{5.8}$$

The relation between the static spring deflection δ_s (positive for compression) and the damper stroke q (negative for compression) is established by equating the vertical height of both the spring and damper, giving the following constraint:

$$l_b + l_o - \delta_s = (l_d + q)\sin(45^o), \tag{5.9}$$

where l_o is the free (unloaded) length of the spring, l_b is the height of any necessary mounting structure for the spring, and l_d is the fully extended damper length. The damper should statically rest at mid-stroke ($q = -3$ in, for a total available stroke of 6 in) to ensure adequate stroking in both compression and extension. Substituting equation 5.9 into equation 5.8 and rearranging,

$$l_b + l_o = \frac{m_q g + k_d q \sin(45^o)}{k_a} + (l_d + q)\sin(45^o). \tag{5.10}$$

Additionally, the axial stiffness of a coil compression spring is given by [59, 73] as

$$k_a = c_s \frac{G d_w^4}{8nD^3}, \tag{5.11}$$

where G is the torsional modulus of elasticity of steel (11.5×10^6 psi), d_w is the wire diameter, n is the number of coils, D is the average coil diameter, and c_s is the stress or curvature correction factor. The lateral stiffness of a coil compression spring is given by [73] as

$$k_l = \frac{1}{c_l} \frac{E d_w^4}{15nD(0.408(l_o - \delta_s)^2 + 0.53D^2)}, \tag{5.12}$$

where E is the tensile modulus of elasticity of steel (30×10^6 psi), l_o is the free (unloaded) length of the spring, and δ_s is the axial static deflection of the spring, and c_l is the lateral stiffness correction factor.

While observing the contraints imposed by equations 5.7, 5.10, 5.11, and 5.12, the spring's geometric properties d_w, n, D, l_o, and l_b can be found, given k_a, k_d, l_d, q, and m_q are all known. This is typically an iterative process which terminates once the stability criteria is satisfied.

The following properties were chosen for this design: $d_w = 0.5$ in, $n = 7.8$, $D = 5.18$ in, $l_o = 10.9$ in, and $l_b = 5.25$ in. These values offer an axial stiffness of

$k_a = 16.7$ kN/m (95.3 lb/in), and lateral stiffness $k_l = 8.5$ kN/m (48.5 lb/in), using a static deflection of $\delta_s = 1.66$ in, and correction factors $c_s = 1.15$, and $c_l = 1.3$.

5.2.2.1 Characterization

The axial stiffness of the coil spring was measured on an MTS 810 material testing system and was found to equal 19.6 kN/m (112 lb/in). This is larger than the theoretical axial value, but closely matches the desired value. The lateral stiffness was measured by installing the spring on a single-axis, lateral shake table seen in figure 5.9. The upper and lower sliding surfaces were constrained to only allow lateral motion. Figure 5.10 shows the lateral transmissibility of the suspension leg with only the coil spring installed (ie. no MR damper). This curve was obtained by exciting the base with a random white noise signal and measuring the relative accerleration magnitudes between the top and bottom sliding surfaces. Using this method, the undamped natural frequency of the leg, when loaded with a 300 lb mass, was determined to be 1.29 Hz, which corresponds to a lateral stiffness of 8.9 kN/m (51.0 lb/in), which is approximately the calculated theoretical value.

5.3 Performance Metrics

The ability of the suspension to attenuate base disturbances is evaluated using multi-objective performance criteria. The acceleration the payload is exposed to is important as it establishes a threshold to which the payload must be rated. The payload's CG and top corner were the two locations chosen to measure the accel-

Figure 5.9: Lateral 1-DOF shake table test stand.

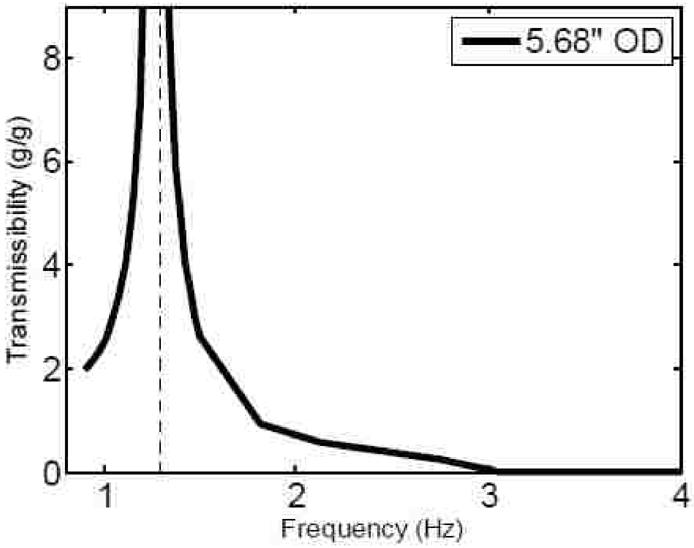

Figure 5.10: Lateral transmissibility of suspension leg, without the MR damper, for 300 lb mass.

eration along the body-fixed x, y, and z axes. The CG is of interest due to the sensitive payload being centered around this point, while the payload's top corner is also significant because the rotations of the payload are resolved through this point. However, for evaluating performance, the measured data at the CG was found to be qualitatively redundant with the data measured at the cabinet top corner. Therefore, only the data measured at the cabinet top corner will be discussed without any sacrifice to the analysis.

The total RMS acceleration is of interest because it gives an idea of the overall acceleration exposure, but all the frequency content is lumped into this single value. It is also desired to consider the RMS acceleration at the individual modal frequencies of the system. These can be determined by calculating the area under the x, y, and z axis PSD plots between specified frequency bands shown in figure 5.11. The width of the frequency bands was chosen to be 0.4 Hz wide for each mode. Additionally, the isolation performance at high frequency ($\approx$ 8 Hz) can be evaluated similarly. Each of these frequency-specific RMS acceleration values form a performance metric as defined in table 5.1. The frequency-specific metrics (m_1 - m_7) are simply a detailed look at the total RMS acceleration, metric m_8.

Several of the metrics incorporate data from multiple axes by combining the data together into a single value using either the function $f(x, y)$ or $f(x, y, z)$ in table 5.1, the latter of which refers to either the expression $\sqrt{x_{rms}^2 + y_{rms}^2 + z_{rms}^2}$ when considering the RMS value, where the subscript rms denotes the root mean square value along the corresponding axis, or the maximum value of the set $\{x_{max}, y_{max}, z_{max}\}$ when considering the maximum value, where the subscript max denotes the maxi-

Table 5.1: Performance metrics of the system.

Symbol	Description	Axis	Units	Type	Location
m_1	1st Rocking Mode	x	(g)	RMS accel.	Cabinet top corner
m_2	1st Rocking Mode	y	(g)		
m_3	2nd Rocking Mode	x	(g)		
m_4	2nd Rocking Mode	y	(g)		
m_5	Vertical Translation Mode	z	(g)		
m_6	Yaw Mode	f(x, y)	(g)		
m_7	High Frequency	f(x, y, z)	(g)		
m_8	Overall RMS accel.	f(x, y, z)	(g)		
m_9	Overall Max. accel.	f(x, y, z)	(g)	Max. accel.	
m_{10}	Impingement	f(x, y, z)	(in)	Max. relative displacement	

mum value along the corresponding axis. The function $f(x, y)$ is defined similarly.

Furthermore, the maximum acceleration and maximum relative displacement of the payload's top corner are also of interest. The maximum acceleration of the payload's top corner (metric m_9) establishes a threshold to which the payload must be rated above. Metric m_{10} is the maximum relative displacement of the payload's top corner in either the x, y, or z axis, which relates to the possibility of a collision between the payload and surrounding objects; however, this metric was not measured experimentally.

5.4 Control Gain Selection

Decentralized control was pursued for experimental testing, which was motivated by several factors. Decentralized control affords a modular design to accomodate payloads of varying mass and geometric size, allowing any number of suspension

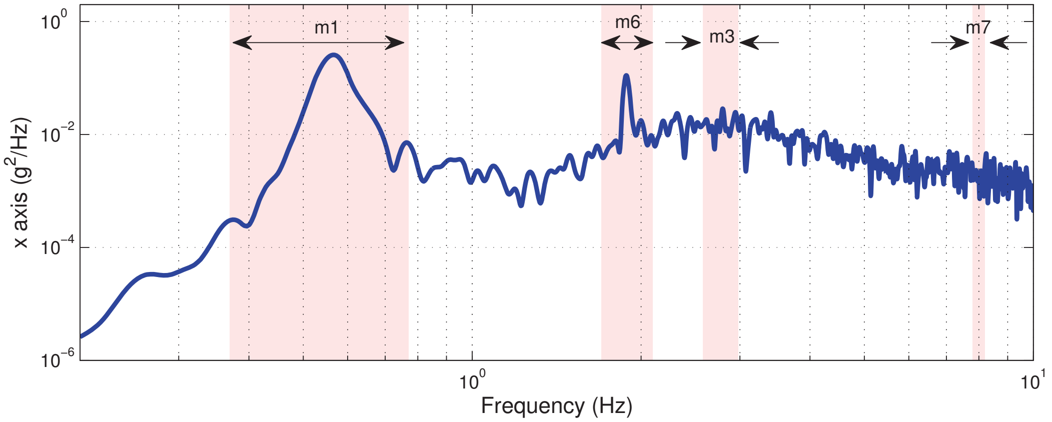

(a) x axis.

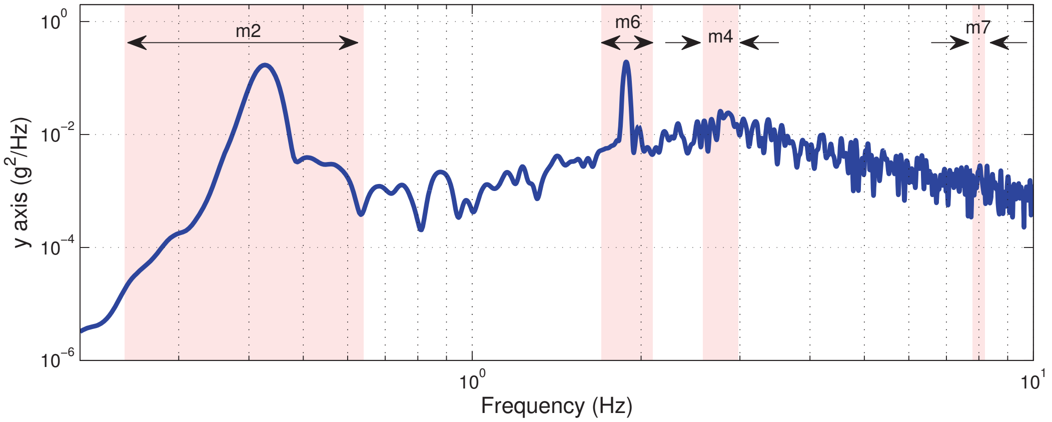

(b) y axis.

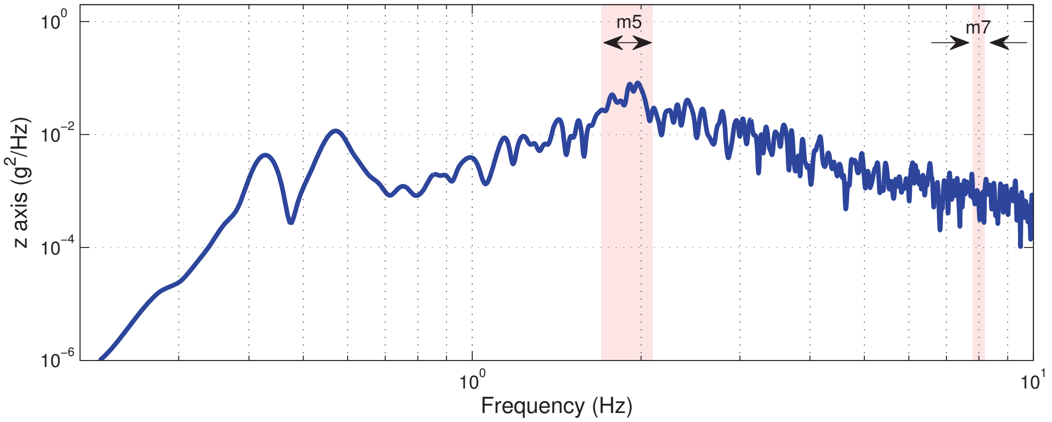

(c) z axis.

Figure 5.11: Representative PSD of the cabinet top corner along the x, y, and z axes illustrating the portions of data considered for each mode specific performance metric in the radar plots.

legs to be placed under the payload without concern about the full system dynamics, only the local dynamics. A decentralized system provides a fail-safe design, so the failing of one leg doesn't affect operation of the other components. Also, a decentralized system allows for a compact layout and packaging of the system's sensors and electronics.

The two decentralized control algorithms evaluated were the 'Skyhook' control, and 'Sliding Mode' control (SMC), which have been described in the previous chapter. The absence of control (ie. zero magnetic field) will be the third control condition and refered to as the 'Control Off' control.

Before testing the full 6-DOF system, the control laws were calibrated with a single suspension leg. The control law gains were determined from single-DOF testing in the vertical z axis direction. While this single-axis test condition does not fully represent the full system motion (ie. 6 DOF), it provided a simplified method to evaluate the control laws. Figure 5.12 shows the 1-DOF testing apparatus to constrain a single suspension leg to motion only in the veritcal direction.

The full system is designed with four suspension legs, so with a full system payload mass of 544 kg (1,200 lb), each suspension leg ideally supports a mass of 136 kg (300 lb), which is used for single-DOF testing.

The control gains were selected experimentally by minimizing performance metrics m_5 and m_7. Figure 5.13 shows the experimentally measured transmissibility of the single-DOF system obtained by exciting the test stand base with a transient signal. The minimized performance metrics are identified in figure 5.14 which correspond to control gains of G = 7,000 and G = 7.5 for the Skyhook and Sliding

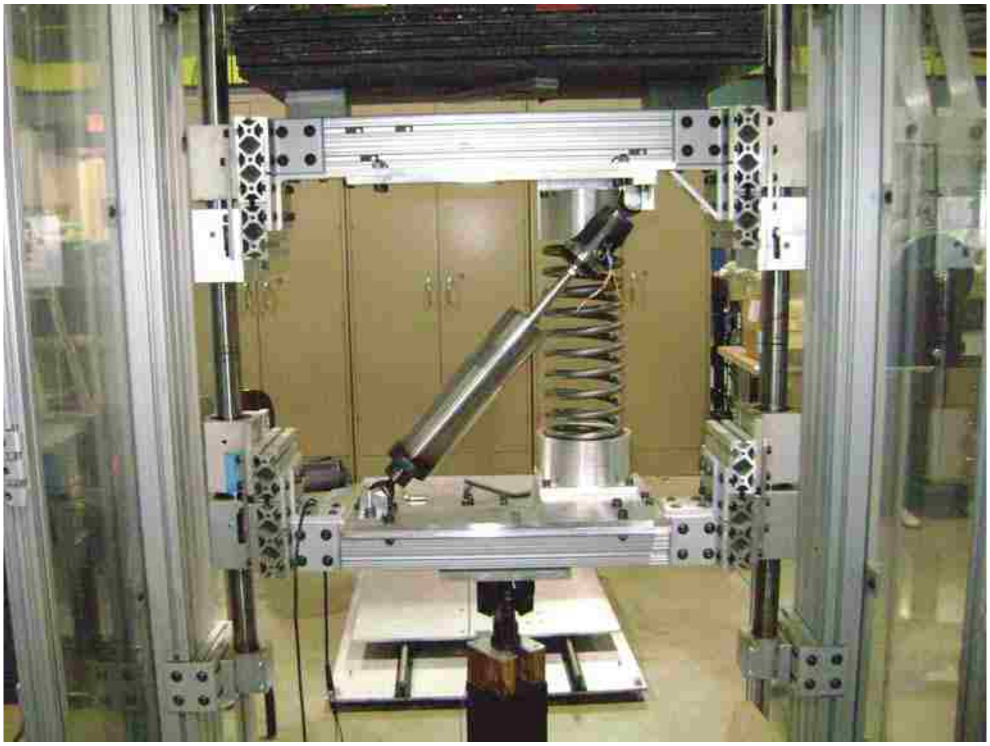

Figure 5.12: Vertical 1-DOF vibration test stand.

Mode control laws, respectively. Metric m_5 shows the controlled systems provide significant resonance attenuation over the Control Off system, however, metric m_7 is smallest for the Control Off system, which is a result of the parasitic damping induced by the control laws.

Figure 5.15 shows both the command electrical current and actual applied current signals, where the delay between the two signals was determined to behave as a first-order filter with a time constant of 25 ms. This time response delay causes undesired damping and is due to limitations of the electromagnetic circuit and power supply [30]. By reducing the delay the semi-active system would approach the performance of the Control Off system at high frequency. This is the standard trade-off between passive and semi-active control. Semi-active control is chosen to enhance performance at resonance while sacrificing some performance at higher disturbance frequencies. Indeed, a passive system would require large damping to match the resonance attenuation capabilities of the semi-active system, causing horrible high frequency performance as a consequence.

Figure 5.13 also shows the modeled transmissibility for the single-DOF system and captures the trend seen in the experimental data for each control law. Using the model, figure 5.16 shows the transmissibility of a passive system with large damping ($\zeta = 2.2$) that offers similar attenuation to that of the controlled systems at resonance (metric m_5 in figure 5.17). The large damping causes the performance metric m_7 in figure 5.17 to be much worse than the controlled systems.

Figure 5.16 also shows the response of a passive suspension, labeled 'Klembczyk', similar to one currently installed on the MLP [47], with a vertical natural frequency of 3.5 Hz and a damping ratio of 0.22. Here, the baseline 'Klembczyk' system has higher vertical stiffness than the semi-active system, increasing the resonant frequency and worsening both metrics.

5.5 6-DOF Experimental Testing

5.5.1 Suspension Configuration

The configuration of the semi-active suspension was selected considering several design criteria. A scalable design was desired to accommodate payloads of varying weight and geometric size. Cubic hexapod configurations are frequently used in 6-DOF manipulators and isolation devices [36, 70, 71], however a hexapod

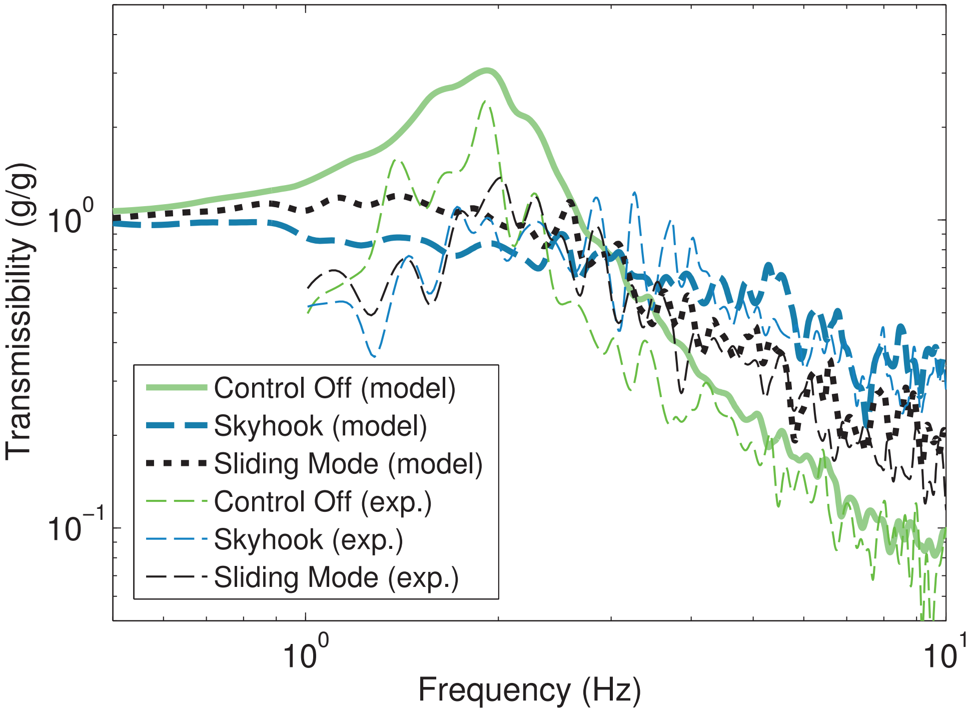

Figure 5.13: Measured and modeled vertical transmissibility of single-DOF leg suspension.

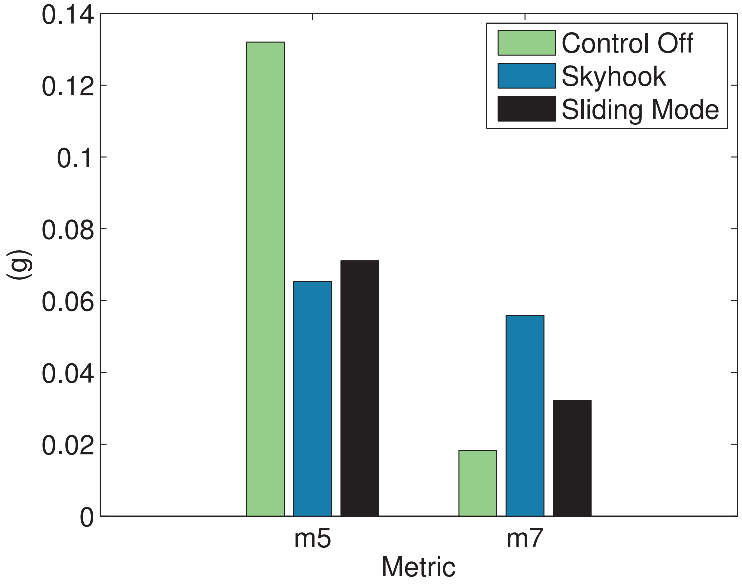

Figure 5.14: Performance metrics m_5 and m_7 from experimental PSD.

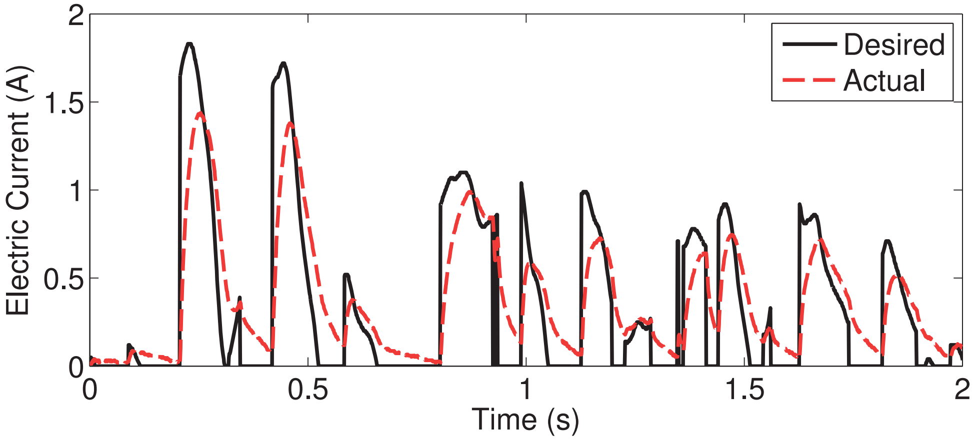

Figure 5.15: Desired and actual applied current experimentally measured from the IC electronics showing 25 ms delay.

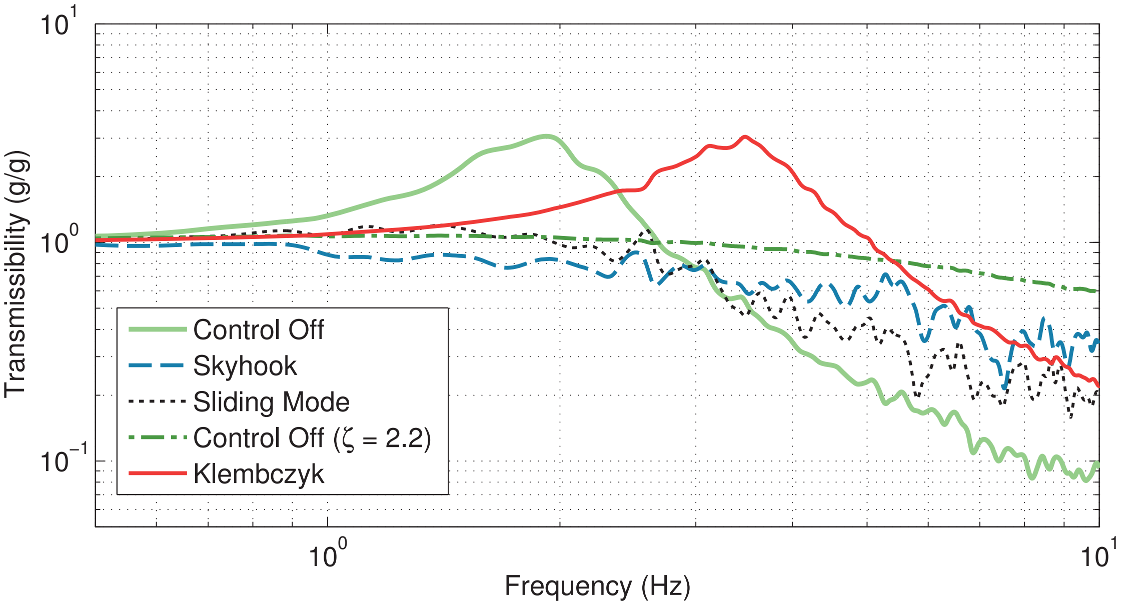

Figure 5.16: Modeled vertical transmissibility of single-DOF leg suspension.

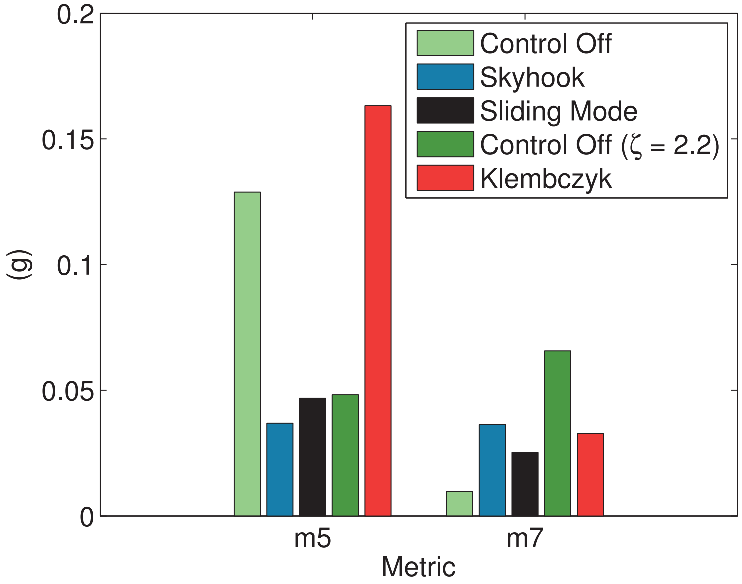

Figure 5.17: Performance metrics m_5 and m_7 from model.

configuration requires exactly six control linkages, which does not foster a scalable design and allow the addition or subtraction of support linkages. The ability to add or subtract individual leg subsystems from the suspension accommodates payloads of varying size and mass without the need to redesign a fixed number of MR dampers or springs. Furthermore, it was desired to govern the semi-active suspension with decentralized control to promote scalability and provide robust operation in the event of a subsystem failure.

A modular design approach was chosen and comprises of several individual suspension legs (one coil spring and one MR damper), each one governed with decentralized control. A modular approach entertains several ways the dampers and coil springs can be oriented underneath the payload. The following were the key criteria used to select the orientations: (1) It is desired to provide a geometrically compact design by keeping the suspension legs and hardware inside the payload planform footprint. (2) The springs should maximize the restoring moment of the system to resist against roll-over instability. (3) The MR dampers should be oriented in such a way to provide the maximum control authority over the motion of the payload. (4) Furthermore, the dampers should be oriented in a symmetric fashion to balance the stiffness forces associated with each. This is to ensure the dampers statically rest at mid-stroke to avoid an end-stop impact during operation.

Figure 6.1 shows the semi-active suspension, with four MR damper and coil spring pairs, installed underneath the payload. The four MR dampers are oriented at at right angles to one another and at 45 degree angles to the horizontal. This provides damping in all three orthogonal directions and symmetrically balances the static stiffness forces from each damper. The four coil springs are installed vertically at each corner of the payload to maximize the roll-over restoring moment. The semi-active MR dampers are not force generators unlike fully active actuators, necessitating the need for restoring springs. To avoid the possibility of the suspension collapsing to one side, the coil springs are not concentric with the linear-stroke dampers due to the spherical joint end connections of the damper, which allow only axial forces to be transmitted. Instead, the coil springs are oriented vertically with clamped end conditions to utilize the three-dimensional axial and lateral stiffness of each spring.

5.5.2 Experimental Setup

Full scale experimental testing was conducted using the GW-NSF Shake Table at the Earthquake Engineering Laboratory at George Washington University

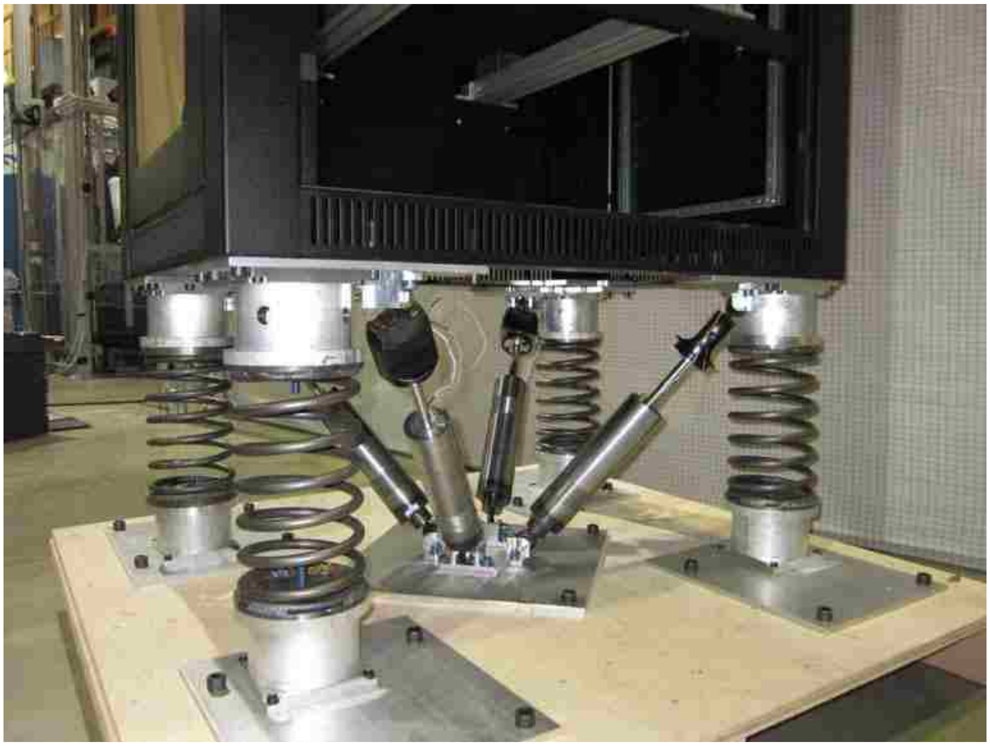

Figure 5.18: Pyramid configuration of suspension.

in Ashburn, VA, USA. This hydraulic powered shaker table, seen in figure 5.19, is equipped with six actuators (three oriented vertically and three oriented horizontally) that can apply dynamics loads (up to 80 kN), causing the platform to move. The platform surface measures 10 ft by 10 ft, and is capable of 6 DOF motion: translation and rotation in three-dimensional space.

A ENC21710S Hoffman seismic cabinet (with overall dimensions as 84.05 x 27.55 x 39.37 in) was selected as a representative GSE enclosure for the space shuttle, shown in figure 5.20(a), and was equipped to mount several 50 lb steel plates shown in figure 5.20(b), serving as the representative payload mass. Several mounting positions gave flexibility to adjusting the payload weight and center of gravity (CG) location. The mass of the payload was set as 544 kg (1,200 lb) and symmetrically distributed throughout the cabinet so that the center of gravity was located at 1/3 the cabinet height, measured from the bottom, and to give a diagonal moment of inertia tensor in the body frame such that $I_{xx} = 200 \text{ kg m}^2$, $I_{yy} = 214 \text{ kg m}^2$, $I_{zz} = 68 \text{ kg m}^2$, and the off-diagonal entries $I_{ij} = 0$, for $i \neq j$. Figure 5.21 shows the entire full-scale, semi-active suspension system installed underneath the GSE cabinet, where the MR dampers are oriented at 45^0 from vertical, sharing a common attachment point at the floor and attach toward the outer corners of the cabinet.

Figure 5.22 shows the integrated circuit (IC) control electronics boxes, or 'IC boxes'. These IC boxes monitor the displacement and acceleration sensors for each MR damper and serve to regulate the applied electric current to the damper coils. These IC boxes each have a fixed-point microcontroller, 6 g MEMS accelerometer, 70 g MEMS accelerometer, a damper stroke sensor circuit, an applied current monitoring circuit, data logging capability to a microSD card, and a digital signal processor which processes the necessry control algorithms based on the acceleration and displacement values and generates the required current for the MR damper. There is a current conditioning circuit that takes care of the rise and fall times of the current flowing through the damper so that optimum results are achieved. The power supply input passes through a current sensor before going to the boards, and as a result current is continuously monitored and appropriate action can be taken if the current increases beyond the desired value. An external buzzer is used to warn against any fault condition.

The data acquisition (DAQ) setup used for the experimental testing is shown in figure 5.23. Accelerations in all three x, y, and z axes were measured at three

Figure 5.19: GW-NSF hydraulic shake table at George Washington University.

locations shown in figure 5.20(b): the shaker table floor, the CG of the cabinet, and the top left rear corner of the cabinet. PCB Piezoelectronic, model #356A14, ICP® tri-axial accelerometers were used to measured acceleration. The measured acceleration data was read by a National Instruments® BNC-2110 DAQ adaptor and USB-6259 multifunction DAQ module, and recorded using the Data Acquisition toolbox available in Matlab®. The four MR dampers each had a decentralized integrated circuit (IC) control electronics box (or, 'IC box') which served to govern the applied current to the damper as well as record data specific to the damper. The data recorded by the four individual IC boxes was all synchronized in time together through a common power supply, in addition to being synchronized with the measured cabinet and floor acceleration data through the use of an additional accelerometer that was collocated with the accelerometer inside one of the IC boxes.

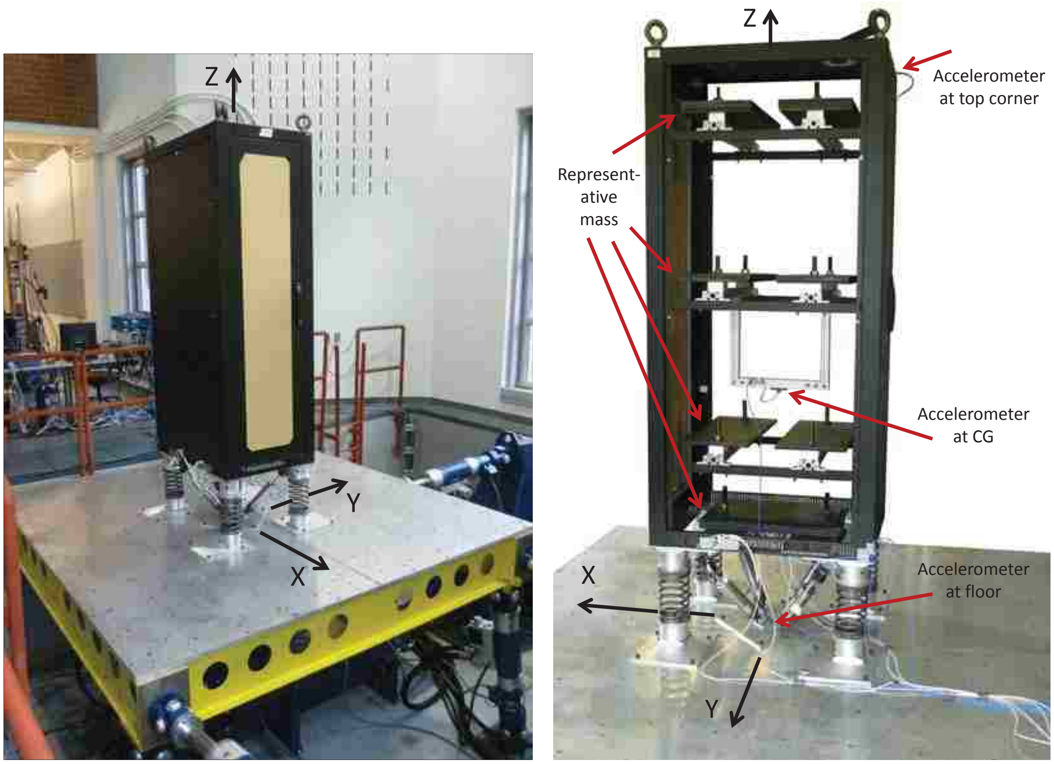

(a) Cabinet installed on 6 DOF hydraulic shaker table.

(b) Tri-axial accelerometer sensors and representative mass locations.

Figure 5.20: Fully instrumented GSE cabinet at test facility.

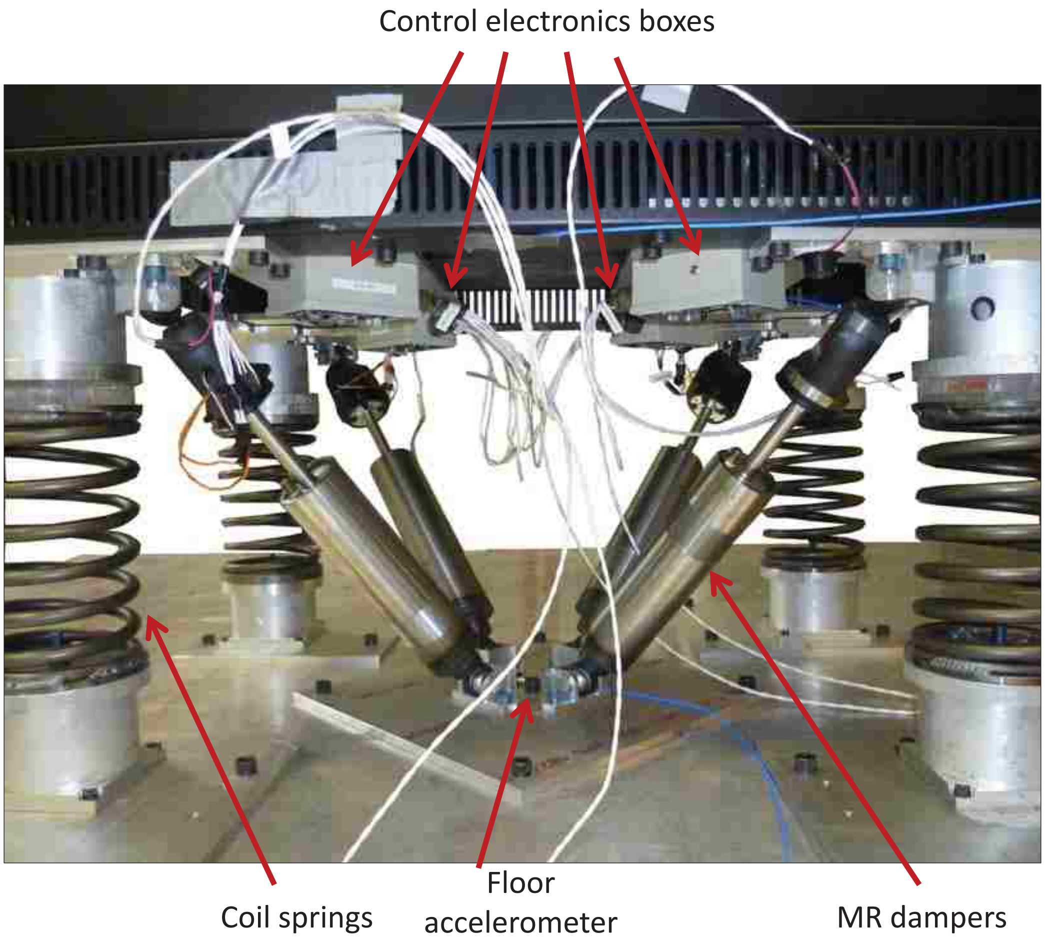

Figure 5.21: Semi-active suspension and IC control electronics underneath the GSE cabinet.

Figure 5.22: Integrated Circuit (IC) control boxes.

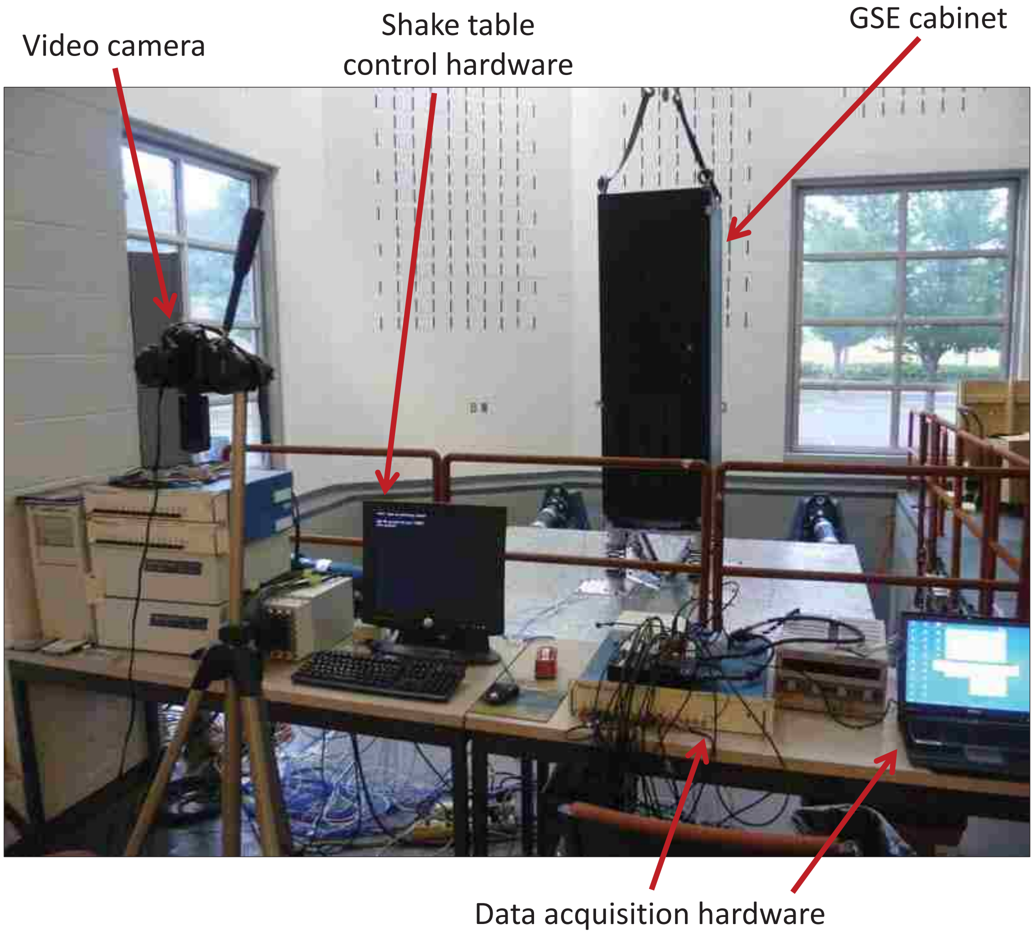

Figure 5.23: Data acquisition and experimental setup.

5.5.3 System Disturbances

Acceleration data measured on NASA's Space Shuttle Mobile Launch Platform (MLP) during the STS-31 (61-B) Shuttle launch was chosen as a representative vibration disturbance for the system. The acceleration data is from the floor structure to which a HIM (Hardware Interface Module) equipment rack is mounted inside the MLP (MLP-2, rm. 7A, mean), and the PSD of the data is shown in figure 5.24 for the three orthogonal x, y, and z axes. The 'Desired' line is the original PSD profile, where the 'Measured' line is the profile experimentally measured during the current testing which tries to match the 'Desired'. The power spectra is defined from 1 to 10 Hz, but the dominate frequency content lies between 4 to 10 Hz. Figure 5.25 shows the time domain displacement signals derived from the x, y, and z PSD profiles which are used as input floor disturbances to the system and will be referred to as the 'Representative (Rep.) Launch' excitation.

An additional disturbance is chosen to more uniformly characterize the system's behavior over a broader frequency range. White noise provides a uniform power spectra, without any dominant frequency content, over a wide frequency band, which is a desirable feature, allowing all frequencies to be excited with equal power. Using white noise as the input to the system is often performed to characterize the frequency response of a linear system for system identification. However, most real systems have nonlinearities (ie. friction), causing the output of the system to not be linearly proportional to the input. The behavior of a nonlinear system may be completely different depending on the magnitude of the frequency content.

Therefore it is important to characterize the system near the operating point of interest.

Three criteria were established to ensure the system was characterized near its operating point but to also ensure the system would not become unstable, causing the cabinet payload to toppled onto its side. These criteria were:

(1) The MR dampers must stroke a minimum of ± 0.25 in from their static position,

(2) the cabinet CG must not laterally translate beyond the horizontal perimeter established by the coil spring attachment points to the base floor,

(3) and the coil springs must not be extended or compressed more than their outer diameter (5.68 in).

With these criteria in mind, the mathematical model was used to select a qualifying disturbance and the PSD is shown in figure 5.26. Again, the 'Desired' line is the original PSD profile, where the 'Measured' line is the profile experimentally measured during the current testing. The magnitude of the PSD is linearly proportional to frequency, with the lowest frequency content defined at 0.2 Hz as 5×10^{-5} g^2/Hz and the highest frequency content defined at 10 Hz as 0.1 g^2/Hz. The positive slope of the PSD magnitude does not have a constant dB/octave value, unlike white noise (0 dB/octave) or blue noise (3 dB/octave), therefore this excitation will be referred to as 'Colored' noise. Figure 5.27 shows the time domain displacement signals derived from the x, y, and z PSD profiles which are used as input floor disturbances to the system.

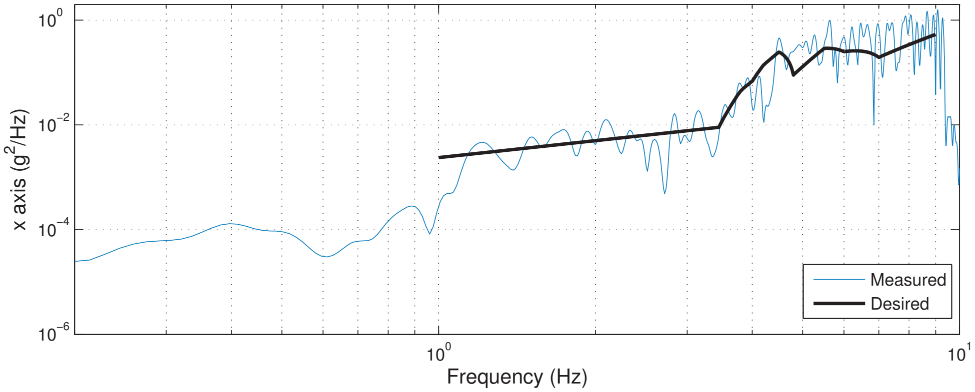

(a) x axis.

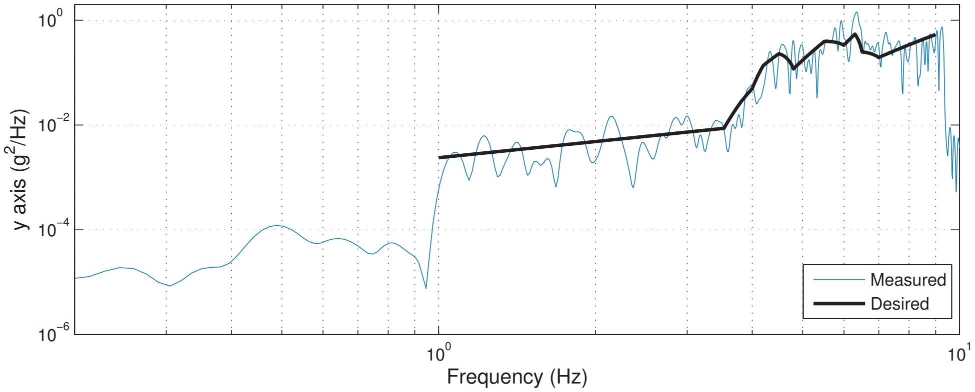

(b) y axis.

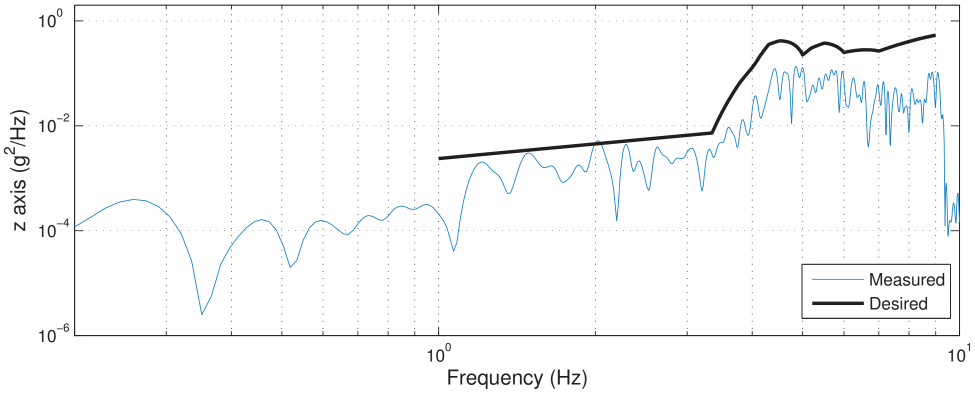

(c) z axis.

Figure 5.24: PSD of the Rep. Launch excitation: desired and measured.

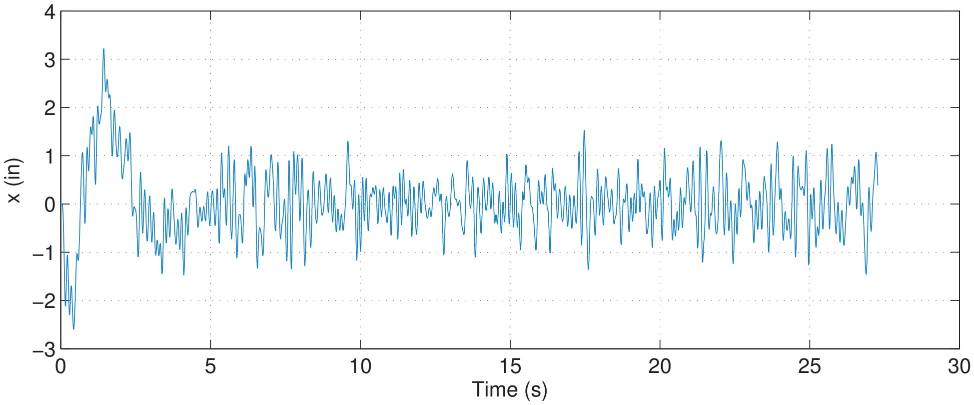

(a) x axis.

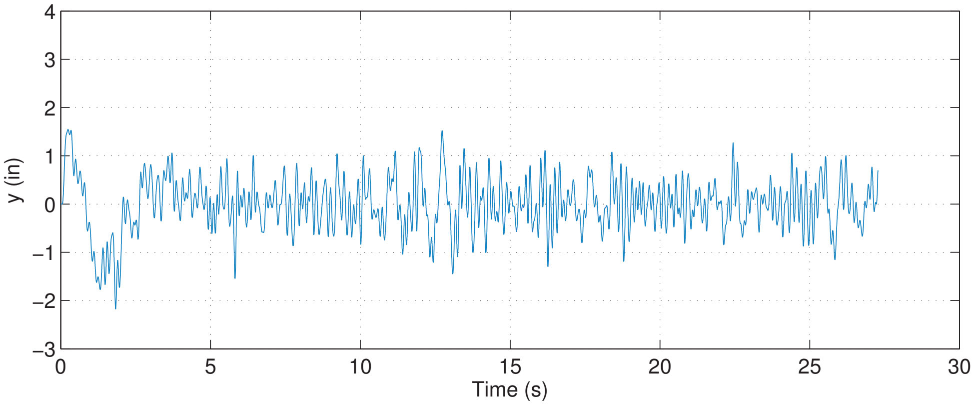

(b) y axis.

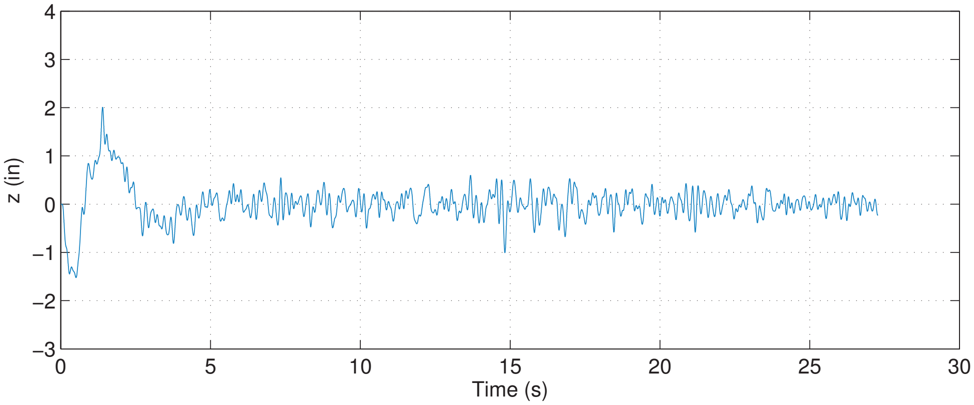

(c) z axis.

Figure 5.25: Measured floor displacement signal of the Rep. Launch excitation.

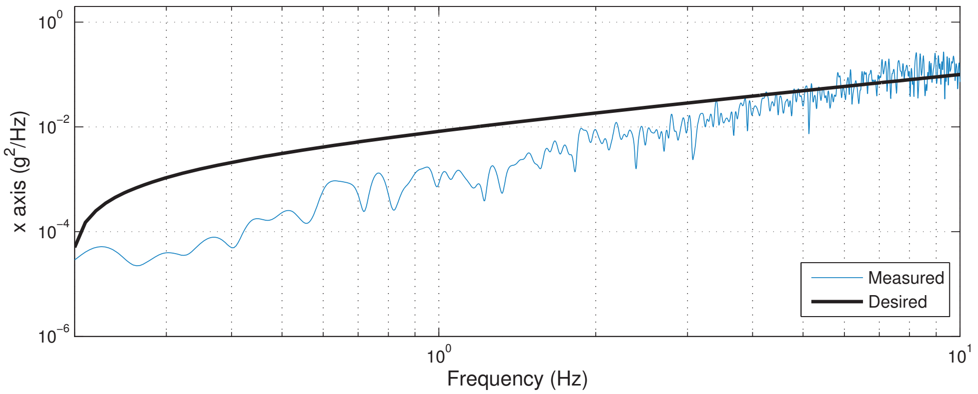

(a) x axis.

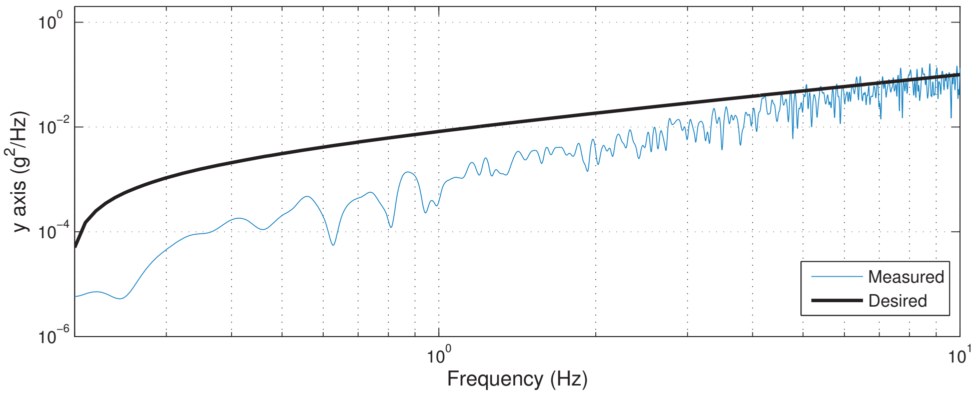

(b) y axis.

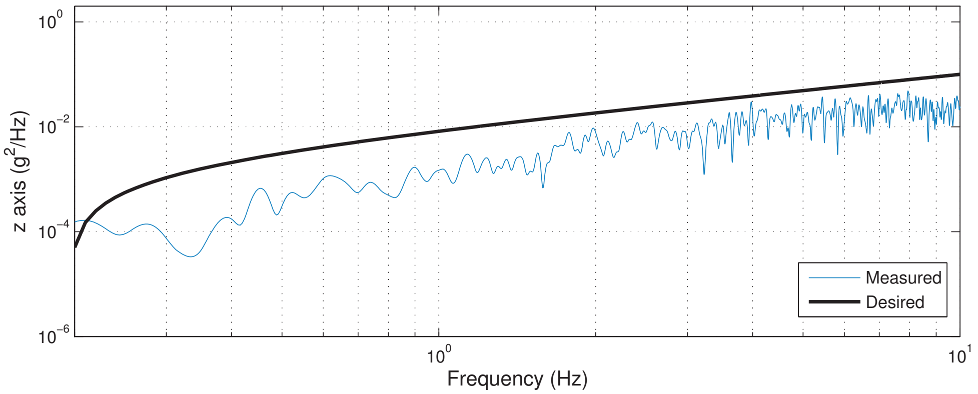

(c) z axis.

Figure 5.26: PSD of the Colored excitation: desired and measured.

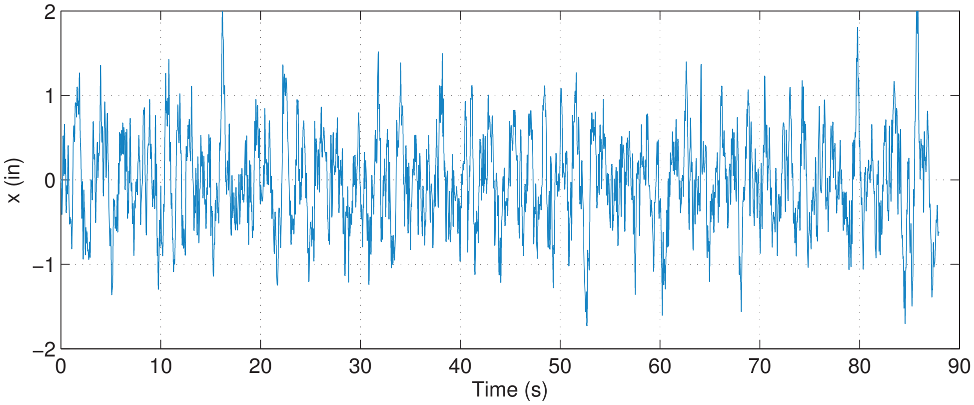

(a) x axis.

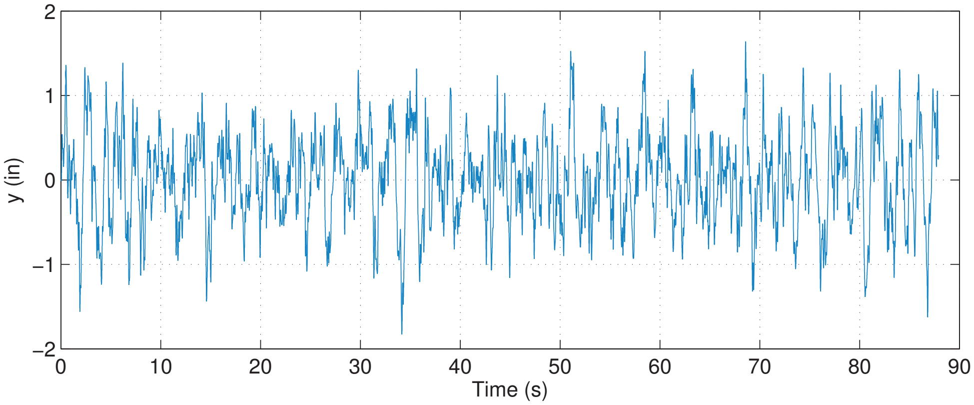

(b) y axis.

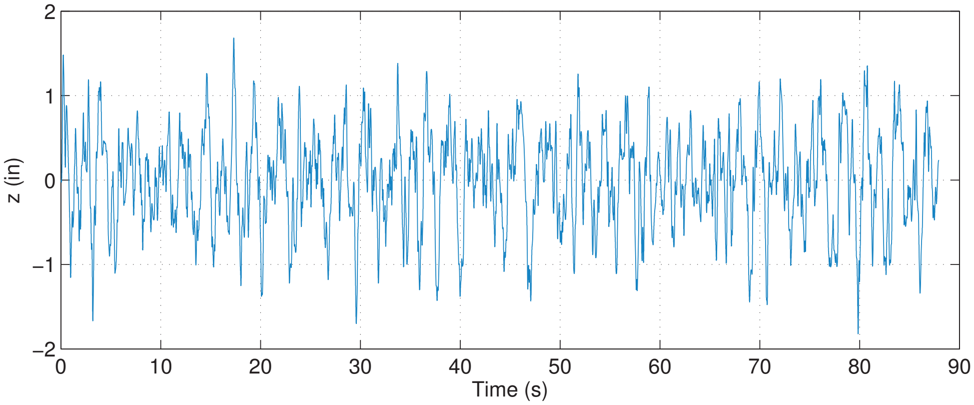

(c) z axis.

Figure 5.27: Measured floor displacement signal of the Colored excitation.

5.6 Results

The goal of the full-scale 6-DOF experimental testing was to both characterized the system behavior and demonstrate the isolaton performance of the semi-active suspension. Figure 5.21 shows the suspension instrumented with the control electronics underneath the GSE cabinet.

The system was characterized with the Colored disturbance, measuring the outputs while exciting the floor one axis at a time, allowing the full input/output response of the system to be identified. This was in order to decouple the system response from the behavior experienced when all three directions are excited simultaneously. Only the characterization tests required single floor axis excitation. All the other performance tests excited all three floor axes simultaneously. The Colored disturbance was used to characterize the system because it has a wide band of frequency content spanning all the natural frequencies of the system.

5.6.1 System Characterization

Figure 5.28 shows the measured transmissibility of the system along the x, y, and z axes at the cabinet top corner, in response to the Colored noise disturbance, with a cabinet weight of 1200 lb and the CG located at 1/3 of the cabinet height, capturing the full input/output response of the baseline GSE system.

There are several pronounced resonant features measured at the cabinet top corner in figure 5.28, the first of which is along the x axis at 0.4 Hz where neither Skyhook or SMC control algorithms are capable of attenuating this mode. This is the 1^{st} rocking mode of the system along the x axis and is attributed to a lack of damper stroke as the cabinet pivots about the common connection the dampers make with the floor instead of stroking the dampers. This motion, depicted in figure 5.32(e), degrades the control authority the dampers have on the payload and the ability to damp this mode.

At 1.9 Hz all three x, y, and z axes shows large resonances, where both control algorithms show modest attenuation along x and y directions and excellent attenuation along the z direction, with the Skyhook algorithm offering the best. The resonance along the z axis is the vertical translational mode, depicted in figure 5.32(a) and similar to a single-DOF system, while the x and y resonances are due to the same yawing mode, depicted in figure 5.32(d), which is excited by the vertical motion of the cabinet and caused by any dissymmetry in the moments applied by the dampers. It can be seen that the yaw mode is caused due to excitation along the vertical z axis.

Around 2.5 Hz the x and y axes show a less pronounced resonance where both control algorithms offer modest attenuation over the Control Off case. These resonances are the 2^{nd} rocking modes of the system, depicted in figures 5.32(f) and 5.32(c), respectively, and the dampers are capable of damping this mode due to the bottom of the cabinet moving in such a manner that requires the dampers to stroke, thus allowing a large amount of control authority.

The 1^{st} rocking mode along the y axis, depicted in figure 5.32(b), is not observed from the data in figure 5.28. This is attributed to that mode having a frequency below the frequency spectrum of the Colored disturbance, causing the mode to not be excited.

5.6.2 Performance Evaluation

5.6.2.1 Colored Disturbance

Figure 5.33 shows the measured PSD of the cabinet top corner along the x, y, and z axes in response to the Colored disturbance with a cabinet weight of 1,200 lb and the CG located at 1/3 the cabinet height (from here forward, all three base axes are excited simultaneously unless otherwise stated). Both controlled systems attenuate four out of the five excited modes defined in figure 5.32. The 1^{st} rocking mode along the x axis is the only excited mode not attenuated by the controlled system, resulting in similar acceleration magnitudes for both controlled and uncontrolled systems. Both SMC and Skyhook controls show similar amounts of attenuation at the resonant peaks in figure 5.33.

Figure 5.34 presents the performance metrics of the system in the form of a radar graph, which is a graphical method to display multivariate data. The data is categorized into performance metrics, as defined in table 5.1, and each metric corresponds to a radial spine of the radar graph which serves as the data axis for each metric, labeled m_i (for $i = 1, 2, ...$). The radial length of each data point along a spine is proportional to the magnitude of the data. Each set of data is connected with a line resulting in a polygon-type appearance. Metric m_2 is not included in figure 5.34 because the 1^{st} rocking mode along the y axis was not excited during testing.

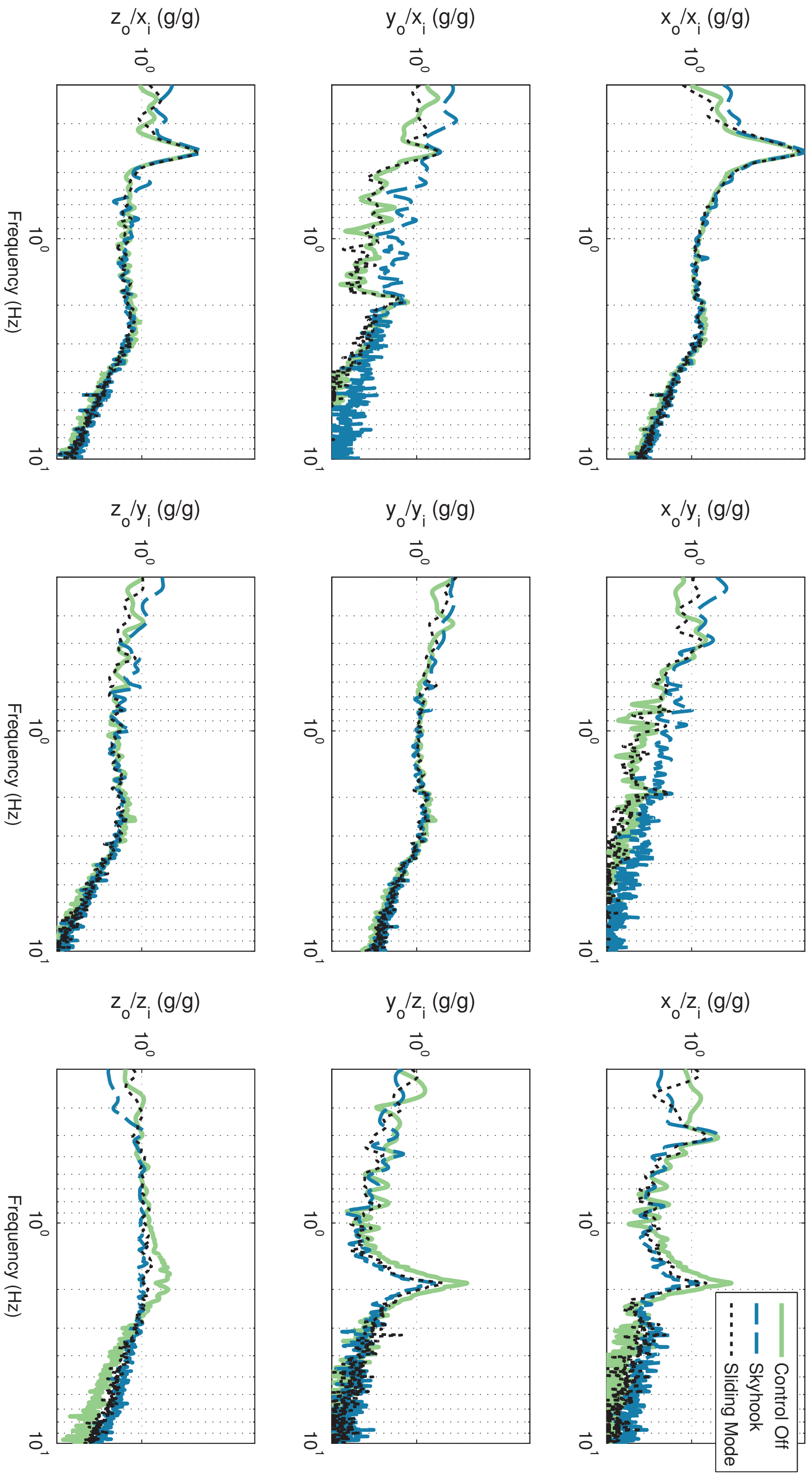

Figure 5.28: Measured transmissibility at the cabinet top corner from the floor input along the x, y, and z axes in response to the Colored excitation with a cabinet weight of 1200 lb and the CG located at 1/3 the cabinet height.

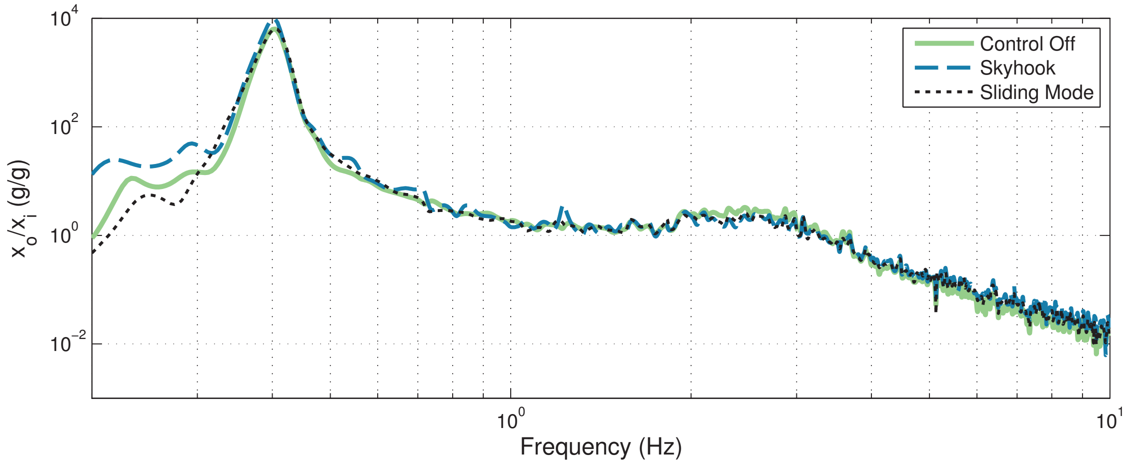

(a) .

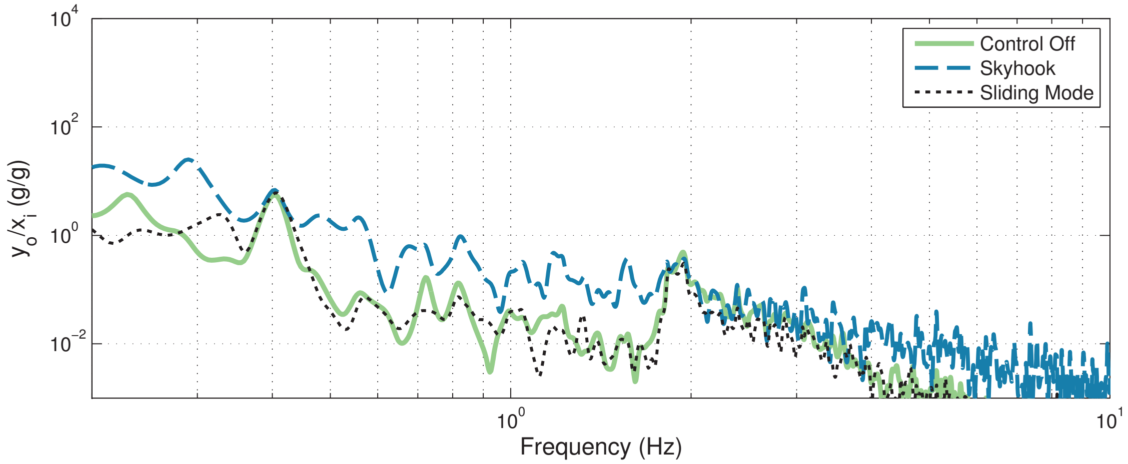

(b) .

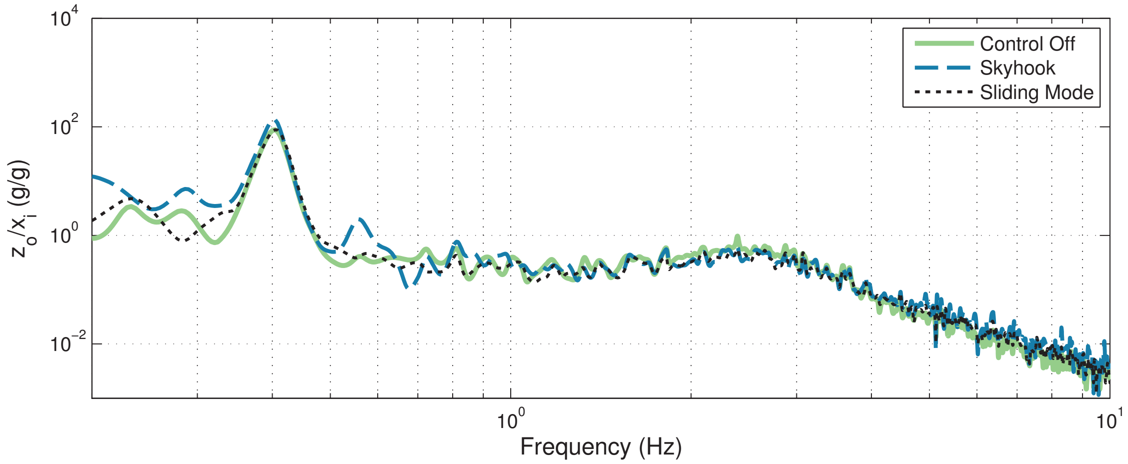

(c) .

Figure 5.29: Expanded view of figure 5.28. Excitation along only the floor x axis.

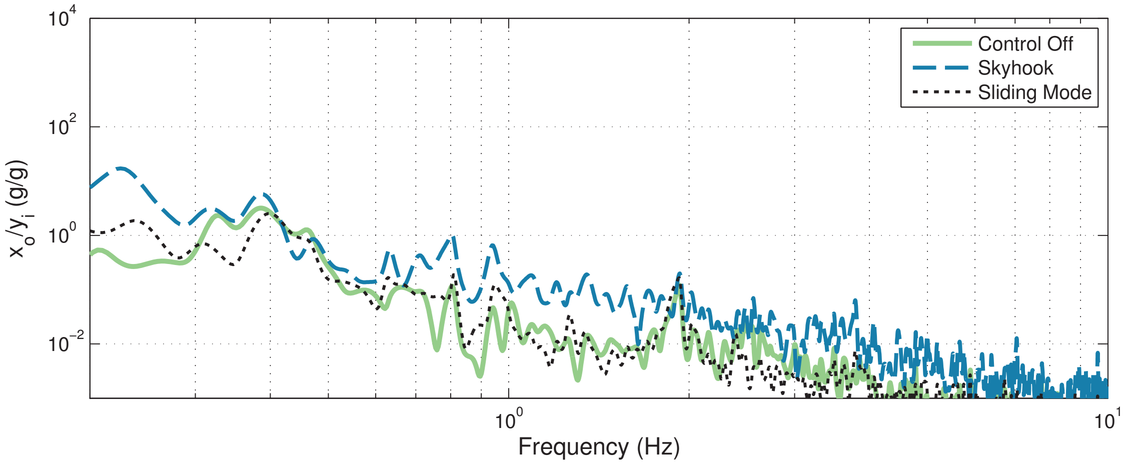

(a) .

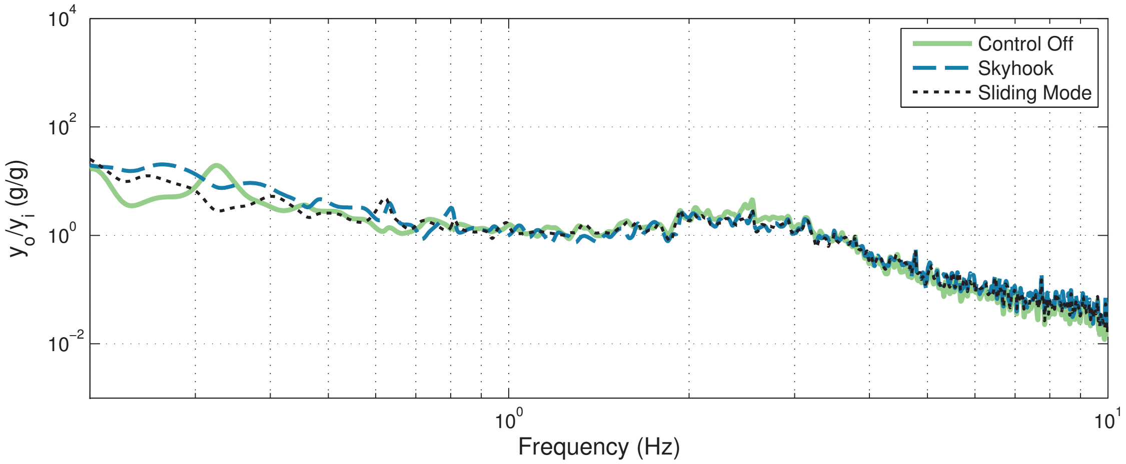

(b) .

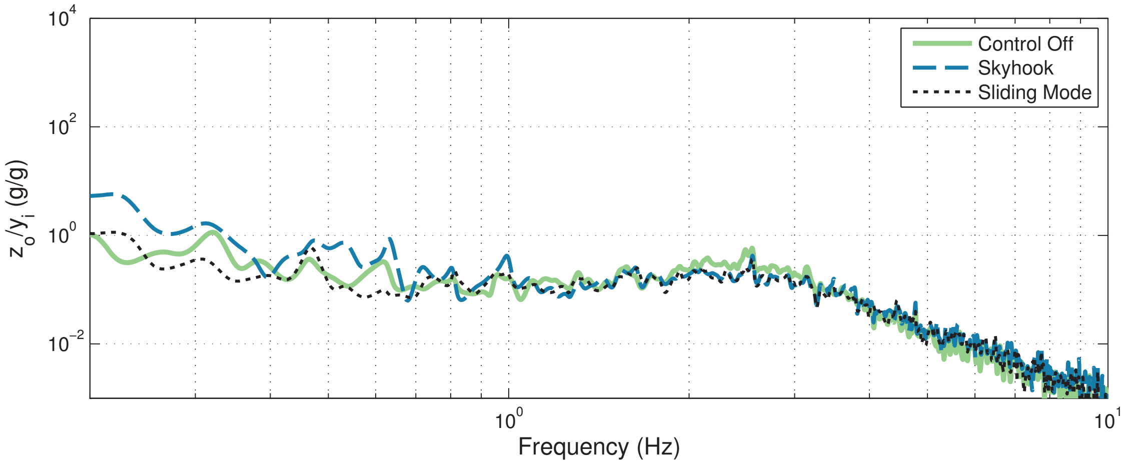

(c) .

Figure 5.30: Expanded view of figure 5.28. Excitation along only the floor y axis.

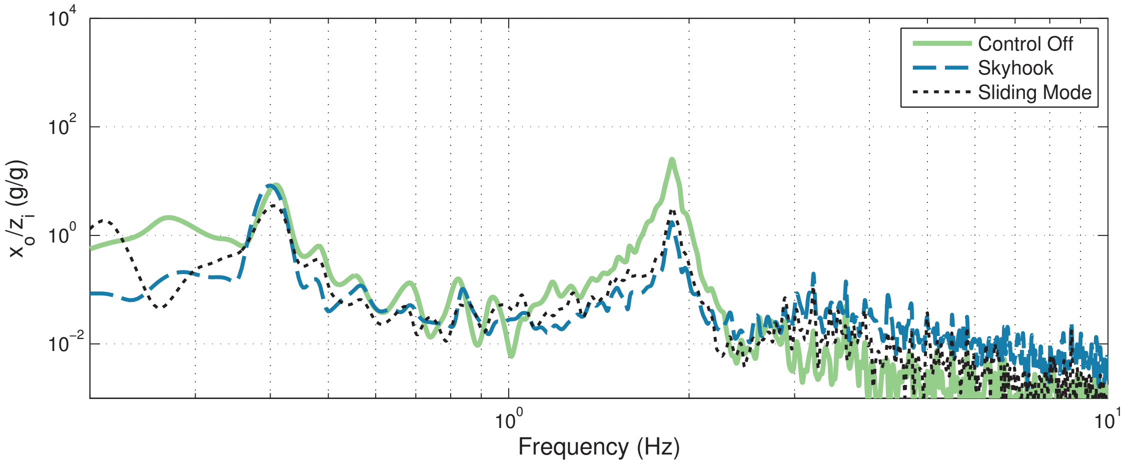

(a) .

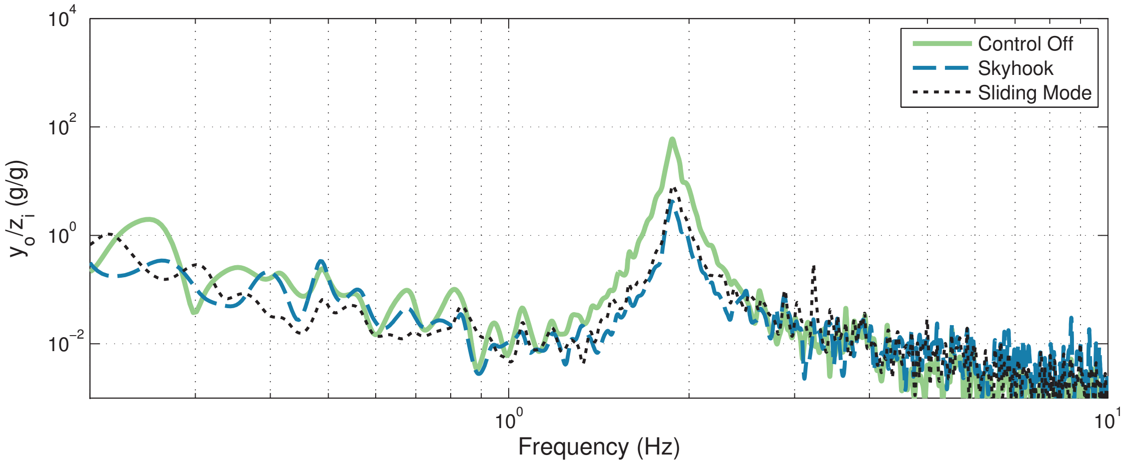

(b) .

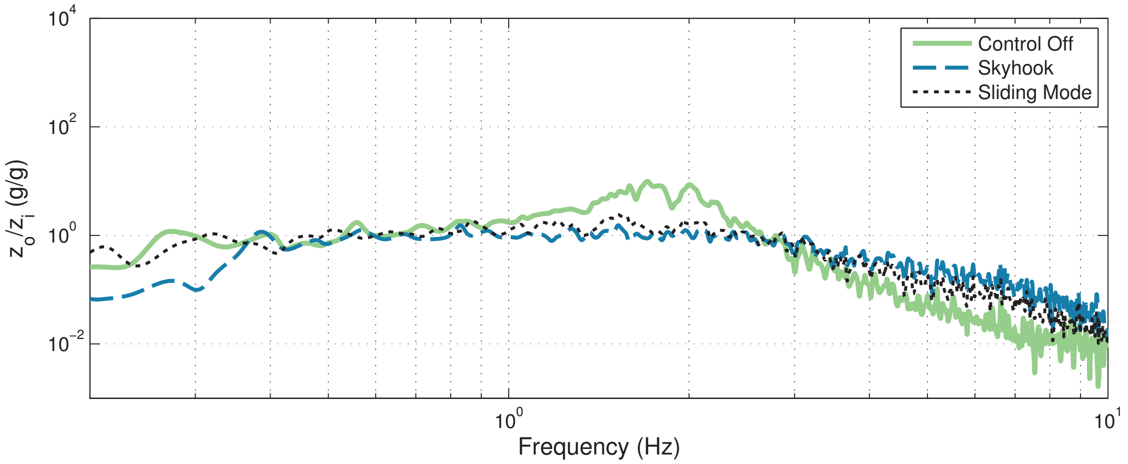

(c) .

Figure 5.31: Expanded view of figure 5.28. Excitation along only the floor z axis.

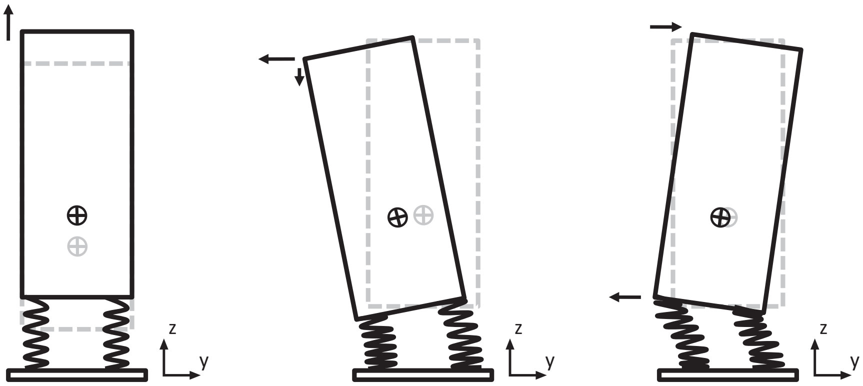

(a) Vertical translational mode.
(b) 1^{st} rocking mode along y axis.
(c) 2^{nd} rocking mode along y axis.

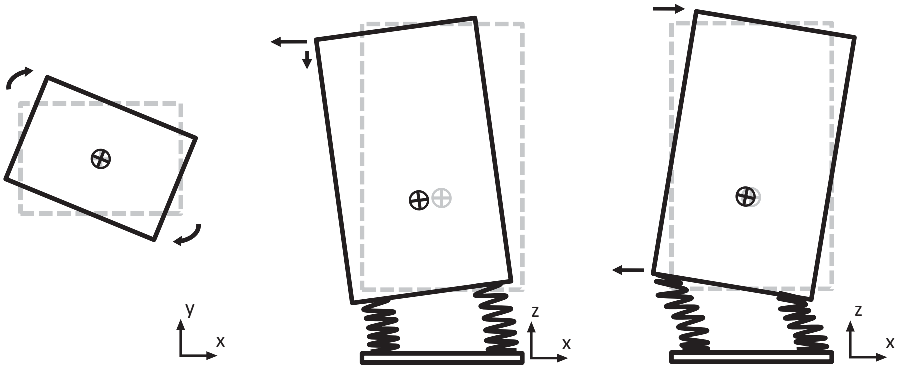

(d) Yaw mode.
(e) 1^{st} rocking mode along x axis.
(f) 2^{nd} rocking mode along x axis.

Figure 5.32: Mode shapes of the system.

Figure 5.34 shows the controlled systems have a smaller radar footprint at resonant disturbances (m_1, m_3, m_4, m_5, m_6), showing up to a 57% reduction in the performance metrics over the Control Off system, highlighting the enhanced vibration attenuation they offer. Also, the radar footprint for metric m_1 reiterates that both controlled systems have minimal control authority over the 1^{st} rocking mode along the x axis, sharing nearly the same level of acceleration as the Control Off system. However, the Control Off system has a smaller radar footprint for metric m_7 (up to 45% smaller compared to Skyhook control) due to better isolation at high frequency disturbances ($>$ 4 Hz) compared to the controlled systems which inherit a level of parasitic damping and degrade performance. The high frequency performance of each system has a more significant impact on the overall RMS acceleration transmitted to the cabinet because the Colored disturbance PSD is high frequency weighted. This explains why the Control Off system provides only slightly worse total RMS attenuation (m_8) compared to either controlled system. Indeed, this difference in performance would be even further magnified if the disturbance was low frequency weighted ($<$ 4 Hz), allowing the controlled systems to exhibit even greater attenuation compared to the Control Off system.

Table 5.2 shows the measured RMS and maximum accelerations along each axis, as well as the composite $f(x, y, z)$ values m_8 and m_9, respectively. The *Rigid* case represents the measured floor acceleration, or a fictitious rigid system with infinite stiffness. The Sliding Mode control offers the best isolation performance, providing the smallest total RMS and maximum acceleration at the cabinet top corner. In terms of the composite $f(x, y, z)$ values, the Control Off system offers

Table 5.2: Measured performance of the system in response to the Colored excitation with a cabinet weight of 1,200 lb and CG location at 1/3 the cabinet height (*red* indicating the control with largest reduction).

		Cabinet Top Corner			
		RMS		Maximum	
Control	Axis	(g)	% Reduction from Rigid	(g)	% Reduction from Rigid
Rigid	x	0.786	0	3.46	0
	y	0.608	0	2.98	0
	z	0.394	0	2.11	0
	f(x,y,z)	1.07	0	3.46	0
Off	x	0.307	60.9	1.38	60.1
	y	0.302	50.3	1.14	61.7
	z	0.233	40.9	0.863	59.1
	f(x,y,z)	0.489	54.3	1.38	60.1
Sky	x	0.306	61.1	1.26	63.6
	y	0.282	53.6	1.52	49.0
	z	0.217	44.9	2.48	-17.5
	f(x,y,z)	0.469	56.2	2.48	28.3
SMC	x	0.287	**63.5**	1.04	**69.9**
	y	0.26	**57.2**	1.08	**63.8**
	z	0.196	**50.3**	0.715	**66.1**
	f(x,y,z)	0.434	**59.4**	1.08	**68.8**

the worst RMS isolation at the top corner, albeit only slightly worst (within 5% of the controlled systems). The SMC control reduced the total transmitted RMS acceleration (m_8) to the cabinet top corner by 59%, and in terms of maximum acceleration (m_9), the SMC control provided reductions to the cabinet top corner by 69%. The Skyhook control offers the worst maximum acceleration at the top corner due to a single, large, transient z axis acceleration shown in figure 5.35.

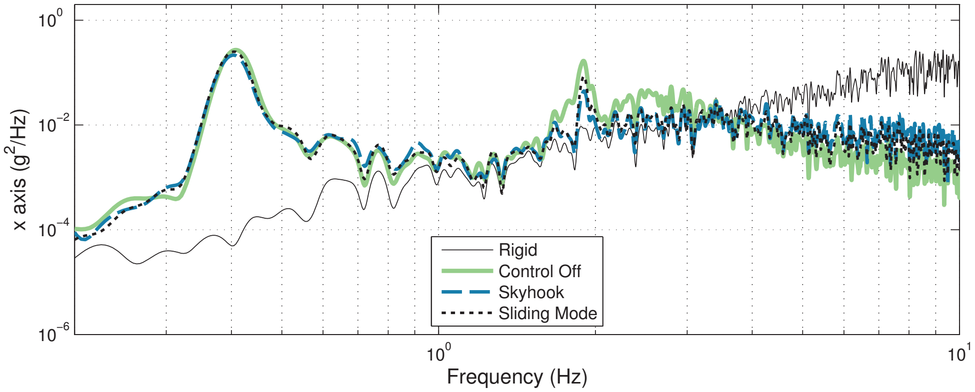

(a) x axis.

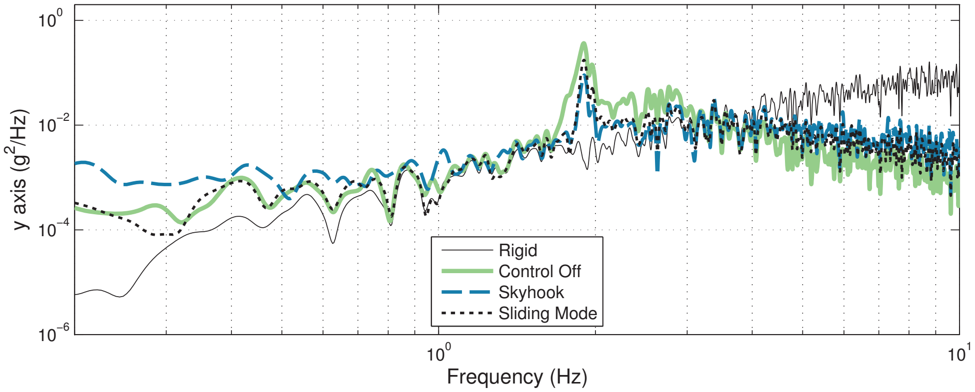

(b) y axis.

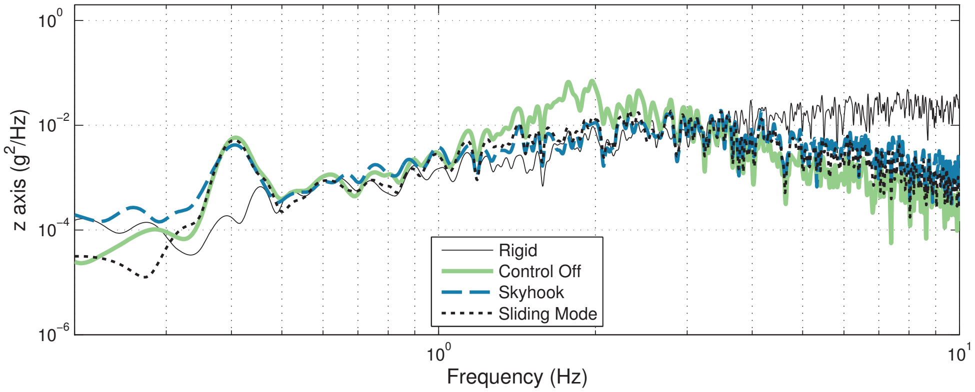

(c) z axis.

Figure 5.33: Measured PSD of the cabinet top corner along the x, y, and z axes in response to the Colored excitation with a cabinet weight of 1,200 lb and the CG located at 1/3 the cabinet height.

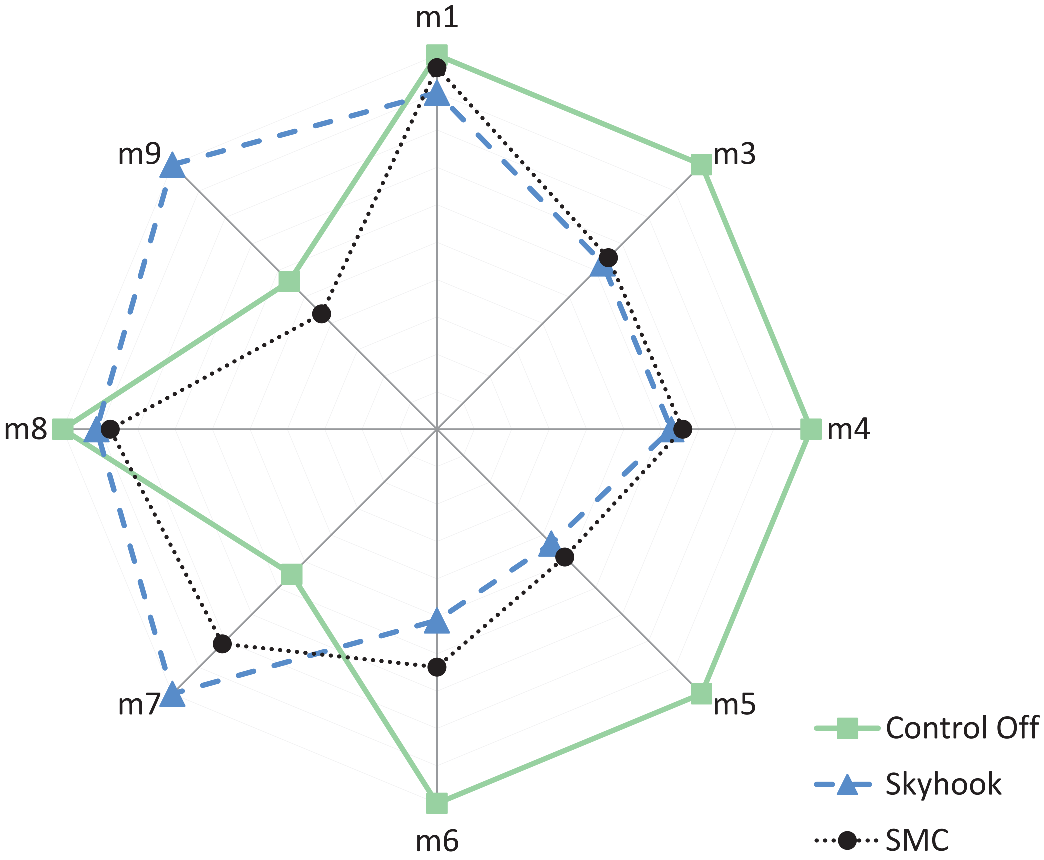

Figure 5.34: Radar plot of the performance metrics in response to the Colored excitation with a cabinet weight of 1,200 lb and the CG located at 1/3 the cabinet height.

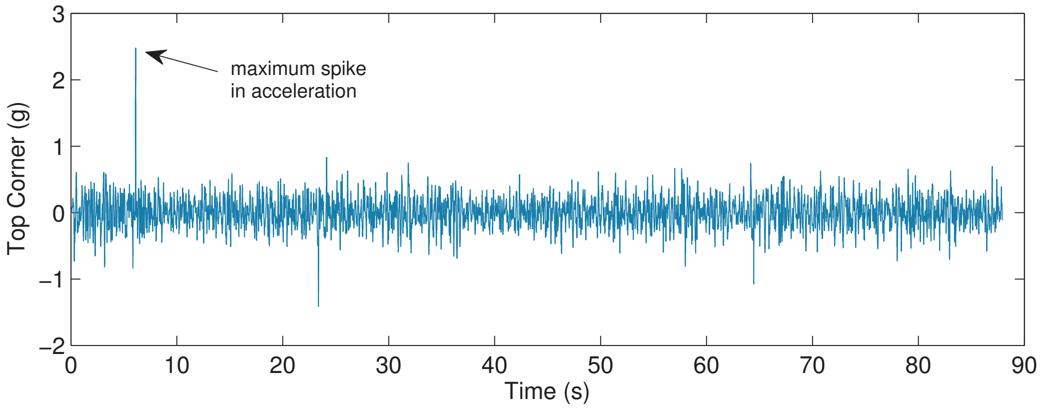

Figure 5.35: Measured z axis acceleration signals at the cabinet top corner for Skyhook control.

5.6.2.2 Representative Launch

Figure 5.36 shows the measured PSD of the cabinet top corner along the x, y, and z axes in response to the Rep. Launch excitation with a cabinet weight of 1,200 lb and the CG located at 1/3 the cabinet height. It can be seen that both the Skyhook and SMC controlled systems provided similar performance and showed improved attenuation compared to the Control Off system near 2 Hz, along all three x, y, and z axes. Again, the controlled systems do not attenuate the 1^{st} rocking mode along the x axis, and the Control Off system provides better high frequency ($>$ 4 Hz) isolation.

Figure 5.37 shows the controlled systems (Skyhook and SMC) have a smaller radar footprint at resonant disturbances (m_1, m_3 - m_6), highlighting the enhanced vibration attenuation they offer at resonance compared to the Control Off system. However, the Control Off system again has a smaller radar footprint for metric m_7 due to better isolation at high disturbance frequencies ($>$ 4 Hz) compared to the controlled systems. Also, the radar footprint for metric m_1 reiterates that both controlled systems have minimal control authority over the 1^{st} rocking mode along the x axis, sharing nearly the same level of acceleration as the Control Off system.

Table 5.3 shows the measured RMS and maximum accelerations along each axis, as well as the composite $f(x, y, z)$ values m_8 and m_9, respectively. Both controlled and uncontrolled systems provide substantial attenuation along all three axes from the 'Rigid' floor excitation, while the Control Off system offers the best performance in terms of the composite $f(x, y, z)$ values. The Control Off system reduced the transmitted RMS acceleration (m_8) to the cabinet top corner by 72%, and the maximum acceleration (m_9) by 76%. The Sliding Mode control offers the next best performance (only slightly worse than Control Off), while the Skyhook control offers the worst performance for metrics m_8 and m_9.

The Control Off system provides the best total RMS acceleration (m_8) because the Rep. Launch disturbance is dominated by high frequency content above 4 Hz (larger than the Colored disturbance), which is above all of the resonant frequencies of the system ($<$ 3 Hz). However, this obfuscates the benefits of the controlled system. The semi-actively controlled system approaches the level of isolation of the lightly damped passive system at high frequency, but has the added benefit of attenuating vibration at the resonant frequencies of the system. At frequencies far above resonance the semi-actively controlled system tries to mimic the behavior of the Control Off system; however, due to the algorithm of the control law and time delays in the application of the desired control, the controlled system adds parasitic damping and degrades isolation. The Rep. Launch excitation considered here is only a single disturbance to which the system may be exposed, while another disturbance may contain more lower frequency content (ie. different Shuttle launch, or during ground transportation of the Shuttle), allowing the controlled system to offer superior isolation.

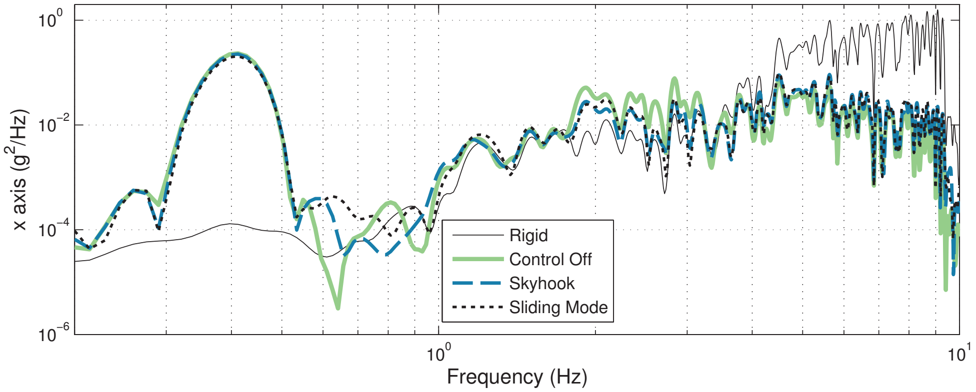

(a) x axis.

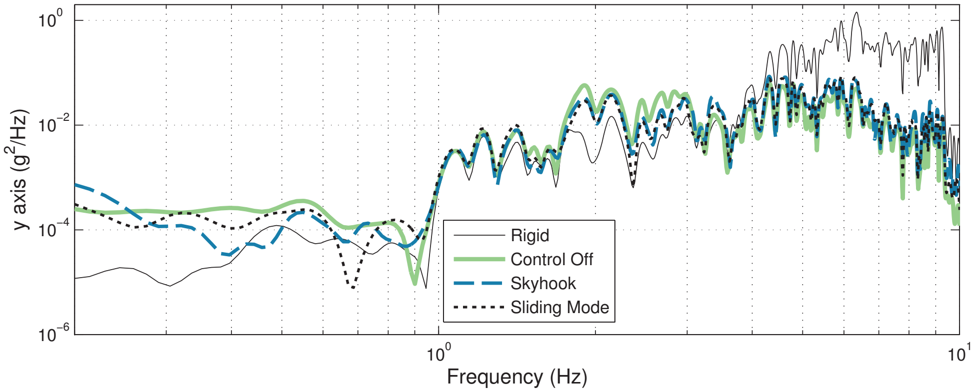

(b) y axis.

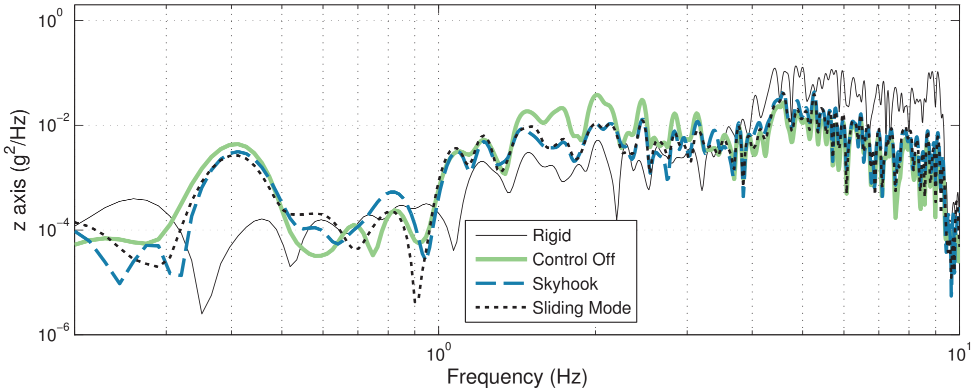

(c) z axis.

Figure 5.36: Measured PSD of the cabinet top corner along the x, y, and z axes in response to the Rep. Launch excitation with a cabinet weight of 1,200 lb and the CG located at 1/3 the cabinet height.

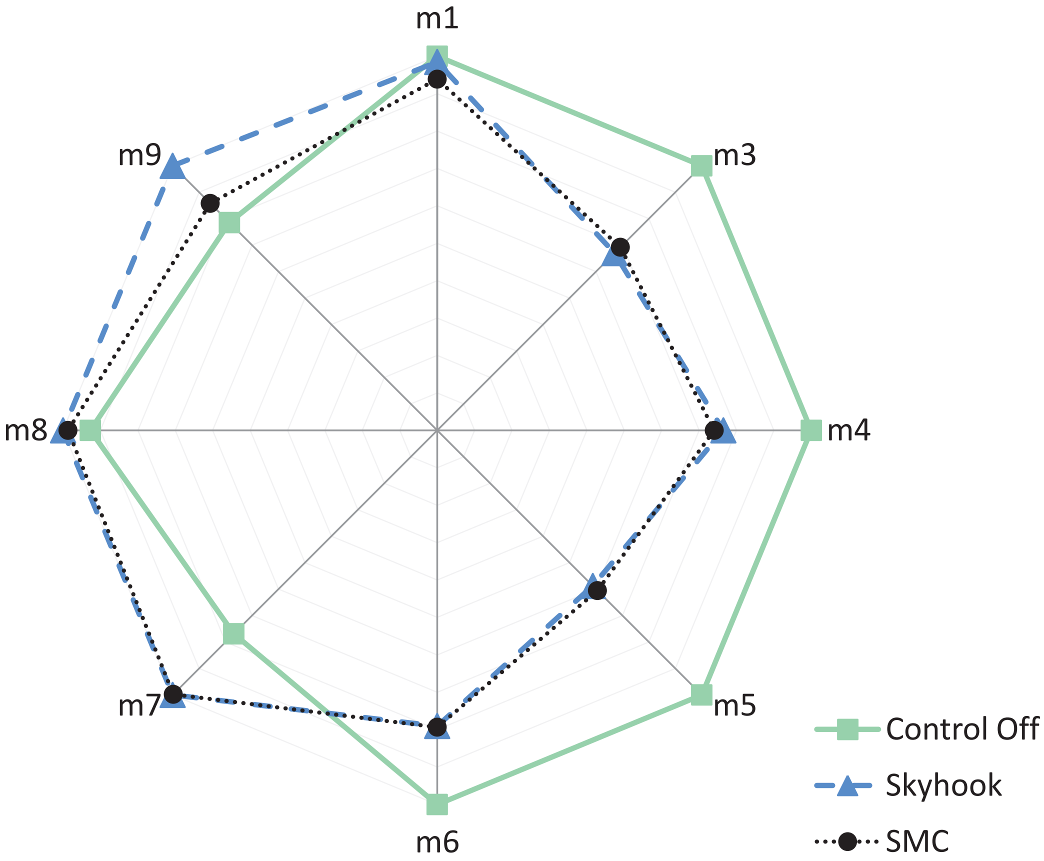

Figure 5.37: Radar plot of the performance metrics in response to the Rep. Launch excitation with a cabinet weight of 1,200 lb and the CG located at 1/3 the cabinet height.

Table 5.3: Measured performance of the system in response to the Rep. Launch excitation with a cabinet weight of 1,200 lb and the CG location at 1/3 the cabinet height(*red* indicating the control with largest reduction).

		Cabinet Top Corner			
		RMS		Maximum	
Control	Axis	(g)	% Reduction from Rigid	(g)	% Reduction from Rigid
Rigid	x	1.59	0	5.71	0
	y	1.3	0	5.2	0
	z	0.494	0	1.87	0
	f(x,y,z)	2.11	0	5.71	0
Off	x	0.408	**74.3**	1.36	**76.2**
	y	0.348	**73.2**	1.32	**74.6**
	z	0.244	**50.6**	0.807	56.8
	f(x,y,z)	0.59	**72.0**	1.36	**76.2**
Sky	x	0.437	72.5	1.51	73.6
	y	0.396	69.5	1.73	66.7
	z	0.258	47.8	0.84	55.1
	f(x,y,z)	0.644	69.5	1.73	69.7
SMC	x	0.426	73.2	1.41	75.3
	y	0.385	70.4	1.48	71.5
	z	0.247	50.0	0.802	**57.1**
	f(x,y,z)	0.625	70.4	1.48	74.1

5.7 Model Validation

The mathematical model was validated using the experimental data measured in response to the Colored disturbance. Figure 5.38 shows the PSD of the base disturbances for both the model and experiment along the x, y, and z axes. The 'Experiment' curve is from acceleration data measured at the base of the shake table. The 'Model' curve is calculated from displacement data measured by sensors installed on the hyraulic actuators of the shake table. Both PSD curves match closely, but are not exactly the same because they originate from different measurements. For simulation, the mathematical model requires knowledge of the base velocity and displacement, in addition to acceleration. It was found that integrating the acceleration signal to obtain displacement resulted in poor accuracy due to small levels of noise in the measured acceleration signal causing large cumulative errors in displacement (ie. drift effect). Alternatively, it was found that differentiating the measured base displacement signal to obtain acceleration gave accurate results. Thus, the measured base displacement was chosen as the input to the model.

Figure 5.42 summarizes the performance metric values in table 5.4 for the rigid system and gives a detailed comparison of the agreement between the model and experiment. The agreement is good for all metrics. Furthermore, the difference in total RMS acceleration (m_8) is only 2%. This error is due to measurement noise, and since the base disturbance is the input into the system, indicates a level of accuracy between model and experiment.

Figures 5.39 - 5.41 show the measured PSD of the cabinet top corner along the

x, y, and z axes for the Control Off, Skyhook, and Sliding Mode systems, respectively, in response to the Colored disturbance. The PSD plots show good agreement between the frequency responses of the model and experiment. The translational mode, yaw mode, 2^{nd} rocking modes, and high frequency behavior all occur at the same frequency and have similar PSD profiles. The model accurately predicts the magnitude of 1^{st} x-axis rocking mode, but suggests it occurs at a slightly higher frequency of 0.55 Hz, rather than the measured 0.4 Hz. The model predicts the 1^{st} y-axis rocking mode to occur at 0.4 Hz, however this mode was not measured experimentally because it was not excited by the disturbance spectrum. The discrepancy between model and experiment for the 1^{st} rocking modes may be due to the modeling of the coil springs. Perhaps extending the axial and lateral linear stiffness model to include bending and rotation of the coil spring would improve the model agreement.

Figures 5.43 - 5.45 summarize the performance metrics in table 5.4 for the Control Off, Skyhook, and SMC systems. The radar plots indicate the agreement between model and experiment is good for some metrics and less good at others. The model underpredicts the magnitude of the PSD at several of the system modes, however the model does a good job of predicting metrics m_1, m_5, and m_7 for the Control Off system, and metrics m_5, m_6, and m_9 for the SMC controlled system. Furthermore, the difference in total RMS acceleration (m_8) is 18%, 10%, and 3% for the Control Off, Skyhook, and SMC systems, respectively. While there is some discrepancy between model and experiment, the model is considered a good representation of the physical system and will be used for further investigation.

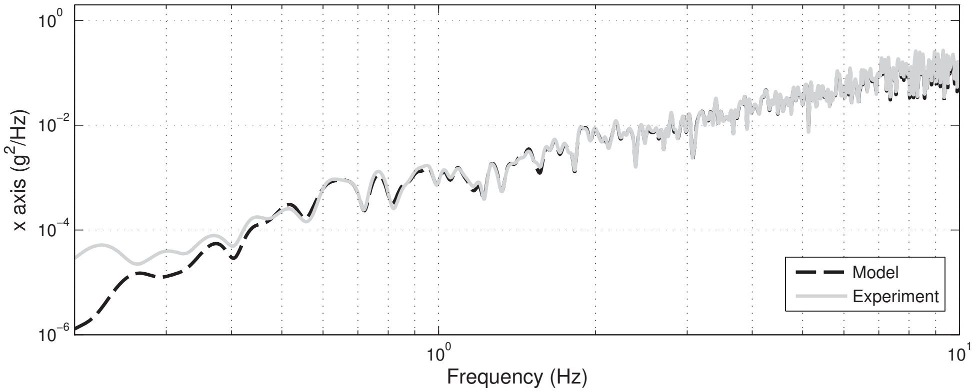

(a) x axis.

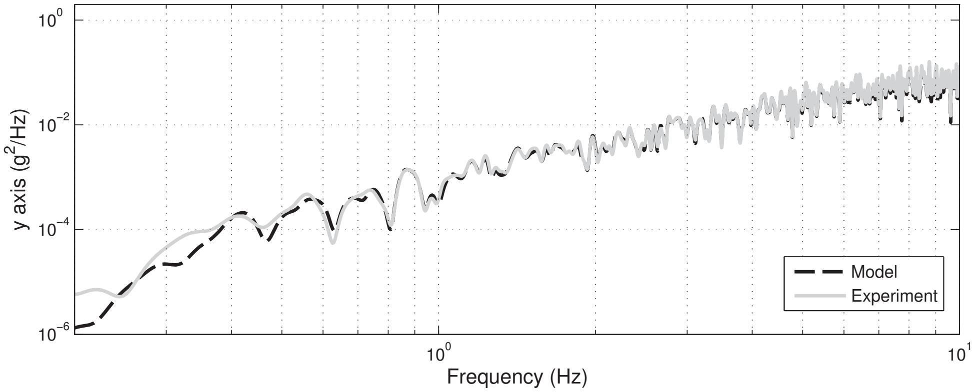

(b) y axis.

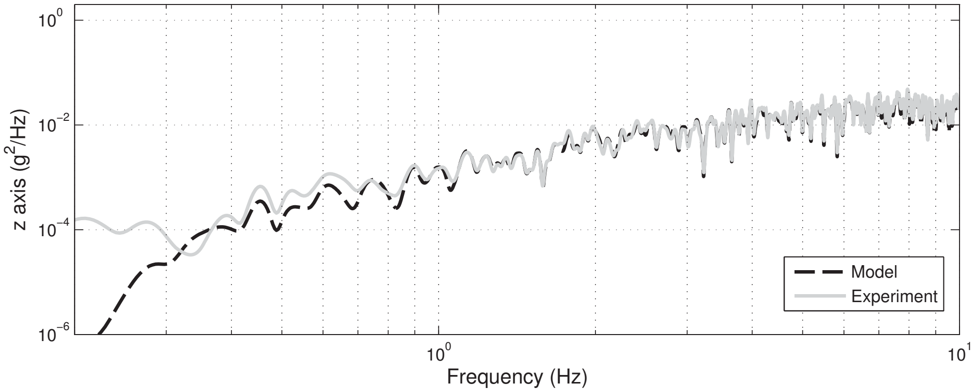

(c) z axis.

Figure 5.38: Measured PSD of the floor input along the x, y, and z axes for the Colored excitation.

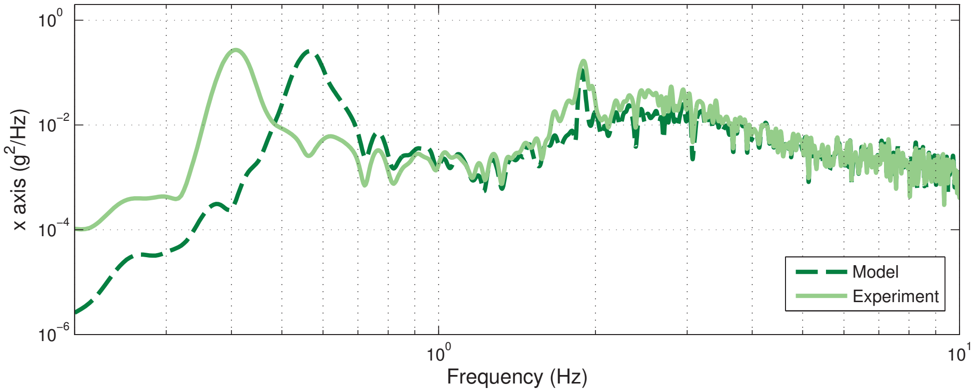

(a) x axis.

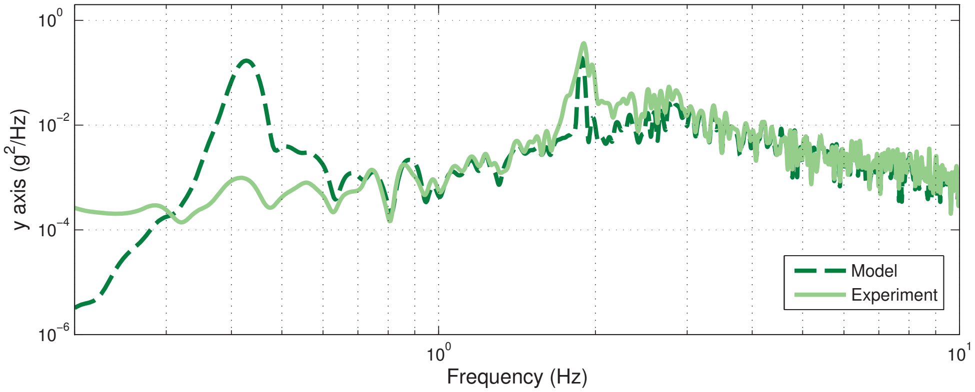

(b) y axis.

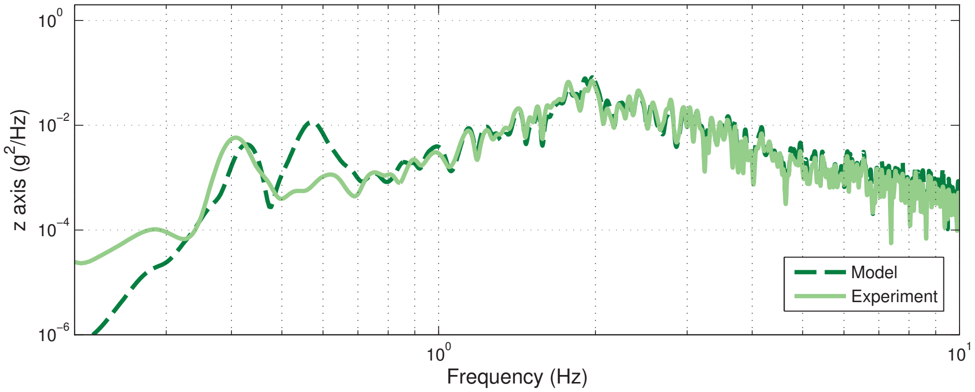

(c) z axis.

Figure 5.39: Measured PSD of the cabinet top corner along the x, y, and z axes for the Control Off system, in response to the Colored excitation with a cabinet weight of 1,200 lb and the CG located at 1/3 the cabinet height.

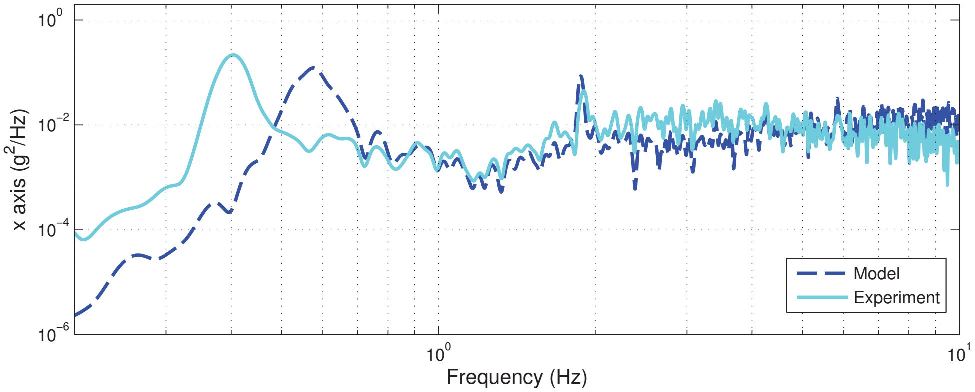

(a) x axis.

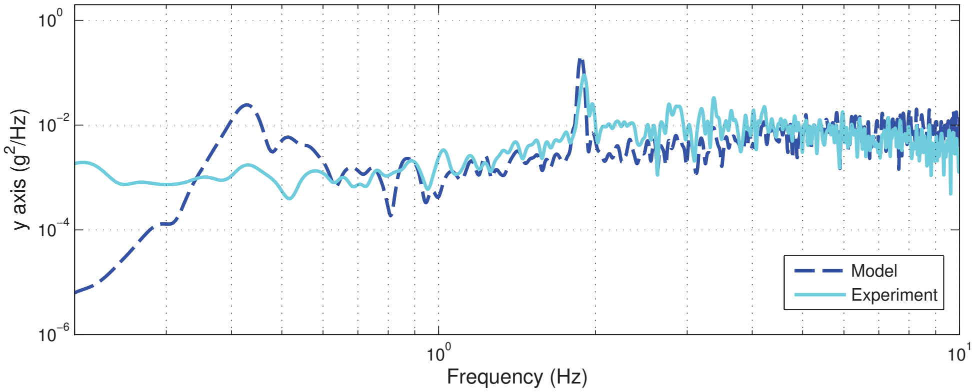

(b) y axis.

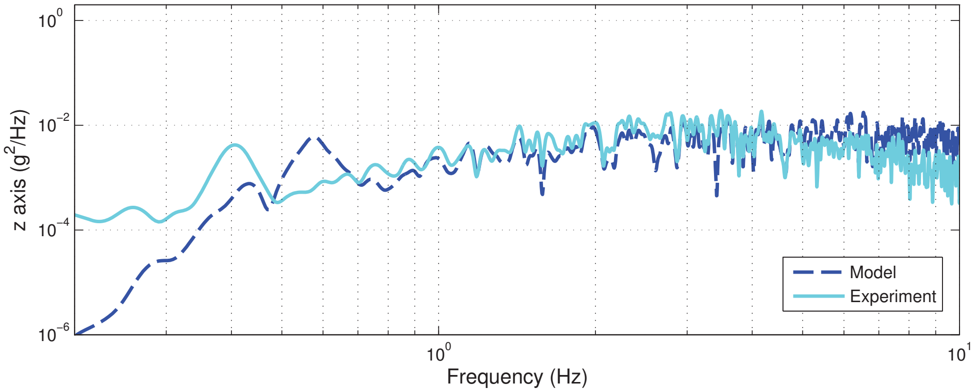

(c) z axis.

Figure 5.40: Measured PSD of the cabinet top corner along the x, y, and z axes for the Skyhook control system, in response to the Colored excitation with a cabinet weight of 1,200 lb and the CG located at 1/3 the cabinet height.

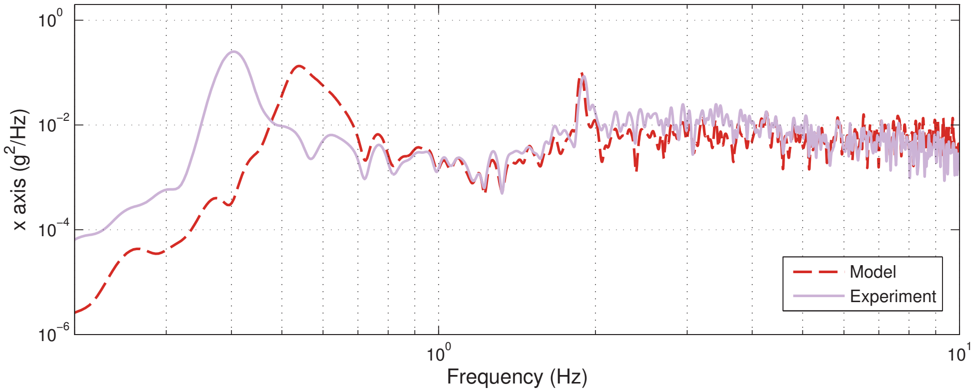

(a) x axis.

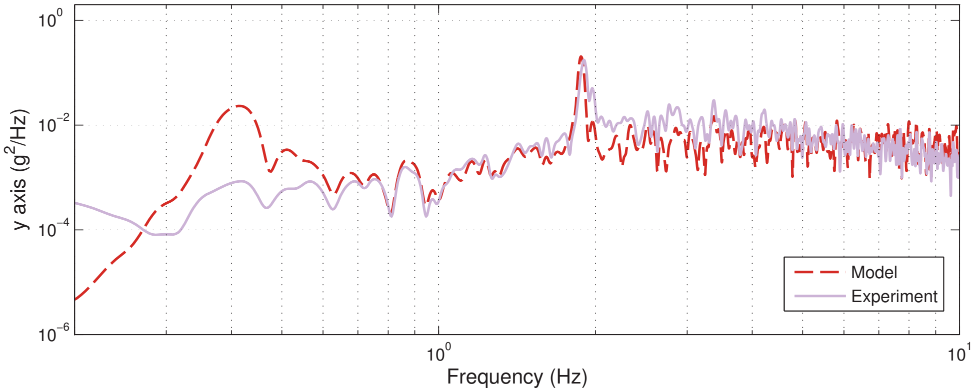

(b) y axis.

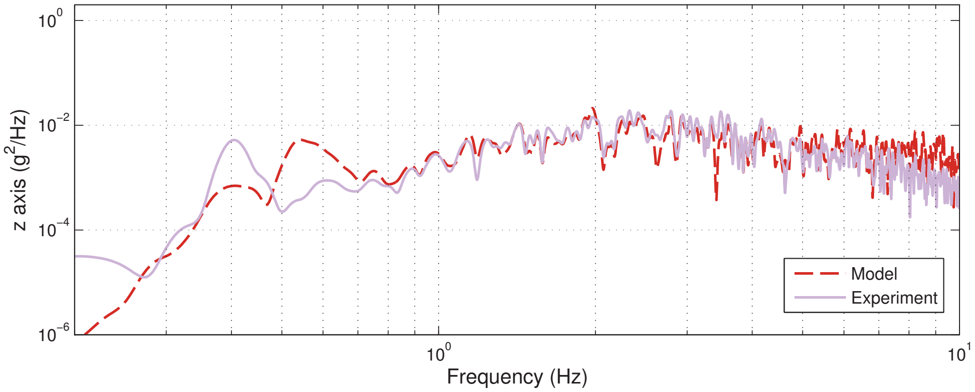

(c) z axis.

Figure 5.41: Measured PSD of the cabinet top corner along the x, y, and z axes for the SMC control system, in response to the Colored excitation with a cabinet weight of 1,200 lb and the CG located at 1/3 the cabinet height.

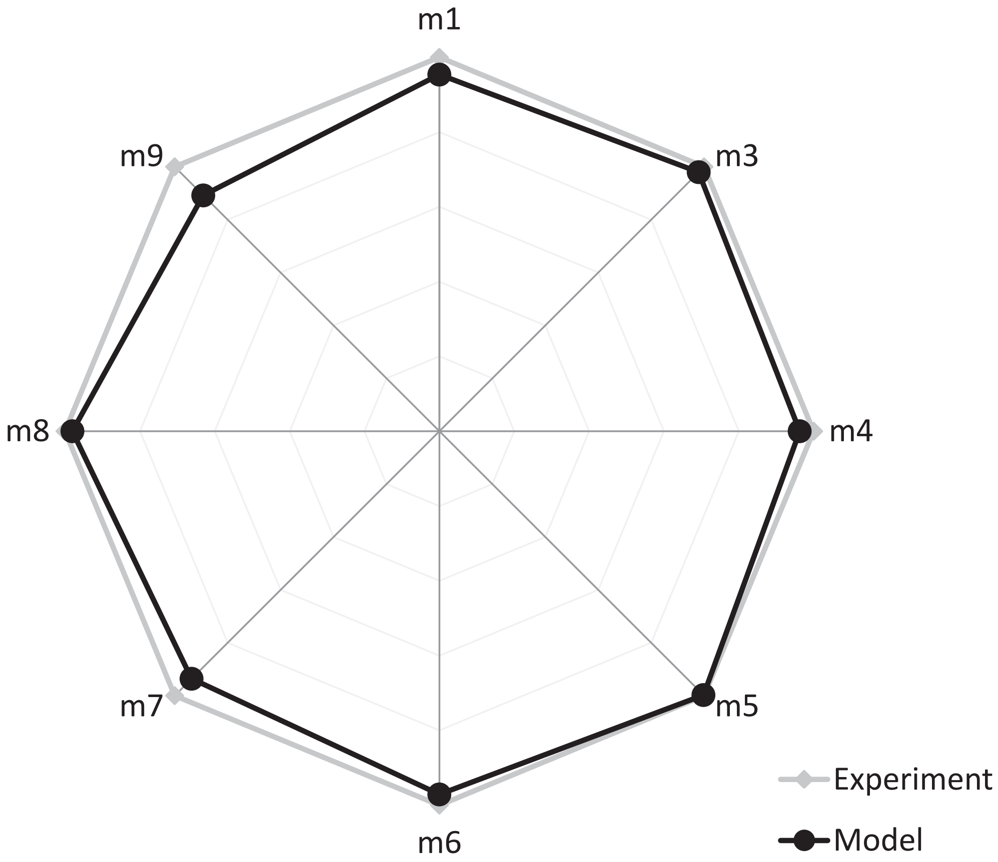

Figure 5.42: Performance metrics of a system rigidly attached to the base disturbance, for both model and experiment. In response to the Colored excitation.

Table 5.4: Performance metrics for both model and experiment. In response to the Colored excitation with a cabinet weight of 1,200 lb and CG location at 1/3 the cabinet height.

Metric	Rigid		Control Off		Skyhook Control		SMC Control		Units
	Experiment	Model	Experiment	Model	Experiment	Model	Experiment	Model	
m_1	0.013	0.012	0.125	0.124	0.113	0.089	0.121	0.094	g
m_3	0.060	0.058	0.115	0.077	0.069	0.045	0.072	0.052	g
m_4	0.062	0.059	0.102	0.079	0.055	0.040	0.063	0.043	g
m_5	0.046	0.046	0.129	0.125	0.052	0.041	0.058	0.056	g
m_6	0.059	0.058	0.241	0.124	0.115	0.091	0.150	0.131	g
m_7	0.284	0.266	0.040	0.040	0.072	0.105	0.059	0.074	g
m_8	1.016	0.996	0.494	0.406	0.449	0.492	0.431	0.417	g
m_9	34.346	30.633	13.559	7.547	24.290	11.984	10.591	10.861	g

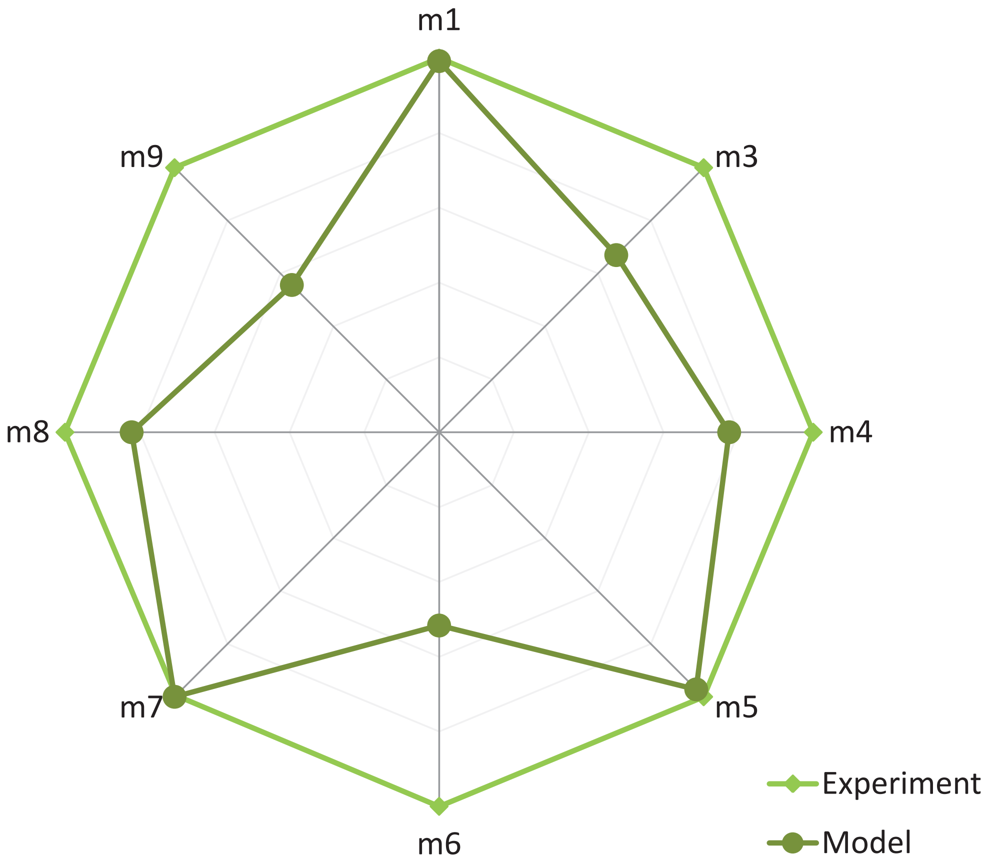

Figure 5.43: Performance metrics of the Control Off system, for both model and experiment. In response to the Colored excitation with a cabinet weight of 1,200 lb and CG location at 1/3 the cabinet height.

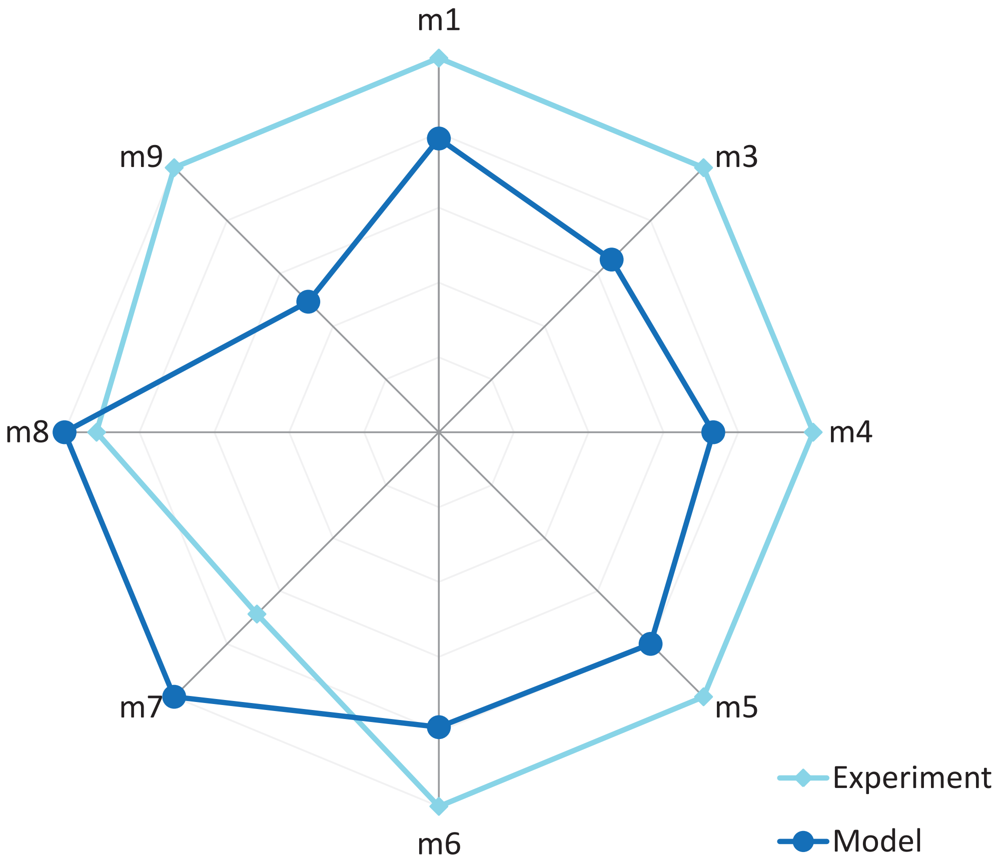

Figure 5.44: Performance metrics of the Skyhook controlled system, for both model and experiment. In response to the Colored excitation with a cabinet weight of 1,200 lb and CG location at 1/3 the cabinet height.

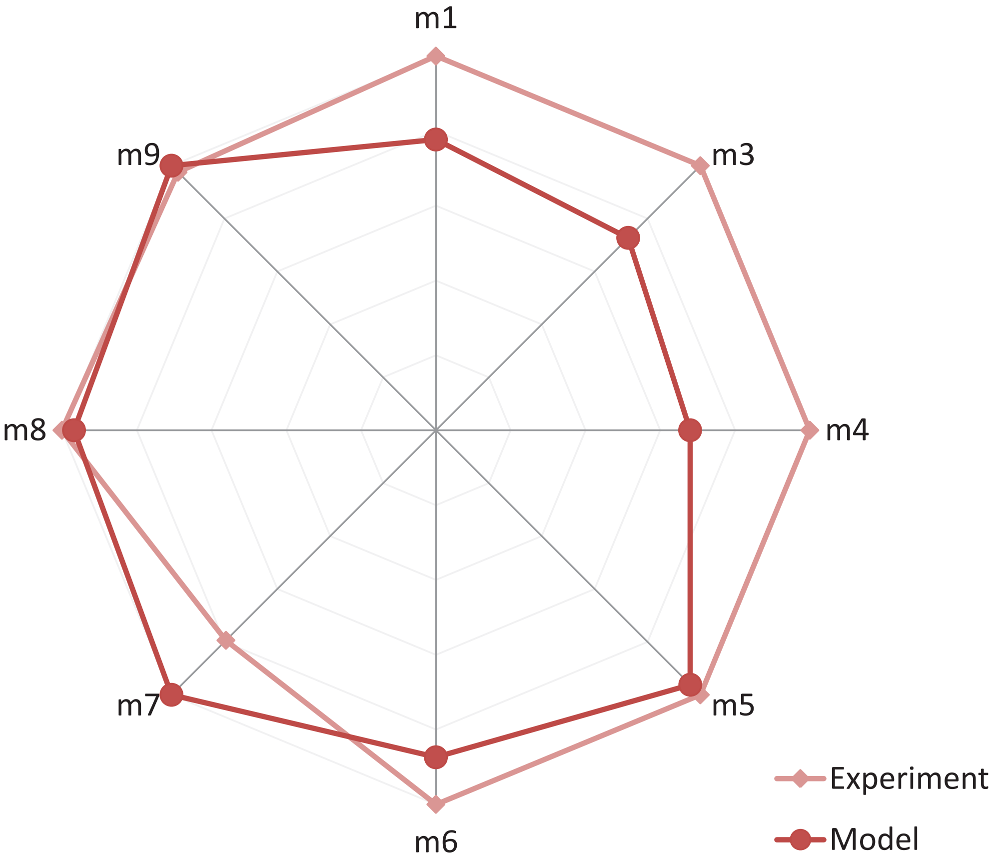

Figure 5.45: Performance metrics of the SMC controlled system, for both model and experiment. In response to the Colored excitation with a cabinet weight of 1,200 lb and CG location at 1/3 the cabinet height.

5.8 Conclusions

The experimental design, setup, and testing of a semi-active 6-DOF suspension was presented in this chapter. Both the MR dampers and coil springs were characterized and a simplified, quarter-scale suspension was used to calibrate the control law gains. Several performance metrics were established to evaluate the isolation performance of the system. The system was evaluated with two disturbance spectrums and the measured data was used to validate a mathematical model of the system.

The semi-active suspension provided significant reductions in vibration transmitted to the payload from the floor input disturbance. Each of the excited resonant modes of the system were attenuated with the semi-active control laws, with the only exception being the 1^{st} rocking mode along the x axis. The controlled cases reduced the performance metrics m_3 - m_6 up to 57% over the Control Off system. Only the rocking mode metric m_1 was similar for both controlled and uncontrolled systems, due to the orientation of the dampers. The pivoting phenomenon caused a lack in damper stroke, offering little control authority over the 1^{st} rocking mode of the system.

The Control Off system provides better high frequency isolation due to the induced parasitic damping of the semi-active clipping associated with the control laws. This fact is reflected through metric m_7, with the Control Off system having up to a 45% lower value compared to the worst controlled system. This is a consequence of the power limitations of the power supply and the inductance of the electromagnetic coil, which affect the response time of the applied control commands. By either improving the power supply or improving the semi-active clipping algorithm the controlled system will approach the high frequency performance of a passive system.

The overall broadband isolation performance of the system is a combination of metrics m_1 - m_7. In response to the Colored Noise disturbance, metric m_8 shows that both the Skyhook and SMC semi-actively controlled systems improved broadband RMS acceleration isolation by 4% and 11%, respectively, compared to the zero-field system without control. This is a result of the Colored disturbance having lower frequency content. However, when excited by the Rep. Launch disturbance, the zero-field system without control provided slightly better broadband RMS acceleration isolation than the controlled systems because the disturbance has predominately high frequency content ($>$ 4 Hz), above all the resonant frequencies of the system, where the Control Off system excels. At frequencies far away from resonant behavior the semi-actively controlled system tries to mimic the behavior of the Control Off system, however, due to the algorithm of the control law and time delays in the application of the desired control, the controlled system adds parasitic damping and degrades isolation. This is the standard trade-off between passive and semi-active control. We choose semi-active to gain resonance performance while sacrificing some high frequency performance. Indeed, a passive system would require a large damping ratio to match the resonance attenuation capabilities of the semi-active system, causing poor high frequency performance. The semi-actively controlled system excels at attenuating resonance behavior while also nearly enjoying the full benefits of a lightly-damped passive system.

The Rep. Launch excitation considered here is only a single disturbance to which the system may be exposed, while another disturbance, such as the Colored Noise, may contain greater lower frequency content (ie. different Shuttle launch, or during ground transportation of the Shuttle), allowing the controlled system to offer superior isolation and reveal the advantages to having an adaptable system that can better attenuate the lower frequency modes, while also providing the high frequency advantages of a passive system. Nevertheless, the semi-active suspension was shown to reduce the transmitted RMS acceleration to the cabinet top corner by up to 72% and maximum acclerations up to 76%, considering the Rep. Launch disturbance, and reduce the RMS acceleration by up to 59% and maximum acclerations up to 69%, considering the Colored Noise disturbance.

The mathematical model developed in chapter 4 was validated with the experimental data, and good agreement was found for the uncontrolled and controlled systems. The translational mode, yaw mode, 2^{nd} rocking modes, and high frequency behavior all occur at the same frequency and show similar magnitudes in the frequency responses. The model captures both the 1^{st} rocking modes, but suggest they occur at slightly higher frequencies compared to the measured data. This discrepancy may be due to the modeling of the coil springs, and perhaps extending the axial and lateral linear stiffness model to include bending and rotation of the coil spring would improve the model agreement. The error in total RMS acceleration (m_8) between model and experiment is 18%, 10%, and 3% for the Control Off, Skyhook, and SMC systems, respectively. While there is some discrepancy between model and experiment, the model is considered a good representation of the physical system.

Chapter 6

Analysis of a 6-DOF Magnetorheological Suspension

6.1 Introduction

The semi-active 6-DOF suspension system is analyzed here by investigating several features of the system. First, modal analysis is used to study the orientation of the MR dampers and determine a configuration that best attenuates all six modes of the system. Second, the control laws are revisited to compare centralized and decentralized control. Last, the performance of the system is studied when it is subjected to perturbations in payload mass, center of gravity, and temperature.

6.2 Damper Orientation

The suspension studied in the previous chapter orients the MR dampers underneath the payload such that the dampers attach to each of the cabinet's four

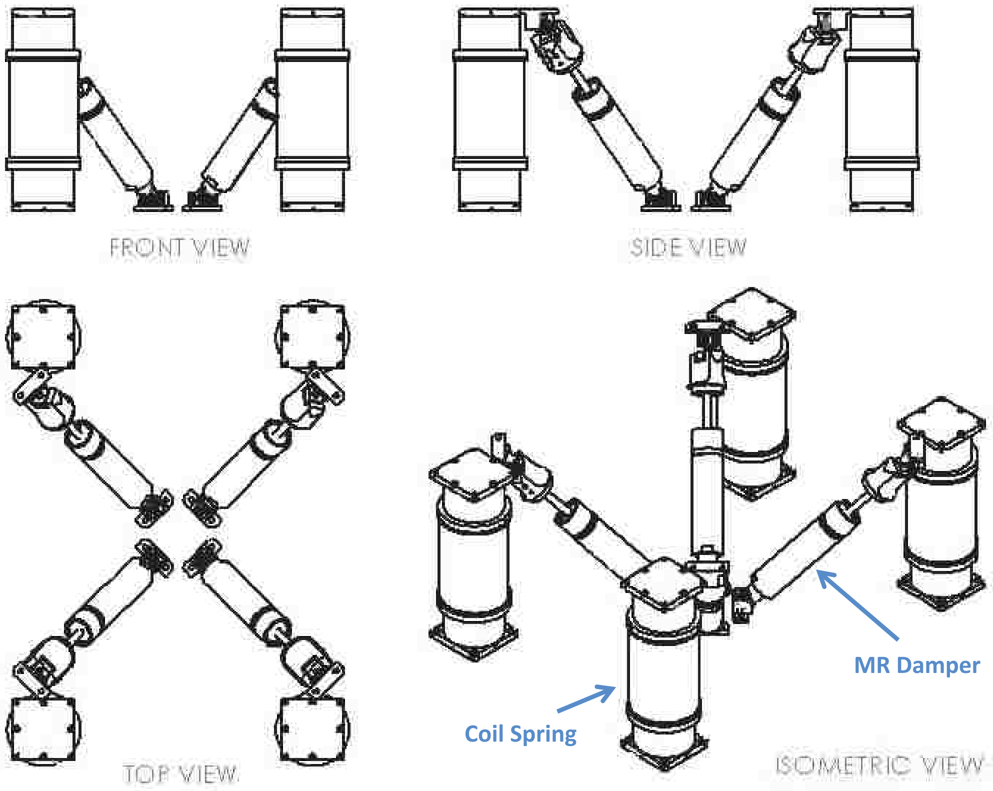

Figure 6.1: Pyramid configuration of suspension.

corners and nearly share a common attachment point at the base floor, forming an upside-down, square pyramid. This configuration of the MR dampers, shown in figure 6.1 is refered to as the Pyramid configuration. This configuration was chosen so that the dampers could provide damping along each of the x, y, and z axes. However, it was found that the Pyramid configuration has little control authority over the 1^{st} rocking modes along the x and y axes. This is due to the payload pivoting about the common connection point shared by all four dampers, prohibiting the dampers from stroking and providing attenuation. It is desired to improve the suspension design by orienting the dampers such that the suspension has control authority over all six modes.

6.2.1 Controllability

One property of the system that is of interest is whether or not the system is controllable. Controllability describes the ability of an external input to move the internal state of a system from any initial state to any final state in finite time [58]. This notion of controllability can be determined by finding the controllability matrix Q_c of a linear, time-invariant system and evaluating the rank of the matrix. However, the system studied here is nonlinear. Linearization is a useful approach to study nonlinear systems in which a system is linearized about some nominal operating point, allowing linear analysis to be used to study the local behavior of the system.

A further complication is the external control input is semi-active, requiring motion for the MR dampers to apply resistive control forces. The system may not be controllable if there is no motion (ie. ${}^O\overline{\boldsymbol{x}} - {}^O\overline{\boldsymbol{w}} = {}^O\dot{\overline{\boldsymbol{x}}} - {}^O\dot{\overline{\boldsymbol{w}}} = {}^O\ddot{\overline{\boldsymbol{x}}} - {}^O\ddot{\overline{\boldsymbol{w}}} = \mathbf{0}$). Therefore, the controllability will be evaluated for each mode of the system, as these are the most critical operating points.

The state space model from chapter 4 is linearized about the static equilibrium position ${}^O\overline{\boldsymbol{x}} = {}^O\overline{\boldsymbol{x}}^*$. The damped natural frequencies and mode shapes of the system are identified from the state matrix A, assuming zero applied current. Here, the system will be evaluated with a cabinet weight of 1,200 lb and CG location at 1/3 the cabinet height. The j^{th} column of the normalized eigenvector matrix

$$\boldsymbol{V} = \begin{bmatrix} 1 & 0 & -.336 & 0 & 0 & 0 \\ 0 & 1 & 0 & .356 & 0 & 0 \\ 0 & 0 & 0 & 0 & 1 & 0 \\ 0 & -.909 & 0 & 1 & 0 & 0 \\ .854 & 0 & 1 & 0 & 0 & 0 \\ 0 & 0 & 0 & 0 & 0 & 1 \end{bmatrix} \tag{6.1}$$

is the mode shape $\boldsymbol{V}_j$ corresponding to the j^{th} damped natural frequency in the set $\{0.58, 0.45, 2.79, 2.78, 1.93, 1.88\}$ Hz. It is assumed ${}^{O}\dot{\boldsymbol{x}} = \boldsymbol{V}_j$, giving a constant state matrix A and input matrix B. The mode shapes identified from the state matrix A may be complex-valued, indicating the relative phase shift between each DOF. For undamped systems, or systems with proportional damping (ie. proportional to the mass or stiffness), each DOF will either be in phase or 180^o out of phase relative to each other, meaning each DOF experiences its maximum absolute displacement at exactly the same time, behaving according to what are called the real normal modes [24]. The zero-field damping of the system studied here is not proportional damping and instead the eigenvectors are called complex modes, where each DOF will not necessarily be in phase or 180^o out of phase relative to each other. However, the relative phase shift between each DOF for all six modes was found to deviate no more than $\pm 6^o$ from either 0^o or 180^o, and $\cos(6^o) \approx 1$, so the complex modes in equation 6.1 will be used for analysis as if they were the real normal modes.

The controllability matrix is given as [58]

$$Q_c = \begin{bmatrix} B & AB & A^2B & ... & A^{n-1}B \end{bmatrix} \tag{6.2}$$

where n is the number of states. The system is controllable if the controllability matrix Q_c has full rank (ie. $\text{rank}(Q_c) = n$). For the Pyramid configuration, the controllability matrix is of full rank for all six modes, indicating the ability of the external control to locally move all the states of the system toward a desired state, assuming the motion of the system is described by one of its modal shapes.

The rank of the controllability matrix indicates whether or not the system in controllable, but the amount of control influence the system has on each mode is also of interest. Despite the Pyramid configuration being controllable, the 1^{st} rocking modes along the x and y axes are not well damped. The control influence is defined here as how well the suspension can attenuate transmitted vibration. If the motion of the system is such that the dampers stroke very little, then the dampers have limited control influence to attenuate that motion. However, if the motion of the system causes the dampers to stroke significantly, then the dampers can provide effective attenuation.

To quantify the amount of control influence the system has for each mode, the motion of the dampers at each mode is evaluated. The resulting motion of the top connection point of the i^{th} damper (point d_i) due to the j^{th} natural mode is given as

$$ {}^{O}\boldsymbol{v}_{d_i,j} = \begin{bmatrix} \boldsymbol{I}_{3\times3} & -{}^{O}\boldsymbol{P}_{d_iB} \end{bmatrix} \boldsymbol{V}_j, \tag{6.3} $$

The amount of control authority the suspension has for the j^{th} mode can be evaluated by defining an effectiveness factor ϵ_j given as

$$ \epsilon_j = \frac{1}{N} \sum_{i=1}^{N} \frac{\left| {}^{O}\boldsymbol{v}_{d_i,j}^{T} \; {}^{O}\boldsymbol{l}_{d_iD_i}^{*} \right|}{\left\| {}^{O}\boldsymbol{v}_{d_i,j} \right\| \left\| {}^{O}\boldsymbol{l}_{d_iD_i}^{*} \right\|}, \tag{6.4} $$

where N is the number of dampers, and ${}^{O}\boldsymbol{l}^{*}_{d_i D_i}$ is the orientation vector of the i^{th} damper when the system is at the static equilibrium position. A value of $\epsilon_j = 1$ means the suspension has a large amount of control authority over the j^{th} mode, and a value of $\epsilon_j = 0$ means the suspension has no control authority. More simply, ϵ_j indicates the extent the j^{th} mode causes motion along the axial directions of the dampers. If the motion is parallel to the damper axis, then the term inside the summation in equation 6.4 will equal unity, and if the motion is perpendicular to the damper axis, then that same term will be zero. A total effectiveness factor ϵ can be defined as

$$\epsilon = \frac{1}{6}\sum_{j=1}^{6} \epsilon_j, \tag{6.5}$$

to give the average effectiveness of the system's ability to attenuate all six modes.

The effectiveness factors of Pyramid suspension configuration are given in table 6.1 and confirm this orientation of the dampers has little control authority over the 1^{st} rocking modes along the x and y axes with $\epsilon_1 = 0.2$ and $\epsilon_2 = 0.33$, and even less influence for the yaw mode ϵ_6. The effectiveness terms ϵ_3, ϵ_4 and ϵ_5 are much better, giving an average effectiveness of $\epsilon = 0.43$ for the Pyramid configuration. While this analysis only holds for the local behavior of the model near the linearization at static equilibrium, it provides very clear, useful information for suspension design.

Table 6.1: Effectiveness factor for several suspension configurations with a cabinet weight of 1,200 lb and CG location at 1/3 the cabinet height (*red* indicating largest value for a given mode).

		Damper Configuration				
Mode	Effectiveness Factor	Pyramid	Vertical	Trapezoid	Vee	Hexapod
1st rock. x axis	ε_1	0.20	0.66	0.61	0.23	0.41
1st rock. y axis	ε_2	0.33	0.82	0.76	0.70	0.39
2nd rock. x axis	ε_3	0.64	0.20	0.36	0.72	0.57
2nd rock. y axis	ε_4	0.64	0.25	0.30	0.21	0.59
Vertical translation	ε_5	0.74	1.00	0.99	0.84	0.57
Yaw	ε_6	0.01	0.00	0.05	0.39	0.71
Average	ε	0.43	0.49	0.51	0.52	0.54

6.2.2 Damper Orientation Evaluation

Several other damper configurations are now proposed and evaluated in an effort to improve on the Pyramid configuration and provide more uniform control authority over all six modes.

The pivoting phenomenon exhibited by the Pyramid configuration (figure 6.1) is due to the dampers pivoting about the common connection point at the base floor, prohibiting the dampers to stroke. This explains why the Pyramid configuration has poor control authority over the 1st rocking modes along both x and y axes. This can be corrected by eliminating the common base connection and orienting the dampers in a vertical fashion seen in figure 7.2(a). This forces the dampers to stroke when 1st rocking modes are excited. Table 6.1 confirms this as the effectiveness factors ϵ_1 and ϵ_2 are dramatically increased, giving an average effectiveness of $\epsilon = 0.49$ for the Vertical configuration. However, ϵ_3 and ϵ_4 indicate the system now has poor attenuation capability over the 2^{nd} rocking modes with the Vertical configuration.

In order to provide enhanced control authority over both the 1^{st} and 2^{nd} rocking modes, a compromise between the Pyramid and Vertical configurations is made. The base floor connections of the dampers are made toward the center similar to the Pyramid configuration but with greater separation among each damper as seen in figure 6.3, thus reducing the amount the payload can pivot. This configuration visually looks like the frustum of a truncated square pyramid with trapezoidal faces and consequently is refered to as the Trapezoid configuration. Table 6.1 shows that ϵ_1, ϵ_2 and ϵ_5 nearly match those of the Vertical configuration while also enhancing ϵ_3 and ϵ_4, giving an average effectiveness of $\epsilon = 0.51$ for the Trapezoid configuration. However, the yaw mode control authority is still neglected with all three configurations described thus far.

In order to address the yaw mode, a fourth configuration is established which maintains the inclined orientation of the dampers relative to the horizon but positions the dampers in-plane with two opposing sides of the cabinet payload as seen in figure 7.2(b). Each pair of dampers share a common base floor connection point, forming a shape similar to the alphebetic letter *V*, and is consequently refered to as the Vee configuration. Table 6.1 shows the yaw mode effectiveness ϵ_6 is dramatically enhanced, while also providing excellent values for ϵ_2, ϵ_3 and ϵ_5, giving an average effectiveness of $\epsilon = 0.52$. However, ϵ_1 and ϵ_4 are quite poor due to the shared base connection point of each pair of dampers.

For comparison purposes, it is interesting to consider a cubic hexapod configuration seen in figure 6.5. This is because the cubic configuration provides independent damping for all six DOFs, providing control authority for all six modes of the system. Table 6.1 shows the cubic hexapod configuration offers the most uniform control authority for all six modes, including the best effectiveness ϵ_6 over the yaw mode. This gives the hexapod configuration the best average effectiveness of $\epsilon = 0.54$, but at a cost. A cubic hexapod configuration was not pursued because it was desired to have a modular suspension design that could scale with payload mass and geometric size by either adding linkages to the suspension, or increasing the separation between the linkages. A cubic hexapod suspension is not modular in the sense that it requires exactly six linkages. Adding linkages would disrupt the orthogonality of the cubic configuration. The ability to add or subtract individual legs from the suspension accommodates payloads of varying size and mass without the need to redesign a fixed number of MR dampers or springs. Furthermore, reducing the amount of hardware and the number of linkages (ie. MR dampers) equates to reducing the cost and maintanance of the suspension.

The Trapezoid and Vee configurations show that all six modes can be controllable with the modular semi-active suspension. There may still exist some singularities in the controllability matrix (unlike a cubic hexapod), but no singularities when the system motion is described by one of the six modes. For a payload with a larger footprint, the rocking modes would be less of a concern as the dampers could have greater separation, resulting in more control leverage (larger ϵ_1 - ϵ_4).

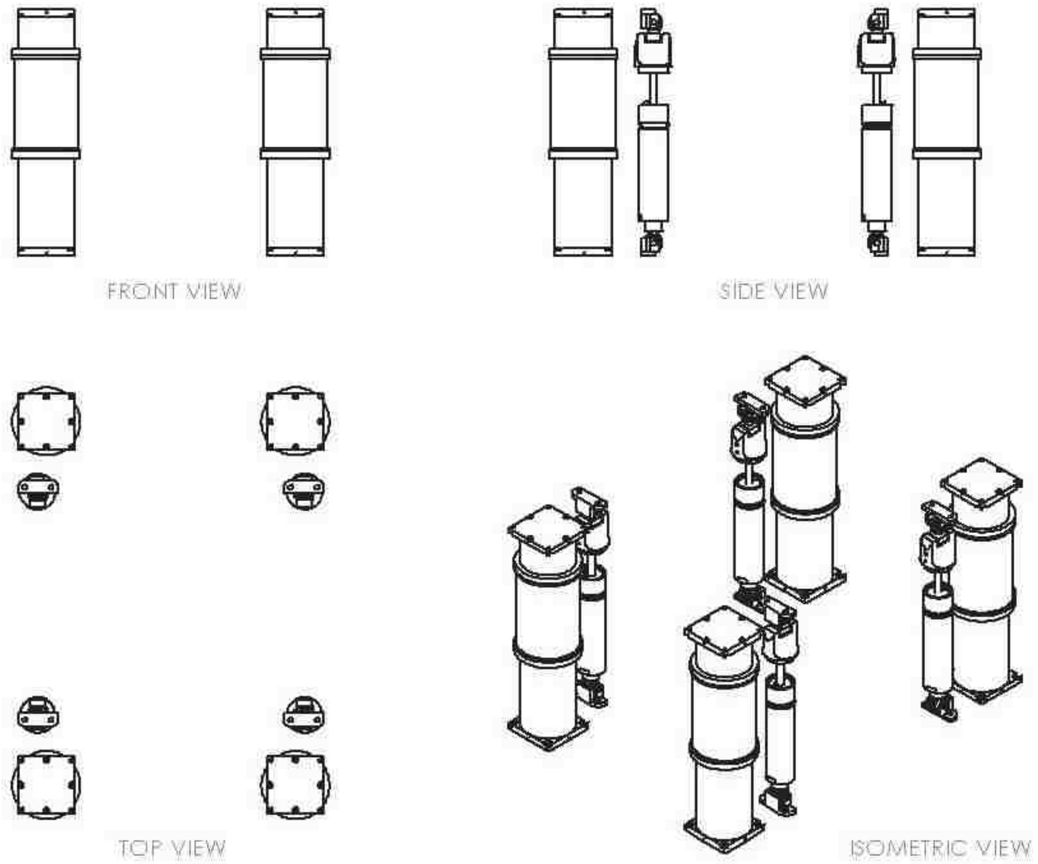

Figure 6.2: Vertical configuration of suspension.

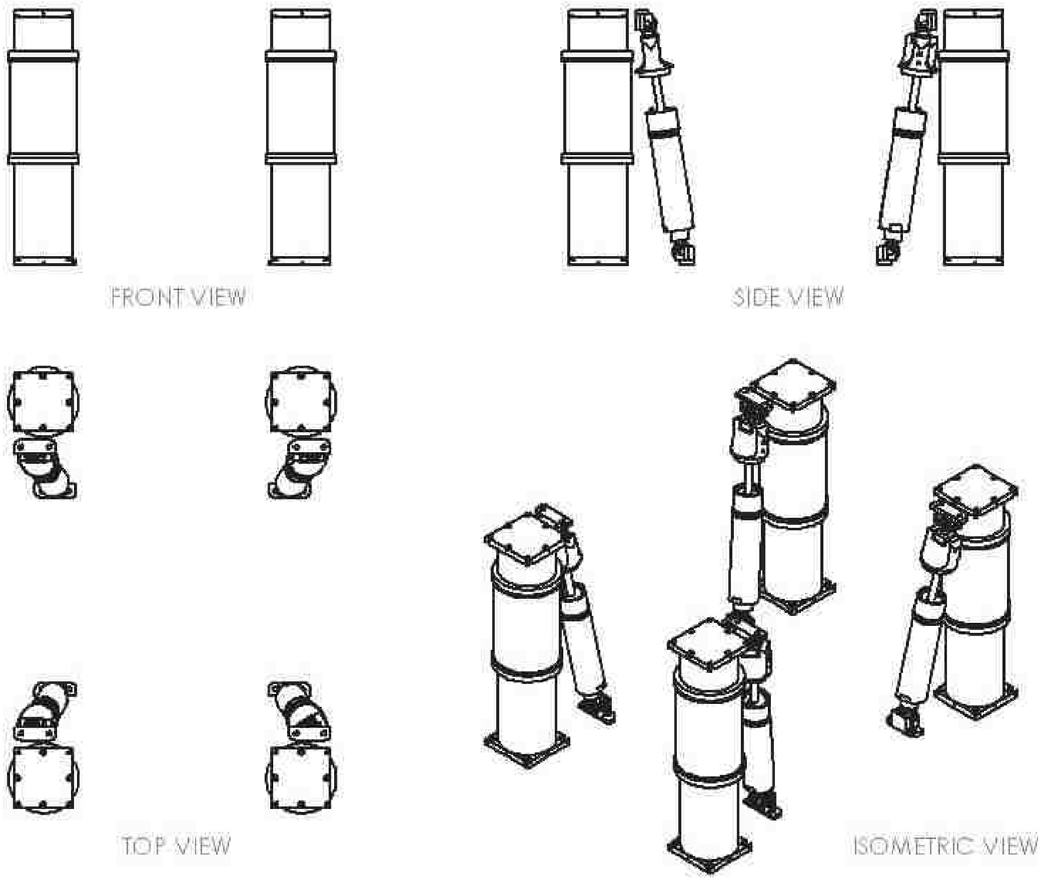

Figure 6.3: Trapezoid configuration of suspension.

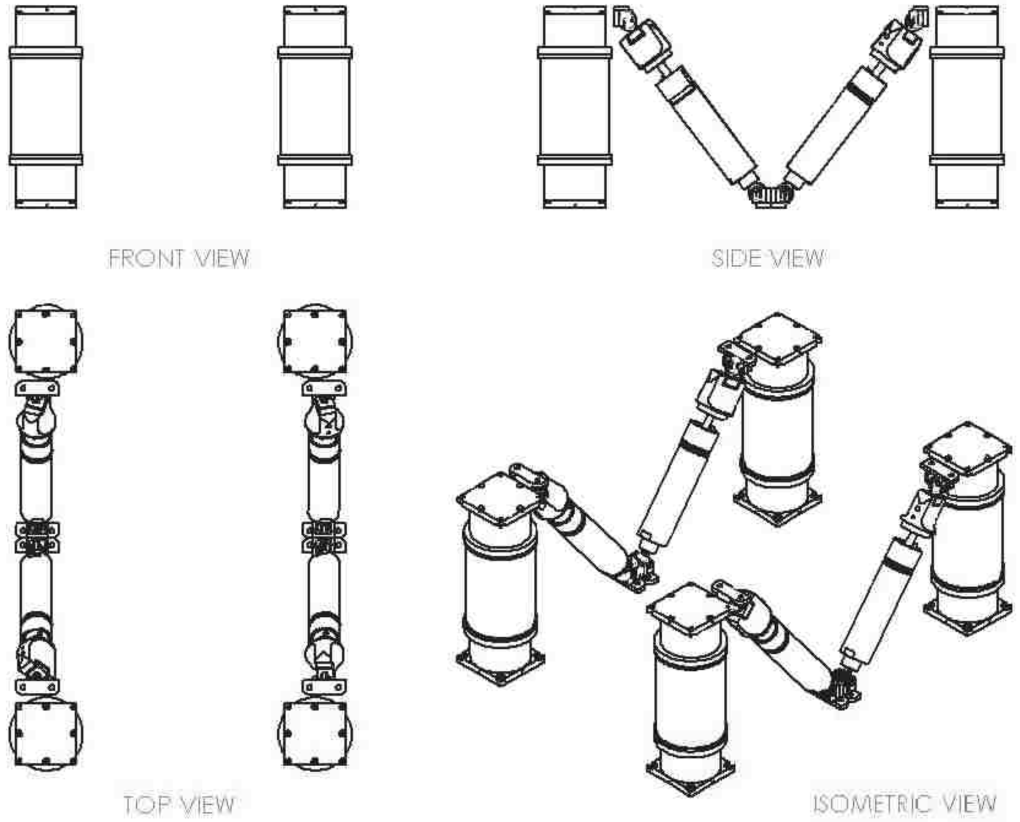

Figure 6.4: Vee configuration of suspension.

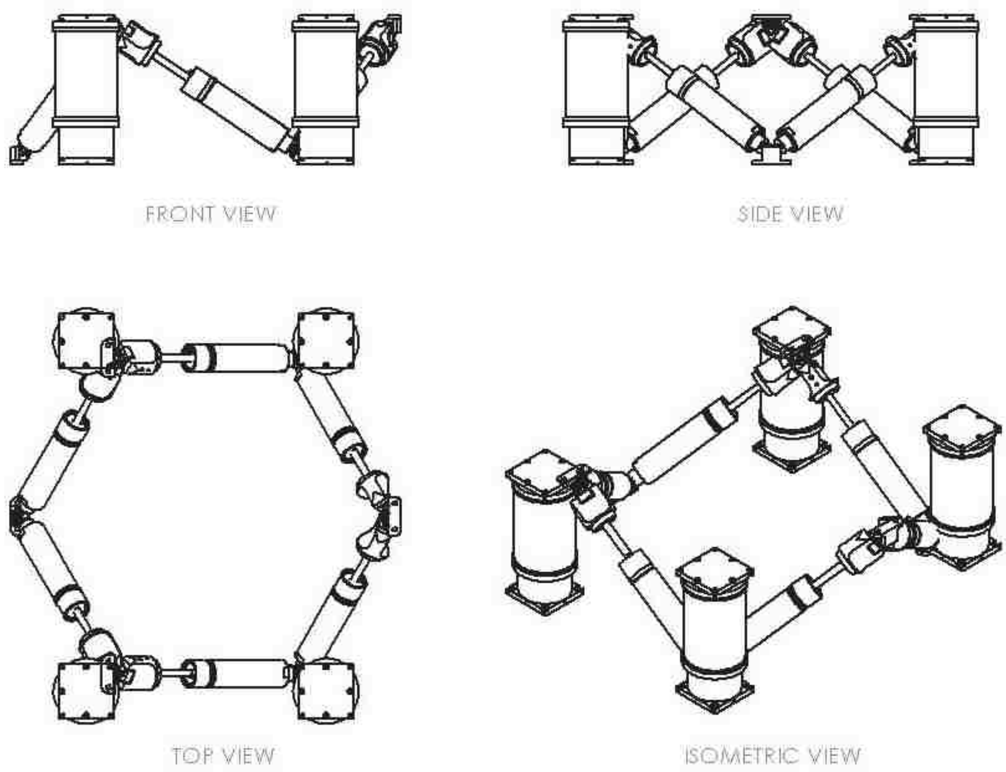

Figure 6.5: Hexapod configuration of suspension.

6.2.3 Performance of Configurations

The performance of each damper configuration was evaluated in response to the Colored disturbance with a cabinet weight of 1,200 lb and the CG located at 1/3 the cabinet height. Figure 6.6 shows a radar graph of the performance metrics m_1 - m_{10} from table 6.2 for all five damper configurations governed by Skyhook control. For the cubic hexapod, the damper forces were scaled by a factor of 4/6 to make an equivalent comparison with the other modular, 4-damper leg configurations.

The radar graph supports the assertions made with the effectiveness factors ϵ_1 - ϵ_6 in table 6.1. The Pyramid configuration offers the worst attenuation for the 1^{st} rocking modes and yaw mode. The Vertical and Vee configurations offer poor 2^{nd} rocking mode attenuation as indicated by metrics m_3 and m_4, respectively. The Hexapod configuration generally provides the best attenuation for metrics m_1 through m_6. The Trapezoid configuration provides similar performance to the cubic hexapod, with the exception of metric m_4 and the yaw mode metric m_6. Furthermore, the Trapezoid configuration also provides excellent high frequency isolation with metric m_7, the lowest total RMS acceleration with m_8, and minimizes the maximum relative displacement of cabinet top corner with metric m_{10}. The Trapezoid configuration offers good overall performance as well as provides the lowest RMS acceleration (m_8), thus one could argue it is a good candidate for the modular semi-active suspension.

It is interesting to compare the semi-active Trapezoid suspension with a passive suspension. Klembczyk and Mosher [47] describe an established passive 6-DOF suspension installed on NASA's MLP for isolation of ground support equipment. The vertical damping ratio (0.22) and vertical natural frequency (3.5 Hz) of the suspension were adapted to the system modeled here to give a baseline level of performance. Figure 6.7 summarizes the performance metrics in table 6.3 for both the Trapezoid configuration and passive Klembczyk and Mosher [47] suspensions. The Trapezoid suspension, even in its passive state without any semi-active control, provides much better isolation performance than the passive Klembczyk and Mosher suspension, with the only exceptions being the 2^{nd} rocking mode metrics m_3 and m_4. Applying semi-active control (Skyhook or SMC control) improves the performance further, offering large improvements over the Klembczyk and Mosher design for all ten metrics, including a 62% improvement in the RMS acceleration experienced at the payload top corner. Only the high frequency metric m_7 is the best for the Trapezoid suspension in its passive state due to the control response delay from the semi-active clipping.

It is concluded here that a modular semi-active suspension (with only 4 dampers) can provide control authority and attenuation for all six modes, as well as for high frequency disturbances. The semi-active suspension can provide superior performance compared to the baseline passive suspension described by Klembczyk and Mosher [47] as well as a similarly designed passive suspension.

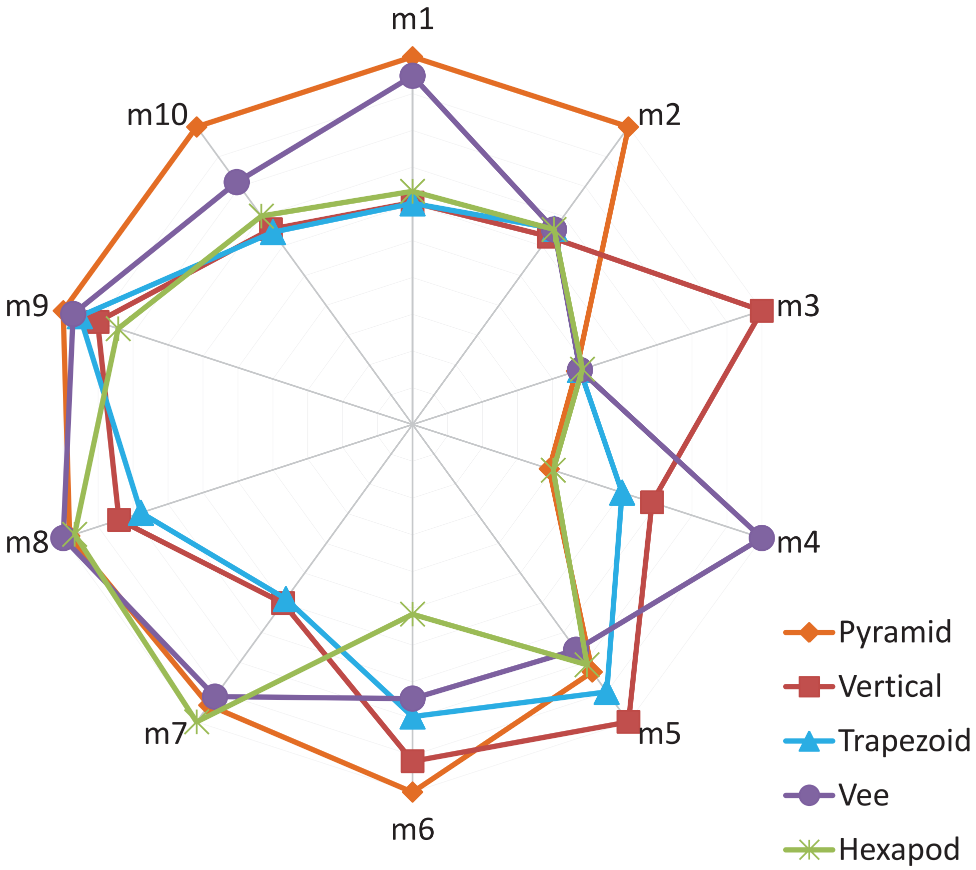

Figure 6.6: Performance metrics of all the damper configurations.

Table 6.2: Performance metrics of all the damper configurations.

Metric	Pyramid	Vertical	Trapezoid	Vee	Hexapod	Units
m_1	0.089	0.054	0.053	0.084	0.056	g
m_2	0.042	0.026	0.027	0.027	0.027	g
m_3	0.045	0.096	0.046	0.046	0.047	g
m_4	0.040	0.070	0.062	0.103	0.041	g
m_5	0.041	0.050	0.045	0.038	0.040	g
m_6	0.091	0.083	0.072	0.068	0.047	g
m_7	0.105	0.067	0.065	0.102	0.111	g
m_8	0.492	0.421	0.390	0.501	0.485	g
m_9	11.984	10.805	11.415	11.645	10.099	g
m_{10}	7.791	5.114	5.039	6.346	5.457	in

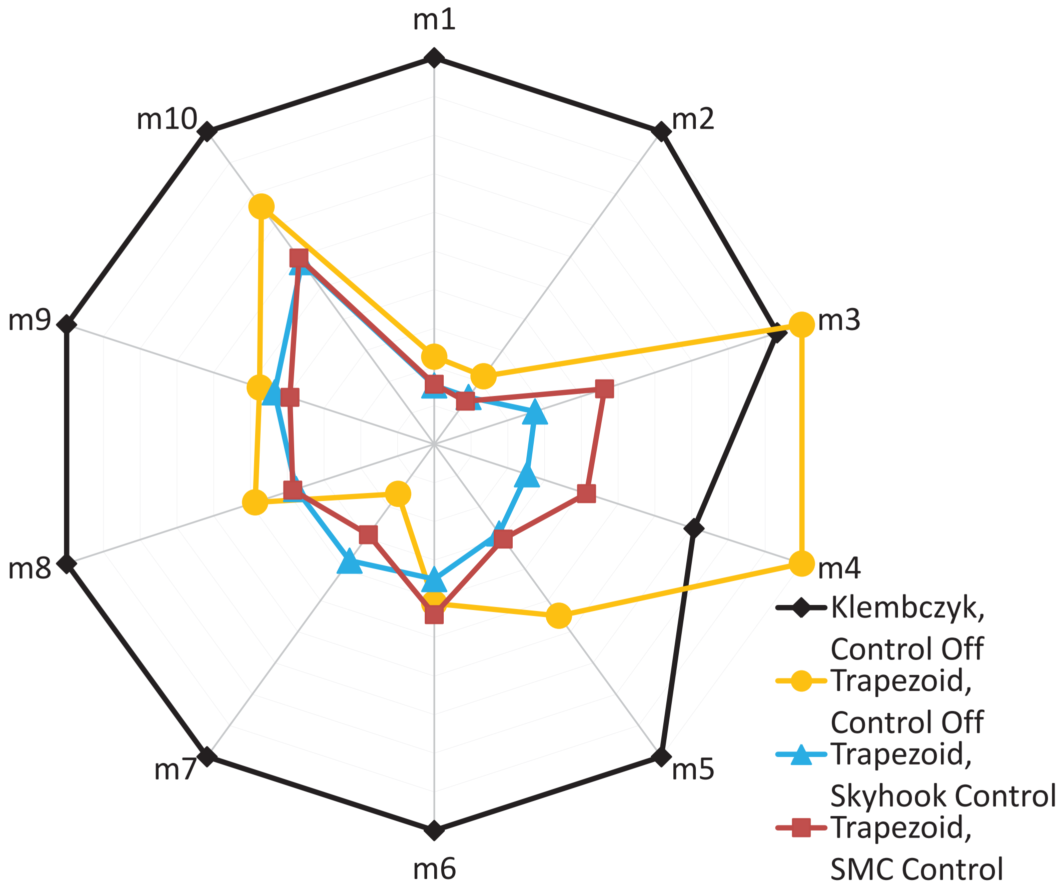

Figure 6.7: Performance metrics of the Trapezoid configuration and the passive suspension described by Klembczyk and Mosher [47].

Table 6.3: Performance metrics of the Trapezoid configuration and the passive suspension described by Klembczyk and Mosher [47].

Metric	Klembczyk, Control Off	Trapezoid, Control Off	Trapezoid, Sky Control	Trapezoid, SMC Control	Units
m_1	0.351	0.080	0.053	0.055	g
m_2	0.181	0.039	0.027	0.025	g
m_3	0.157	0.168	0.046	0.078	g
m_4	0.172	0.244	0.062	0.101	g
m_5	0.156	0.086	0.045	0.047	g
m_6	0.206	0.085	0.072	0.091	g
m_7	0.175	0.028	0.065	0.051	g
m_8	1.037	0.505	0.390	0.399	g
m_9	26.294	12.479	11.415	10.317	g
m_{10}	8.654	6.579	5.039	5.154	in

6.3 Centralized Control

Centralized control considers the entire state of the system and commands control inputs correspondingly. This is different from decentralized control where each control device operates without knowledge of the other control devices. Butsuen [10] notes, with a simplified ground vehicle suspension, that centralized and decentralized control laws can yield similar perfromance when the commanded control inputs are highly correlated due to minimal coupling between each leg of the suspension. The performance of both control philosophies is compared here using the centralized and decentralized Skyhook control laws defined in chapter 4.

Figure 6.8 shows the performance metrics of both the decentralized and centralized Skyhook control laws. The vertical translational mode, m_5, performance is the same for both, while the centralized strategy provides better attenuation for each rotational mode (ie. m_1 - m_4, m_6). If the system experienced only the vertical translation mode, the entire suspension would act as a single DOF system and each damper would symmetrically stroke in unison. This would cause both the centralized and decentralized control laws to command similar control inputs to each damper, explaining the same value for m_5 in figure 6.8. However, when the cabinet rotates, as it does for the remaining modes, the stroking can be different for each damper. Differences in stroking between each damper will cause the decentralized control to command different inputs for each, without knowledge of the effect it has on the rest of the system. However, the centralized strategy applies control commands to each damper based on the state of the entire system, explaining the enhanced performance it offers for the rotational modes (ie. m_1 - m_4, m_6).

The high frequency isolation (m_7) is the same for both strategies, and is attributed to both having the same time response delay for the semi-active control clipping. Also, the RMS and maximum acceleration metrics (m_8 - m_9) are approximately the same. The maximum relative displacement (m_{10}) is better for the centralized control law, which is attributed to the enhanced attenuation of the rotational modes.

While the centralized Skyhook control provides improved resonance suppression, the algorithm is dependent on the placement of the dampers, which detracts from the modularity of the design. Also, centralized control is more complex than decentralized control and is less robust to a loss in control of a single damper. Therefore, a trade-off must be established when selecting the control strategy. Importance must be placed on either optimal full-system performance, or on the modularity and robustness of the suspension that decentralized control provides.

6.4 System Perturbations

A key feature of the suspension design is it's adaptability to practical system perturbations. A passive suspension can possess either high damping for excellent resonance suppression, or low damping for excellent high frequency isolation; however, it can not have both. A semi-active suspension has the ability to provide both high and low damping, and it is this essential feature that allows the semi-active suspension to adapt to broad spectrum disturbances. This ability to provide both

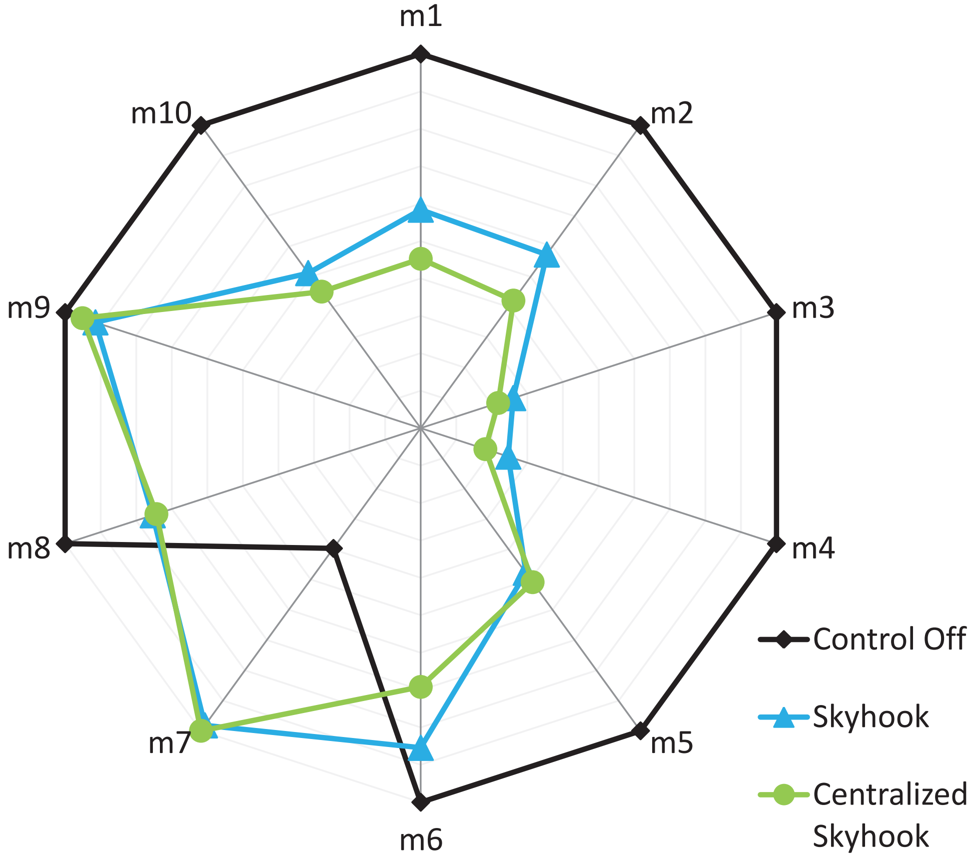

Figure 6.8: Performance metrics of both centralized and decentralized Skyhook control laws. Payload weight of 1,200 lb, CG located at 1/3 the cabinet height, Trapezoid configuration, and Colored disturbance.

high and low damping also allows the suspension to adapt to perturbations in the inertia properties (ie. mass and moment of inertia) and operating temperature of the system. A passive suspension has a fixed amount of damping, and can only be optimized for a fixed set of system properties. A semi-active suspension can increase or decrease the amount of damping in response to a change in the system.

Mass perturbations could be the consequence of adding hardware to an equipment rack cabinet, or the addition of passengers of varying mass to an occupant vehicle. Perturbations in CG could result from installing equipment hardware in different vertical locations or from passengers sitting or standing. Perturbations in operating temperature of the MR damper are simply due to the dissipation of mechanical energy, or electrical energy (from the MR damper's electromagnetic coil), into thermal energy. This section investigates the behavior of the semi-active suspension (Trapezoid configuration) subjected to perturbations in payload mass, center of gravity, and temperature.

The performance metrics m_1 - m_7 that have been used for analysis up to this point are derived from the output PSD measured at the cabinet top corner. The magnitude of the output PSD is dependent on the magnitude of the input disturbance PSD, and if the magnitude of the input PSD is frequency dependent, as is the case with the Colored Noise disturbance, then the magnitude of the output will also be frequency dependent. Perturbations in payload mass and CG location will shift the natural frequencies of the system, so comparing the shifted resonant modes of two systems, simply using the PSD curves, does not give a fair comparison. Instead, alternative performance metrics, $\hat{m}_i$, will be used in place of metrics

m_i, where $i = 1, 2, ... 7$. These alternative metrics are similar to the originals, but are determined from calculating the area under the transmissibility curves instead of the PSD curves. Since the transmissibility is normalized relative to the input disturbance, these alternative metrics allow for a proper comparison between systems with shifted natural frequencies due to perturbations in payload mass or CG location.

The transmissibility curves considered here are not exactly proper transmissibility curves, rather psuedo-transmissibilities or normalized PSD curves. Proper transmissibility curves for a multiple-input/multiple-output (MIMO) system specify the frequency response of output j due solely to input k, creating a $m \times n$ matrix of curves, where $j = 1, ... m$ and $k = 1, ... n$. However, the outputs considered here are in response to all the inputs excited simultaneously. It is assumed here that the coupling between axes is minimal, meaning the output response j is primarily due to input $k = j$, and the off-diagonal entries of the transmissibility matrix ($j \neq k$) are negligible. Therefore, only the diagonal entries of the psuedo-transmissibility matrix are evaluated. These diagonal entries are simply the x, y, and z output PSD curves from the cabinet top corner normalized by the x, y, and z input PSD curves from the base, respectively, resulting in three psuedo-transmissibility curves from which the alternative performance metrics $\hat{m}_1 - \hat{m}_7$ are derived. These alternative metrics $\hat{m}_i$ are very similar to the original metrics derived from the PSD curves, except now the psuedo-transmissibility curves are used.

6.4.1 Mass Perturbation

Two payload masses are considered here, 272 kg (600 lb) and 544 kg (1,200 lb), both with a center of gravity located at 1/3 the payload height measured from the bottom. The moment of inertia tensor of the payload

$$^{B}\boldsymbol{I} = \begin{bmatrix} I_{xx} & -I_{xy} & -I_{zx} \\ -I_{xy} & I_{yy} & -I_{yz} \\ -I_{zx} & -I_{yz} & I_{zz} \end{bmatrix} \tag{6.6}$$

has values of either $I_{xx} = 162 \ \mathrm{kg\,m^2}$, $I_{yy} = 176 \ \mathrm{kg\,m^2}$, and $I_{zz} = 51 \ \mathrm{kg\,m^2}$, or $I_{xx} = 200 \ \mathrm{kg\,m^2}$, $I_{yy} = 214 \ \mathrm{kg\,m^2}$, and $I_{zz} = 68 \ \mathrm{kg\,m^2}$, respectively. The mass distribution is sysmetric, so the off-diagonal entries $I_{ij} = 0$, for $i \neq j$.

Figure 6.9 summarizes the performance metrics in table 6.4 for both payload weights of 600 lb and 1,200 lb. With the Control Off system, doubling the payload weight from 600 lb to 1,200 lb worsens all the resonant mode metrics, m_1 - m_6. Despite this 100% increase in weight, the Skyhook controlled system experiences only a 5% degradation in the vertical translation mode metric, $\hat{m}_5$, compared to the 13% degradation for the Control Off system. This is the same result discussed in chapter 3 for a single DOF system, where the Skyhook control is able to provide high damping to the suspension, reducing the sensitivity to a change in damping ratio. The Skyhook control also offers robust performance for metrics $\hat{m}_3$, $\hat{m}_4$, and $\hat{m}_6$. It appears that while the dampers apply more damping to the system, metrics $\hat{m}_1$ and $\hat{m}_2$ worsen as the payload weight increases. Nevertheless, the Skyhook control still provides greatly improved values for $\hat{m}_1$ and $\hat{m}_2$ over the passive Control Off system.

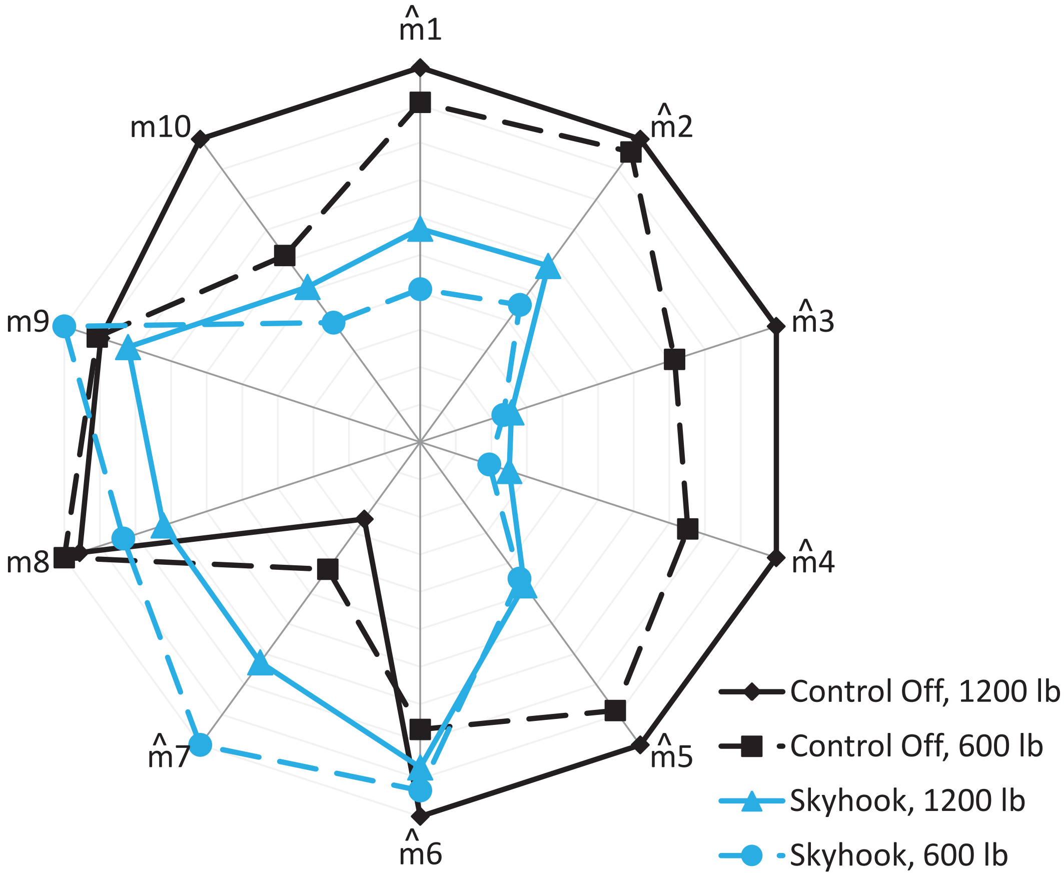

Figure 6.9: Performance metrics of the system with payload weights of 1,200 lb or 600 lb, using Control Off or Skyhook control.

As payload mass increases from 600 lb to 1,200 lb, the high frequency isolation improves, as shown with metric $\hat{m}_7$, which is expected due to the higher inertia and also noted in chapter 3 for a single DOF system. For Skyhook control, metric m_8 shows that increasing the payload mass improves RMS acceleration. This is attributed to the better high frequency isolation of the 1,200 lb system. The results for metric m_9 are scattered and no clear trend is shown. Metric m_{10} shows that increasing payload mass worsens the maximum relative displacement, however the controlled system still provides improved performance compared to the passive Control Off system.

Table 6.4: Performance metrics of the system with payload weights of 1,200 lb or 600 lb, using Control Off or Skyhook control.

Metric	Control Off, 1200 lb	Control Off, 600 lb	Skyhook, 1200 lb	Skyhook, 600 lb	Units
$\hat{m}_1$	2.66	2.41	1.51	1.08	-
$\hat{m}_2$	1.87	1.80	1.09	0.85	-
$\hat{m}_3$	1.22	0.87	0.31	0.28	-
$\hat{m}_4$	1.63	1.23	0.41	0.32	-
$\hat{m}_5$	0.79	0.70	0.37	0.35	-
$\hat{m}_6$	0.86	0.66	0.74	0.80	-
$\hat{m}_7$	0.09	0.14	0.25	0.34	-
m_8	0.52	0.54	0.39	0.45	g
m_9	12.48	12.62	11.42	13.91	g
m_{10}	9.84	6.06	5.04	3.88	in

6.4.2 CG Perturbation

Two vertical CG positions are considered here, both with a payload weight of 1,200 lb. The CG is located at a distance of either 1/3 or 1/2 of the cabinet height, as measured from the bottom of the cabinet, and results in a moment of inertia tensor of either $I_{xx} = 200\ \mathrm{kg\,m^2}$, $I_{yy} = 214\ \mathrm{kg\,m^2}$, and $I_{zz} = 68\ \mathrm{kg\,m^2}$, or $I_{xx} = 311\ \mathrm{kg\,m^2}$, $I_{yy} = 325\ \mathrm{kg\,m^2}$, and $I_{zz} = 68\ \mathrm{kg\,m^2}$, respectively. The mass distribution is sysmetric, so the off-diagonal entries $I_{ij} = 0$, for $i \neq j$.

Figure 6.10 summarizes the performance metrics of the system in table 6.5 with the CG at 1/3 or 1/2 payload height, using Control Off or Skyhook control. Regardless of whether the suspension is controlled or uncontrolled, the system with the CG at 1/2 the payload height has an elevated CG position and larger moments of inertia I_{xx} and I_{yy}, causing the payload to be more resistive to rotation. This explains the uniformly improved performance of the 1/2 height CG systems across all ten performance metrics, which is seen in figure 6.10 with the 1/2 height CG metrics closer to the origin than the 1/3 height CG metrics. Metric $\hat{m}_5$ is the only purely translational mode, and the performance for either controlled or uncontrolled is roughly the same regardless of CG position. The Skyhook control provides superior resonance attenuation for all the resonant modes at both 1/3 and 1/2 CG height compared to the Control Off system, with the yaw mode at 1/2 CG being the only exception.

The high frequency isolation metric $\hat{m}_7$ is worse for the controlled system and improves with an increase in inertia. For both CG positions, the controlled system improves the RMS and maximum acceleration metrics m_8 and m_9, respectively. Despite an elevated CG position, the controlled suspension maintains improved attenuation of the relative maximum displacement of the payload (m_{10}) over the passive Control Off system. It must be noted that although raising the CG location generally improves attenuation performance, consideration must be given to the static stability of the system. An asymmetry in the suspension stiffness could cause the payload to lean to one side, which could worsen with an elevated CG location.

6.4.3 Temperature Perturbation

Figure 6.11 summarizes the performance metrics in table 6.6 of the system operating at temperatures of 0^0C and 100^0C, with either Control Off or Skyhook control, and a payload weight of 1,200 lb and the CG located at 1/3 the payload height. Considering the amount the performance metrics change in value, the sys-

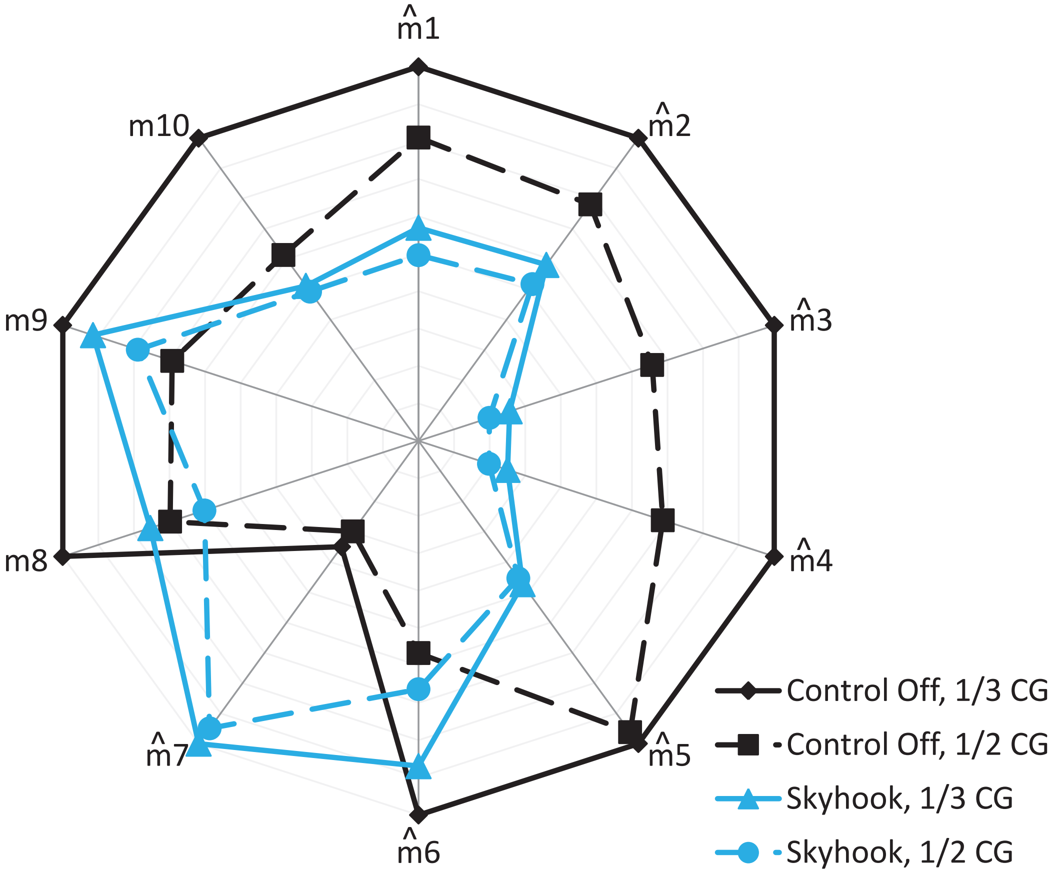

Figure 6.10: Performance metrics of system with the CG at 1/3 or 1/2 payload height, using Control Off or Skyhook control.

Table 6.5: Performance metrics of system with the CG at 1/3 or 1/2 payload height, using Control Off or Skyhook control.

Metric	Control Off, 1/3 CG	Control Off, 1/2 CG	Skyhook, 1/3 CG	Skyhook, 1/2 CG	Units
$\hat{m}_1$	2.66	2.15	1.51	1.32	-
$\hat{m}_2$	1.87	1.47	1.09	0.97	-
$\hat{m}_3$	1.22	0.80	0.31	0.24	-
$\hat{m}_4$	1.63	1.12	0.41	0.32	-
$\hat{m}_5$	0.79	0.76	0.37	0.36	-
$\hat{m}_6$	0.86	0.48	0.74	0.57	-
$\hat{m}_7$	0.09	0.07	0.25	0.24	-
m_8	0.52	0.36	0.39	0.31	g
m_9	12.48	8.64	11.42	9.84	g
m_{10}	9.84	6.04	5.04	4.85	in

tem shows greater robust operation with semi-active Skyhook control compared to without control, especially with metrics m_5 and m_8 - m_{10}. The metrics for the rotational modes (m_1 - m_4, and m_6) are less robust to the change in temperature, but the controlled system is still more robust than with the Control Off. These results are similar to those found in chapter 3 for a single-DOF system excited along its vertical axis. With Skyhook control, the metric m_5 increases only 50% compared to a 130% increase for the Control Off system. The performance of the controlled system is more robust to temperature perturbations than the Control Off system, and the high frequency isolation (m_7) benefits from an increased operating temperature.

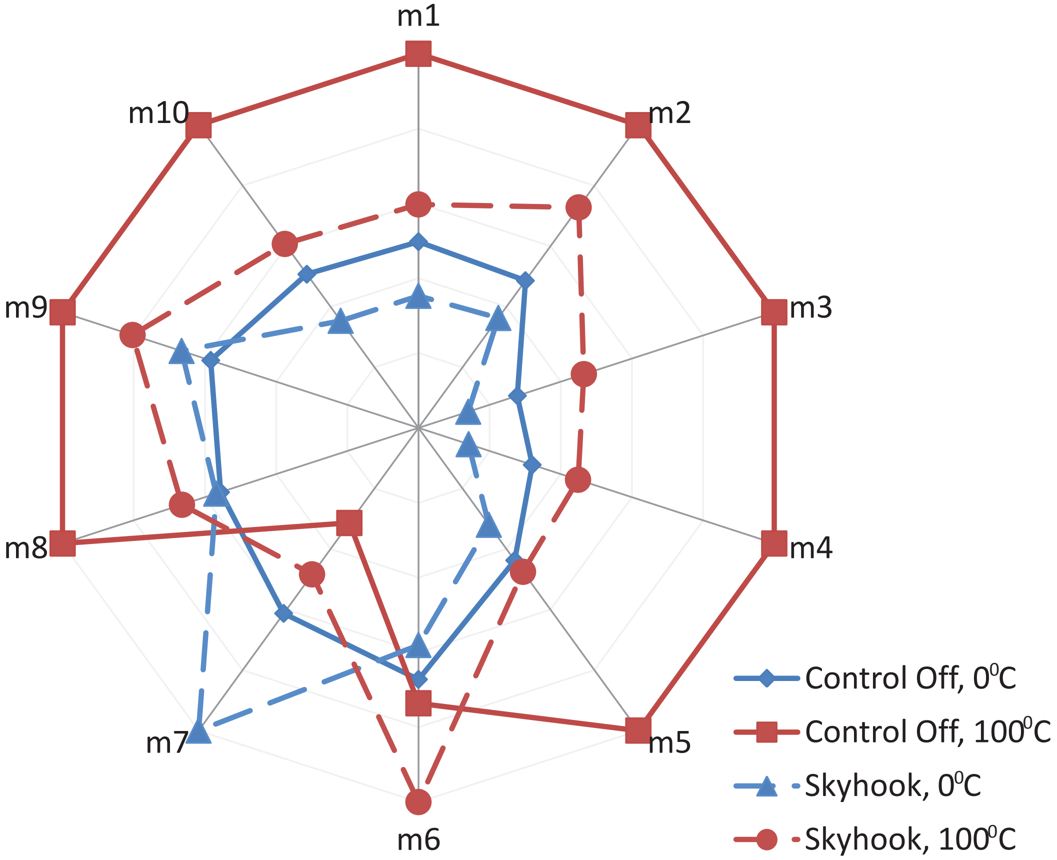

Figure 6.11: Performance metrics of system operating at temperatures of 0^0C and 100^0C, with either Control Off or Skyhook control.

Table 6.6: Performance metrics of system operating at temperatures of 0^0C and 100^0C, with either Control Off or Skyhook control.

Metric	Control Off, 0^{o}C	Control Off, 100^{o}C	Skyhook, 0^{o}C	Skyhook, 100^{o}C	Units
m_1	0.065	0.131	0.046	0.079	g
m_2	0.025	0.051	0.019	0.037	g
m_3	0.081	0.290	0.041	0.135	g
m_4	0.116	0.361	0.051	0.162	g
m_5	0.058	0.133	0.042	0.063	g
m_6	0.083	0.091	0.072	0.124	g
m_7	0.044	0.022	0.071	0.035	g
m_8	0.384	0.691	0.393	0.459	g
m_9	9.481	16.243	10.812	13.050	g
m_{10}	6.500	12.807	4.531	7.783	in

6.5 Conclusions

The configuration of the semi-active suspension was investigated further in this chapter. Effectiveness factors were defined to assess the control authority the suspension had over a practicular system mode. It was shown that the dampers could be oriented in the suspension to provide control authority over all six resonant modes of the system. A performance analysis showed the cubic hexapod configuration offers the best attenuation over all six modes, however at the expense of additional dampers. Reducing the number of linkages (ie. MR dampers) and supporting hardware equates to reducing the cost and maintanance of the suspension. The semi-active suspension can provide control authority over all six modes with less than six dampers. Furthermore, the modular design allows for a scalable suspension, in that dampers and spring elements can be added to the suspension to accommodate a large spectrum of payload masses and geometric sizes.

The performance of centralized and decentralized control philosophies were compared. Centralized control considers the entire state of the system and commands control inputs accordingly, which explains why the performance is superior to decentralized control. While the centralized control provides enhanced performance, the algorithm is dependent on the placement of the dampers, which adds complexity to the implementation. Also, the centralized algorithm is less robust to a loss in control of a signle damper, where decentralized control would be unaffected. Therefore, a trade-off must be established when selecting the control strategy. Importance must be placed on either optimal full-system performance, or on the simplicity and robustness of the suspension that decentralized control provides.

The ability of the semi-active suspension to provide robust performance when the system experiences perturbations in payload mass, CG location, and operating temperature was investigated. Despite a 100% increase in payload mass, a shift in CG from 1/3 to 1/2 the payload height, or a change in operating temperature from 0^0C to 100^0C, the change in most of the performance metrics is small for the controlled system compared to the passive system without control.

Chapter 7

Conclusions

7.1 Original Contributions

A semi-active suspension (Pyramid configuration) was developed and built to provide 6-DOF vibration control for seismic equipment racks for the Mobile Launch Platform. This body of work expands on previous studies of passive suspensions [47] and semi-active, cubic hexapod suspensions [2, 43]. This work considers a modular design with eccentric coil springs and MR dampers, providing the ability to scale the suspension with payload mass and geometric size. The suspension benefits from semi-active, MR fluid technology due to its adaptive capabilities, low power consumption (< 75 W), and stable, fail-safe operation.

7.1.1 MR damper, hydro-mechanical analysis considering temperature

A hydro-mechanical analysis was developed to model MR damper behavior considering temperature, and provides a lump parameter force model with a physical connection to damper geometry and fluid properties. The model was capable of capturing measured force behavior as the operating temperature of the damper increased from 0^0C to 100^0C. Across this temperature range, the yield force decreased up to 30% and the post-yield viscous damping decreased up to 85%. The model captured the effects of the fluid inertia and the pneumatic accumulator pressure, which impacted the post-yield flow of the damper.

7.1.2 Robust operation of MR suspensions to perturbations in temperature, mass, and center of gravity

It was demonstrated that MR suspensions governed by semi-active control are robust to perturbations in temperature, mass, and center of gravity. As temperature increased from 0^0C to 100^0C, the peak transmissibility of a 1-DOF system at resonance increased by only 15%, despite the large reductions in force from the MR damper. As payload mass increased from 46.5 kg to 96 kg, the peak transmissibility at system resonance increased by only 2%. This robust nature of semi-acitve control was explained with equivalent damping, ζ_{eq}. By maintaining $\zeta_{eq} > 0.7$, the transmissibility had low sensitivity to a change in damping, $\Delta\zeta_{eq}$.

The ability of the semi-active 6-DOF suspension to provide robust performance when the system experiences perturbations in payload mass, CG location, and operating temperature was investigated. A 100% increase in payload mass, a shift in center of gravity from 1/3 to 1/2 the payload height, or a change in operating temperature from 0^0C to 100^0C can alter the performance of the system; however, semi-active control provides superior performance over the Control Off system for each perturbation.

7.1.3 Effectiveness of semi-active decentralized control compared to semi-active centralized control

Semi-active decentralized and centralized control laws were established for 6-DOF vibration control. It was demonstrated that centralized control can provide enhanced performance beyond that of decentralized control (specifically for the rotational system modes), however at the expense of algorithm complexity and loss of the robust, fail-safe, independent operation that decentralized control provides. Furthermore, semi-active decentralized control is nearly as effective as semi-active centralized control for many of the multi-objective performance metrics, such as metrics m_5 and m_7 - m_{10}.

7.1.4 Multi-objective performance improvement of the vibration control system

The multi-objective performance of the vibration control system was enhanced with a semi-active MR suspension compared to the state-of-the-art, passive suspension. Experimentally, the suspension (Pyramid configuration) was shown to reduce the transmitted RMS acceleration measured at the cabinet top corner, caused by rocket-induced base disturbances, up to 72%. It was demonstrated that the MR dampers could be oriented in such a way to attenuate all six modes of the system with fewer than 6 dampers. The Trapezoid configuration was shown to improve the RMS acceleration experienced at the payload top corner by 62% over the state-of-

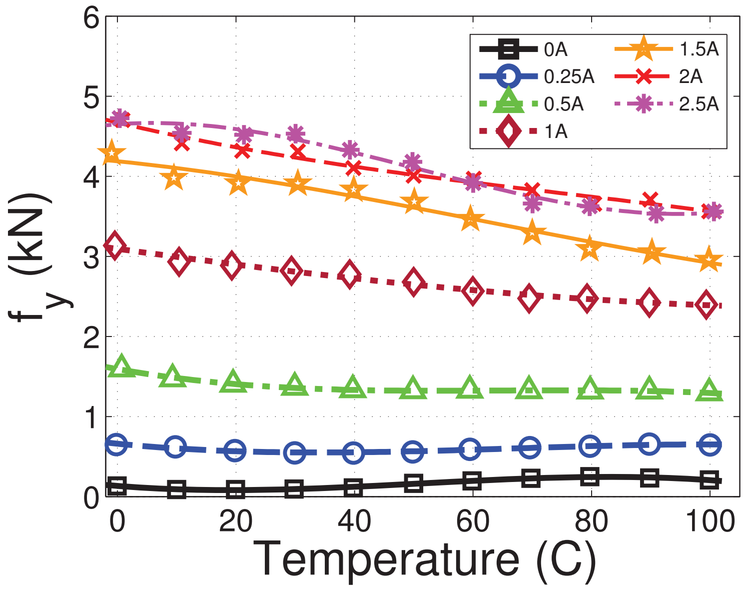

Figure 7.1: MR yield force vs. fluid temperature.

the-art suspension described by Klembczyk and Mosher [47].

7.2 Future Work

This section identifies several topics of research that are suggested by this dissertation for future work.

7.2.1 MR yield force temperature dependence

Future research could investigate the physics behind the loss in MR yield force as fuild temperature increases. Figure 7.1 shows the yield force decreasing up to 30% at an applied current of 2.5 A. This large decrease could not be explained by a change in iron magnetization, MR volume fraction, or Reynolds number alone.

7.2.2 Additional 6-DOF testing

The analysis discussed in chapter 6 was not conducted experimentally due to a lack of testing facility availability. Future work could include experimentally evaluating the alternative damper configurations for a 6-DOF suspension discussed in chapter 6. Figure 7.2 shows both the Vertical and Vee suspension configurations that were built, but never tested. Also, a centralized control strategy could be implemented experimentally and the performance could be compared with decentralized control.

This body of work could also be extended to other applications as well. Similar 6-DOF isolation suspensions can be implemented into systems that are not rigidly attached to the disturbance source, such as high-performance off-road vehicles or marine-based vessels operating in severe disturbance environments (ie. bumpy off-road terrain, or rough ocean conditions).

7.2.3 Multi-body systems

This study could extend the analysis to multi-body systems, such as a system with “ganged” cabinets that are connected to one another, as shown in figure 7.3.

7.2.4 High frequency isolation of the semi-active system

Furthermore, efforts can be made to eliminate the parasitic damping introduced by the semi-active clipping algorithms in order to improve high frequency isolation. Figure 7.4 shows the time delay between the desired and actual applied

(a) Vertical configuration. (b) Vee configuration.

Figure 7.2: 6-DOF MR suspensions that were built, but not tested.

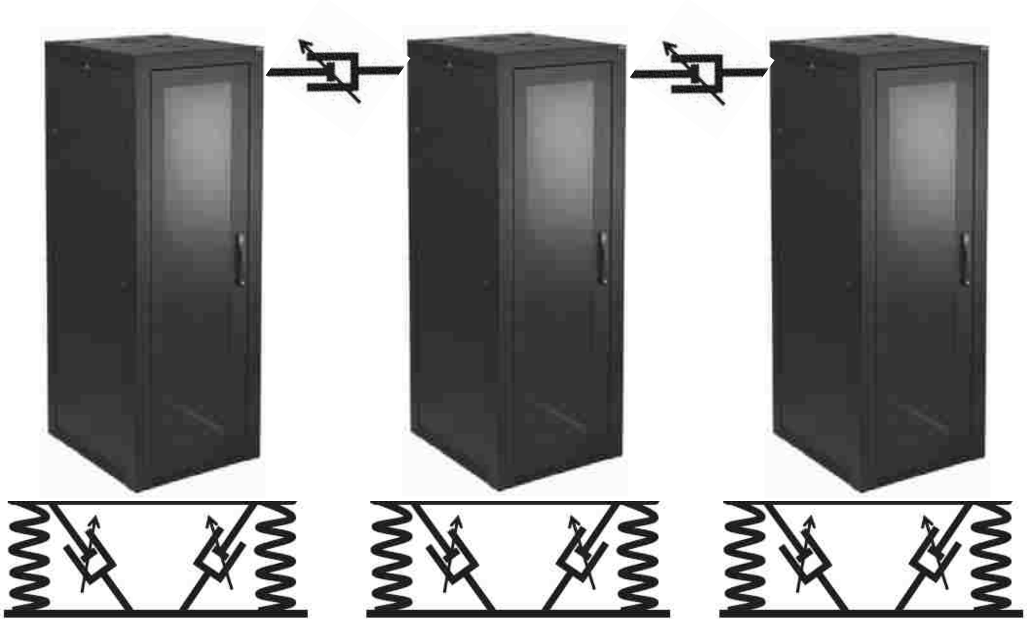

Figure 7.3: Multi-body system of “ganged” cabinets.

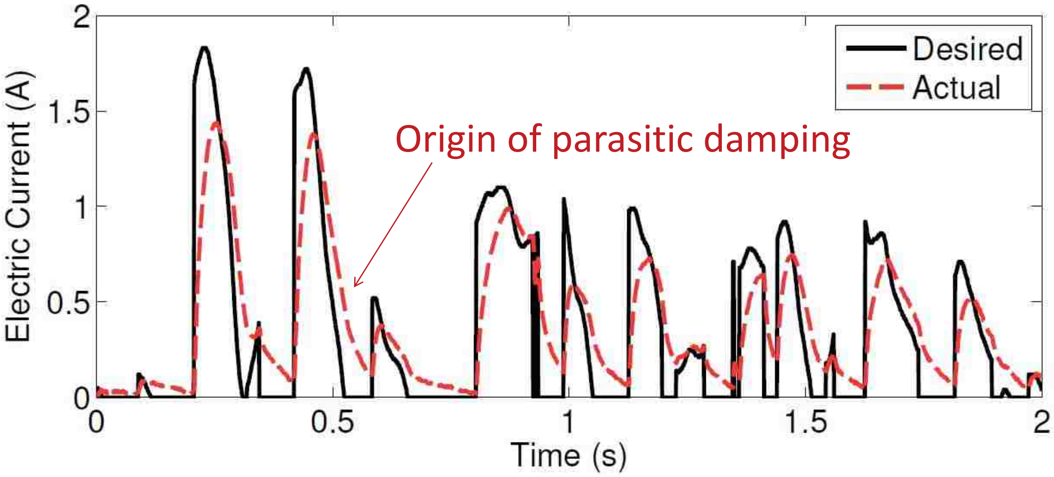

Figure 7.4: Origin of parasitic damping. Time history of desired and actual applied electrical current to the MR damper.

current to the MR damper, and the windows of time when the actual current is greater than the desired current are when unwanted parasitic damping is introduced to the system. Possible approaches to tackle this challenge could include control algorithm improvements to anticipate sharp changes in desired electrical current, or reductions in response time for iron particle chain formation, or implementing a more responsive electro-magnetic circuit between the MR coil and power supply.

Bibliography

[1] Going with the flow. In *The Economist*. The Economist Newspaper Ltd., June 10 . Technology Quarterly: Q2 2004.

[2] Red team too - darpa grand challenge 2005 technical paper. Technical report, Carnegie Mellon University, 5000 Forbes Ave., Pittsburgh, PA 15213, 2005.

[3] Shockwave seats. website, December 23 2011. http://shockwaveseats.com/.

[4] M. Ahmadian and N. Vahdati. Transient dynamics of semiactive suspensions with hybrid control. *Journal of Intelligent Material Systems and Structures*, 17(2):145–153, Feb. 2006. doi: 10.1177/1045389X06056458.

[5] Mehdi Ahmadian, Xubin Song, and Steve C. Southward. No-jerk skyhook control methods for semiactive suspensions. *Journal of Vibrations and Acoustics*, 126(4):580–584, Oct. 2000. doi: 10.1115/1.1805001.

[6] R. W. Balke, R. R. Lynn, and R. K. Wernicke. *Rotary Wing Pylon Mounting System.* U.S. Patent 3,698,663, issued Oct. 17, 1972.

[7] David Batterbee and Neil D. Sims. Temperature sensitive controller performance of mr dampers. *Journal of Intelligent Material Systems and Structures*, 20(3):297–309, 2009. doi: 10.1177/1045389X08093824.

[8] David C. Batterbee, Neil D. Sims, R. Stanway, and M. Rennison. Magnetorheological landing gear: 2. validation using experimental data. *Smart Materials and Structures*, 16(6):2441–2452, 2007. doi: 10.1088/0964-1726/16/6/047.

[9] M. Brigley, Y. T. Choi, N. M. Wereley, and S. B. Choi. Magnetorheological isolators using multiple fluid modes. *Journal of Intelligent Material Systems and Structures*, 18(12):1143–1148, Dec. 2007. doi: 10.1177/1045389X07083129.

[10] Tetsuro Butsuen. *The Design of Semi-Active Suspensions for Automotive Vehicles.* PhD dissertation, Massachusetts Institute of Technology, Department of Mechanical Engineering, 1989.

[11] J. D. Carlson. What makes a good mr fluid. In *MR Technology Workshop*, Tokyo, Japan, 2008. Lord Corporation.

[12] J. David Carlson. Mr fluids and devices in the real world. *ER Fluids and MR Suspensions, 9th Proceedings*, pages 531–538, 2004.

[13] J. David Carlson and Mark R. Jolly. Mr fluid, foam and elastomer devices. *Mechatronics*, 10(4-5): 555–569, June 2000. doi: 10.1016/S0957-4158(99)00064-1.

[14] Sevki Çeşmeci and Tahsin Engin. Modeling and testing of a field-controllable magnetorheological fluid damper. *International Journal of Mechanical Sciences*, 52(8):1036–1046, Aug. 2010. doi: 10.1016/j.ijmecsci.2010.04.007.

[15] Y. A. Çengel and M. A. Boles. *Thermodynamics: An Engineering Approach.* McGraw-Hill, New York, NY, 4th edition, 2002.

[16] S. B. Choi, Y. T. Choi, D. W. Park, and H. G. Lee. A robust feedback control of a full-car er suspension system. In *Proceedings of SPIE, Passive Damping and Isolation*, volume 3329, pages 439–450, San Diego, CA, U.S.A., March 1998. SPIE. doi: 10.1117/12.316913.

[17] S. B. Choi, Young Tai Choi, and D. W. Park. A sliding mode control of a full-car electrorheological suspension system via hardware-in-the-loop simulation. *Journal of Dynamic Systems, Measurement and Control*, 122(1):114–121, March 2000. doi: 10.1115/1.482435.

[18] Y.-T. Choi and N. M. Wereley. Vibration control of a landing gear system featuring electrorheological/magnetorheological fluids. *AIAA Journal of Aircraft*, 40(3):432–439, 2003. doi: 10.2514/2.3138.

[19] Y.-T. Choi and N. M. Wereley. Vibration control of a landing gear system featuring electrorheological/magnetorheological fluids. *AIAA Journal of Aircraft*, 40(3):432–439, 2003. doi: 10.2514/2.3138.

[20] Y.-T. Choi and N. M. Wereley. Biodynamic response mitigation to shock loads using magnetorheological helicopter crew seat suspensions. *AIAA Journal of Aircraft*, 42(5):1288–1295, Sept. - Oct. 2005. doi: 10.2514/1.6839.

[21] Young Tai Choi and Norman M. Wereley. Mitigation of biodynamic response to vibratory and blast-induced shock loads using magnetorheological seat suspensions. *Proc. Inst. Mech. Eng., Part D: Journal of Automobile Engineering*, 219(6):741–753, June 2005. doi: 10.1243/095440705X28330.

[22] Young Tai Choi, Norman M. Wereley, and Young Sik Jeon. Semi-active vibration isolation using magnetorheological isolators. *AIAA Journal of Aircraft*, 42(5):1244–1251, September 2005.

[23] D. Cleveland, L. J. O'Brien, and Norman M. Wereley. An automated aid for isolating defects in the heat exchanger tubing of nuclear steam generators. *ISA Transactions*, 25(3):61–72, 1986.

[24] Roy R. Craig and Andrew J. Kurdila. *Fundamentals of Structural Dynamics*. John Wiley, Hoboken, N.J., 2nd edition, 2006.

[25] C. E. Crede. *Vibrations and Shock Isolation*. John Wiley & Sons, Inc., New York, 1951.

[26] M. Baris Dogruoz, Eric L. Wang, Faramarz Gordaninejad, and Arthur J. Stipanovic. Augmenting heat transfer from fail-safe magnetorheological fluid dampers using fins. *Journal of Intelligent Material Systems and Structures*, 14(2):79–86, Feb. 2003. doi: 10.1177/1045389X03014002002.

[27] Y. Dong-won, S. Young-su, P. Hee-chang, C. Sang-kyu, and P. Cheol-hun. Design of a novel mr rotary brake. In *World Congress on Computer Science and Information Engineering*, pages 664–668, Los Angeles, CA, USA, Mar. - Apr. 2009. IEEE. doi: 10.1109/CSIE.2009.757.

[28] S. J. Dyke, B. F. Spencer, M. K. Sain, and J. D. Carlson. Modeling and control of magnetorheological dampers for seismic response reduction. *Smart Materials and Structures*, 5(5):565–575, 1996. doi: 10.1088/0964-1726/5/5/006.

[29] D. R. Gamota and F. E. Filisko. Dynamic mechanical studies of electrorheological materials: Moderate frequencies. *Journal of Rheology*, 35(3):399–425, 1991. doi: 10.1122/1.550221.

[30] H. Gavin, J. Hoagg, and M. Dobossy. Optimal design of mr dampers. In *Proc. U.S.-Japan Workshop on Smart Structures for Improved Seismic Performance in Urban Regions*, pages 225–236, Seattle, WA, USA, Aug. 2001.

[31] Faramarz Gordaninejad and Darrell G. Breese. Heating of magnetorheological fluid dampers. *Journal of Intelligent Material Systems and Structures*, 10(8):634–645, Aug. 1999. doi: 10.1106/55D1-XAXP-YFH6-B2FB.

[32] V. E. Gough. Contribution to discussion of papers on research in automotive stability, control and tyre performance. *Proc. Auto Div. Inst. Mech. Eng.*, pages 392–394, 1956-1957.

[33] Rebecca Grilli, Ramkumar Krishnan, Wei Hu, Norman M. Wereley, and Thierry Sieg. Mechanisms-based analysis of filled elastomeric dampers under single and dual frequency excitations. *Journal of the American Helicopter Society*, 53(3):252–266, July 2008. doi: 10.4050/JAHS.53.252.

[34] T. Gunston and M. J. Griffin. The isolation performance of a suspension seat over a range of vibration magnitudes tested with an anthropodynamic dummy and human subjects. In *Proceedings of the* 28^{th} *International Congress and Exposition on Noise Control Engineering*, pages 949–954, Florida, U.S.A., December 1999. INCE-USA.

[35] Shuqi Guo, Shaopu Yang, and Cunzhi Pan. Dynamic modeling of magnetorheological damper behaviors. *Journal of Intelligent Material Systems and Structures*, 17(1):3–14, 2006. doi: 10.1177/1045389X06055860.

[36] Ahmed Abu Hanieh. *Active Isolation and Damping of Vibrations via Stewart Platform*. PhD dissertation, Universite Libre De Bruxelles, Department of Mechanical Engineering and Robotics, 2003.

[37] G. Hiemenz, W. Hu, G. Ngatu, and N. Wereley. Rotary vane magnetorheological (mr) energy absorber, Dec. 2010. U.S. Patent 2010/0300819 A1.

[38] Gergory J. Hiemenz, Wei Hu, and Norman M. Wereley. Semi-active magnetorheological helicopter crew seat suspension for vibration isolation. *AIAA Journal of Aircraft*, 45(3):945–953, 2008. doi: 10.2514/1.32736.

[39] Gregory J. Hiemenz, Wei Hu, and Norman M. Wereley. Semi-active magnetorheological helicopter crew seat suspension for vibration isolation. In *48th AIAA/ASME/ASCE/AHS/ASC Structures, Structural Dynamics, and Materials Conference*, Honolulu, Hawaii, April 2007. AIAA.

[40] S. R. Hong, S. B. Choi, Young Tai Choi, and Norman M. Wereley. A hydro-mechanical model for hysteretic damping force prediction of ef damper: Experimental verification. *Journal of Sound and Vibration*, 285(4-5):1180–1188, February 2005. doi: 10.1016/j.jsv.2004.10.031.

[41] W. Hu and N. M. Wereley. Magnetorheological fluid and elastomeric lag damper for helicopter stability augmentation. *International Journal of Modern Physics Part B*, 19(7-9):1471–1477, 2005. doi: 10.1142/S0217979205030463.

[42] Wei Hu, Nicholas L. Wilson, Gregory J. Hiemenz, and Norman M. Wereley. Magnetorheological shock absorber for crew seats in the expeditionary fighting vehicle. In *Conference on Smart Materials, Adaptive Structures and Intelligent Systems*, Ellicott City, MD, October 2008. ASME.

[43] Pierrick Jean, Roger Ohayon, and Dominique Le Bihan. Semi-active control using magneto-rheological dampers for payload launch vibration isolation. In *Smart Structures and Materials 2006: Damping and Isolation*, volume 6169, San Diego, CA, U.S.A., Feb. 27 - Mar. 1 2006. SPIE.

[44] Gopalakrishna M. Kamath and Norman M. Wereley. Nonlinear viscoelastic-plastic mechanisms-based model of an electrorheological damper. *Journal of Guidance, Control, and Dynamics*, 20(6):1125–1132, 1997. doi: 10.2514/2.4167.

[45] Dean C. Karnopp, Michael J. Crosby, and R. A. Harwood. Vibration control using semi-active force generators. *Journal of Engineering for Industry*, 96(2):619 – 626, May 1974.

[46] M. Kciuk and R. Turczyn. Properties and application of magnetorheological fluids. *Journal of Achievements in Materials and Manufacturing Engineering*, 18(1-2):127–130, 2006.

[47] Alan R. Klembczyk and Michael W. Mosher. Simulation, development, and field measurement validation of an isolation system for a new electronics cabinet in the space shuttle launch environment within the mobile launch platform. Technical report, Taylor Devices, Inc., Carleton Technologies, Inc., New York, 2006.

[48] N. M. Kwok, Q.P. Ha, T. H. Nguyen, J. Li, and B. Samali. A novel hysteretic model for magnetorheological fluid dampers and parameter identification using particle swarm optimization. *Sensors and Actuators A: Physical*, 132(2):441–451, 2006. doi: 10.1016/j.sna.2006.03.015.

[49] Yanming Liu, Faramarz Gordaninejad, Cahit A. Evrensel, Umit Dogruer, Moon Su Yeo, Enver S. Karakas, and Alan Fuchs. Temperature dependent skyhook control of hmmwv suspension using a failsafe magneto-rheological damper. In *Proceedings of the SPIE, Smart Structures and Materials: Industrial and Commercial Applications of Smart Structures Technologies*, volume 5054, pages 332–340, San Diego, CA, 2003. SPIE.

[50] Kamran Majidifakhr, Siavash Kazemirad, and Farzam Farahmand. Robotic assisted reduction of femoral shaft fractures using stewart platform. In J. D. Westewood, editor, *Medicine Meets Virtual Reality 17 - NextMed: Design for/the Well Being*, volume 142, pages 177–179. IOS Press, 2009.

[51] Min Mao, Young-Tai Choi, and Norman M. Wereley. Effective design strategy for a magneto-rheological damper using a nonlinear flow model. In *Smart Structures and Materials 2005: Damping and Isolation*, volume 5760, pages 446–455. SPIE, May 2005.

[52] Min Mao, Wei Hu, Norman M. Wereley, Alan L. Browne, and John C. Ulicny. A nonlinear analytical model for magnetorheological energy absorbers under impact conditions. In *Proceedings of ASME Conference on Smart Materials, Adaptive Structures and Intelligent Systems*, Oxnard, CA, U.S.A., September 2009. ASME.

[53] MATLAB. In *Partial Differential Equation Toolbox*, Natick, MA, 2009. The Math Works, Inc.

[54] Michael McKee, Xiaojie Wang, and Faramarz Gordaninejad. Behavior of a compressible magnetorheological fluid damper at high temperatures. In *Proc. ASME 2011 Conference on Smart Materials, Adaptive Structures and Intelligent Systems*, Scottsdale, AZ, USA, Sept. 2011. ASME.

[55] Leonard Meirovitch. *Fundamentals Of Vibrations*. McGraw-Hill, New York, NY, 2001.

[56] Lane R. Miller. *An Approach to Semi-Active Control of Multiple Degree-of-Freedom Systems*. PhD dissertation, North Carolina State University, Department of Mechanical and Aerospace Engineering, 1988.

[57] Allan H. Morrish. *The Physical Principles of Magnetism*. IEEE Press, New York, NY, 2001.

[58] Norman S. Nise. *Control Systems Engineering*. John C. Wiley, Inc., 4th edition, 2004.

[59] Erik Oberg, Franklin D. Jones, Holbrook L. Horton, and Henry H. Ryfel. *Machinery's Handbook*. Industrial Press Inc., New York, 1996.

[60] Chanho Park and Doyoung Jeon. Semiactive vibration control of a smart seat with an mr fluid damper considering its time delay. *Journal of Intelligent Material Systems and Structures*, 13(7-8):521–524, July 2002. doi: 10.1106/104538902030343.

[61] D. J. Peel, R. Stanway, and W. A. Bullough. Dynamic modelling of an er vibration damper for vehicle suspension applications. *Smart Materials and Structures*, 5(5):591–606, 1996. doi: doi:10.1088/0964-1726/5/5/008.

[62] David L. Platus. Negative-stiffness-mechanism vibration isolation systems. In *Vibration Control in Microelectronics, Optics, and Metrology*, volume 1619, pages 44–54. SPIE, 1991.

[63] J. A. Powell. Application of a nonlinear phenomenological model to the oscillatory behavior of er materials. *Journal of Rheology*, 39(5):1075–1094, 1995. doi: 10.1122/1.550618.

[64] Huseyin Sahin, Xiaojie Wang, and Faramarz Gordaninejad. Temperature dependence of magneto-rheological materials. *Journal of Intelligent Material Systems and Structures*, 20(18):2215–2222, 2009. doi: 10.1177/1045389X09351608.

[65] P. D. Samuel and D. J. Pines. A review of vibration-based techniques for helicopter transmission diagnostics. *Journal of Sound and Vibration*, 282(1-2):475–508, April 2005. doi: 10.1016/j.jsv.2004.02.058.

[66] Pan Sheng, Wu Jianyao, Hu Lin, Shen Feng, Sun Meng, and Zhou Luwei. Yield stress temperature effect of magneto-rheological fluids. *Journal of Functional Materials*, 28(3):264–267, 1997.

[67] D. E. Simon and M. Ahmadian. An alternative semiactive control method for sport utility vehicles. *Proc. Inst. Mech. Eng., Part D: Journal of Automobile Engineering*, 216(2):125–139, Feb. 2002. doi: 10.1243/0954407021528977.

[68] Neil D. Sims, N. J. Holmes, and R. Stanway. A unified modelling and model updating procedure for electrorheological and magnetorheological vibration dampers. *Journal of Smart Materials and Structures*, 13(1):100–121, 2004. doi: 10.1088/0964-1726/13/1/012.

[69] R. Singh, G. Kim, and P. V. Ravindra. Linear analysis of automotive hydro-mechanical mount with emphasis on decoupler characteristics. *Journal of Sound and Vibration*, 158(2):219–243, 1992. doi: 10.1016/0022-460X(92)90047-2.

[70] D. Stewart. A platform with six degrees of freedom. *Proc. Institution of Mechanical Engineers*, 180 (1):371–386, June 1965. doi: 10.1243/PIME_PROC_1965_180_029_02.

[71] D. Thayer, M. Campbell, and J. Vagners. Six axis vibration isolation using modern control techniques. In *Proc. 21st Annual AAS Guidance and Control Conference*, Breckenridge, CO, USA, Feb. 1998. AAS.

[72] Memet Unsal. *Semi-Active Vibration Control of a Parallel Platform Mechanism Using Magnetorheological Damping*. PhD dissertation, University of Florida, Department of Mechanical and Aerospace Engineering, 2006.

[73] Arthur Munzenmaier Wahl. *Mechanical Springs*. Penton Pub. Co., 1944.

[74] D. H. Wang and W. H. Liao. Magnetorheological fluid dampers: A review of parametric modelling. *Smart Materials and Structures*, 20(2):264–267, 2011. doi: 10.1088/0964-1726/20/2/023001.

[75] J. Wang, G. Meng, N. Feng, and E. J. Hahn. Dynamic performance and control of squeeze mode mr fluid damper-rotor system. *Smart Materials and Structures*, 14(4):529–539, 2005. doi: 10.1088/0964-1726/14/4/011.

[76] N. M. Wereley, Y.-T. Choi, and H. J. Singh. Adaptive energy absorbers for drop-induced shock mitigation. *Journal of Intelligent Material Systems and Structures*, 22(6):515–519, 2011. doi: 10.1177/1045389X10393767.

[77] Norman M. Wereley and Li Pang. Nondimensional analysis of semi-active electrorheological and magnetorheological dampers using approximate parallel plate models. *Smart Materials and Structures*, 7 (5):732–743, 1998. doi: 10.1088/0964-1726/7/5/015.

[78] Norman M. Wereley, Li Pang, and Gopalakrishna M. Kamath. Idealized hysteresis modeling of electrorheological and magnetorheological dampers. *Journal of Intelligent Material Systems and Structures*, 9(8):642–649, Aug. 1998. doi: 10.1177/1045389X9800900810.

[79] N. Wilson, N. Wereley, W. Hu, and G. Hiemenz. Analysis of a magnetorheological damper incorporating temperature dependence. *International Journal of Vehicle Design*. (In review).

[80] P. L. Wong, R. Wang, and S. Lingard. Pressure and temperature dependence of the density of liquid lubricants. *Wear*, 201(1-2):58–63, Dec. 1996. doi: 10.1016/S0043-1648(96)06980-3.

[81] Guangqiang Yang, Billie F. Spencer Jr., Hyung-Jo Jung, and J. David Carlson. Dynamic modeling of large-scale magnetorheological damper systems for civil engineering applications. *Journal of Engineering Mechanics*, 130(9):1107 (8 pages), Sept. 2004. doi: 10.1061/(ASCE)0733-9399(2004)130:9(1107).

[82] X.-J. Zhang, A. Farjoud, M. Ahmadian, K.-H. Guo, and M. Craft. Dynamic testing and modeling of an mr squeeze mount. *Journal of Intelligent Material Systems and Structures*, 22(15):1717–1728, Oct. 2011. doi: 10.1177/1045389X11424217.

[83] L. Zheng, Y. N. Li, and A. Baz. Fuzzy-sliding mode control of semi-active suspension systems with mr dampers. In F. Gordaninejad, editor, *Proc. on Electrorheological Fluids and Magnetorheological Suspensions*, pages 487–495. World Scientific, 2007.